Universitat
de les Illes Balears

Departament de Física

DOCTORAL THESIS
2017

HIGH-FREQUENCY WAVES AND INSTABILITIES IN MULTI-FLUID PARTIALLY IONIZED SOLAR PLASMAS

David Martínez Gómez

Universitat
de les Illes Balears

Departament de Física

DOCTORAL THESIS
2017
Doctoral Programme of Physics

HIGH-FREQUENCY WAVES AND INSTABILITIES IN MULTI-FLUID PARTIALLY IONIZED SOLAR PLASMAS

David Martínez Gómez

Thesis Supervisor: Roberto Soler Juan
Thesis Supervisor: Jaume Terradas Calafell
Thesis Tutor: Alicia Sintes Olives

Doctor by the Universitat de les Illes Balears

Universitat
de les Illes Balears

WE, THE UNDERSIGNED, DECLARE:

That the Thesis titled “High-frequency waves and instabilities in multi-fluid partially ionized solar plasmas”, presented by Sr. David Martínez Gómez to obtain a doctoral degree, has been completed under the supervision of Drs. Roberto Soler Juan and Jaume Terradas Calafell and meets the requirements to opt for an International Doctorate.

For all intents and purposes, we hereby sign this document:

Sr. David Martínez Gómez

Dr. Roberto Soler Juan

Dr. Jaume Terradas Calafell

Palma de Mallorca,

A mis padres y mi hermano

Contents

Summary

The solar atmosphere is a highly dynamic environment in which a huge diversity of waves and instabilities has been detected. The matter in that region is in plasma state, and thus is affected by the presence of electromagnetic fields. To understand its dynamics, a theory that combines the equations describing the properties and evolution of fluids with those for electric and magnetic fields is required.

Among the several available alternatives that fulfill the mentioned conditions, ideal magnetohydrodynamics (MHD) is a useful description when the phenomena of interest are associated with low frequencies. For long temporal scales, all the species that compose a plasma are strongly coupled and they can be treated as a single fluid. However, when the temporal scales are shorter, the coupling is weaker and collisions between the different species produce a deviation on the properties of waves from those predicted by ideal MHD. Consequently, a more complex and accurate theory is needed.

In this Thesis, a multi-fluid theory that takes into account the effects of ion-neutral collisions, Coulomb collisions and magnetic diffusivity, and makes use of a generalized Ohm's law that includes Hall's term is presented. Then, it is applied to the investigation of waves and instabilities in several layers and structures of the solar atmosphere, such as the fully ionized solar corona and solar wind, and the partially ionized chromosphere and quiescent prominences or filaments.

By means of numerical simulations and the analysis of the dispersion relation for small-amplitude transverse perturbations, the impact of collisions on the properties of the low-frequency Alfvén waves and the high-frequency ion-cyclotron and whistler modes is studied. It is shown that the damping caused by collisional friction is dominated by the ion-neutral interaction at low frequencies and by Coulomb collisions and magnetic diffusivity at high frequencies. Moreover, the cut-off regions and resonances that the ion-cyclotron waves have in collisionless fluids are removed when collisions are taken into account. It is also demonstrated that the consideration of Hall's term in the induction equation is fundamental for the proper description of high-frequency waves in weakly ionized plasmas.

Non-linear effects, such as heating, and perturbations of large-amplitude are also studied. On the one hand, it is shown that the ponderomotive force generated by non-linear Alfvén waves, which induces variations of density and pressure of the plasma, is greatly affected by the interaction of ions with neutrals. On the other hand, friction due to collisions causes dissipation of the energy of the perturbations. A fraction of that energy is transformed into heat and rises the temperature of the fluid. In this way, the plasma in quiescent prominences or in the chromosphere may be heated by ion-neutral collisions.

Finally, the effect of shear flows at the interface between two partially ionized media are also investigated. The presence of a shear flow velocity leads to the development of the Kelvin-Helmholtz instability. Here, the onset of such instability is studied for partially ionized magnetic flux tubes and an application to cylindrical filament threads is given. It is found that the collisional coupling between ions and neutrals reduces the growth rates of the instability for sub-Alfvénic shear flows but cannot completely suppress it, which means that partially ionized plasmas are unstable for any value of the shear flow. The comparison of the analytical results with observations performed by other authors show that, for a range of parameters of the perturbations, the computed growth rates are compatible with the typical lifetimes of threads.

Resumen en castellano

La atmósfera solar es un ambiente altamente dinámico en el que se ha detectado una gran variedad de ondas e inestabilidades. La materia en tal región se encuentra en estado de plasma, por lo que es afectada por la presencia de campos electromagnéticos. Para comprender su dinámica, se requiere una teoría que combine las ecuaciones que describen las propiedades y evolución de los fluidos con las de los campos eléctricos y magnéticos.

Entre las diferentes alternativas disponibles que cumplen las condiciones mencionadas, la magnetohidrodinámica (MHD) ideal es una descripción útil cuando los fenómenos de interés están asociados a frecuencias bajas. Para escalas temporales largas, las especies componentes del plasma están fuertemente acopladas y pueden ser tratadas como un fluido único. Para escalas temporales más cortas, el acoplamiento es más débil y las colisiones entre las distintas especies producen un desvío en las propiedades de las ondas respecto a las predichas por la MHD ideal. Consecuentemente, se necesita una teoría más compleja y precisa.

En esta Tesis se presenta una teoría multi-fluido que tiene en cuenta los efectos de las colisiones ión-neutro, las colisiones de Coulomb y la difusividad magnética, y usa una ley de Ohm generalizada que incluye el término de Hall. Tal teoría es luego aplicada a la investigación de ondas e inestabilidades en varias capas y estructuras de la atmósfera solar, como la corona y el viento solar, que están completamente ionizados, y la cromosfera y protuberancias, que se hayan parcialmente ionizadas.

Mediante simulaciones numéricas y el análisis de la relación de dispersión para perturbaciones transversales de pequeña amplitud, se estudia el impacto que las colisiones tienen en las propiedades de las ondas de Alfvén, de baja frecuencia, y los modos ión-ciclotrón y *whistler*, de alta frecuencia. El atenuamiento causado por la fricción debida a las colisiones está dominado por la interacción ión-neutro a bajas frecuencias y por las colisiones de Coulomb y la difusividad magnética a altas frecuencias. Además, las regiones de corte y resonancias que las ondas ión-ciclotrón tienen en fluidos sin colisiones desaparecen cuando éstas son tenidas en cuenta. También se muestra que la inclusión del término de Hall es fundamental para describir correctamente las ondas de alta frecuencia en plasmas débilmente ionizados.

También se estudian efectos no lineales, como el calentamiento, y perturbaciones de gran amplitud. Por una parte, se demuestra que la fuerza ponderomotriz generada por ondas de Alfvén no lineales, que causan variaciones en la densidad y presión del plasma, es fuertemente afectada por la interacción de iones con neutros. Por otra, la fricción debida a colisiones causa la disipación de la energía de las perturbaciones. Una fracción de esa energía es transformada en calor y aumenta la temperatura del fluido. Así, el plasma en una protuberancia quiescente o en la cromosfera puede ser calentado mediante las colisiones ión-neutro.

Finalmente, también se investiga el efecto de flujos de cizalladura en la interfaz entre dos medios parcialmente ionizados. La presencia de dichos flujos lleva al desarrollo de la inestabilidad de Kelvin-Helmholtz. Aquí, se estudia la fase inicial de dicha inestabilidad, con la aplicación al caso particular de hilos cilíndricos de filamentos solares. El acoplamiento mediante colisiones entre iones y neutros reduce los ritmos de crecimiento de la inestabilidad para flujos sub-Alfvénicos pero no evita por completo su aparición, lo que significa que los plasmas parcialmente ionizados son inestables para cualquier valor del flujo de cizalladura. La comparación de los resultados analíticos con observaciones realizadas por otros autores muestra que, para un rango de parametros de las perturbaciones, los ritmos de crecimiento calculados

son compatibles con la vida media típica de los hilos.

Resum en català

L'atmosfera solar és un ambient altament dinàmic en el que s'ha detectat una gran varietat d'ones i inestabilitats. La matèria en aquesta regió es troba en estat de plasma, i per tant es veu afectada per la presència de camps electromagnètics. Per comprendre la seva dinàmica es requereix una teoria que combini les equacions que descriuen les propietats i l'evolució dels fluids amb les del camps elèctrics i magnètics.

De les diverses alternatives disponibles que compleixen els requeriments anteriorment citats, la magnetohidrodinàmica (MHD) ideal és una descripció útil quan els fenòmens d'interès estan associats a freqüències baixes. Per escales temporals llargues, les espècies que componen el plasma es troben fortament acoblades i poden ser tractades com a un únic fluid. Pel contrari, quan les escales temporals són més curtes, l'acoblament és més feble i les col·lisions entre les distintes espècies produeixen desviacions en les propietats de les ones respecte a les esperades en MHD ideal. En conseqüència, és necessàri una teoria més complexa i precisa.

En aquesta Tesi es presenta una teoria multi-fluid que té en compte els efectes de les col·lisions ió-neutre, les col·lisions de Coulomb i la difusivitat magnètica, i utilitza una llei d'Ohm generalitzada que inclou el terme de Hall. Aquesta teoria s'aplica a la invesigació d'ones i inestabilitats en diverses capes i estructures de l'atmosfera solar, com són la corona i el vent solar, que estan completament ionitzats, i la cromosfera i protuberàncies, que es troben parcialment ionitzats.

Mitjançat les simulaciones numèriques i l'anàlisi de la relació de dispersió per pertorbacions transversals de petita amplitud, s'estudia l'impacte que les col·lisions tenen en les propietats de les ones d'Alfvén, de baixa freqüència i els modes ió-ciclotró i *whistler*, d'alta freqüència. L'atenuació produïda per la fricció deguda a les col·lisions està dominada per la interacció ió-neutre a baixes freqüències i per les col·lisions de Coulomb i la difusivitat magnètica a altes freqüències. A més, les regions de tall i ressonàncies que les ones ió-ciclotró tenen en els fluids sense col·lisions desapareixen quan aquestes s'inclouen al model. També s'ha trobat que l'efecte del terme de Hall és fonamental per descriure correctament les ones d'alta freqüència en plasmes dèbilment ionitzats.

També s'estudien efectes no lineals, com és l'escalfament, i pertorbacions de gran amplitud. Per una banda, se demostra que la força ponderomotriu generada per ones d'Alfvén no lineals, que causen variacions en la densitat i pressió del plasma, està fortament afectada per la interacció del ions amb els neutres. Per altra banda, la fricció deguda a les col·lisions causa la dissipació de l'energia de les pertorbacions. Una fracció d'aquesta energia és transformada en calor i augmenta la temperatura del fluid. D'aquesta manera, el plasma en una protuberància quiescent o en la cromosfera pot ser escalfat mitjançant les col·lisions ió-neutre.

Finalment, també s'investiga l'efecte d'un flux amb cisalladura en l'interfase entre dos medis parcialment ionitzats. La presència del flux dona lloc al desenvolupament de l'inestabilitat de Kelvin-Helmholtz. Aquí, s'estudia la fase inicial d'aquesta inestabilitat, aplicada al cas particular de fils cilíndrics en filaments solars. L'acoblament a través de les col·lisions entre ions i neutres redueix el ritme de creixement de l'inestabilitat per fluxos sub-Alfvénics però no evita per complet la seva aparició, el que significa que els plasmes parcialment ionitzats són inestables per qualsevol valor del flux de cisalladura. La comparació dels resultats analítics amb observacions realitzades per altres autors mostra que, per un rang de paràmetres de les pertorbacions, els ritmes de creixement calculats són compatibles amb la vida mitja típica dels fils a protuberàncies.

Acknowledgments

The present Thesis is the result of more than four years of work, which could not have been carried out without the support of a quite large number of people. That is why I would like to thank all those who, in one way or another, have helped me in completing this long-term goal.

In the first place, I would like to thank Prof. José Luis Ballester for giving me the chance to become a member of the Solar Physics Group of the University of Balearic Islands, and Drs. Jaume Terradas and Roberto Soler for guiding and supervising my research during my time as a PhD student. Their extensive knowledge on the field of solar physics, and their experience and advice have been essential for the development of this Thesis. I would also like to thank the remaining present and former members of this fantastic group, Ramón Oliver, Marc Carbonell, Maciej Zápior, Toni Díaz, Andreu Adrover, Nabil Freij and Elie Soubrié, for the nice and friendly work environment that I could enjoy during these years. I have been very fortunate to spend my working time in such a good company.

Then, I am very grateful to Drs. Tom Van Doorsselaere and Marcel Goossens, from the Centre for mathematical Plasma-Astrophysics (KU Leuven, Belgium), and Drs. Judith Karpen and Karin Muglach, from the Goddard Space Flight Center (NASA, USA), for their kind hospitality during my stays at their respective institutions.

I acknowledge the financial support from the Ministerio de Economía y Competitividad through an FPI fellowship and additional grants that allowed me to visit the aforementioned foreign centers and to attend to several scientific meetings and workshops.

Back to the islands, there are many people who deserve to be mentioned for making my life in Mallorca easier or more amusing, or both. Thus, I am grateful to my office mates, Diego Carrió, Aquilina Pérez, Miguel Bezares, Alex Vañó, Moner Al Chawa and Daniel Salas, and to members of other research groups like Ángel Amores, María Cardell, David Morate, Borja Miñano and Fabio Galán. I also give my sincere thanks to Toni Mesquida, Víctor Lillo, María Hidalgo and Mario Rodríguez.

In addition, since there is a world beyond the Balearic Islands, I want to mention a few people who are still very important to me despite the distance that now exists between us. Therefore, I would like to thank Pablo Rodríguez, Luis Marcos, Laura Fernández and Estefanía Casal for our long-lasting friendship.

And last but not least, I would like to thank my brother, Héctor, for all the good moments we have shared, and my parents, Agustín and Pastora, for all the efforts they have made so that I could reach this far, through a rather lengthy journey since my first "why?".

I am really grateful to all of you!

List of publications

The research included in this Thesis has been published in the following peer-reviewed articles:

1. David Martínez-Gómez, Roberto Soler, and Jaume Terradas; 2015, *Onset of the Kelvin-Helmholtz instability in partially ionized magnetic flux tubes*, Astronomy and Astrophysics, 578, A104.
2. David Martínez-Gómez, Roberto Soler, and Jaume Terradas; 2016, *Multi-fluid approach to high-frequency waves in plasmas. I. Small-amplitude regime in fully ionized medium*, The Astrophysical Journal, 832:101.
3. David Martínez-Gómez, Roberto Soler, and Jaume Terradas; 2017, *Multi-fluid approach to high-frequency waves in plasmas. II. Small-amplitude regime in partially ionized media*, The Astrophysical Journal, 837:80.
4. David Martínez-Gómez, Roberto Soler, and Jaume Terradas; 2017, *Multi-fluid approach to high-frequency waves in plasmas. III. Nonlinear regime and plasma heating*, (in preparation).

Additional research not included in this Thesis:

1. Maciej Zapiór and David Martínez-Gómez; 2016, *Direct detection of the helical magnetic field geometry from 3D reconstruction of prominence knot trajectories*, The Astrophysical Journal, 817:123.

Chapter 1

Introduction

1.1 Definition and basic properties of plasmas

The everyday experience of human beings is dominated by three of the four fundamental states of ordinary matter, namely solid, liquid and gas. However, none of them is the most abundant state in the Universe. Such status belongs, with an overwhelming margin, to the last one to be discovered by humanity, which is known as plasma. This fourth state of matter comprises more than 99% of the matter in the visible universe and can be roughly thought of as an ionized gas that conducts electricity and is affected by magnetic fields. Nevertheless, a more precise definition was provided by Chen [1984], who described a plasma as *a quasi-neutral gas of charged and neutral particles which exhibits collective behavior*.

On Earth's surface, naturally occurring plasmas are rare, with lightnings being almost the only examples. Nonetheless, it is not necessary to go very far from the surface to find the boundary from which plasma becomes the most abundant form of matter in the rest of the Universe. This limit can be found at about 50 km above the surface, where the layer of Earth's atmosphere known as ionosphere has its inner edge. In this layer, incident photons from the Sun have enough energy to separate electrons from the rest of components of the atoms or molecules that are present in the environment. Hence, electrons can move freely and their motions with respect to the positive ions give rise to magnetic fields which, in turn, affect the behavior of the electric charges. Due to the existing electromagnetic forces, the motion of each individual particle is influenced by the presence of those surrounding it. This kind of collective behavior is what characterizes the ionosphere as a plasma. From this layer of our planet out to the rest of the corners of the Cosmos, the vast majority of what can be seen, i.e., stars, nebulae, accretion discs around stars, jets in active galaxies, or the interplanetary, interstellar and intergalactic media, is composed of plasma. Hence, to understand a huge variety of the phenomena in the observable Universe it is necessary to delve into the properties of the fourth state of matter.

The identification of plasma as a fourth state different from the three classic ones is relatively recent. It was the English chemist and physicist Sir William Crookes who first described the behavior of rarefied gases inside a high vacuum cathode ray tube as a new form of matter, which he termed "radiant matter". Crookes [1879] proposed that this new fundamental state was composed of negatively charged molecules. Later, British physicist J.J. Thomson demonstrated that the components of the rays were not molecules or atoms but previously unknown subatomic particles. Thomson [1897] gave those particles the name of "corpuscles" but they are now known as electrons. The use of the term "plasma" to refer to the new state of matter was promoted by Irving Langmuir [1928]. According to Harold Mott-Smith [1971], while investigating mercury-vapor discharges Langmuir *pointed out that the "equilibrium" part of the discharge acted as a sort of sub-stratum carrying particles of special kinds, like high-velocity electrons from thermionic filaments, molecules and ions of gas impurities*, which reminded him of *the way blood plasma carries around red and white cells, proteins, hormones and germs*.

Since those initial studies, the field of plasma physics has experimented a huge growth and it is nowadays in the core of many technological applications. Plasmas are used, for instance, for display purposes (as in television screens), for illumination (fluorescence lamps and neon signs), for industrial manufacturing (cutting of materials with welding arcs, cleaning and coating of surfaces, fabrication of semiconductors, waste disposal, etcetera) or for medicinal practices (e.g., bio-decontamination and sterilization), among many other applications. Furthermore, plasmas provide a promising solution for one of the most relevant issues that our civilization faces: the ever-growing demand of electric energy. In the search of an efficient, abundant and sustainable source of energy, the fusion of plasmas rises as the best alternative to the energy generation methods that are available at present. Unfortunately, it is still in development and it seems that it will take decades until a commercial fusion power plant becomes fully operational.

As shown by the previous lines, the study of plasmas is a field of enormous interest not only for the mere sake of knowledge (which in many cases is the main motivation that drives scientists on their research) but also for a wide number of practical reasons. The technological progress of our civilization greatly depends on improving our understanding of the fourth fundamental state of the matter. However, there is another essential reason that does not come from our technology but from nature itself. Life on Earth ultimately depends on the Sun. Solar heat warms our planet's atmosphere and surface and is the basic driver of the weather. Moreover, the influence of Sun's magnetic field extends throughout the entire solar system and it greatly affects Earth's magnetosphere. This region around our planet is continuously distorted by the stream of charged particles outgoing from the Sun, which receives the name of solar wind, and by events like solar flares or coronal mass ejections. These events are explosive releases into space of matter and electromagnetic radiation. Such perturbations of the magnetosphere may produce phenomena as alluring as the aurora or polar lights (see an example in Figure 1.1), but can also have detrimental consequences to our society by, for instance, disrupting long-distance radio communications, damaging satellite electronics or causing electrical power blackouts. As any other star, the Sun is a gigantic ball of plasma. Hence, to understand how its magnetic field is generated and varies over time and to grasp the details of the tight interaction between the Sun and Earth, it is indispensable to investigate the nature of plasmas.

In the previous paragraphs, some vague definitions of what a plasma is have been presented. However, to clearly distinguish this fundamental state of matter from the other ones, more precise definitions are required. It has been said that a plasma is an ionized gas, but this statement leads immediately to the following question: is any ionized gas a plasma? The answer is no, because, to be considered a plasma, the fluid ought to show a special type of collective behavior. Furthermore, a small degree of ionization is present in every gas (Chen [1984]) but not every gas acts like a plasma, a fact that rises a new question: what is the minimum degree of ionization in a fluid that allows the appearance of the collective behavior associated to plasmas? The answer is not straightforward and in this Thesis it will be shown

Figure 1.1: Photograph of an aurora taken from the International Space Station on January 20, 2016 (Credit: ESA / NASA).

that even in fluids with ionization degrees as low as 10^{-5} charged particles per neutral atom the effects caused by ions cannot be overlooked. The degree of ionization in a gas in thermal equilibrium can be estimated by using Saha's equation, which is given by

$$\frac{n_i}{n_n} = \left(\frac{2\pi m_e k_\mathrm{B}}{h^2}\right)^{3/2} \frac{T^{3/2}}{n_e} \exp\left(\frac{-U_i}{k_\mathrm{B}T}\right), \tag{1.1}$$

where n_i, n_n and n_e are the number densities of ions, neutral particles and electrons, respectively, $m_e \approx 9.1 \times 10^{-31}$ kg is the electron mass, $k_\mathrm{B} \approx 1.38 \times 10^{-23}$ J K^{-1} is the Boltzmann constant, $h \approx 6.63 \times 10^{-34}$ J s is Planck's constant, T is the temperature of the gas and U_i is the ionization energy, i.e., the energy required to remove an electron from the neutral atom (values of the ionization energies are typically given in electron-volts, abbreviated as "eV", which have the equivalence of 1 eV $= 1.602 \times 10^{-19}$ J). Due to their exponential dependence on temperature, ionization degrees vary throughout an immense range of orders of magnitude. This can be checked by inspecting the data shown in Table 1.1, where the parameters of three different environments are presented and their corresponding degrees of ionization are computed (the calculation assumes that $n_e \approx n_i$). For air at room temperature, $n_i/n_n \ll 1$, i.e., air has a ridiculous quantity of free charged particles. Air is a gas, not a plasma, and its general behavior is described by the laws of hydrodynamics without the influence of electromagnetic fields. Conversely, inside the fusion devices known as *tokamaks* (which are contraptions of toroidal shape where matter is confined by means of intense magnetic fields), with $n_i/n_n \approx 2.4 \times 10^{13}$, or in the solar corona (where $n_i/n_n \approx 2.1 \times 10^{18}$) there are much more ions than neutral particles. Hence, the dynamics of those two environments are certainly governed by the interaction between charges and electromagnetic fields.

Table 1.1: Degrees of ionization of various fluids

Fluid	T (K)	U_i (eV)	n_n (m^{-3})	n_i (m^{-3})	n_i/n_n
Air	300	14.5	3×10^{25}	–	10^{-122}
Tokamak	10^8	13.6	–	10^{20}	2.4×10^{13}
Solar corona	10^6	13.6	–	10^{12}	2.1×10^{18}

Values of n_n, T and U_i are taken from Goedbloed and Poedts [2004]. Note that Saha's equation allows to compute n_i if n_n is known, and vice versa. Hence, this table only shows the value that it is known for each fluid before performing the computation.

The ionization degree gives the intuitive idea that fluids behave as plasmas if $n_i/n_n \gtrsim 1$ and as gases if $n_i/n_n \ll 1$. Nevertheless, it does not provides a precise criterion to differentiate the two states of matter and to determine the minimal proportion of charges that are necessary for the plasma behavior to emerge. Hence, some other characteristics of the fluid need to be checked.

One of the main properties of plasmas is that they tend to stay electrically neutral. Any perturbation of the balance between positive and negative charges generates strong electrostatic forces that act to nullify that perturbation and to recover the neutrality of the fluid. This fact establishes a length scale below which the fluid cannot be treated as a plasma. The size of this length scale can be estimated by assuming that the aforementioned perturbations may be caused by thermal fluctuations. The energy of those fluctuations is given by k_BT and it needs to be compared with the electrostatic energy of the affected particles, which is given by $e\phi$, where $e = 1.602 \times 10^{-19}$ C is the elementary electric charge and ϕ is the electrostatic potential. The potential ϕ can be obtained from Poisson's equation, namely

$$\nabla^2 \phi = \frac{-e}{\epsilon_0}(n_i - n_e), \tag{1.2}$$

where $\epsilon_0 = 8.854 \times 10^{-12}$ F m^{-1} is the electric permittivity of the vacuum.

Assuming that the plasma is in thermal equilibrium, the statistical distribution function of velocities of electrons and ions is given by the Maxwell-Boltzmann distribution, which can be written as (see, e.g., Chen [1984])

$$f(u) = A \exp\left[\frac{-\left(mu^2/2 + q\phi\right)}{k_BT}\right], \tag{1.3}$$

where u represents the velocity, q is the charge of the particle and A is a normalization constant whose value is not relevant at the moment. The Maxwell-Boltzmann distribution expresses that there are more particles in the regions where the potential energy is small because not all particles have enough energy to reach the regions where the electrostatic potential is large.

From this distribution, it is possible to obtain the number density function for ions and electrons, which are then given by

$$n_i = n_0 \exp\left(\frac{-e\phi}{k_\mathrm{B}T}\right) \tag{1.4}$$

and

$$n_e = n_0 \exp\left(\frac{e\phi}{k_{\mathrm{B}}T}\right), \tag{1.5}$$

respectively, where $n_0 = n(\phi = 0)$, i.e., n_0 represents the number density of particles in a region far away from the perturbation. Hence, by expressing the Laplacian in spherical coordinates, Equation (1.2) can be rewritten in the following way:

$$\frac{1}{r^2}\frac{\partial}{\partial r}\left(r^2\frac{\partial\phi}{\partial r}\right) = \frac{2en_0}{\epsilon_0}\sinh\left(\frac{e\phi}{k_{\mathrm{B}}T}\right). \tag{1.6}$$

If the thermal energy is larger than the electrostatic energy, i.e., if $k_{\mathrm{B}}T > e\phi$, the factor $\sinh\left(\frac{e\phi}{k_{\mathrm{B}}T}\right)$ can be approximated by $e\phi/(k_{\mathrm{B}}T)$ and the previous equation becomes

$$\frac{1}{r^2}\frac{\partial}{\partial r}\left(r^2\frac{\partial\phi}{\partial r}\right) = \frac{2e^2n_0\phi}{\epsilon_0 k_{\mathrm{B}}T}. \tag{1.7}$$

whose solution, after imposing that ϕ tends to zero when r tends to infinity, is

$$\phi = \phi_0 \exp\left(-\frac{r}{\lambda_{\mathrm{D}}}\right), \tag{1.8}$$

where $\phi_0 = q/(4\pi\epsilon_0 r)$ is the electrostatic potential created by a charge in vacuum. The parameter λ_D has units of length, is defined as

$$\lambda_D \equiv \sqrt{\frac{\epsilon_0 k_{\mathrm{B}}T}{2e^2n_0}}, \tag{1.9}$$

and is referred to as the Debye shielding length. Thus, according to Equation (1.8), the potential generated by the charge imbalance decreases exponentially with the distance and its effect is negligible at distances of several λ_{D} because it is shielded by the presence of the rest of ions and electrons. The Debye length is also related to the property of quasi-neutrality that holds in plasmas. If the length scales of the dynamics of an ionized fluid, denoted by L, are much larger than λ_{D}, the condition of quasi-neutrality is satisfied because the effects of any external potential or local charge concentrations can only arise in scales of the order of λ_{D} due to the shielding caused by the fast rearrangement of the particles. This rearrangement prevents the appearance of large potentials in the whole plasma and keeps it quasi-neutral in terms of its total charge, i.e.,

$$\frac{|\sum_i Z_i n_i - n_e|}{n_e} \ll 1. \tag{1.10}$$

The previous formula assumes that the plasma may be composed of several positive ions, each one with a different signed charge number, Z_i.

The Debye shielding is one of the fundamental characteristics of the behavior of plasmas but it is only present when there are enough particles inside what is known as a Debye sphere, a volume with a radius given by the Debye length. As it would be expected, a scarce number of charges cannot fully nullify the potential created by a perturbation in the fluid. Thus, a new question comes forth: how many particles are enough? The answer is provided by the so-called

Debye number, which obviously depends on the density of the fluid and the Debye length. It is defined as

$$N_{\rm D} = \frac{4}{3}\pi n_e \lambda_{\rm D}^3 \approx 1.38 \times 10^6 \sqrt{\frac{T^3}{n_e}}. \tag{1.11}$$

It is considered that there are enough particles in a Debye sphere for statistical considerations to be valid and for the collective behavior to be present when $N_{\rm D} \gg 1$.

The long-range Coulomb interaction between charged particles is not the only type of interaction that can be found in a gas if it is not fully ionized. Ions and electrons can also collide with neutral particles, a short-range binary interaction which is the main effect investigated in this Thesis. The nature of the fluid depends on which process dominates. The dynamics of gases are controlled by hydrodynamic forces due to charged particles colliding so frequently with neutrals. In contrast, when Coulomb interactions prevail over collisions with neutrals, the fluid behaves as a plasma. If τ is defined as the time scale of the collective motion and τ_n is the mean time between collisions of charged particles with neutrals, the condition for an ionized gas to be a plasma is that

$$\tau \ll \tau_n. \tag{1.12}$$

An approximate expression for τ_n is given by

$$\tau_n \approx \frac{10^{17}}{n_n\sqrt{T}}. \tag{1.13}$$

The previous formula (see Goedbloed and Poedts [2004]) has been computed by dividing the mean free path, λ_{mfp}, of particles in a hydrogen gas by the thermal speed, v_{th}, i.e., $\tau_n \approx \lambda_{mfp}/v_{th}$. The mean free path is computed as $\lambda_{mfp} = 1/(n_n\sigma)$, where the cross-section is given, in the hard-sphere approximation, by $\sigma = \pi a^2 \approx 10^{-19}$ m^2, with $a \approx 2 \times 10^{10}$ m the radius of a neutral atom. The thermal velocity is given by $v_{th} \approx \sqrt{k_{\rm B}T/m_p}$, where $m_p = 1.6726 \times 10^{-27}$ kg is the proton mass.

Hence, as a summary, the typical collective behavior of plasmas appears when the following conditions are fulfilled:

1. the length scales of the dynamics are much larger than the Debye length, i.e., $L \gg \lambda_D$,
2. there are enough charged particles in a Debye sphere to produce the shielding from external electric fields and to allow the statistical treatment, i.e., $N_D \gg 1$, and
3. the time scales of the global motions are much shorter than the collisional time with neutrals, i.e., $\tau \ll \tau_n$.

Table 1.2 shows the values that are obtained when the previous conditions are computed for the ionized gases in a tokamak and the solar corona. The plasma conditions are easily satisfied in a tokamak: the Debye length is small compared to the typical size of this kind of nuclear reactors (of the order of 1 m), the number of ions in a Debye sphere is more than enough for statistical considerations, i.e, $N_{\rm D} \gg 1$, and the collective oscillatory motions have periods much lower than τ_n. The same happens in the solar corona: typical structures than can be found in the corona have length scales of $\lambda \sim 10^7$ m, the plasma parameters is $N_{\rm D} \gg 1$ and τ_n is larger than the age of the Universe.

Table 1.2: Comparison of plasma conditions for several environments

Fluid	n_n (m^{-3})	λ_{D} (m)	N_{D}	τ_n (s)
Tokamak	4.2×10^{6}	5×10^{-5}	5×10^{7}	2.4×10^{6}
Solar corona	4.7×10^{-7}	0.05	5×10^{8}	2×10^{20}

The conditions analyzed above correspond to the microscopic level of the properties of plasmas. They are related to electrostatic, collisional and thermal effects but they ignore one of the fundamental characteristics of plasmas, which is that they are affected by magnetic fields. The consideration of the magnetic field introduces additional conditions, which are macroscopic because they affect the plasma as a whole and not only to a local portion of the fluid (see, e.g., Goedbloed and Poedts [2004]). These new conditions are related to the cyclotron motions of electrons and ions, and can be expressed in terms of the cyclotron frequency or gyrofrequency, $\Omega_{e,i}$ (e for electrons and i for ions), defined as

$$\Omega_{e,i} = \frac{q_{e,i} B}{m_{e,i}}, \tag{1.14}$$

and the cyclotron radius (also known as gyroradius or Larmor radius), given by

$$r_{e,i} = \frac{m_{e,i} v_{\perp e,i}}{|q_{e,i}| B}, \tag{1.15}$$

where $v_{\perp e,i}$ is the component of the particle velocity perpendicular to the direction of the magnetic field.

The macroscopic condition for the time scales is established by the inverse of the cyclotron frequencies, $\Omega_{e,i}^{-1}$. The global length and time scales are required to be large enough to allow averaging over the microscopic dynamics, which means that they should be much larger than $r_{e,i}$ and $\Omega_{e,i}^{-1}$, respectively. As both quantities of interest are directly proportional to the mass of the particles, the most limiting conditions are related to ions (the mass of the proton is about 1840 times the mass of the electron). In addition, the two cyclotron parameters are inversely proportional to the magnetic field and, thus, the macroscopic conditions are more easily satisfied when the magnetic field is large. The corresponding conditions for a *tokamak* and the solar corona are shown in Table 1.3, where the Larmor radii have been computed by assuming that the perpendicular velocity is given by the thermal velocity, i.e., $v_{\perp e,i} \approx v_{th\ e,i} \approx (k_{\mathrm{B}} T / m_{e,i})^{1/2}$. In the same way as the microscopic conditions, these macroscopic requirements are easily satisfied in the considered environments.

Table 1.3: Macroscopic plasma conditions

Fluid	B (G)	Ω_e^{-1} (s)	Ω_i^{-1} (s)	r_e (m)	r_i (m)
Tokamak	3×10^{4}	1.9×10^{-12}	3.5×10^{-9}	7×10^{-5}	0.003
Solar corona	10^{-3}	5.7×10^{-9}	10^{-5}	0.02	1

Once the conditions that differentiate plasmas from the other three fundamental states of ordinary matter have been explained, the next step is to mention how plasma dynamics can be described. One rough possibility is to follow the motion of each particle of the plasma by applying the single particle orbit theory. In this description, each particle has an equation of motion which governs how it reacts to the presence of electric and magnetic fields. However, this approach is not practical due to the large numbers of particles in a plasma and, moreover, it would be valid only when the density of particles is so low that the interactions between them can be neglected.

A more appropriate option comes from the kinetic plasma theory. This approach, which takes into account the interaction between the large number of particles, treats the plasma statistically. The main element of the kinetic theory is the distribution function, which expresses how the particles of the plasma are distributed throughout the *phase space*, i.e., the six-dimensional space formed by the three coordinates of the position vector, $\boldsymbol{x} = (x, y, z)^T$, and the three components of the velocity, $\boldsymbol{v} = (v_x, v_y, v_z)^T$. Then, the dynamics of the plasma is obtained from the temporal evolution of the distribution function. The kinetic approach has the advantages that it is extremely accurate and retains all the relevant physical information of the plasma, but at the expense of a large complexity.

Magnetohydrodynamics (MHD), which focus on the macroscopic processes of the plasma, is a much simpler alternative to the kinetic theory. It describes the evolution of plasmas in terms of average macroscopic variables, like the density or the temperature, which depend on $\boldsymbol{x}$ but not on $\boldsymbol{v}$. This approach is applicable when length scales are much larger than the Debye length and the gyroradii of ions and electrons. In addition, it assumes that all the species of the plasma are strongly coupled, which means that there are frequent enough collisions between the particles to establish the fluid behavior. Thus, the time scales must be much larger than the inverse of the collision frequencies. Those collision frequencies can be obtained from the friction coefficients shown in Section 2.2.1.

An intermediate step between the kinetic and the MHD descriptions is provided by multi-fluid theories, like the model presented in this Thesis, in which not all the species that compose the plasma are strongly coupled. Additional details of the multi-fluid theory are given in Chapter 2.

1.2 The Sun

1.2.1 General aspects of the Sun and its interior

Since the Sun is the closest star to Earth, it occupies a prominent place in the human worldview: it is at the center of the Solar System and accounts for about 99.86 % of its mass. However, from the astronomical point of view, it is not so special: even only within the limits of our galaxy, the Milky Way, more than one hundred million stars akin to the Sun can be found. This fact has a very important advantage for the field of astrophysics: what can be learned about the Sun may be easily extrapolated to an enormous number of other stars. This is another reason why it is so important to obtain a deep understanding of the processes that develop in the Sun. Its main physical parameters are summarized in Table 1.4 and a scheme of the structure of its interior and its atmosphere is shown in Figure 1.2.

In terms of mass, the Sun is composed of a 73% of hydrogen, a 25% of helium, a 0.77% of oxygen, and then smaller quantities of other heavier elements like carbon, iron, neon, nitrogen, silicon, magnesium or sulfur. It has been given by astronomers the spectral classification G2V, which corresponds to main-sequence dwarf stars with prominent H and K lines of singly ionized calcium and weak hydrogen lines in their spectra. The Sun is commonly referred to as a yellow

Table 1.4: Physical parameters of the Sun

Parameter	Value
Mass, $M_\odot$	1.99×10^{30} kg
Equatorial radius, $R_\odot$	6.96×10^{8} m
Flattening	9×10^{-6}
Equatorial surface gravity	274 m s^{-2} (27.94 g)
Average density	1408 kg m^{-3}
Luminosity, $L_\odot$	3.828×10^{26} W
Effective temperature	5776 K
Age	≈ 4.6 Gyr

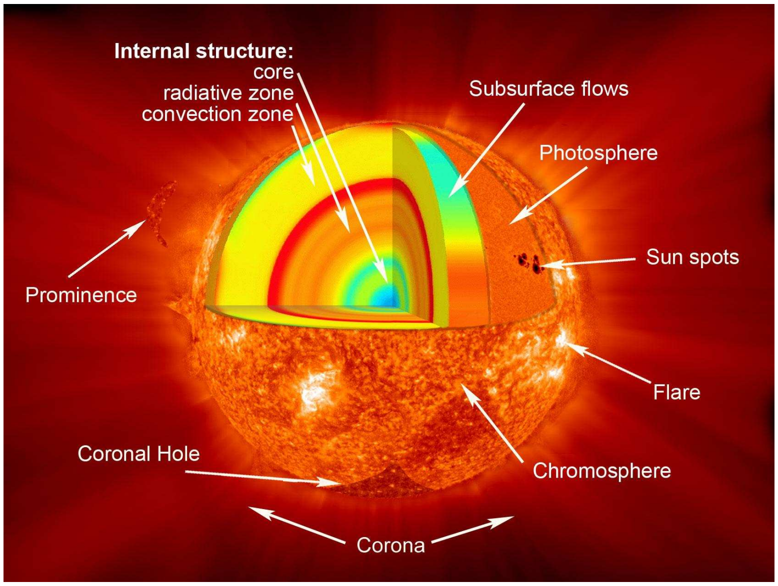

Figure 1.2: Structure of the Sun's interior and atmosphere (Credit: NASA / Goddard).

dwarf, although its actual color is white.

The internal structure of the Sun can be divided in four regions, namely core, radiative zone, tachocline and convective zone, whose characteristics are detailed in the following paragraphs.

Core

This region extends from the center of the star to about 0.2 $R_\odot$. Here, hydrogen is being transformed into helium by means of nuclear fusion. This process is possible due to the large densities, of the order of 1.6×10^5 kg m^{-3}, and temperatures, around 1.6×10^7 K.

Radiative zone

Photons are continuously emitted, absorbed and re-emitted by protons and helium nuclei in the radiative zone, which extends up to ~ 0.7 $R_\odot$. This layer owes its name to the mechanism of energy transfer that dominates, namely the thermal radiation: energy travels in the form of electromagnetic radiation. The matter in this zone is so dense that photons can travel very short distances before being absorbed or scattered by another particles, which explains the very long time it takes to cross this region. The temperature drops from about 7 million K at the bottom of the radiative zone to about 2 million K at its top.

Tachocline

Located at a distance of $\sim 0.7\ \mathrm{R}_\odot$ from the center of the Sun, this thin layer, with an approximate thickness of $0.03\ \mathrm{R}_\odot$, serves as a transition region between the radiative zone and the convective zone. It is believed that the Sun's magnetic field is generated in this layer due to a magnetic dynamo effect by which kinetic energy is transformed into electromagnetic energy.

Convective zone

The convective zone extends from $\sim 0.7\ \mathrm{R}_\odot$ to the surface. In this region, the plasma is not dense or hot enough for the energy to be transfered primarily by thermal radiation. Due to the large temperature gradients, matter is unstable to convection. The convective motions consists in hot and light volumes of plasma rising towards the surface, where the heat they carry is released. There, the material cools, becomes denser and sinks again towards the bottom, where the cycle starts again. Thanks to this cycle, the energy generated at the core can finally reach the surface of the Sun, the photosphere, whose granular appearance is produced by the top of the thermal cells formed during the convection process.

1.2.2 Layers of the solar atmosphere

The atmosphere of the Sun can also be divided in several regions with clearly different values of composition, temperature and density. The variation of the latter two parameters with height is represented in Figure 1.3, where it can be seen that, as it would be expected, the density decreases with height but, surprisingly, the temperature does not follow the same behavior at large heights and increases by several orders of magnitude. This anti-intuitive demeanor leads to the so-called coronal heating problem: several mechanisms have been proposed to explain the rise of temperature, but the precise answer to the issue is not known yet.

Moreover, not all the regions of the solar atmosphere can be seen with the naked eye under normal conditions. The lower layer, the photosphere, is the visible surface of the star, and the corona and a small fraction of the chromosphere can be briefly seen during solar eclipses. However, ordinarily the outer layers can only be observed by means of special instruments.

Photosphere

The lower layer of the solar atmosphere is the region where almost all of the energy generated by the nuclear reactions at the core can finally escape to the space. It has a thickness of about 550 km, a temperature of ~ 5700 K at its bottom and ~ 4500 K at its top, and a density of the order of 10^{23} particles per m^3. A visible light image of the photosphere is shown in the left panel of Figure 1.4. Several dark spots can be seen in that picture. Those features are known as sunspots and they appear darker than the surroundings because they are colder. They have temperatures of about 4000 K and, according to the black-body radiation laws, they emit less energy.

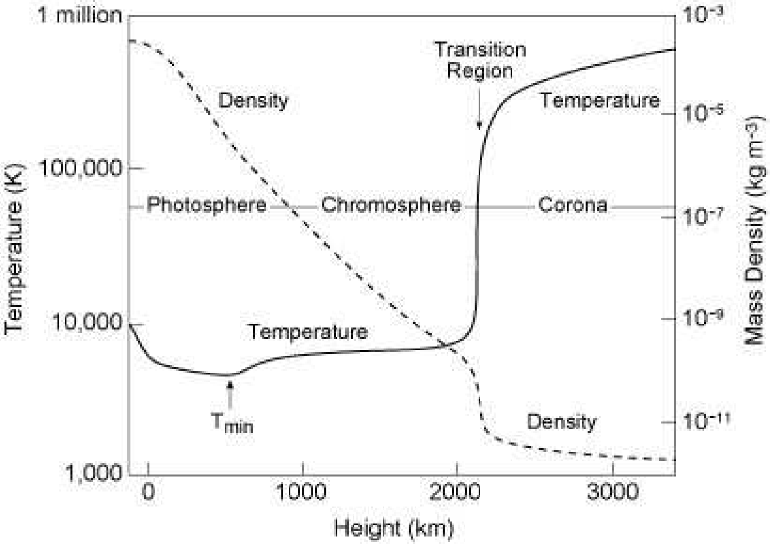

Figure 1.3: Temperature and mass density in the solar atmosphere as functions of height (Credit: Eugene Avrett / Smithsonian Astrophysical Observatory).

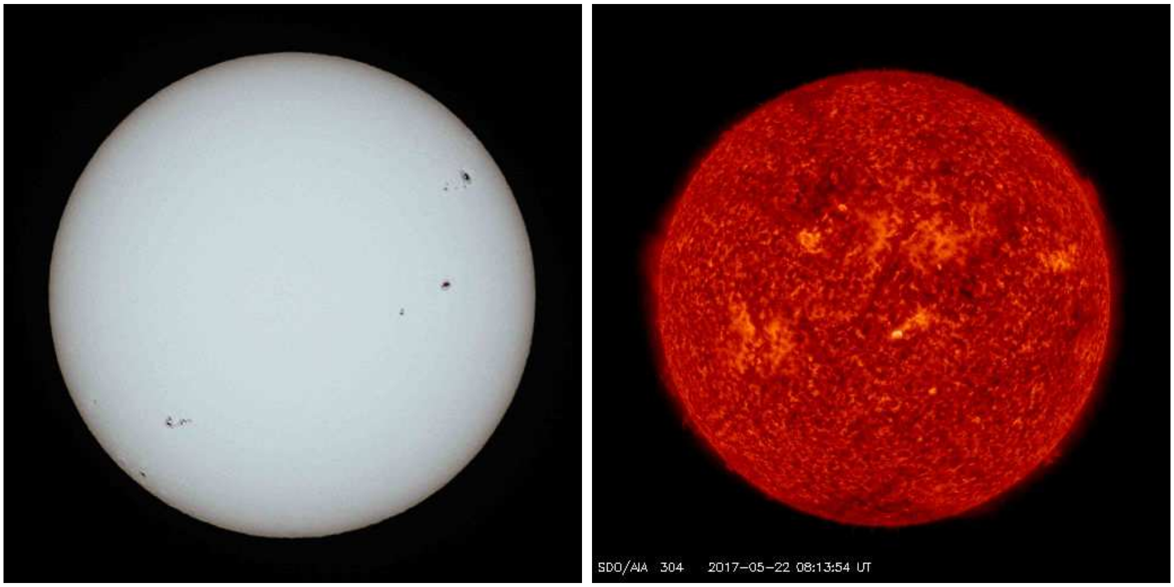

Figure 1.4: Left: Sun's photosphere observed in visible light with a solar filter (Credit: Geoff Elston / Society for Popular Astronomy). Right: Sun's chromosphere as seen in the He II 304 Å line by the instrument SDO/AIA (Credit: NASA).

Chromosphere

Right above the photosphere there is a region where the minimum temperature of the atmosphere is reached, with a value of about 4100 K. After this minimum, the temperature rises again with altitude in the chromosphere, a layer with a thickness of $\sim$ 2000 km. At the top of this region, the temperature is of the order of 2×10^4 K. During solar eclipses a portion of the chromosphere can be seen in pink and red tones. An image of the chromosphere as seen by

SDO at the wavelength 30.4 nm, caused by atoms of singly ionized helium, is shown in the right panel of Figure 1.4. Some features protruding from the solar limb can be seen: they receive the name of prominences.

Transition region

A narrow transition region, with a thickness of a few tens of kilometers, exists between the chromosphere and the next layer of the atmosphere, the corona. In this transition region the temperature of the plasma rises to 10^6 K.

Corona

The temperature of the plasma keeps increasing in the corona and can reach values of the order of 10^7 K. In contrast with the photosphere and the chromosphere, where a non-negligible amount of neutral particles is present, the much lighter plasma of the corona is almost fully ionized. The enormous temperatures of this environment have been inferred from the analysis of the spectral lines, which reveals the presence of highly ionized states of heavier elements like calcium or iron.

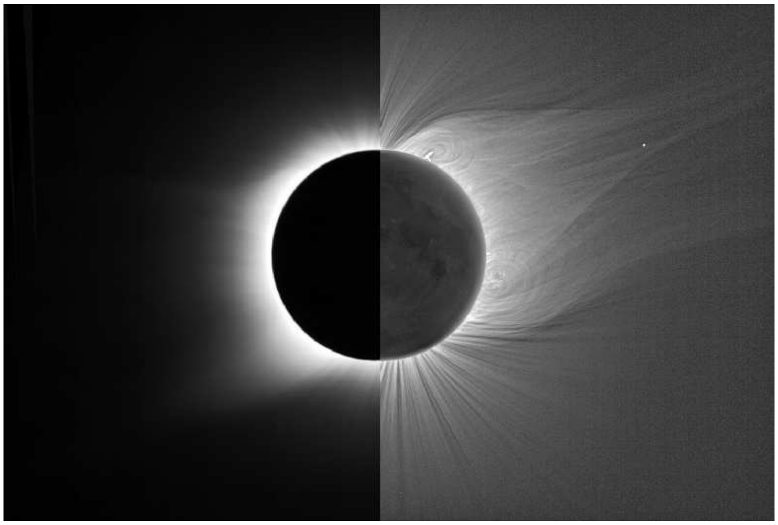

Figure 1.5: White-light corona during a solar eclipse. The right side has been digitally processed to enhance low-contrast structures invisible to the human eye. From Rušin et al. [2010].

The corona is very dim in visible light compared to the lower layers. This is the reason why it can only be seen with the naked eye during solar eclipses (see Figure 1.5) or by using coronagraphs that hide the much brighter solar disk. Nevertheless, it is very bright in the range of ultraviolet radiation and X-rays. Most of X-ray and ultraviolet photons coming from the Sun are absorbed by Earth's atmosphere and do not reach its surface. Hence, the vast majority of information about the bright corona is obtained by means of satellites in outer space. Observations performed with the most modern instruments have revealed the highly dynamic nature of the corona, where the magnetic field plays a prominent role in phenomena like coronal loops, flares or coronal mass ejections.

Heliosphere

The last layer of the solar atmosphere starts at a distance of ~ 20 $R_\odot$ and it can be said that it marks the limits of the Solar System. It is a bubble-like structure created by the solar wind that extends far beyond the orbits of the outer planets. The particles of the solar wind travel outwards from the Sun until they are stopped by the pressure of the interstellar medium, i.e., by the stellar winds of the surrounding stars. According to measures taken by the *Voyager 1* spacecraft, the human-made object that has gone farthest from Earth, the outer boundary of the heliosphere, known as heliopause, is located at a distance of 121 astronomical units (AU).

1.3 Structures and dynamics in the solar atmosphere

The Sun is not a quiet and perfectly uniform sphere of plasma but several kinds of features and phenomena can be observed throughout the different layers of its atmosphere. The properties of some of those features and their dynamics, which are strongly related to the interaction between the plasma and the magnetic fields, are detailed below.

1.3.1 Waves in the chromosphere

The existence of waves in the chromosphere has been known at least from the early 60s, when Leighton et al. [1962] reported the detection of propagating oscillations, although wave-based mechanisms for heating this layer of the chromosphere were proposed long before (see, e.g., Biermann [1946], Schwarzschild [1948]). In addition, during the last twenty years an overwhelming amount of evidence about the existence of MHD waves in the chromosphere has been gathered. For instance, De Pontieu et al. [2007] reported the detection of Alfvénic waves and various observed twist motions were interpreted as torsional Alfvén waves by Jess et al. [2009] and De Pontieu et al. [2012]. More details about the observations of MHD waves can be found in, e.g., Morton et al. [2012] or Jess et al. [2015].

Physical parameters such as temperature, density, ionization degree or magnetic field strength present strong variations throughout the chromosphere. For example, the total density at the bottom is about five orders of magnitude larger than at its top, with values of about 10^{-5} and 10^{-10} kg m^{-3}, respectively. The temperature increases with height by an order of magnitude, while the magnetic field decreases with height, with a value about 500 G at the bottom and of the order of 20 G at the top. The change of temperature creates huge differences in the ionization degree of the plasma, which leads to a remarkable variation of the properties of MHD waves. Neutrals are much more abundant than ions in the low chromosphere, while the opposite occurs at the higher end. This fact is illustrated by Figure 1.6, which shows the ratio of a given neutral or ionized species with respect to the total density of the plasma as a function of height. The data have been taken from the hydrodynamic model developed by Fontenla et al. [1993] for a chromospheric bright region.

It has been known since the middle of the last century that a non-negligible amount of neutrals may have a dramatic impact on the dynamics of a plasma and, in particular, on the oscillations that may appear in such a fluid (see, e.g., Piddington [1956], Watanabe [1961a,b], Kulsrud and Pearce [1969]). The main effect is that neutrals exchange momentum with ions by means of collisions, which leads to an attenuation of the amplitude of MHD waves. In addition,

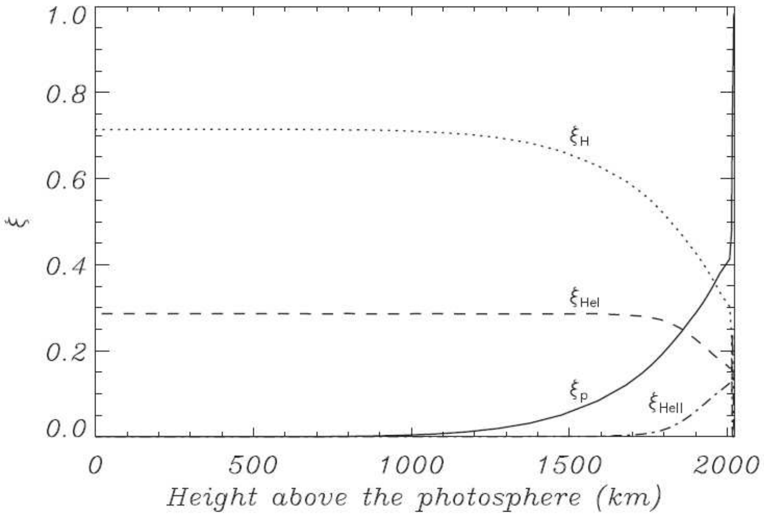

Figure 1.6: Relative abundances, $\xi_s \equiv \rho_s/\rho$, where ρ is the total density, of protons, neutral hydrogen, neutral helium and singly-ionized helium as a function of the height according to the chromospheric model F of Fontenla et al. [1993]. Adapted from Soler et al. [2015b].

if the collisions occur frequently enough, the period of the Alfvénic waves is increased while their propagation speed is reduced (see, e.g., Kumar and Roberts [2003]). Hence, taking into account the dependence on height of the relative abundances of neutral and ionized species shown in Figure 1.6, the properties of MHD waves are greatly affected by neutrals in a large part of the chromosphere. In this Thesis, several effects of the presence of neutrals at different heights of the chromosphere are investigated in Chapter 4.

1.3.2 Prominences and filaments

Prominences are volumes of plasma that is denser and cooler than the surrounding environment. They are anchored in the photosphere and extend through the corona. They are supported against gravity by the effect of the magnetic field. An example of this kind of structures is shown in the left panel of Figure 1.7, where the plasma can be clearly seen protruding from the limb of the Sun. They form along the polarity inversion lines (PIL) of the magnetic field, i.e., the lines that divide two regions of opposite magnetic field polarity in the photosphere, but the precise mechanism of its formation is still under active research. Their temperatures are typically one hundred times lower than those found in the corona, of the order of 10^4 K, reason why the prominence plasma is partially ionized instead of fully ionized. In contrast, they are between one hundred and one thousand times denser than the corona, with densities of the order of 10^{-12} to 10^{-10} kg m^{-3}. Their heights are of the order of 10^4 km, their widths vary between 4 and 30 thousand kilometers and their lengths are of the order of 10^5 km.

Filaments are the same type of feature than prominences. The only differences between both are their position in the Sun and their brightness when compared to the surrounding background: prominences extend from the limb of the Sun and appear bright in comparison with the space in the background. On the other hand, filaments are located over the solar disk and show up as dark lines. An example of the appearance of a filament is shown on the right panel of Figure 1.7. Prominences and filaments can be classified in two categories: quiescent and active. The quiescent class is more stable and can have lifetimes of up to several months. A typical value of the magnetic field strength in these structures is 10 G. Active prominences form faster, are associated with sunspot groups and have much shorter lifetimes, of minutes to hours. They also have stronger magnetic fields. Some prominences may suffer an eruption, detaching from the Sun and ejecting their material into space. More detailed portrayals of the properties of these structures can be found in, e.g., Labrosse et al. [2010], Mackay et al. [2010] or Parenti [2014].

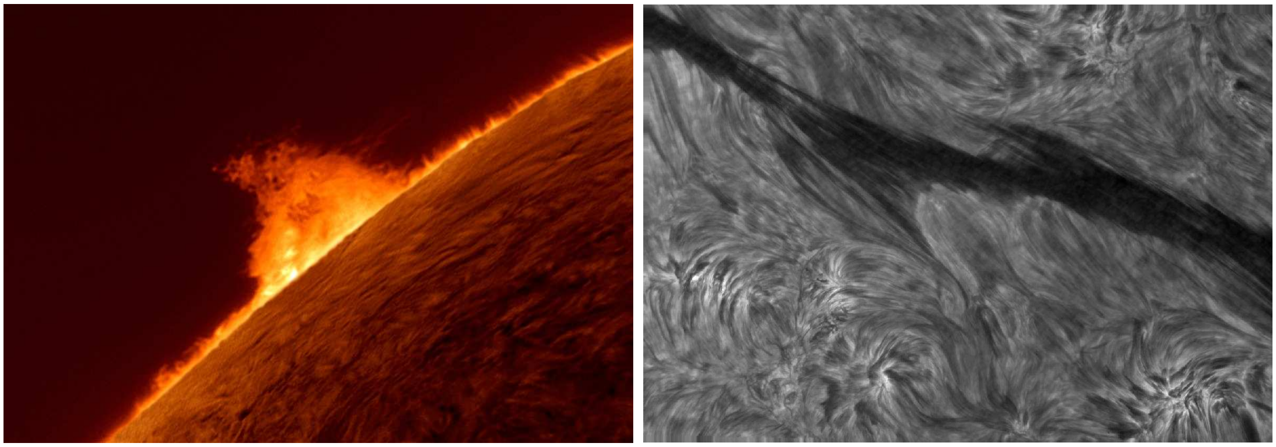

Figure 1.7: Left: image of a prominence extending from the limb of the Sun (Credit: Gary Palmer / Royal Museums Greenwich). Right: Hα image of a filament (Credit: Y. Lin).

The first historical record of the description of a solar prominence appears in the *Laurentian Codex* or *Chronicle of Novgorod*, written in the 14th century by Russian monk Laurentius (see, Sviatsky [1923]). In that text, the solar eclipse of 1 May 1185 is mentioned as follows: "*In the evening there was a sign on the Sun. The night fell on the Earth and stars could be seen [...]. The Sun became like the Moon and from the horns of the crescent came out somewhat like live embers*". However, as it occurs with many aspects of the Sun, most of what is known about prominences has been discovered in the last twenty or thirty years. Earlier observations like those analyzed in de Jager [1959] or Kuperus and Tandberg-Hanssen [1967] suggested that prominences and filaments have a fine structure. Nevertheless, this fact was not confirmed until more recent observations with higher resolution were performed (Lin et al. [2005], Heinzel and Anzer [2006], Lin et al. [2007], Okamoto et al. [2007], Berger et al. [2008]) and showed that prominences are composed of long and thin threads or fibrils. The width of the threads is about 200 km and its length vary from ~ 3500 to $\sim 28,000$ km. The fine structure of prominences can be noticed in Figure 1.8, an image obtained in H_α, which is caused by the radiation emitted by neutral hydrogen when its electron falls from the third to its second lowest energy level. This line, whose wavelength is 656.3 nm, appears in the red part of the visible range of the electromagnetic spectrum.

Observations in Hα, ultraviolet (UV) and extreme-ultraviolet (EUV) lines also reveal a rich dynamics in prominences and filaments. For instance, mass flows along the threads axes and transverse to them have been frequently reported (Engvold [1976, 1981], Zirker et al. [1994], Lin et al. [2003, 2005], Chae et al. [2008], Schmieder et al. [2010]). The typical speeds

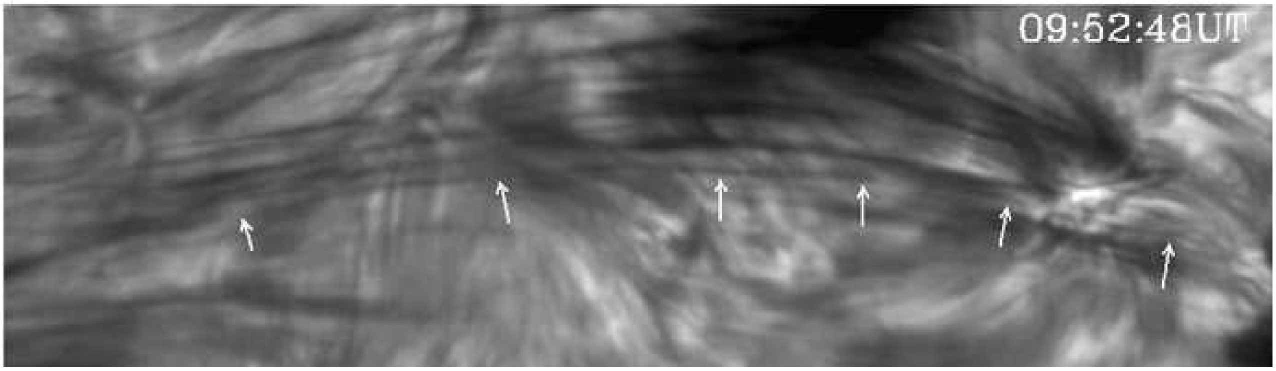

Figure 1.8: Threads of a quiescent filament observed with the Swedish 1-m Solar Telescope. From Lin [2011].

of the flows in quiescent filaments vary from 5 to 30 km s^{-1}, while higher speeds have been detected in active region prominences: Chae et al. [2000] reported motions with speeds of up to 40 km s^{-1} and, later, Chae [2003] detected jet-like and eruptive behaviors with speeds from 80 to 250 km s^{-1}. The presence of flows may lead to the appearance of instabilities like the Kelvin-Helmholtz instability (see, e.g., Soler et al. [2012b]). More details about this instability and how is affected by partial ionization are given in Chapter 6 of this Thesis.

In addition to the mass flows mentioned in the previous paragraph, oscillatory motions have also been detected in prominences and filaments. The first observations of this kind of motion correspond to what is now known as large-amplitude oscillations, which are typically caused by disturbances coming from flares. The relation between large-amplitude oscillations and nearby flares was demonstrated by Moreton and Ramsey [1960]: waves propagating at speeds between 500 and 1500 km s^{-1} impact on prominences and cause them to vibrate during a few periods with amplitudes of the order of 20 km s^{-1}. These oscillations, which are global, i.e., affect the whole prominence, are quite rare events, although in the last years a growing number of observations has been reported (Eto et al. [2002], Jing et al. [2003], Okamoto et al. [2004], Gilbert et al. [2008], Luna and Karpen [2012]). However, the nature of large-amplitude oscillations is still poorly understood. More details about the research on this subject can be found in Tripathi et al. [2009]. The topic of large-amplitude waves in partially ionized plasmas, with an application to the particular case of a quiescent prominence, is addressed in Chapter 5 of the present Thesis.

Prominences are also subject to oscillatory motions of small amplitude, which have been commonly interpreted in terms of standing or propagating magnetohydrodynamic (MHD) waves. This kind of oscillations were first detected in quiescent structures by Harvey [1969], who measured amplitudes of the order of 2 km s^{-1}. With the improvement of the observing techniques and of the resolution of the instruments, a wider range of oscillations were detected (see, e.g., Landman et al. [1977], Bashkirtsev et al. [1983], Bashkirtsev and Mashnich [1984], Wiehr et al. [1984], Balthasar et al. [1986]), which lead to classify them in three categories according to their periods: short (3 to 10 min), intermediate (10 to 40 min) and long (40 to 80 min). Nonetheless, oscillations with periods of less than 1 min (e.g., Balthasar et al. [1993]) and longer than several hours (e.g., Foullon et al. [2004], Pouget et al. [2006], Foullon et al. [2009]) have also been reported. Small-amplitude oscillations are typically of local nature, i.e., they do not normally affect the whole prominence at the same time and different parts of a given structure may show dissimilar oscillatory motions. Usually, they are not related to flare activity but the mechanism that triggers them remains unknown. They may be produced by a continuous driver like the 5-min photospheric and the 3-min chromospheric oscillations, or by external impulsive agents, like magnetic reconnection events (Vial and Engvold [2015]). Authors like Harvey [1969] or Yi and Engvold [1991] suggested that Alfvén waves propagate upwards from the photosphere and the chromosphere and induce a periodic motion in the material of the prominence.

Observations by, e.g., Landman et al. [1977] and Tsubaki and Takeuchi [1986] hinted that small-amplitude oscillations are damped in time and they disappear after a few periods. This behavior was confirmed by later works like Wiehr et al. [1989], Molowny-Horas et al. [1999], Terradas et al. [2002] or Lin [2004]. To address that behavior, several damping mechanisms, such as thermal processes (see, e.g., Carbonell et al. [2004], Terradas et al. [2005]), ion-neutral collisions (Forteza et al. [2007, 2008]), resonant damping (see, e.g., Ionson [1978], Arregui et al. [2008], Soler et al. [2009b]) or wave leakage (van den Oord and Kuperus [1992], Schutgens [1997a,b]), have been proposed. The state of the research about this issue has been reviewed by, e.g., Oliver [2009], Mackay et al. [2010], Arregui and Ballester [2011] or Arregui et al. [2012].

Among all the mentioned mechanisms, this Thesis focuses on the collisional damping. The effect of the interaction between ions and neutrals was previously investigated by, e.g., Carbonell et al. [2010], Zaqarashvili et al. [2011b] and Soler et al. [2013a]. Those authors found that friction due to ion-neutral collisions can efficiently dissipate Alfvén and fast MHD waves, while the damping of slow modes is much smaller. However, they did not explore the range of high-frequency waves, which is one of the motivations of this Thesis. Hence, Chapter 4, where small-amplitude waves in partially ionized plasmas are studied by means of a multi-fluid model, includes applications to the case of quiescent prominences.

1.3.3 Waves in the corona

Uchida [1970] suggested the study of MHD propagating waves as a method to investigate the properties of the corona and the structures that can be found in such environment. Roberts et al. [1984] broadened the research by including the analysis of standing waves. Those two works were the pioneers of a new field in solar physics now known as *coronal seismology*. This field tries to obtain a better understanding of the physical characteristics of the coronal plasma by comparing properties of the waves (like periods, amplitudes, wavelengths or damping times) extracted from observations with those predicted by theoretical models.

In the earlier times of coronal seismology, most of the information about the corona was obtained during eclipses (see, e.g., Liebenberg and Hoffman [1974]) or from observations in the radio band. Some of those early results are reviewed in Aschwanden [1987], Tsubaki [1988] and Aschwanden et al. [1999]. Although the first observations from space were not of high resolution, some hints of oscillations were provided by the measurements of the OSO-7 and Skylab satellites in extreme-ultraviolet lines and X-rays (Chapman et al. [1972], Antonucci et al. [1984]). From the theoretical perspective, Wentzel [1979], Edwin and Roberts [1983] and Roberts et al. [1984] developed models of oscillations for cylindrical coronal tubes and studied the properties of waves that can propagate in such tubes. However, the full development of the field of coronal seismology had to wait until better instruments and more precise measurements were available.

The launch of the SOHO and TRACE spacecrafts in the mid and late 90s gave a huge impulse to the research of waves in the corona. The imaging and spectroscopic capacities of the instruments aboard those two satellites allowed the indubitable demonstration of the existence of wave-like dynamics in the corona (see, e.g., Ofman et al. [1997], DeForest and Gurman [1998], Nightingale et al. [1999]). For example, the first spatially resolved observations of oscillations in coronal loops were provided by TRACE (Schrijver et al. [1999], Aschwanden et al. [1999]). Coronal loops are bright arcs of plasma above the Sun's surface (an example of this kind of structure can be found in Figure 1.9). They are usually found around sunspots and in active regions, and are associated with closed magnetic lines that connect regions of opposite magnetic polarity on the solar surface.

Figure 1.9: Coronal loop observed by the TRACE satellite (Credit: NASA).

Subsequent observations with SOHO and TRACE allowed the identification of several oscillations modes of MHD waves in loops. For example, Aschwanden et al. [1999] detected standing fast kink modes with periods between 3 and 5 minutes, Wang et al. [2002] and Kliem et al. [2002] reported standing slow modes with periods between 10 and 20 minutes. Propagating MHD waves have also been observed. For instance, DeForest and Gurman [1998], Berghmans and Clette [1999] and Robbrecht et al. [2001] measured slow waves propagating upwards along the loop at speeds of 75 to 200 km s^{-1}, and Verwichte et al. [2005] detected fast kink waves with speeds between 100 and 500 km s^{-1}. In addition, observations with the Coronal Multi-Channel Polarimeter (CoMP), installed in the High Altitude Observatory (HAO) in Colorado, revealed the existence of disturbances with Doppler velocity fluctuations of the order of 0.3 km s^{-1} in extended regions of the corona, from 1.05 to 1.35 $R_{\odot}$. They were interpreted as Alfvén waves propagating along the coronal magnetic field, with phase speeds between 1000 to 4000 km s^{-1} (Tomczyk et al. [2007], Tomczyk and McIntosh [2009]). Finally, even more recent spacecrafts, such as Hinode or SDO, have shown that Alfvén waves are common in the transition region and the corona (McIntosh et al. [2011], De Pontieu et al. [2011]).

In contrast with the plasma in the chromosphere or in prominences, the material in the solar corona is fully ionized. Hence, the properties of waves in this environment would not be affected by the presence of neutrals. Nevertheless, multi-fluid models (see, e.g., Labrosse et al. [2006], Mecheri and Marsch [2008]) are still required under circumstances in which single-fluid descriptions do not give accurate results, such as in the range of high frequecies. A great number of ionized species can be found in the corona and, for instance, the collisional interaction between them may be of great relevance. The effect of the Coulomb interaction between charged species on the properties of Alfvén and high-frequency waves is addressed in Chapter 3 of this Thesis, which is devoted to the study of small-amplitude waves in fully ionized plasmas.

1.3.4 Solar wind

The solar wind is an unceasing stream of charged particles emanating from the Sun. The existence of such feature was suggested early in the 20th century by Eddington [1910]. However, it was Parker [1958] the first person to refer to such stream as *solar wind*. He studied an equilibrium model of the structure of the corona and showed that, although Sun's gravity is strong, the enormous temperatures of the corona allowed the particles to escape from the solar atmosphere due to their large thermal velocities. The first direct observations of the solar wind were performed by the Soviet satellites Luna 1, 2 and 3 (Gringauz et al. [1960]). In the last years, the Voyager missions have revealed that this stream of particles extends far beyond the outermost planets of the Solar System.

Magnetohydrodynamics waves have been detected in the solar wind also. For example, the presence of Alfvén waves was suggested by Coleman [1966] and later confirmed by Unti and Neugebauer [1968], Belcher et al. [1969] and Belcher and Davis [1971]. Then, Burlaga [1968], Whang and Ness [1970] and Burlaga [1971] presented evidences of fast waves propagating obliquely to the background magnetic field. A review about those observations, the properties of the waves and their implications for the heating and acceleration of the solar wind can be found in Hollweg [1975]. Higher-frequency waves, like the ion-cyclotron and whistler waves, which are left-handed and right-handed circularly polarized modes, respectively, with frequencies close to the cyclotron frequencies of ions, have also been detected in this environment (see, e.g., Murphy et al. [1995] and Farrell et al. [1996]). The rich variety of oscillations modes that have been observed has led to a large number of works devoted to investigate the influence of those waves in issues like the heating or the acceleration of the solar wind (see, e.g., Ofman [2010], Banerjee and Krishna Prasad [2016]). For example, it has been suggested that the dissipation of Alfvén and ion-cyclotron modes and the phenomena of cyclotron resonance may play an important role in the mentioned issues (Tu and Marsch [1997], Hollweg and Markovskii [2002]). In addition, the generation of the solar wind by ion-cyclotron waves was studied by, e.g., Isenberg and Vasquez [2011] and Mecheri [2013].

In the same way as the solar corona, the solar wind is fully ionized and, although heavier elements can be found in it, the most abundant species are protons, doubly ionized helium, and electrons. Hence, the application of the multi-fluid model developed in this Thesis to the case of waves in the solar wind is shown in Chapter 3.

1.4 Outline of the Thesis

The previous sections have enumerated several reasons why the study of the Sun, and its atmosphere in particular, is of great interest. Waves are ubiquitous in such environment and are deeply related to fundamental processes that take place in the Sun. The general characteristics of such processes are known in most of the cases but more specific details are yet to be determined and there are still open questions. The answers to those issues cannot be reached without a better understanding about the generation and propagation of waves. Hence, the goal of this Thesis is to make a step forward by investigating some of the effects that collisions between different species have on the properties of waves and instabilities. The main focus is put on partially ionized plasmas of the solar atmosphere and on the low-frequency Alfvén modes and the high-frequency ion-cyclotron and whistler modes, in addition to the Kelvin-Helmholtz instability. The following paragraphs describe how the research performed in this Thesis is organized:

- Chapter 2 presents the equations that will be used throughout this Thesis and explains the reasons why that set of equations has been chosen instead of other alternatives. There are two main descriptions that can be used in the investigation of plasmas, namely kinetic and fluid theories. The results presented in this Thesis are based in the latter, the fluid approach. Within such description, there are several approximations that can be taken, depending on the degree of accuracy that may be needed to explain the properties and evolution of a given fluid. Moreover, even when they may be composed of various distinct species, plasmas can be analyzed from a single-fluid or a multi-fluid perspective. This work is based on a multi-fluid approach where each species is described by the so-called five-moment approximation, with the inclusion of the corresponding momentum and heat transfer terms due to elastic collisions. The interaction with electromagnetic fields is taken into account by a generalized Ohm's law.

- The non-linearity of the model chosen for this research allows the study of perturbations with both small and large amplitudes. In this Thesis, such studies are performed by a combination of analytical methods and numerical simulations. The investigation of small-amplitude perturbations starts in Chapter 3, where a general dispersion relation for transverse waves in static homogeneous multi-component plasmas is derived and the details of the numerical code MolMHD are explained. Then, Chapter 3 focus on fully ionized plasmas and the effects that Coulomb collisions have in the propagation and damping of low- and high-frequency Alfvénic waves and on ion cyclotron resonances. In this chapter, the multi-fluid model is applied to three regions of the solar atmosphere: an upper layer of the chromosphere, the lower corona and the solar wind at a distance of 1 AU.

- Chapter 4 continues with the investigation of small-amplitude perturbations, but applied to the more general case of partially ionized plasmas. In addition, the effects of resistivity or magnetic diffusivity, which were previously ignored, are taken into account. Following a similar procedure to that presented in the preceding chapter, the multi-fluid approach is used to analyze the properties of waves at several heights of the chromosphere and in a quiescent prominence. A comparison of the damping caused by the different collisional interactions (Coulomb and ion-neutral elastic collisions, and resistivity) and their dependence on frequency, wavenumber and polarization of the perturbation is performed. In addition, the great influence of Hall's current in weakly ionized plasmas is studied. Furthermore, a non-linear effect is briefly analyzed: the dissipation of kinetic energy of the initial perturbation and its transformation into internal energy of the plasma by means of the collisional friction.

- Chapter 5 is devoted to the investigation of large-amplitude perturbations. In the first place, numerical simulations of standing waves excited by an impulsive driver in a plasma with prominence conditions are performed. In contrast with the small-amplitude case, it can be seen that noticeable fluctuations in the pressure and density of the plasma are generated. This fact is explained in terms of the ponderomotive force created by non-linear Alfvén waves, and comparisons between the fully and partially ionized cases are performed. Then, the heating due to ion-neutral collisions caused by a Gaussian perturbation is studied as a function of its width.

- And last but not least, in Chapter 6, a simplified version of the multi-fluid model is applied to the investigation of the Kelvin-Helmholtz instability in partially ionized magnetic flux tubes. A two-fluid approach is used to study the properties of waves in cylindrical prominence threads made of protons and neutral hydrogen when they are subject to shear flows. The influence of the collisional coupling on the onset of the instability is analyzed and comparisons between the growth times of the instability and typical lifetimes of threads are performed.

Finally, the last pages of this Thesis present a brief summary of the obtained results, outlining the main conclusions of the research described in the previous chapters, and a discussion of possible lines of future work.

Part I

Formal description of plasmas

Chapter 2

Multi-fluid theory

2.1 Motivation for a multi-fluid theory

The most fundamental description that has been developed in the research of plasmas is the kinetic one, an extension of the kinetic theory of gases. This description is of statistical nature, i.e., it can be applied when a large number of particles is present in the system of interest. It is based on the use of a distribution function, $f(\boldsymbol{x}, \boldsymbol{v}, t)$, that describes how the particles are allocated at a given time throughout the phase space, that is the space of all possible values of position, $\boldsymbol{x}$, and velocity, $\boldsymbol{v}$. Then, the dynamics of each species s of the plasma is obtained by solving the Boltzmann transport equation, which describes the statistical behavior of a thermodynamic system. This equation is given by

$$\frac{\partial f_s}{\partial t} + \boldsymbol{v_s} \cdot \nabla f_s + \frac{\boldsymbol{F}}{m_s} \cdot \nabla_{v_s} f_s = \left(\frac{\partial f_s}{\partial t} \right)_{\text{collisions}}, \tag{2.1}$$

where ∇_{v_s} is the gradient in the velocity space, i.e., $\nabla_{v_s} \equiv \left(\partial / \partial v_{s,x},\ \partial / \partial v_{s,y},\ \partial / \partial v_{s,z}\right)^T$. The function $\boldsymbol{F}$ is the sum of forces acting on the particles, whose mass is given by m_s. The term in the right hand side accounts for the variation in the distribution caused by collisions between particles. Macroscopic quantities such as number densities, velocities and pressures can then be obtained by integrating over velocity space the resulting distribution function. For instance, the number density and the average velocity are defined as

$$n_s\left(\boldsymbol{x}, t\right) \equiv \int f_s\left(\boldsymbol{x}, \boldsymbol{v}, t\right)\, d^3 v \tag{2.2}$$

and

$$\boldsymbol{u_s} \equiv \frac{1}{n_s\left(\boldsymbol{x}, t\right)} \int \boldsymbol{v_s} f_s\left(\boldsymbol{x}, \boldsymbol{v}, t\right)\, d^3 v, \tag{2.3}$$

respectively.

The kinetic approach is the most accurate but, due to its complexity, it is not the most efficient under some circumstances in which there are alternatives that yield the same results by means of much simpler computations. One of such alternatives is the MHD theory, which is based on macroscopic quantities instead of distribution functions. In magnetohydrodynamics, the plasma is treated as a continuum, which means that the length-scales of its dynamics is larger than the cyclotron radii. It is also assumed to be in thermodynamic equilibrium, i.e., the time-scales are much larger than the collision times between the components of the plasma and the length-scales are also larger than the mean free path of the particles. Regarding the investigation of oscillatory motions, ideal MHD is applicable when the frequencies of the waves are much lower than the electron and ion plasma frequencies, ω_{pe} and ω_{pi}, respectively, and the ion gyrofrequencies. The latter are given by Equation (1.14), while the former are computed as

$$\omega_{pe,i} = \sqrt{\frac{n_{e,i} Z_{e,i}^2 e^2}{\epsilon_0 m_{e,i}}}, \tag{2.4}$$

and represent the rate at which electrons and ions react to changes in the electrostatic potential.

The two descriptions mentioned in the previous paragraphs are not unrelated, but the fluid approach can be derived from the kinetic theory. The fluid equations that rule the evolution of macroscopic quantities like the density, velocity, pressure and energy can be obtained by taking velocity moments of the Boltzmann equation (see, e.g., Braginskii [1965], Bittencourt [1986], Meier [2011], Khomenko et al. [2014]).

Since its origin with the prediction by Alfvén [1942] about the existence of low-frequency waves driven by magnetic tension, ideal MHD has become a remarkable successful theory for understanding the general properties of plasmas. For instance, Alfvén's prediction was soon experimentally confirmed in a laboratory by Lundquist [1949] and corroborated later by Lehnert [1954] and Jephcott [1959]. Then, Alfvén waves have also been found in Earth's aurora (Chmyrev et al. [1988]), in planetary ionospheres (Berthold et al. [1960], Gurnett and Goertz [1981]), the interstellar medium (Arons and Max [1975], Balsara [1996]), and in the solar atmosphere, as already mentioned in Section 1.3.

However, ideal MHD is not accurate enough when applied to the investigation of waves with higher frequencies, which in the solar atmosphere may be driven by small-scale magnetic activity in the chromospheric network and reconnection of field lines (Axford and McKenzie [1992], Tu and Marsch [1997]) or by cascading from low frequencies in the corona (Isenberg and Hollweg [1983], Tu [1987]). Ideal MHD resorts to simplifications such as treating the plasma as if it were fully ionized, that is ignoring the possible presence of neutral particles, neglecting Hall's term in the induction equation and considering all ionized species together as a single fluid. Those approximations are reasonable when the frequencies of the oscillations are much lower than the collision frequencies between the different species in the plasma. In that case, collisions cause a strong coupling between all species and they can be treated as a single-fluid.

On the other hand, when the oscillation frequencies are larger (or, equivalently, when the relaxation time of collisions between unlike species is much larger than the period of the waves), each species may react to perturbations in different time-scales and the coupling is weaker than before. At that range of frequencies, the use of a multi-fluid theory is more appropriate. The multi-fluid approach consists in a set of equations for each species of the plasma, with additional terms that describe the interactions between them. Depending on the specific equations employed and the interactions considered, a multi-fluid model may be applicable up to frequencies of the order of the ion-cyclotron frequencies, but does not reach the range of electron or ion plasma frequencies, in which the kinetic theory is required. Nevertheless, the applicability range of the multi-fluid theory is enough to study the phenomena of interest for this Thesis. Hence, in the present work a multi-fluid model that takes into account the effect of partial ionization, Hall's current and resistivity is used. The equations that compose such model are detailed in the following section.

2.2 Equations for a multi-component plasma

The investigation of plasmas under the multi-fluid perspective requires the combination of the hydrodynamic equations that describe the evolution of each species in the plasma with Maxwell's equations, which detail the evolution of electromagnetic fields, and some closure equations that are given by the thermodynamic equation of state of each species.

2.2.1 Five-moment transport equations and collisional terms

The dynamics of a given fluid is described by the set of so-called transport equations that can be obtained by taking velocity moments of the Boltzmann equation, that is multiplying Equation (2.1) by powers of $\boldsymbol{v_s}$ and integrating over velocity space. Due to the complexity of this process, the computations are not shown here, only the resulting equations. They do not constitute a closed set and, hence, the adoption of an approximate expression for the fluid velocity distribution is required (Schunk [1977]). In this work, a Maxwellian distribution is chosen, i.e.,

$$f_s = n_s \left(\frac{m_s}{2\pi k_B T_s} \right)^{3/2} \exp \left(\frac{-m_s \widetilde{v}_s^2}{2 k_B T_s} \right), \tag{2.5}$$

where n_s, m_s, and T_s are the number density, mass and temperature of the species s. The variable $\widetilde{\boldsymbol{v}}_s$ is the random part of the velocity and is defined as $\widetilde{\boldsymbol{v}}_s \equiv \boldsymbol{v}_s - \boldsymbol{u}_s$, where $\boldsymbol{u}_s$ is the average part of the velocity. This choice, which is valid when the fluid is close to thermodynamic equilibrium, leads to the five-moment transport approximation, where the dynamics of each species is given by the conservation equations for mass, the three components of momentum and energy, and effects like thermal diffusion, thermal conduction or anisotropy of pressure are neglected. The influence of stress and heat flows can be considered by assuming a more complicated function for the velocity distribution and taking a higher-order moment approximation, at the expense of more complex computations. Nevertheless, the five-moment approximation is accurate enough for the investigation developed in this Thesis.

The equation for the conservation of mass, also known as mass continuity equation, is given by

$$\frac{D(m_s n_s)}{Dt} + m_s n_s \nabla \cdot \boldsymbol{V_s} = 0, \tag{2.6}$$

where $\boldsymbol{V_s}$ is the velocity of species s and $\frac{D}{Dt} \equiv \frac{\partial}{\partial t} + \boldsymbol{V_s} \cdot \nabla$ is the material derivative for time variations following the plasma motion.

The equation of motion, which expresses the conservation of momentum, is given by

$$m_s n_s \frac{D\boldsymbol{V_s}}{Dt} = -\nabla P_s + \boldsymbol{F}, \tag{2.7}$$

where P_s is the thermodynamic pressure, which has been assumed to be isotropic, and the term $\boldsymbol{F}$ includes all the forces (actually, force densities) that may act on the fluid, such as the Lorentz force felt by charged particles, gravity or the variation of momentum due to collisions with the other components of the plasma.

The Lorentz and gravity force densities are given by

$$\boldsymbol{F_L} = q_s n_s \left(\boldsymbol{E} + \boldsymbol{V_s} \times \boldsymbol{B} \right) \tag{2.8}$$

and

$$\boldsymbol{F_g} = m_s n_s \boldsymbol{g}, \tag{2.9}$$

respectively, where $q_s = Z_s e$ is the electrical charge, with Z_s the signed charged number and e the elementary electric charge. $\boldsymbol{E}$, $\boldsymbol{B}$ and $\boldsymbol{g}$ are the electric and magnetic fields and the acceleration of gravity, respectively. The collisional interaction is represented by the term $\sum_{t\neq s} \boldsymbol{R_{st}}$, whose precise definition is given later.

For numerical purposes, it is useful to write the mass continuity and the momentum equations in conservative form. In this way, the left-hand side of the equation consists of the temporal evolution of the quantity that is conserved plus the divergence of a certain flux. The right-hand side corresponds to a source term (which may be equal to zero). Therefore, due to the definition of the material derivative, Equation (2.6) is equivalent to

$$\frac{\partial(m_s n_s)}{\partial t} + \boldsymbol{V_s} \cdot \nabla \left(m_s n_s\right) + m_s n_s \nabla \cdot \boldsymbol{V_s} = 0, \tag{2.10}$$

which can be rewritten in conservative form as

$$\frac{\partial(m_s n_s)}{\partial t} + \nabla \cdot \left(m_s n_s \boldsymbol{V_s}\right) = 0. \tag{2.11}$$

Likewise, the left-hand side of Equation (2.7) can be expressed as

$$m_s n_s \frac{\partial \boldsymbol{V_s}}{\partial t} + m_s n_s \boldsymbol{V_s} \cdot \nabla \boldsymbol{V_s} = \frac{\partial \left(m_s n_s \boldsymbol{V_s}\right)}{\partial t} - \boldsymbol{V_s} \frac{\partial \left(m_s n_s\right)}{\partial t} + m_s n_s \boldsymbol{V_s} \cdot \nabla \boldsymbol{V_s}. \tag{2.12}$$

Taking into account that, according to Equation (2.11), $\frac{\partial(m_s n_s)}{\partial t} = -\nabla \cdot \left(m_s n_s \boldsymbol{V_s}\right)$ and using vector identities, the expression above is equivalent to

$$\frac{\partial \left(m_s n_s \boldsymbol{V_s}\right)}{\partial t} + \nabla \cdot \left(m_s n_s \boldsymbol{V_s V_s}\right), \tag{2.13}$$

where $\boldsymbol{V_s V_s}$ is a dyadic product, which can be written in matrix form as

$$\boldsymbol{V_s V_s} = \begin{pmatrix} V_{s,x}^2 & V_{s,x} V_{s,y} & V_{s,x} V_{s,z} \\ V_{s,y} V_{s,x} & V_{s,y}^2 & V_{s,y} V_{s,z} \\ V_{s,z} V_{s,x} & V_{s,z} V_{s,y} & V_{s,z}^2 \end{pmatrix}. \tag{2.14}$$

Hence, the conservation of momentum can be finally expressed as

$$\frac{\partial \left(m_s n_s \boldsymbol{V_s}\right)}{\partial t} + \nabla \cdot \left(m_s n_s \boldsymbol{V_s V_s} + P_s \mathbb{I}\right) = q_s n_s \left(\boldsymbol{E} + \boldsymbol{V_s} \times \boldsymbol{B}\right) + m_s n_s \boldsymbol{g} + \sum_{t \neq s} \boldsymbol{R_{st}}, \tag{2.15}$$

where the pressure term in the right-hand side of Equation (2.7) has been moved to the left-hand side and the relation $\nabla P_s = \nabla \cdot (P_s \mathbb{I})$, with $\mathbb{I}$ the identity matrix, has been used.

The last equation of the five-moment approximation concerns the conservation of energy. For the purposes of this Thesis, it will be expressed in terms of the pressure, in the following way:

$$\frac{\partial P_s}{\partial t} = -\left(\boldsymbol{V_s} \cdot \nabla\right) P_s - \gamma P_s \nabla \cdot \boldsymbol{V_s} + (\gamma - 1) \sum_{t \neq s} Q_{st}, \tag{2.16}$$

where $\gamma = 5/3$ is the adiabatic constant for mono-atomic ideal gases and Q_{st} is the term that takes into account the variation of energy caused by the collisional interaction with the rest of the species. Since pressure is not a conserved quantity, this equation cannot be written in conservative form.

There are several reasons to solve this equation in terms of the pressure instead of a related quantity. For instance, it is straightforward to compute the internal energy density of each species s, denoted by $e_{P,s}$, from the pressure since those variables are related by the following formula:

$$e_{P,s} = \frac{P_s}{\gamma - 1}. \tag{2.17}$$

An alternative approach commonly used in single-fluid models is to solve one equation for the total energy density, which is the sum of the kinetic, internal and magnetic energy densities. In this approach, numerical issues may appear when computing the pressure from the total energy. Pressure must have always positive values but, in the process of subtracting the kinetic and the magnetic energy from the total energy, negative values may be obtained due to unwanted numerical effects. In the multi-fluid formalism used in this Thesis, there is not a unique equation that accounts for the conservation of the total energy of the plasma but several equations connected to the temporal evolution of the internal energy of the different species. Nevertheless, the total energy is a conserved magnitude, which is given by

$$E_T = \int_{\mathcal{V}} \left[\sum_s \left(e_{P,s} + \frac{1}{2} m_s n_s \boldsymbol{V_s}^2 \right) + \frac{\boldsymbol{B}^2}{2\mu_0} \right] d\mathcal{V}, \tag{2.18}$$

where $\mathcal{V}$ is the volume of the plasma.

The functions $\boldsymbol{R_{st}}$ and Q_{st} represent the momentum and the heat transfer due to elastic collisions between two species s and t, and are defined as (see, e.g., Schunk [1977], Draine [1986], Leake et al. [2014], Khomenko et al. [2014])

$$\boldsymbol{R_{st}} \equiv \alpha_{st} \left(\boldsymbol{V_t} - \boldsymbol{V_s} \right) \Phi_{st}, \tag{2.19}$$

and

$$Q_{st} \equiv \frac{2\alpha_{st}}{m_s + m_t} \left[\frac{A_{st}}{2} k_{\mathrm{B}} \left(T_t - T_s \right) \Psi_{st} + \frac{1}{2} m_t \left(\boldsymbol{V_t} - \boldsymbol{V_s} \right)^2 \Phi_{st} \right], \tag{2.20}$$

respectively, where $A_{st} = 4$ for collisions between electrons and neutral species and $A_{st} = 3$ for the remaining types of collisions. The difference in the values of A_{st} is a consequence of the different velocity dependence used to calculate the scattering cross-sections of each interaction. A detailed explanation can be found in Draine [1986]. The parameter $\alpha_{st} = \alpha_{ts}$ is the friction coefficient for collisions between species s and t. The mass, temperature and velocity of species s are denoted by m_s, T_s and $\boldsymbol{V_s}$, respectively and k_{B} is the Boltzmann constant. From the definition of the momentum transfer term it can be checked that $\boldsymbol{R_{ts}} = -\boldsymbol{R_{st}}$, which means that the momentum lost by one of the species involved in a binary collision is gained by the other one, and viceversa. The functions Φ_{st} and Ψ_{st} depend on the drift speed, $|\boldsymbol{V_s} - \boldsymbol{V_t}|$, and on the reduced thermal speed, $V_{therm} \equiv \sqrt{2k_{\mathrm{B}} \left(m_t T_s + m_s T_t \right) / \left(m_s m_t \right)}$, and can be taken as equal to unity when the drift speed is much smaller than the thermal speed (Schunk [1977]). Although collisions tend to heat the plasma, the precise effect on each species depends on which of the two terms of the right-hand side of Equation (2.20) dominates. If the difference of temperature between the species s and t is large enough, the first term dominates over that associated with the velocity drifts. For instance, in a case with $T_t > T_s$, the heat transfer Q_{st} would be positive while Q_{ts} would be negative. Consequently, the temperature of species s would rise and the temperature of species t would decrease. This would continue until they had the same temperatures. Thus, collisions tend to equalize the temperatures of the components of the plasma. On the other hand, if all the species already have the same temperature, the Q_{st} terms are always positive because of their quadratic dependence on the velocity drifts, which means that all the species are heated.

The friction coefficients have different expressions depending on whether the collisions involve only ionized species or also neutral species (Braginskii [1965], Callen [2006]). For the case of collisions between two ionized species s and t, the friction coefficient is given by

$$\alpha_{st} = \frac{n_s n_t Z_s^2 Z_t^2 e^4 \ln \Lambda_{st}}{6\pi\sqrt{2\pi}\epsilon_0^2 m_{st} \left(k_{\mathrm{B}} T_s / m_s + k_{\mathrm{B}} T_t / m_t\right)^{3/2}}, \tag{2.21}$$

where n_s is the number density of species s, ϵ_0 is the vacuum electrical permittivity, and $m_{\mathrm{st}} = m_s m_t / \left(m_s + m_t\right)$ is the reduced mass. The function $\ln \Lambda_{st}$, known as Coulomb's logarithm (see, e.g., Spitzer [1962], Vranjes and Krstic [2013]), represents the factor by which the cumulative effect of the small-angle Coulomb collisions dominates over large-angle hard-sphere collisions and is given by

$$\ln \Lambda_{st} = \ln \left[\frac{12\pi \epsilon_0^{3/2} k_{\mathrm{B}}^{3/2} \left(T_s + T_t\right)}{|Z_s Z_t| e^3} \left(\frac{T_s T_t}{Z_s^2 n_s T_t + Z_t^2 n_t T_s}\right)^{1/2}\right]. \tag{2.22}$$

For collisions between neutral species n and another species s, that can be either neutral or ionized, the friction coefficient is

$$\alpha_{sn} = n_s n_n m_{sn} \frac{4}{3} \left[\frac{8}{\pi} \left(\frac{k_{\mathrm{B}} T_s}{m_s} + \frac{k_{\mathrm{B}} T_n}{m_n}\right)\right]^{1/2} \sigma_{sn}, \tag{2.23}$$

where σ_{sn} is the collisional cross-section. Values of this parameter for the collisions in hydrogen and helium plasmas are shown in Table 2.1. Some of the cross-sections are taken from quantum-mechanical models but to the best of our knowledge such accurate computations are not available for all types of collisions. Hence, in the case that quantum-mechanical computations are not available, the cross sections have been computed using the classical hard-sphere model, in which the cross-section of a collision between two species s and t is given by

$$\sigma_{st} = \pi \left(r_s + r_t\right)^2, \tag{2.24}$$

where r_s is the radius of a particle of the species s.

As shown by Vranjes and Krstic [2013], the hard-sphere model may underestimate the correct values of the cross-sections by one or two orders of magnitude. However, since the dominant ion in the plasmas studied in the present work is proton, it is not expected that the use of larger cross-sections for $\sigma_{\mathrm{HHe\ II}}$, $\sigma_{\mathrm{HHe\ III}}$ and $\sigma_{\mathrm{HeHe\ III}}$ would significantly modify the results that are discussed in the present Thesis. In addition, it must be noted that the cross-sections are actually not constants but functions of the temperature. However, according to Vranjes and Krstic [2013], the variation of the cross-sections in the range of temperatures considered in this Thesis is small. Consequently, the values included in Table 2.1 are good enough approximations.

Table 2.1: Cross-sections of collisions with neutral species

	Value (m^{-2})	Model
$\sigma_{p\mathrm{H}}$	10^{-18}	Vranjes and Krstic [2013]
$\sigma_{p\mathrm{He}}$	10^{-19}	Vranjes and Krstic [2013]
$\sigma_{e\mathrm{H}}$	1.5×10^{-19}	Vranjes and Krstic [2013]
$\sigma_{e\mathrm{He}}$	5×10^{-20}	Vranjes and Krstic [2013]
σ_{HHe}	1.5×10^{-19}	Lewkow et al. [2012]
$\sigma_{\mathrm{HHe\ II}}$	2×10^{-20}	Hard sphere
$\sigma_{\mathrm{HHe\ III}}$	1×10^{-20}	Hard sphere
$\sigma_{\mathrm{HeHe\ II}}$	5×10^{-19}	Dickinson et al. [1999]
$\sigma_{\mathrm{HeHe\ III}}$	3×10^{-21}	Hard sphere

The system given by the five-moment transport equations contains more unknowns than equations. For each species in the plasma there are five unknowns (number density, three-components of the momentum and pressure) with their respective five equations. But additionally, there are other unknowns related to the three components of the magnetic field, the three components of the electric field and the temperature of each species. Hence, the system is not closed and must be completed with additional equations. Such equations are presented in the following sections.

2.2.2 Maxwell's equations

The properties and the evolution of the electric and the magnetic fields are provided by the set of four classical electrodynamics relations, known as Maxwell's equations. Those relations can be expressed in several mathematically equivalent formulations, but the most useful for magnetohydrodynamics is the differential formulation, given by the following equations:

$$\nabla \cdot \boldsymbol{E} = \frac{\tau}{\epsilon_0}, \tag{2.25}$$

$$\nabla \cdot \boldsymbol{B} = 0, \tag{2.26}$$

$$\nabla \times \boldsymbol{E} = -\frac{\partial \boldsymbol{B}}{\partial t}, \tag{2.27}$$

and

$$\nabla \times \boldsymbol{B} = \mu_0 \boldsymbol{j} + \frac{1}{c^2}\frac{\partial \boldsymbol{E}}{\partial t}, \tag{2.28}$$

where the constant c is the speed of light in vacuum and is related to the electric permittivity, ϵ_0, and the magnetic permeability, μ_0, by

$$c^2 = \frac{1}{\epsilon_0 \mu_0}. \tag{2.29}$$

The variables τ and $\boldsymbol{j}$ represent the charge and current density, respectively, which are given by

$$\tau = \sum_s q_s n_s \tag{2.30}$$

and

$$\boldsymbol{j} = \sum_s q_s n_s \boldsymbol{V_s}. \tag{2.31}$$

The current density can be written in a more compact form, which will be useful for later calculations, as

$$\boldsymbol{j} = en_e(\boldsymbol{V} - \boldsymbol{V_e}). \tag{2.32}$$

The velocity $\boldsymbol{V}$ is related to the ions and is given by

$$\boldsymbol{V} \equiv \frac{\sum_i^M Z_i n_i \boldsymbol{V_i}}{n_e}, \tag{2.33}$$

where M is the number of ionized species and n_e is given by the condition of quasi-neutrality for a plasma, $\sum_s Z_s n_s \approx 0$, so $n_e \approx \sum_i^M Z_i n_i$.

Equation (2.25), known as Gauss's law, describes how the electric charges are the sources of the electric field. The corresponding Gauss's law for the magnetic field, Equation (2.26), implies that there are no magnetic monopoles and that the total magnetic flux through a closed surface is zero, contrary to the case of the electric flux, which is proportional to the total charge enclosed by the surface. Equation (2.27), known as Faraday's law, relates the temporal variation of the magnetic field to the spatial variation of the electric field. Finally, Equation (2.28) shows that magnetic fields are created by electric currents and by time varying electric fields.

By restricting to non-relativistic velocities, i.e., $v \ll c$, the displacement current term, $\frac{1}{c^2}\frac{\partial \boldsymbol{E}}{\partial t}$, becomes negligible and the current density can also be computed as

$$\boldsymbol{j} = \frac{\nabla \times \boldsymbol{B}}{\mu_0}, \tag{2.34}$$

an expression that is known as Ampère's law. The small relevance of the displacement current in the non-relativistic regime can be checked by comparing the orders of magnitude of the different terms in the two last Maxwell's equations. From Faraday's law, such estimation shows that

$$\frac{E}{L_0} \sim \frac{B}{T_0} \Rightarrow E \sim \frac{BL_0}{T_0}, \tag{2.35}$$

where E and B are some representatives values of the magnitudes of the electric and magnetic fields, and L_0 and T_0 are the length scale of spatial variations and the time scale of temporal variations, respectively. Applying the same procedure to Equation (2.28), it can be seen that

$$\frac{1}{c^2}\left|\frac{\partial \boldsymbol{E}}{\partial t}\right| \sim \frac{1}{c^2}\frac{E}{T_0} \sim \frac{v_0^2}{c^2}\frac{B}{L_0} \sim \frac{v_0^2}{c^2}\left|\nabla \times \boldsymbol{B}\right|, \tag{2.36}$$

where $v_0 \sim L_0/T_0$ is a characteristic velocity of the plasma. Thus, since v is assumed to be much lower than the speed of light, the displacement current can be neglected in comparison to the spatial variations of the magnetic field. One important consequence of overlooking the displacement current is that the presence of electromagnetic waves cannot be considered.

2.2.3 Generalized Ohm's law and induction equation

In ideal MHD, the electric field becomes a secondary variable that is obtained from Ohm's law for a perfectly conducting fluid, which states that the electric field in a frame moving with the fluid vanishes. Such law is mathematically expressed as

$$\boldsymbol{E'} \equiv \boldsymbol{E} + \boldsymbol{v} \times \boldsymbol{B} = 0 \Rightarrow \boldsymbol{E} = -\boldsymbol{v} \times \boldsymbol{B}, \tag{2.37}$$

where $\boldsymbol{E'}$ is the electric field in the moving frame and $\boldsymbol{v}$ is the velocity of such frame.

The multi-fluid theory follows a similar procedure and makes use of a generalized Ohm's law, that can be obtained from the momentum equation for electrons,

$$\frac{\partial\left(m_e n_s \boldsymbol{V_e}\right)}{\partial t} + \nabla \cdot \left(m_e n_e \boldsymbol{V_e}\boldsymbol{V_e} + P_e \mathbb{I}\right) = -e n_e \left(\boldsymbol{E} + \boldsymbol{V_e} \times \boldsymbol{B}\right) + m_e n_e \boldsymbol{g} + \sum_{t\neq e} \boldsymbol{R_{et}}. \tag{2.38}$$

If the variations of momentum of electrons are considered to be negligible (which is justified by the very small mass of those particles), then the first two terms on the left-hand side of Equation (2.38) can be neglected and the electric field can be expressed as

$$\boldsymbol{E} = -\boldsymbol{V_e} \times \boldsymbol{B} - \frac{\nabla P_e}{e n_e} + \frac{m_e}{e}\boldsymbol{g} + \frac{1}{e n_e}\sum_{t\neq e} \boldsymbol{R_{et}}. \tag{2.39}$$

The previous equation depends on the velocity of electrons, which is treated in magnetohydrodynamics as a secondary variable and can be obtained from the formula for the current density. By rewriting Equation (2.32) as $\boldsymbol{V_e} = \boldsymbol{V} - \boldsymbol{j}/e n_e$ and taking into account that $\boldsymbol{R_{et}} = \alpha_{et}\left(\boldsymbol{V_t} - \boldsymbol{V_e}\right)$, the generalized Ohm's law is transformed into

$$\boldsymbol{E} = -\boldsymbol{V} \times \boldsymbol{B} + \frac{\boldsymbol{j} \times \boldsymbol{B}}{e n_e} - \frac{\nabla P_e}{e n_e} + \frac{m_e}{e}\boldsymbol{g} + \eta \boldsymbol{j} + \frac{1}{e n_e}\sum_{t\neq e} \alpha_{et}\left(\boldsymbol{V_t} - \boldsymbol{V}\right). \tag{2.40}$$

The second and the third terms on the right-hand side of Equation (2.40) are known as Hall's and Biermann's battery terms. The last two terms in Equation (2.40), where the parameter η is known as the coefficient of resistivity or magnetic diffusivity and is given by

$$\eta = \frac{\sum_{t\neq e} \alpha_{et}}{\left(e n_e\right)^2}, \tag{2.41}$$

account for the Ohmic diffusion caused by collisions with electrons. The role and relevance of several of the terms of the generalized Ohm's law are discussed below, after the induction equation for the magnetic field is introduced. This equation can be obtained by combining Equation (2.40) with Faraday's and Ampère's laws. Then, the temporal evolution of the magnetic field is given by

$$\begin{aligned} \frac{\partial \boldsymbol{B}}{\partial t} &= \nabla \times \left[\boldsymbol{V} \times \boldsymbol{B} - \frac{\left(\nabla \times \boldsymbol{B}\right) \times \boldsymbol{B}}{e n_e \mu_0} - \frac{\eta}{\mu_0}\nabla \times \boldsymbol{B} - \frac{1}{e n_e}\sum_{t\neq e} \alpha_{et}\left(\boldsymbol{V_t} - \boldsymbol{V}\right)\right] \\ &+ \nabla \times \left[\frac{\nabla P_e}{e n_e} - \frac{m_e}{e}\boldsymbol{g}\right]. \end{aligned} \tag{2.42}$$

The first term in the right-hand side of the equation above is commonly known as the convective term. If only this term is taken into account, the resulting expression corresponds to the induction equation of a perfectly conducting fluid or ideal induction equation. In a perfect conductor, the magnetic field lines move with the fluid and they are said to be "frozen" in the plasma. Consequently, motions along the field lines do not modify the field but transverse motions do. A demonstration of this "frozen-in" condition can be found in, e.g., Section 4.3.3 of Goedbloed and Poedts [2004].

On the other hand, the consideration of any of the remaining terms of Equation (2.42) produces a departure from the ideal scenario. For instance, due to Hall's term (the second term on the right-hand side), ions are not completely frozen to the magnetic field and may have a different dynamics than that of electrons. When a perturbation is applied to the plasma, electrons are more able to follow the fluctuations of the magnetic field than ions due to their smaller inertia. In the case of waves in fully ionized plasmas, the effect of Hall's term produces a differentiation in the properties of the left-handed and right-handed circularly polarized waves. This effect grows when the wave frequency approaches the cyclotron frequencies of ions but can be neglected when the oscillation frequency is much lower. In partially ionized plasmas, the presence of neutrals increases the importance of Hall's effect, specially in weakly ionized plasmas, as shown by Pandey and Wardle [2006, 2008] and later in this Thesis.

To know under which conditions the terms related to collisions with electrons are required to correctly describe the evolution of the magnetic field, it is interesting to perform a dimensional analysis. This procedure leads to the following relations:

$$\left|\nabla \times (\boldsymbol{V} \times \boldsymbol{B})\right| \sim \frac{v_0 B}{L_0}, \tag{2.43}$$

$$\left|\nabla \times \left(\frac{\eta}{\mu_0} \nabla \times \boldsymbol{B}\right)\right| \sim \frac{\eta B}{\mu_0 L_0^2}, \tag{2.44}$$

where the parameters L_0, T_0, and v_0 have been defined in the previous section. The ratio between Equations (2.43) and (2.44) is known as the magnetic Reynolds number, R_m, and is given by

$$R_m = \frac{\mu_0 L_0 v_0}{\eta}. \tag{2.45}$$

The influence of the resistive term in the evolution of the magnetic field is comparable to that of the convective term when $R_m \sim 1$. Since η is typically very small in solar plasmas, a low R_m requires very small values of L_0, which correspond to large wavenumbers. Later in this Thesis, it will be checked that the effect of resistivity is negligible at small wavenumbers but it must be taken into account at larger wavenumbers.

The Biermann's battery term, which is the term related to the gradient of pressure, is usually neglected in the study of solar atmospheric plasmas because its effect is much smaller than the other terms of the induction equation. It is only relevant when large pressure gradients are present. Nevertheless, there are other astrophysical scenarios, like the generation of magnetic fields in the early universe, in which it may have a great relevance since it is a source term for the magnetic field. Even in the case of a system with no initial magnetic field, the battery term generates magnetic fields from gradients of electron pressure and density. If only the Biermann battery term is considered, the induction equation can be rewritten as

$$\frac{\partial \boldsymbol{B}}{\partial t} = -\frac{\nabla n_e \times \nabla P_e}{e n_e^2}, \tag{2.46}$$

which shows that magnetic fields can be generated from electron pressure and density gradients only if those gradients are not parallel.

Magnetic tension and magnetic pressure

If the generalized Ohm's law is inserted into the momentum equation, Equation (2.15), a term that is proportional to $\boldsymbol{j} \times \boldsymbol{B}$ appears. In the case of single-fluid plasmas, it coincides with the Lorentz force given by Equation (2.8). However, it must be noted that when multi-fluid plasmas are considered, the Lorentz force includes additional contributions due to the velocity drifts between the different ions. In any case, using Ampère's law, this term can be expressed as

$$\boldsymbol{j} \times \boldsymbol{B} = \frac{\nabla \times \boldsymbol{B}}{\mu_0} \times \boldsymbol{B}, \tag{2.47}$$

which is equivalent to

$$\frac{\left(\boldsymbol{B} \cdot \nabla\right) \boldsymbol{B}}{\mu_0} - \frac{1}{2\mu_0} \nabla \left(\boldsymbol{B} \cdot \boldsymbol{B}\right). \tag{2.48}$$

The first term in the previous formula represents the magnetic tension, a force that appears when magnetic field lines are curved and acts towards their centre of curvature. The second term can be written as

$$-\nabla \left(\frac{B^2}{2\mu_0}\right) = -\nabla P_m, \tag{2.49}$$

where P_m is the magnetic pressure. Hence, a plasma is affected by a total pressure given by the sum of the gas pressure, $\sum_s P_s$, and the magnetic pressure generated by the magnetic field. A common parameter used in the investigation of plasmas, known as the plasma β, gives the ratio between the two kinds of pressures. This parameter is defined as

$$\beta = \frac{\sum_s P_s}{P_m} = \frac{2\mu_0 \sum_s P_s}{B^2}. \tag{2.50}$$

If $\beta \ll 1$, a scenario usually found in the solar corona, the Lorentz force dominates over the gradients of gas pressure.

2.2.4 Equation of state

The last equation required to close the system is an equation of state that establishes a relation between several of the thermodynamic variables of each fluid. In this work, such relation is given by the ideal gas law, in which pressure is expressed as a function of the temperature and the number density, namely

$$P_s = n_s k_{\mathrm{B}} T_s. \tag{2.51}$$

2.2.5 Summary of multi-fluid equations

To summarize, the closed set of equations that describe the temporal evolution of a multi-component plasma is given by

$$\frac{\partial\left(m_s n_s\right)}{\partial t}+\nabla\cdot\left(m_s n_s \boldsymbol{V_s}\right)=0, \tag{2.52}$$

$$\frac{\partial\left(m_s n_s \boldsymbol{V_s}\right)}{\partial t}+\nabla\cdot\left(m_s n_s \boldsymbol{V_s}\boldsymbol{V_s}+P_s\mathbb{I}\right)=q_s n_s\left(\boldsymbol{E}+\boldsymbol{V_s}\times\boldsymbol{B}\right)+m_s n_s\boldsymbol{g}+\sum_{t\neq s}\boldsymbol{R_{st}}, \tag{2.53}$$

$$\frac{\partial P_s}{\partial t}=-\left(\boldsymbol{V_s}\cdot\nabla\right)P_s-\gamma P_s\nabla\cdot\boldsymbol{V_s}+\left(\gamma-1\right)\sum_{t\neq s}Q_{st}, \tag{2.54}$$

$$\begin{aligned}\frac{\partial\boldsymbol{B}}{\partial t} &= \nabla\times\left[\boldsymbol{V}\times\boldsymbol{B}-\frac{\left(\nabla\times\boldsymbol{B}\right)\times\boldsymbol{B}}{en_e\mu_0}-\frac{\eta}{\mu_0}\nabla\times\boldsymbol{B}-\frac{1}{en_e}\sum_{t\neq e}\alpha_{et}\left(\boldsymbol{V_t}-\boldsymbol{V}\right)\right]\\ &+ \nabla\times\left[\frac{\nabla P_e}{en_e}-\frac{m_e}{e}\boldsymbol{g},\right]\end{aligned} \tag{2.55}$$

with the collisional terms given by

$$\boldsymbol{R_{st}}\equiv\alpha_{st}\left(\boldsymbol{V_t}-\boldsymbol{V_s}\right)\Phi_{st}, \tag{2.56}$$

and

$$Q_{st}\equiv\frac{2\alpha_{st}}{m_s+m_t}\left[\frac{A_{st}}{2}k_{\mathrm{B}}\left(T_t-T_s\right)\Psi_{st}+\frac{1}{2}m_t\left(\boldsymbol{V_t}-\boldsymbol{V_s}\right)^2\Phi_{st}\right], \tag{2.57}$$

and additional relations between some of the variables given by the expressions

$$P_s=n_s k_{\mathrm{B}}T_s, \tag{2.58}$$

$$\boldsymbol{E}=-\boldsymbol{V}\times\boldsymbol{B}+\frac{\boldsymbol{j}\times\boldsymbol{B}}{en_e}-\frac{\nabla P_e}{en_e}+\frac{m_e}{e}\boldsymbol{g}+\eta\boldsymbol{j}+\frac{1}{en_e}\sum_{t\neq e}\alpha_{et}\left(\boldsymbol{V_t}-\boldsymbol{V}\right), \tag{2.59}$$

$$\alpha_{st}=\frac{n_s n_t Z_s^2 Z_t^2 e^4\ln\Lambda_{st}}{6\pi\sqrt{2\pi}\epsilon_0^2 m_{st}\left(k_{\mathrm{B}}T_s/m_s+k_{\mathrm{B}}T_t/m_t\right)^{3/2}}, \tag{2.60}$$

$$\ln\Lambda_{st}=\ln\left[\frac{12\pi\epsilon_0^{3/2}k_{\mathrm{B}}^{3/2}\left(T_s+T_t\right)}{|Z_sZ_t|e^3}\left(\frac{T_sT_t}{Z_s^2n_sT_t+Z_t^2n_tT_s}\right)^{1/2}\right], \tag{2.61}$$

$$\alpha_{sn}=n_sn_nm_{sn}\frac{4}{3}\left[\frac{8}{\pi}\left(\frac{k_{\mathrm{B}}T_s}{m_s}+\frac{k_{\mathrm{B}}T_n}{m_n}\right)\right]^{1/2}\sigma_{sn}, \tag{2.62}$$

and

$$\boldsymbol{V}\equiv\frac{\sum_i^M Z_in_i\boldsymbol{V_i}}{n_e}. \tag{2.63}$$

Part II

Waves in multi-component plasmas

Chapter 3

Small-amplitude perturbations in fully ionized plasmas*

3.1 Introduction

Multi-fluid approaches to describe multicomponent plasmas have been commonly used in aeronomy and space physics (see, e.g., Schunk [1977], Barakat and Schunk [1982]). For instance, such models have been extensively applied to the investigation of Earth's ionosphere (see, e.g., Ganguli and Palmadesso [1988], Konikov et al. [1989], Demars and Schunk [1994], Ganguli [1996]) and the solar wind (Ofman [2004], Echim et al. [2011], Abbo et al. [2016]).

In the case of fully ionized plasmas, applications of multi-fluid descriptions can be found in, e.g., Weber [1973b,a], Isenberg and Hollweg [1982], Krtička and Kubát [2000, 2001], Cramer [2001], Hollweg and Isenberg [2002], Li and Li [2007, 2008] or Rahbarnia et al. [2010]. However, the mentioned works focused only on low-frequency Alfvén waves, considered plasmas composed of only two distinct ionized species, neglected the possible effects that elastic collisions between the ionized particles may have on the properties of waves or did not explicitly take Faraday's law into account. Hence, a step forward in this research field is to use a more general model that includes some of the effects that have not been taken into account by those previous works or that can be applied to plasmas made of a larger number of ionized species.

In the present chapter, the multi-fluid theory described in Chapter 2 will be applied to fully ionized plasmas composed of up to three distinct ionized species. However, it will be shown that the generalization of the obtained results to plasmas with a larger number of ions is straightforward. The goal of this investigation is to study the properties of small-amplitude perturbations superimposed to a static and homogeneous background. The effect of Hall's current will be taken into account and the different species of the plasma will be allowed to interact by means of Coulomb collisions in addition to the usually considered interaction through electromagnetic fields. A wide range of frequencies, that goes from the low-frequency Alfvén waves to the high-frequency ion-cyclotron and whistler modes, will be analyzed. All this will allow to study the influence that the frictional force arising from elastic collisions has on the periods and the damping rates of the different oscillation modes and on the resonances and

---

*This chapter is based on: Martínez-Gómez, D., Soler, R. and Terradas, J.; 2016, *Multif-fluid approach to high-frequency waves in plasmas. I. Small-amplitude regime in fully ionized medium*, The Astrophysical Journal, 832:101 (Martínez-Gómez et al. [2016])

cutoffs associated to the cyclotron motions of ions. Furthermore, the results will be compared with the predictions from ideal MHD, with the goal of checking the range of applicability of the latter and finding under which conditions it becomes inaccurate and the use of the multi-fluid theory is required.

Two different methods will be used for this investigation. The first one consists in the analysis of the solutions of the dispersion relation for incompressible linear perturbations that can be obtained from the set of equations shown in Section 2.2. The derivation of such formula is detailed in Section 3.2. It must be noted that, although this derivation is performed in a general way that allows the inclusion of the interaction with neutrals, this effect is not taken into account in the remaining of the present chapter and is left for Chapter 4. The examination of the solutions given by the dispersion relation for the cases of two- and three-ion plasmas is shown in Section 3.3 and 3.4, respectively. The second method consists in the computation of the full temporal evolution of the perturbations by means of numerical simulations. Such simulations will be performed by means of the numerical code MolMHD Bona et al. [2009], which originally solved the MHD equations, but has been extended by adding a new module to include the multi-fluid equations. The results of this numerical method and the comparison with the predictions from the dispersion relation will be presented in Section 3.5.

3.2 Derivation of the general dispersion relation

The first step in the derivation of the dispersion relation for incompressible small-amplitude perturbations in a homogeneous plasma is to assume that each of the variables that characterize the plasma can be separated into two terms: a constant equilibrium value, which will be denoted by the subscript "0", plus a small-amplitude perturbation, denoted by the subscript "1". Hence, variables can be written as

$$n_s = n_{s,0} + n_{s,1}, \ \boldsymbol{V_s} = \boldsymbol{V_{s,0}} + \boldsymbol{V_{s,1}}, \ P_s = P_{s,0} + P_{s,1}, \ \boldsymbol{E} = \boldsymbol{E_0} + \boldsymbol{E_1}, \ \boldsymbol{B} = \boldsymbol{B_0} + \boldsymbol{B_1}. \tag{3.1}$$

Assuming a straight and constant background magnetic field, a uniform static background and that $\boldsymbol{E_0} = 0$, the temporal and spatial derivatives of the equilibrium values are equal to zero and $\boldsymbol{V_{s,0}} = 0$. Then, $\boldsymbol{V_s} = \boldsymbol{V_{s,1}}$ and from here on the subscript "1" can be dropped from the velocity variables. In addition, from Ampère's law the current density can be expressed as a function of the magnetic field perturbation only, namely

$$\boldsymbol{j} = \frac{\nabla \times \boldsymbol{B_1}}{\mu_0}. \tag{3.2}$$

Then, the multi-fluid equations shown in Section 2.2 are linearized by neglecting second-order products of the perturbed quantities and retaining only those of first order. The resulting equations are

$$\boldsymbol{E_1} = -\boldsymbol{V} \times \boldsymbol{B_0} + \frac{(\nabla \times \boldsymbol{B_1}) \times \boldsymbol{B_0}}{e n_e \mu_0} + \frac{\eta}{\mu_0} \nabla \times \boldsymbol{B_1} + \frac{1}{e n_e} \sum_{t \neq e} \alpha_{et} \left(\boldsymbol{V_t} - \boldsymbol{V}\right), \tag{3.3}$$

$$\frac{\partial \boldsymbol{V_s}}{\partial t} = \frac{Z_s e}{m_s} \left(\boldsymbol{E_1} + \boldsymbol{V_s} \times \boldsymbol{B_0}\right) + \sum_{t \neq s} \nu_{st} \left(\boldsymbol{V_t} - \boldsymbol{V_s}\right), \tag{3.4}$$

and

$$\frac{\partial \boldsymbol{B_1}}{\partial t} = -\nabla \times \boldsymbol{E_1}, \tag{3.5}$$

where $\nu_{st} = \alpha_{st}/\rho_s$ is the collision frequency between two species s and t, and $\rho_s = m_s n_s$ is the mass density of species s. Note that Equation (3.3) uses the generalized ion velocity defined in Equation (2.63). The continuity and pressure equations are here ignored because the perturbations studied in the present and the next chapter do not cause variations of the density or the pressure in the linear regime and thus $n_s = n_{s,0}$ and $P_s = P_{s,0}$. This is also the reason why the Biermann battery term and the pressure term have been dropped from Ohm's law and the momentum equation, respectively. It must also be noted that the effect of gravity has been neglected as well. The reason to do so is that the wavelengths considered in this research are shorter than the gravitational scale height.

The insertion of (3.3) into (3.4) and (3.5) leads to

$$\begin{aligned}\frac{\partial \boldsymbol{V_s}}{\partial t} &= \frac{Z_s e}{m_s}\left[(\boldsymbol{V_s}-\boldsymbol{V})\times\boldsymbol{B_0} + \frac{(\nabla\times\boldsymbol{B_1})\times\boldsymbol{B_0}}{e n_e \mu_0} + \eta\frac{\nabla\times\boldsymbol{B_1}}{\mu_0}\right] \\ &+ \frac{Z_s}{n_e m_s}\sum_{t\neq e}\alpha_{et}\left(\boldsymbol{V_t}-\boldsymbol{V}\right) + \sum_{t\neq s}\nu_{st}\left(\boldsymbol{V_t}-\boldsymbol{V_s}\right),\end{aligned} \tag{3.6}$$

$$\frac{\partial \boldsymbol{B_1}}{\partial t} = \nabla\times\left[\boldsymbol{V}\times\boldsymbol{B_0} - \frac{(\nabla\times\boldsymbol{B_1})\times\boldsymbol{B_0}}{e n_e \mu_0} - \eta\frac{\nabla\times\boldsymbol{B_1}}{\mu_0} - \frac{1}{e n_e}\sum_{t\neq e}\alpha_{et}\left(\boldsymbol{V_t}-\boldsymbol{V}\right)\right]. \tag{3.7}$$

The next step is to express the temporal dependence of the perturbations as proportional to $\exp(-i\omega t)$ with the purpose of performing a normal mode analysis, where ω is the frequency of oscillation. This is also equivalent to assume that the stationary state of wave propagation is considered. In addition, a Fourier analysis in space is performed by imposing that the perturbations are also proportional to $\exp(i\boldsymbol{k}\cdot\boldsymbol{r})$, with $\boldsymbol{k}$ the wave vector and $\boldsymbol{r}$ the position vector.

For the sake of simplicity, to study the properties of perturbations that are transverse to the direction of propagation, a reference frame in which $\boldsymbol{B_0} = (B_x, 0, 0)^T$ and $\boldsymbol{k} = (k_x, 0, 0)^T$ is chosen, while the motions of the perturbations are assumed to be in the y and z directions.

The expansion of the components of Equations (3.6) and (3.7) yields to a set of equations where the $y-$ and $z-$ components are not independent of each other, but they are coupled and, in principle, it is not possible to study the behavior of the perturbations in one direction exclusively while ignoring the other direction. The evolution of the x-component, which is along the background magnetic field direction, is uncoupled from the transverse dynamics in the linear regime. Thus, the x-component of the perturbations is ignored from here on.

At this point, it is possible to obtain the dispersion relation by rearranging the system in matrix form and solving the corresponding characteristic equation. However, it is more convenient to perform some additional steps that, in the end, will simplify the calculations and give a better insight into the results. By defining the following circularly polarized variables (see, e.g., Stix [1992], Cramer [2001]),

$$V_{s,\pm} = V_{s,y} \pm i V_{s,z}, \quad B_{1,\pm} = B_{1,y} \pm i B_{1,z}, \tag{3.8}$$

where the + corresponds to the left-hand polarization and the sign − corresponds to the right-hand polarization, the system of equations can be rewritten as

$$\begin{aligned}\omega V_{s,\pm} &= \Omega_s\left[\pm\left(V_{s,\pm}-V_{\pm}\right)-\frac{k_x}{en_e\mu_0}B_{1,\pm}\right]\mp i\frac{\eta}{\mu_0}\frac{Z_s e k_x}{m_s}B_{1,\pm}+i\frac{Z_s}{n_e m_s}\sum_{t\neq e}\alpha_{et}\left(V_{t,\pm}-V_{\pm}\right)\\ &+ i\sum_{t\neq s,e}\nu_{st}\left(V_{t,\pm}-V_{s,\pm}\right)+i\nu_{se}\left(V_{\pm}-V_{s,\pm}\right)\pm i\frac{\nu_{se}k_x}{en_e\mu_0}B_{1,\pm}, \qquad (3.9)\end{aligned}$$

$$\omega B_{1,\pm}=-k_x B_x V_{\pm}\mp\frac{k_x^2 B_x}{en_e\mu_0}B_{1,\pm}-i\frac{\eta k_x^2}{\mu_0}B_{1,\pm}\pm i\frac{k_x}{en_e}\sum_{t\neq e}\alpha_{et}\left(V_{t,\pm}-V_{\pm}\right), \qquad (3.10)$$

where $\Omega_s = Z_s e B_x/m_s$ is the cyclotron frequency of species s. Note that the cyclotron frequency is zero in the case of neutrals.

It can be checked that the two different polarizations are uncoupled. Hence, thanks to those manipulations, the original problem has been transformed into two independent systems which are much easier to handle. Now, each system can be expressed in matrix form,

$$A_{\pm}\cdot\boldsymbol{u}_{\pm}=0, \qquad (3.11)$$

where $u_{\pm}$ are the vectors of unknowns, which include the velocities of each species, $V_{s,\pm}$, and the perturbation of the magnetic field, $B_{1,\pm}$. For instance, for the case of hydrogen and helium partially ionized plasmas such vectors are given by $u_{\pm}=\left(V_{p,\pm},V_{\text{He II},\pm},V_{\text{He III},\pm},V_{\text{H},\pm},V_{\text{He},\pm},B_{1,\pm}\right)^T$ and the coefficients of the matrices $A_{\pm}$ can be found in Appendix 3.A. The unknown vectors and coefficients for the investigation performed in the remaining of this chapter, i.e., for the case of fully ionized non-resistive plasmas, can be obtained from the previous ones by ignoring the terms related to the neutral species and to collisions with electrons.

Finally, the dispersion relation is the result of solving the characteristic equation for each matrix,

$$\mathcal{D}_{\pm}\left(\omega,k_x\right)\equiv\det A_{\pm}=0. \qquad (3.12)$$

Due to its great number of parameters (e.g., several collision frequencies, the number densities of each species, the cyclotron frequencies, the wavenumber of the perturbations, etc.), the expression resulting from the previous calculation is too complex and the usual procedure it will be solved numerically, although there are some particular cases for which an analytical solution can be provided. The dispersion relation allows the study of the properties of waves excited by both an impulsive driver or a periodic driver, depending on whether it is solved as a function of the wavenumber, k_x, or as a function of the frequency, $\omega_{\pm}$, respectively. It must be noted, however, that the prescribed temporal dependence of the perturbations, $\exp(-i\omega t)$, removes the presence of any transitory effect, which means that the wave propagation is assumed to be in a stationary state.

3.3 Analysis of the dispersion relation for two-ion plasmas

We start by considering a simplified scenario. If the contributions of neutral species and resistivity are ignored and only two different kinds of ions are taken into account, the dispersion relation given by Equation (3.12) is hugely simplified and can be written as follows:

$$\begin{aligned} \omega_{\pm}^{2} \quad & \left[Z_2 n_2 \left(\rho_1 \rho_2 \left(\omega_{\pm} \mp \Omega_1\right) + i\alpha_{12}\left(\rho_1 + \rho_2\right)\right) + Z_1 n_1 \big(\rho_1 \rho_2 \left(\omega_{\pm} \mp \Omega_2\right) + i\alpha_{12}\left(\rho_1 + \rho_2\right)\big)\right] \\ \pm \quad & \frac{B_x k_x^2}{e\mu_0} \big[\rho_1 \rho_2 \left(\omega_{\pm} \mp \Omega_1\right)\left(\omega_{\pm} \mp \Omega_2\right) + i\alpha_{12}\left(\rho_1\left(\omega_{\pm} \mp \Omega_1\right) + \rho_2\left(\omega_{\pm} \mp \Omega_2\right)\right)\big] = 0. \end{aligned} \tag{3.13}$$

Here, the two types of ions are denoted by the subscripts "1" and "2" to allow a more general analysis instead of focusing in a certain kind of plasmas. Nonetheless, particular applications to solar plasmas will be provided later.

One of the main goals of this study is to determine whether collisions between different ions have a relevant role in the propagation of waves. Hence, it is interesting to compare Equation (3.13) with the even more simplified version,

$$\omega_{\pm}^{2} \quad \left[Z_2 n_2 \left(\omega_{\pm} \mp \Omega_1\right) + Z_1 n_1 \left(\omega_{\pm} \mp \Omega_2\right)\right] \pm \frac{B_x k_x^2}{e\mu_0}\left(\omega_{\pm} \mp \Omega_1\right)\left(\omega_{\pm} \mp \Omega_2\right) = 0, \tag{3.14}$$

which corresponds to the case when the effect of elastic collisions between the two ions is not included (Weber [1973b], Cramer [2001]), i.e., when $\alpha_{st} = 0$ in Equation (3.13).

It is also worth comparing the predictions of this two-fluid model with those of ideal MHD. According to ideal MHD, the results for waves excited by an impulsive driver are equivalent to those of waves generated by a periodic driver. On the contrary, the two-fluid model predicts different properties for each class of waves. While the ideal MHD dispersion relation, which is given by

$$\omega^2 = k_x^2 c_{\mathrm{A}}^2, \tag{3.15}$$

provides two solutions for each kind of driver, such symmetry does not exist in the multi-fluid approach. Equations (3.13) and (3.14) are third-order polynomials in the frequency but only second-order polynomials in the wavenumber. Therefore, three oscillation modes can be obtained for waves generated by an impulsive driver but only two modes appear when the driver is periodic.

3.3.1 Impulsive driver

The procedure to analyze the properties of waves excited by an impulsive driver is to solve the dispersion relation as a function of the wavenumber, k_x, which is assumed to be real, while the solutions for the frequency may have both a real and a imaginary part. Each solution can then be written in the form $\omega = \omega_R + i\omega_I$, where ω_R is the actual frequency of oscillation and ω_I represents a damping rate of the amplitude of the perturbations if its value is lower than zero or a growth rate if it is greater than zero. The problems analyzed in the present chapter and in Chapters 4 and 5 do not include any physical mechanism that could lead to the growth of the perturbations and to the appearance of instabilities. Hence, in the mentioned chapters, ω_I will be always negative (or, in certain cases, equal to zero). However, Part III of this work is devoted to the study of instabilities, which means that there the main focus will be put in the modes with positive values of ω_I.

Before solving the dispersion relation numerically, some analytical expressions can be obtained if certain limiting cases are considered. For instance, in the limit of very low wavenumbers, i.e., if $k_x L \ll 1$, where L is a typical length scale of the plasma, one of the three possible solutions of Equation (3.13) is

$$\omega_{\pm} \approx \pm\widetilde{\Omega} - i\alpha_{12}\frac{\rho_1+\rho_2}{\rho_1\rho_2}, \tag{3.16}$$

where

$$\widetilde{\Omega} = \frac{Z_2 n_2 \Omega_1 + Z_1 n_1 \Omega_2}{Z_1 n_1 + Z_2 n_2} \tag{3.17}$$

is the weighted average cyclotron frequency of the ions. This mode is damped because of the collisions between the two ions, as it can be deduced from the presence of a negative imaginary part of the frequency that is proportional to the friction coefficient, α_{12}. As it will be shown later with more clarity, the existence of this mode supposes a difference between the multi-fluid description and ideal MHD, since it is absent from the latter approach.

To find the other two solutions it is necessary to assume that the oscillation frequency is similar to the Alfvén frequency, $\omega_{\pm} \approx \omega_{\mathrm{A}}$, and that they are much smaller than the cyclotron frequencies. The Alfvén frequency is given by $\omega_{\mathrm{A}} = k_x c_{\mathrm{A}}$, where

$$c_{\mathrm{A}} = \frac{B_x}{\sqrt{\mu_0\left(\rho_1+\rho_2\right)}} \tag{3.18}$$

is the two-ion Alfvén speed. After some algebraic manipulations, Equation (3.13) can be rewritten as

$$\omega_{\pm}^2 \pm \omega_{\mathrm{A}}^2 \frac{\left[\left(\frac{\omega_{\pm}}{\Omega_1} \mp 1\right)\left(\frac{\omega_{\pm}}{\Omega_2} \mp 1\right) + i\Gamma\right]}{\left(\frac{\omega_{\pm}}{\widetilde{\Omega}} \mp 1 + i\frac{\alpha_{12}}{\widetilde{\Omega}}\frac{\rho_1+\rho_2}{\rho_1\rho_2}\right)} = 0, \tag{3.19}$$

with the function Γ given by

$$\Gamma = \frac{\alpha_{12}}{\rho_1\rho_2\Omega_1\Omega_2}\left[\left(\rho_1+\rho_2\right)\omega_{\pm} \mp \left(\rho_1\Omega_1 + \rho_2\Omega_2\right)\right]. \tag{3.20}$$

The corresponding version for the case when elastic collisions between the two ions are neglected is

$$\omega_{\pm}^2 \pm \omega_{\mathrm{A}}^2 \frac{\left[\left(\frac{\omega_{\pm}}{\Omega_1} \mp 1\right)\left(\frac{\omega_{\pm}}{\Omega_2} \mp 1\right)\right]}{\left(\frac{\omega_{\pm}}{\widetilde{\Omega}} \mp 1\right)} = 0. \tag{3.21}$$

By following the assumption that $\omega_{\pm} \ll \Omega_1,\ \Omega_2$ and $\widetilde{\Omega}$, two modes with $\omega \approx \pm\omega_{\mathrm{A}}$ are obtained for each polarization. These solutions correspond to the classic Alfvén wave. Hence, as expected, the multi-fluid description recovers the classic Alfvén waves of ideal MHD in the limit of low wave frequencies and no collisions.

Returning to the more general expression of the dispersion relation for two-ion plasmas, i.e., Equation (3.13), if one of the number densities is set equal to zero (for instance, $n_2 = 0$), the equation gets reduced to

$$\omega_{\pm}^2 \pm \frac{\omega_{\mathrm{A1}}^2}{\Omega_1}\omega_{\pm} - \omega_{\mathrm{A1}}^2 = 0, \tag{3.22}$$

where $\omega_{\mathrm{A1}} = k_x c_{\mathrm{A1}}$ and $c_{\mathrm{A1}} = B_x/\sqrt{\mu_0\rho_1}$ are the Alfvén frequency and speed for a single-ion plasma, respectively. This formula corresponds to the dispersion relation for Alfvén waves in Hall MHD (Lighthill [1960], Cramer [2001]). The ideal MHD formula is obtained when $\omega_{\pm} \ll \Omega_1$ and the second term of the equation can be ignored.

Actually, in the derivation of the single-ion dispersion relation from the two-ion formula, an additional term is present, namely $(\omega_\pm \mp \Omega_2)$. This term multiplies Equation (3.22) and gives the solutions $\omega_\pm = \pm\Omega_2$. However, they can be neglected since they are spurious solutions related to a second ion that is not present when a single-ion plasma is considered. They are an artifact of the mathematical derivation and do not have any physical meaning for this case.

After focusing on some particular limits of interest, the next step is to study the dependence of Equations (3.13) and (3.14) on an arbitrary wavenumber. The dispersion relations are expressed in a way that can be applied to any kind of ions. However, hereafter they will be applied to the study of plasmas that can be found in the solar atmosphere. Three regions that are worth analyzing are the upper chromospheric region, the lower solar corona, and the solar wind at 1 astronomical unit (AU). Although those three plasmas share the feature that they are mostly composed of hydrogen and helium, their physical conditions (temperatures, densities and magnetic fields) are quite different, which allows the comparison of the results provided by the multi-fluid theory in a diversity of environments.

Solar corona

Since the abundances of protons and doubly ionized helium are much larger than the abundances of any other ions in the solar corona and the solar wind (see, e.g., Ahmad [1977], Anders and Grevesse [1989]), those environment can be taken as good examples of fully ionized two-fluid plasmas. The case of coronal conditions will be analyzed in the first place.

Some typical parameters for the lower solar corona are $n_p = 2.5 \times 10^{14}$ m^{-3}, $n_{\text{He III}} = 0.1 n_p$, $B_x = 10$ G, and $T = 10^6$ K (see, e.g., Fludra et al. [1999], Sittler and Guhathakurta [1999], Warmuth and Mann [2005]). With these conditions, the Alfvén speed is $c_{\text{A}} \approx 1160$ km s^{-1}, and the collision frequencies are $\nu_{p\text{He III}} \approx 0.15$ Hz and $\nu_{\text{He III}p} \approx 0.39$ Hz. The cyclotron frequencies are $\Omega_p \approx 96000$ rad s^{-1}, $\Omega_{\text{He III}} \approx 48000$ rad s^1, and $\widetilde{\Omega} \approx 55900$ rad s^{-1}.

The results of introducing the previous parameters into the dispersion relations and solving them numerically as functions of the wavenumber are shown in Figure 3.1. The normalized real part of the frequency, ω_R/Ω_p, and the absolute value of the normalized damping rate, $|\omega_I|/\Omega_p$, as functions of the normalized wavenumber, $k_x c_{\text{A}}/\Omega_p$, are displayed on the left and the right panels, respectively.

Only the modes with $\omega_R > 0$ are depicted in Figure 3.1: two of them correspond to the left-hand polarization (and will be denoted by the letter L), while the third corresponds to the right-hand polarization (denoted by R). The region with $\omega_R < 0$ is not plotted because it would be symmetric with respect to the horizontal axis, but with an exchange of the polarizations of the modes. In addition, only the solutions from the dispersion relation that takes collisions into account, Equation (3.13), are shown. The reason to do so are that no clear differences between the results from the two dispersion relations are appreciable in the real part of the frequency, i.e., collisions have a small effect on the frequency of the oscillation of the waves, but $\omega_I = 0$ when friction is not considered.

The left panel of Figure 3.1 reveals that when $k_x c_{\text{A}}/\Omega_p \ll 1$, the multi-fluid description presents two branches with clearly distinct behavior: one of these branches (the red dotted-dashed line) corresponds to the L mode associated with the weighted average cyclotron frequency given by Equation (3.17). It can be noted that there is no ideal MHD solution akin to this high-frequency mode, so it appears exclusively when the plasma is treated as composed by

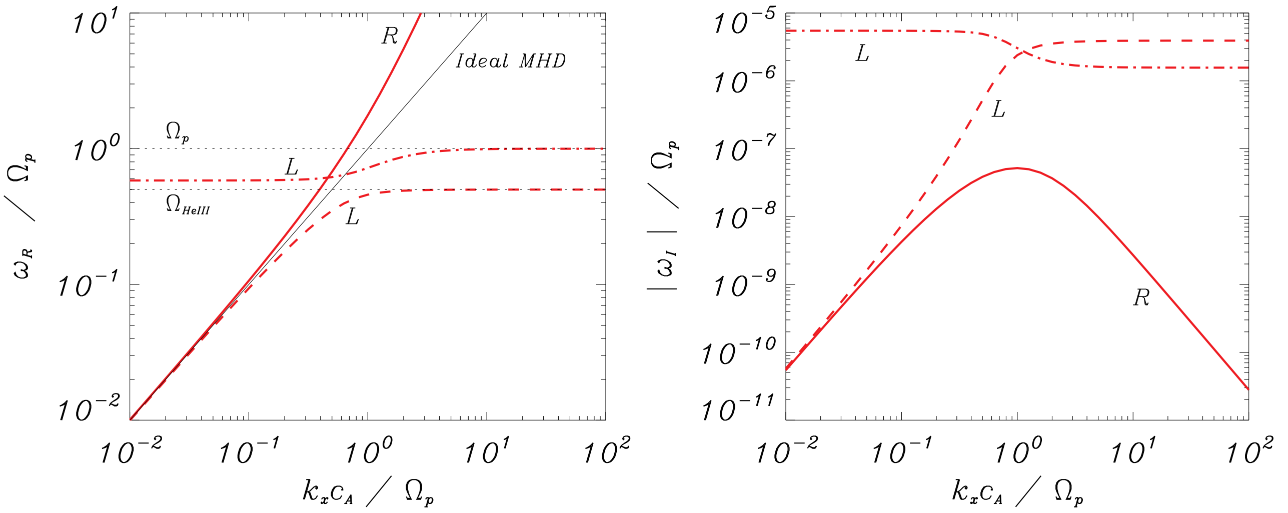

Figure 3.1: Solutions of the dispersion relations for a two-ion plasma with coronal conditions: $n_p = 2.5\times10^{14}$ m^{-3}, $n_{p\text{HeIII}} = 0.1 n_p$, $B_x = 10$ G, $T_p = T_{\text{HeIII}} = 10^6$ K, and $\nu_{p\text{HeIII}} = 0.15$ Hz. Left: normalized frequency, ω_R/Ω_p, as a function of the normalized wavenumber, $k_x c_{\text{A}}/\Omega_p$. Right: absolute value of the normalized damping, $|\omega_I|/\Omega_p$ as a function of $k_x c_{\text{A}}/\Omega_p$. The red lines correspond to the solutions from Equation (3.13) (solid line: R mode; dashed and dot-dashed lines: L modes) and the black thin line represents the ideal MHD results ($\omega = \omega_{\text{A}}$). The dotted lines on the left panel represent the cyclotron frequency of each ion, with $\Omega_p > \Omega_{\text{HeIII}}$.

several fluids.

The second branch contains the remaining L mode (dashed line) and the only R mode with $\omega_R > 0$ (red solid line). These modes have approximately the same value of the frequency, $\omega_R \approx \omega_{\text{A}}$, which means that, in this low wavenumber limit, the frequency of oscillation is almost independent of the direction of polarization. However, at higher wavenumbers, this second branch splits into two and the corresponding waves become dispersive: their phase speeds are not independent of the wavenumber, in contrast to low-frequency waves, which are non-dispersive.

The L and R modes of the second branch start diverging from each other at $k_x c_{\text{A}} \simeq 0.1\Omega_p$. The left-hand solution oscillates always with a frequency below the Alfvén frequency and tends to the cyclotron frequency of the more massive ion, $\Omega_{\text{He III}}$, in the limit of high wavenumbers. On the contrary, the oscillation frequency of the right-hand mode is always higher than the Alfvén frequency, and keeps increasing its frequency without converging to any limiting value in the range of wavenumbers explored in this study (at even higher wavenumbers it tends to the electron cyclotron frequency). Due to their behavior when $k_x c_{\text{A}}/\Omega_p \gtrsim 1$, the two L modes are commonly known as ion cyclotron waves and the R mode is known as the whistler wave (see, e.g., Cramer [2001]).

The right panel show that collisions cause a clearly different damping on each mode of oscillation. The left-handed high-frequency modes are the most affected by the effect of collisions, while the damping on the Alfvénic modes and the high-frequency whistler wave is almost negligible. The cause of this variety of behaviors can be found in the velocity amplitude ratios and the phase shifts associated to each mode. This issue will be analyzed with more detail in the section devoted to the study of a plasma with chromospheric conditions.

Now, the focus will be put in two other useful parameters for the examination of the behavior of waves, namely the quality factor and the damping times, which are defined as

$$Q \equiv \frac{1}{2}\left|\frac{\omega_R}{\omega_I}\right| \tag{3.23}$$

and

$$\tau \equiv \frac{1}{|\omega_I|}, \tag{3.24}$$

respectively. The damping time represents the time interval in which the amplitude of the oscillation is reduced by a factor $\frac{1}{e} \approx 0.368$. In turn, the quality factor gives a measure of the relevance of the damping during an oscillation period. If $Q > 1/2$, the perturbation is said to be underdamped: it oscillates, but its amplitude decreases with time; in the limit when $Q \to \infty$ there is no damping at all. If $Q \leq 1/2$ the wave is overdamped (with the special situation of $Q = 1/2$ known as critically damped): the damping dominates the behavior of the perturbation. When $Q = 0$ the mode is evanescent: there is no oscillation and the amplitude of the oscillation decays exponentially with time.

From the results shown in Figure 3.1, it is easy to check that for all modes $Q \gg 1$, i.e., the perturbations are extremely underdamped and the effect of collisions is almost irrelevant during a single period. However, for longer times the damping may not be negligible. For instance, by setting the wavenumber to $k_x = \pi/10^5$ m^{-1}, the following damping times are obtained: $\tau_- \approx \tau_{+,1} \approx 1.28 \times 10^8$ s and $\tau_{+,2} \approx 1.9$ s. This means that after a few seconds, the perturbation related to the latter mode vanishes and only the other two modes of oscillation remain, almost undamped as if there were no collisions. For much higher wavenumbers, the situation is different. For instance, if the wavenumber is increased to $k_x = \pi/10$ m^{-1} (which corresponds to the normalized value $k_x c_{\mathrm{A}}/\Omega_p \approx 3.8$), the damping times are $\tau_- \approx 670$ s, $\tau_{+,1} \approx 2.1$ s, and $\tau_{+,2} \approx 6.34$ s. Thus, the perturbations associated with the ion cyclotron modes disappear after a few tens of seconds, while the whistler wave has a considerably longer lifespan. In the case where collisions between the two ionized species are not taken into account, none of the modes attenuates with time.

The wave energy dissipated by the effect of collisions is deposited in the plasma and so it contributes to plasma heating. However, such effect cannot be captured by the present linear analysis, since the energy equation has been overlooked. This issue will be studied with detail in Chapter 5, where large-amplitude nonlinear perturbations will be considered and the transformation of the kinetic and magnetic energy of the perturbation into heat will be more noticeable.

Solar wind at 1 AU

The solar wind at 1 AU can be described by the following set of parameters (see, e.g., Aellig et al. [2001], Laming and Feldman [2003], Goedbloed and Poedts [2004]): $n_p = 10^7$ m^{-3}, $n_{\mathrm{HeIII}} = 5 \times 10^5$ m^{-3}, $B_x \approx 5 \times 10^{-5}$ G and $T \approx 10^5$ K, which yields an Alfvén speed of $c_{\mathrm{A}} \approx 31$ km s^{-1}, collision frequencies on the order of 10^{-7} Hz and cyclotron frequencies given by $\Omega_p \approx 0.479$ rad s^{-1} and $\Omega_{\mathrm{HeIII}} \approx 0.239$ rad s^{-1}. Then, the dispersion relations give results for this case that are qualitatively identical to those portrayed in Figure 3.1 for the case of the solar corona, with the difference that now the collision frequencies are so minute that the solar wind can be considered as a completely collisionless fluid from the perspective of this analysis. Due to the low values of the collision frequencies, the damping times are of the order of 10^6 s or larger for a wavenumber $k_x = \pi/10^5\ \mathrm{m}^{-1}$ (which corresponds to the normalized wavenumber $k_x c_{\mathrm{A}}/\Omega_p \approx 2.1$), or even greater for lower values of the normalized wavenumber.

As already stated in the previous section, for Alfvénic waves the predictions given by the multi-fluid approach depart from those of ideal MHD when $k_x c_{\mathrm{A}}/\Omega_p \gtrsim 0.1$. This fact imposes a limit to the range of applicability of ideal MHD. From the previous expression, it is possible to obtain a critical value of wavelength that represents the minimum wavelength that a perturbation can have to be reasonably well described by ideal MHD. This critical wavelength is given by

$$\lambda_c \approx \frac{2\pi c_{\mathrm{A}}}{0.1\Omega_p}. \tag{3.25}$$

The solar wind conditions lead to a critical wavelength of $\lambda_c \approx 4 \times 10^3$ km. The respective value for the solar corona is $\lambda_c \approx 750$ m.

It must be noted that the approximation used for the functions Φ_{st} and Ψ_{st} in the momentum and heat transfer terms, Equations (2.56) and (2.57), is not strictly valid in the solar wind. In this environment, the drift speed may be comparable to the reduced thermal speed and, hence, it would be more appropriate to employ the more general expressions for Φ_{st} and Ψ_{st} given by Schunk [1977]. However, due to the extremely low value of the collision frequencies, the application of those more realistic formulae would not modify in a remarkable way the results explained in the lines above.

Upper chromosphere

One contrasting characteristic of the solar chromosphere in comparison with the two previously analyzed environments is that it contains a non-negligible quantity of neutrals. However, the present chapter is devoted to the study of fully ionized plasmas and, hence, the presence of those neutral species will not be taken into account here but left to be studied in the next chapter. The chromosphere also differs from the corona and the solar wind in the fact that, throughout the majority of its extension, the second most abundant ion is the singly ionized helium instead of the doubly ionized helium. The reason of this dissimilarity is that the temperature is not large enough for helium to be fully ionized.

A model for the temperatures and abundances of hydrogen and helium as functions of height of a bright region of the quiet sun chromospheric network is provided by Table 3 (labeled as Model F) from Fontenla et al. [1993]. Here, the values corresponding to a height of 2000 km above the top of the photosphere are used, namely $n_p = 10^{17}\ \mathrm{m}^{-3}$, $n_{\mathrm{He\ II}} = 10^{16}\ \mathrm{m}^{-3}$ and $T = 10^4$ K. A typical value of the magnetic field at that height is $B_x = 35$ G. Thus, the Alfvén speed is $c_{\mathrm{A}} \approx 204\ \mathrm{km\ s}^{-1}$, the cyclotron frequencies are $\Omega_p = 335268\ \mathrm{rad\ s}^{-1}$, $\Omega_{\mathrm{He\ II}} = 83817.1\ \mathrm{rad\ s}^{-1}$, and $\widetilde{\Omega} = 106676\ \mathrm{rad\ s}^{-1}$, and the collision frequencies are $\nu_{p\mathrm{He\ II}} \approx 8500$ Hz and $\nu_{\mathrm{He\ II}p} \approx 21300$ Hz.

Again, Figure 3.1 can be used to describe the qualitative properties of waves in this plasma, but now it must be taken into account that the collision frequencies are much larger than in the previous scenarios. Now $\nu_{st} \simeq \Omega_s/(2\pi)$ and the damping produced by the collisional interaction of the two ions is considerably greater than before. In a plasma with coronal conditions, the maximum normalized damping was $|\omega_I|/\Omega_p \approx 2 \times 10^{-5}$, while the corresponding value that is obtained for chromospheric conditions is $|\omega_I|/\Omega_p \approx 0.1$, four orders of magnitude larger than the former before.

In the particular case that the wavenumber is set to $k_x = \pi/10^5$ m^{-1}, the Alfvén frequency is $\omega_{\mathrm{A}} \approx 6.41$ rad s^{-1} and the dispersion relation yields the following solutions: $\omega_- = \omega_{+,1} \approx 6.41 - i9.27 \times 10^{-6}$ rad s^{-1} and $\omega_{+,2} \approx 106676 - i29750$ rad s^{-1}. Thus, it can be checked that the quality factor for the Alfvénic modes is still much greater than 1/2, but for the latter mode $Q \approx 1.8$. The damping times are much shorter than in the previous environments: $\tau_- = \tau_{+,1} \approx 10^6$ s and $\tau_{+,2} \approx 3 \times 10^{-5}$ s. If the normalized wavenumber is increased to values larger than 0.1, the damping time of all modes is lower than $\tau = 0.01$ s, which means that all the high-frequency ion cyclotron and whistler waves are extremely short-lived in the upper chromosphere.

Finally, under the conditions of the plasma studied in this section, the critical wavelength that puts a limit to the range of applicability of ideal MHD is $\lambda_c \approx 40$ m. This value is below the spatial resolution of any currently available instrument.

As stated before, a significant amount of neutrals is present in the chromosphere. Hence, the results given here should be interpreted with caution, since the effects of the interactions between ions and neutrals have not been considered.

In the next step of this investigation, the solutions obtained from the dispersion relations are introduced back to Equations (3.9) and (3.10) with the aim of computing the amplitudes of the perturbations associated to each mode. In the linear regime, those amplitudes are proportional to an arbitrary constant whose actual value is not significant. To get rid of that inconvenient factor, amplitude ratios will be calculated, which provide a better insight on the physics of the problem. In addition, it is also interesting to compute the phase shifts associated to those amplitude ratios.

The amplitude ratios $|V_p/V_{\mathrm{He\ II}}|$ and the phase shifts, φ, are shown in the left and right panels of Figure 3.2, respectively. It can be seen that the low-frequency waves, which are represented by the red solid and dashed lines at low wavenumbers when $\nu_{st} \neq 0$ and by the black circles and crosses when $\nu_{st} = 0$, have amplitude ratios of the order of unity and phase shifts that are close to zero. This means that for the given frequencies the magnetic field is able to keep the two ionized fluids strongly coupled. There is almost no velocity drift and, hence, the momentum transfer, which leads to the damping of the oscillations, can be neglected even when collisions are considered.

At higher frequencies, the different inertia and charge number of each species causes them to have an unlike response to the perturbation and the interaction through the magnetic field is not enough to maintain the strong coupling. Thus, velocity drifts appear and, consequently, there is a friction force. The larger the phase drift, the larger the damping caused by the momentum transfer between ions. The modes with larger phase shifts are left-handed polarized. The reasons are that L-modes are affected by the resonances that appear when the oscillation frequency reaches the cyclotron frequencies and that the species with a larger cyclotron frequency can follow the perturbations of the magnetic field more easily than the other species throughout a larger range of frequencies. More details of the cyclotron resonances are given in the next section.

Figure 3.2 can also be applied to the cases of the solar corona and the solar wind, but taking into account that the amplitude ratios and the phase shifts are well described by the collisionles

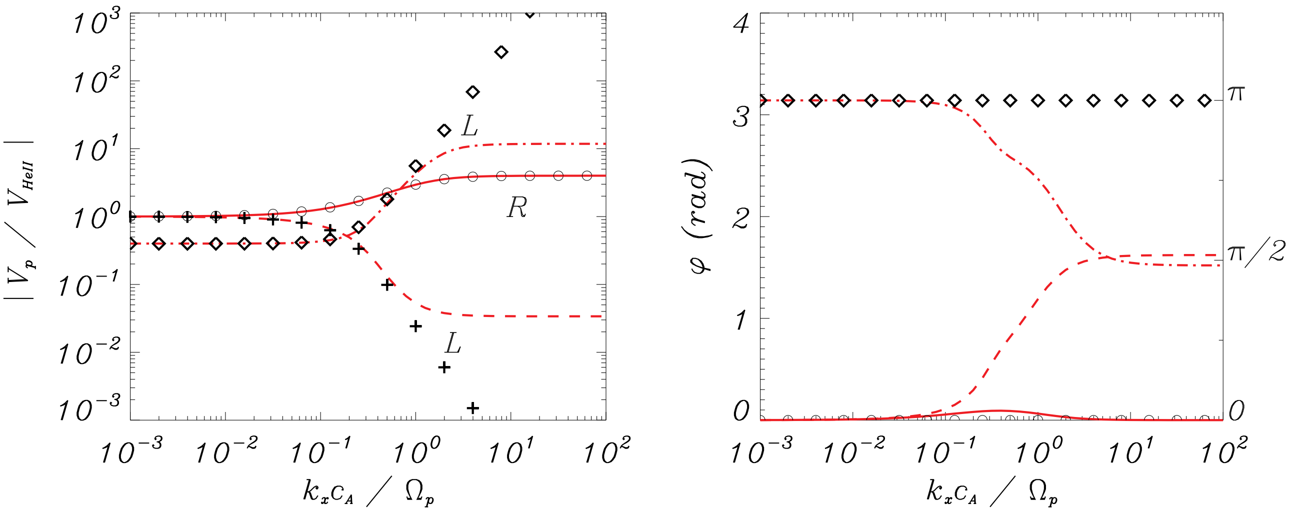

Figure 3.2: Ratio of amplitudes (left) and phase shift (right) of the velocities of ions computed from the solutions of Equations (3.13) (red lines, with the same style code as in Figure 3.1) and (3.14) (black symbols) for a two-ion plasma with upper chromospheric conditions. Note that the black crosses are not shown in the right panel: the reason is that they would overlap the circles.

results. In those environments, for high-frequency waves there are larger differences between the velocity amplitudes of the two species (which in these plasmas are p and He III), except for the right-handed mode.

3.3.2 Periodic driver

The study of waves excited by a periodic driver is performed by solving Equations (3.13) and (3.14) as functions of a real frequency, ω. The wavenumber may be complex and can be written as $k_x = k_R + ik_I$. When the frequency is positive, $k_R > 0$ corresponds to a wave propagating along the positive x-axis, while $k_R < 0$ corresponds to a wave propagating to the opposite direction. When $k_I \neq 0$, it can be found that $\mathrm{sgn}(k_I) = \mathrm{sgn}(k_R)$, which means that the amplitudes of the perturbations are damped in space.

Before solving the dispersion relations, some information can be retrieved by simple inspection. For instance, Equation (3.14), which does not take collisions into account, can be written as

$$k_{x,\pm}^2 = \frac{\omega_\pm^2}{c_\mathrm{A}^2} \frac{\left(1 \mp \frac{\omega_\pm}{\tilde{\Omega}}\right)}{\left(1 \mp \frac{\omega_\pm}{\Omega_1}\right)\left(1 \mp \frac{\omega_\pm}{\Omega_2}\right)}, \tag{3.26}$$

and reveals that the mode $k_{x,+}$ has singular points at $\omega_+ = \Omega_1$ and $\omega_+ = \Omega_2$, while singularities appear for $k_{x,-}$ at $\omega_- = -\Omega_1$ and $\omega_- = -\Omega_2$. These singularities are known as ion cyclotron resonances (see, e.g., Cramer [2001], Rahbarnia et al. [2010]). At a resonance, the wavenumber tends to infinity, which leads to a null phase speed. Hence, the perturbation does not propagate. The energy of the driver is used in increasing the amplitude of the perturbation of the ion associated to the cyclotron frequency at which the resonance appears.

In the same way, Equation (3.13), which takes collisions into account, can be expressed as

$$k_{x,\pm}^2 = \frac{\omega_\pm^2}{c_{\rm A}^2} \frac{\left(1 \mp \frac{\omega_\pm}{\widetilde{\Omega}} \mp i \frac{\alpha_{12}}{\widetilde{\Omega}} \frac{\rho_1+\rho_2}{\rho_1 \rho_2}\right)}{\left(1 \mp \frac{\omega_\pm}{\Omega_1}\right)\left(1 \mp \frac{\omega_\pm}{\Omega_2}\right) + i\Gamma}. \tag{3.27}$$

If the denominator of the previous formula is equated to zero, it can be checked that there is no real ω which solves the resulting equation. The denominator can be expanded in the form of a second degree polynomial on ω and the calculation of its discriminant leads to a complex number, which means that there are no real solutions for the corresponding equation. Hence, when collisions are considered, there are no singularities.

Figure 3.3 shows the results of the study of waves excited by a periodic driver in a plasma with upper chromospheric conditions, using the same physical parameters as in the previous section. The left panel displays the real part of the normalized wavenumber, $k_R c_{\rm A}/\Omega_p$, as a function of the normalized frequency, ω/Ω_p, and the right panel displays the corresponding imaginary part or normalized spatial damping of the waves, $k_I c_{\rm A}/\Omega_p$. The dispersion relations yield two solutions for each state of polarization but, for the sake of simplicity, only those with $k_R > 0$ are shown.

The inspection of Figure 3.3 reveals that there are no remarkable differences between the cases with $\nu_{p\text{He II}} = 0$ and with $\nu_{p\text{He II}} \neq 0$ for low frequencies. Within this limit, the two circularly polarized modes share the same wavenumber, which coincides with the ideal MHD results. If the frequency is increased, the two modes start to diverge from each other and from the prediction of ideal MHD. This separation occurs when $\omega/\Omega_p \gtrsim 0.1$.

If collisions are neglected, the wavenumber of the L mode rises very fast until it reaches a first resonance at $\omega/\Omega_p = 0.25$ (or equivalently, $\omega = \Omega_{\text{He II}}$). Then, it enters a cutoff region where $k_R = 0$ and $k_I > 0$. Thus, this mode becomes evanescent. The cutoff region ends when $\omega = \widetilde{\Omega}$ and k_R increases again until it finds a second resonance at $\omega = \Omega_p$. From this value on, the mode becomes evanescent again. On the contrary, the R mode is not subject to any resonance and its wavenumber keeps increasing with the frequency, but it is always lower than the result provided by ideal MHD. Note that these remarks correspond to the case of positive frequencies. If negative values of ω are considered, the described behavior of the L and R modes is swapped, i.e., resonances appear in the R mode.

By inspecting the solutions that correspond to the collisional cases, it can be checked that this interaction between the two ions has a very small impact on the R mode. In contrast, the behavior of the L mode is dramatically altered: the two resonances are removed and k_R remains finite. Moreover, the first cutoff region is also removed: there is some damping on the perturbations, but they do not turn into evanescent waves. Finally, from $\omega/\Omega_p = 1$ on, the normalized wavenumber suffers a strong decrease and the waves are then overdamped instead of being fully evanescent.

To better illustrate the discussion in the previous paragraph it is useful to compute the quality factor of the perturbations, which is now given by $Q \equiv 1/2|k_R/k_I|$. Figure 3.4 shows the quality factor of the solutions presented in Figure 3.3 as a function of the normalized frequency. The shaded areas mark the cutoff regions of the collisionless L mode and the horizontal dashed line points out the critical value $Q = 1/2$. It can be seen that the R mode is always underdamped, since its quality factor is always larger than $1/2$, and has a minimum around $\omega/\Omega_p = 0.25$, i.e., at the frequency of resonance of singly ionized helium. Waves

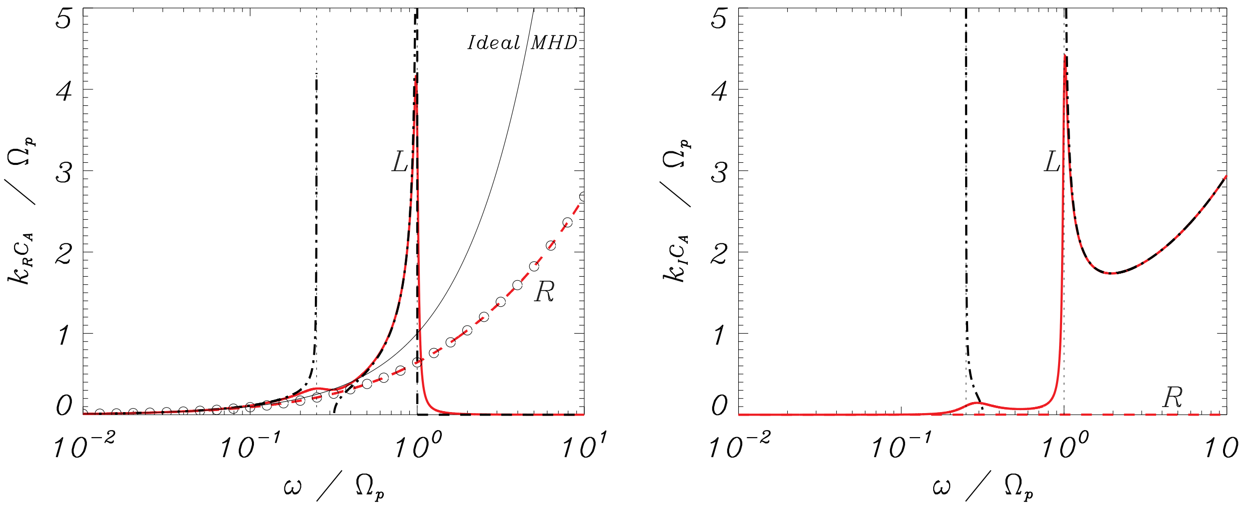

Figure 3.3: Normalized wavenumber (left), $k_R c_\mathrm{A}/\Omega_p$, and normalized spatial damping (right), $k_I c_\mathrm{A}/\Omega_p$, as functions of the normalized frequency, ω/Ω_p, for waves excited by a periodic driver in a two-ion plasma with upper chromospheric conditions: $n_p = 10^{17}$ m^{-3}, $n_{\mathrm{HeII}} = 10^{16}$ m^{-3}, $B_0 = 35$ G, $T_p = T_{\mathrm{HeII}} = 10^4$ K, and $\nu_{p\mathrm{HeII}} = 8500$ Hz. Red solid lines and red dashed lines correspond to the L and R modes, respectively, when the effect of collisions is included. The black dot-dashed lines and the black circles represent the collisionless left-hand and right-hand modes, respectively. The dotted vertical lines show the position of the resonances and the thin black lines represent the solutions from ideal MHD.

associated with the L mode are clearly underdamped at low frequencies. When ω/Ω_p rises, Q decreases until there is a minimum in the first cutoff region. However, even in that region the waves are still underdamped, since $Q \approx 1$. Then, the quality factor increases again and there is a maximum before the $\omega/\Omega_p = 1$, at which the curve crosses the critical value $Q = 1/2$ and oscillations become overdamped. Although $Q \neq 0$ (in contrast to what happens when there are no collisions), Q decreases at a very fast pace in the second cutoff region and waves may well be treated as evanescent for very large frequencies.

The removal of resonances and cutoffs due to collisions is a consequence of the dissipation caused by the friction between the different species. In the case without collisions, waves do not propagate at the resonant frequencies and the energy provided by the driver is used in increasing the radius of gyration of the ions. But if there is friction, a fraction of that energy is transferred to the other species and thus the perturbation is allowed to propagate.

As in the section dedicated to the impulsive driver, the next step of this study is to analyze the amplitudes and phase shifts of the perturbations. The left panel of Figure 3.5 shows the absolute value of the ratio of the velocities, $|V_p/V_{\mathrm{He\ II}}|$, for the solutions presented in Figure 3.3. The phase shifts, on the other hand, are shown in the right panel. It can be seen that at low frequencies the amplitude ratios are close to unity and that there is no phase shift. This means that the magnetic field produces a strong coupling between the two species. But as the frequency increases, the motions of the two fluids become more independent from each other, particularly at the resonances of the L mode. The inclusion of friction causes the fluids to be more coupled. This can be clearly seen at the frequencies of resonance, where the amplitude

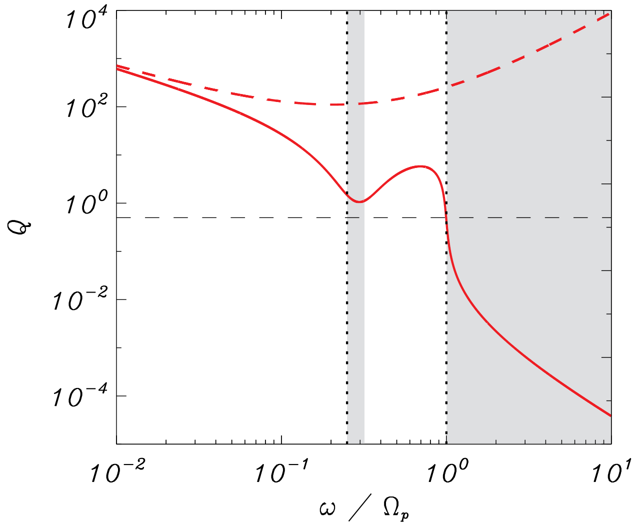

Figure 3.4: Quality factor, Q, as a function of the normalized frequency, ω/Ω_p, computed from the solutions displayed on Figure 3.3. The shaded areas show the cut-off regions of the left-hand polarized mode from Equation (3.27). The red solid and red dashed curves represent the left-hand and right-hand modes of Equation (3.26), respectively. The dotted vertical lines mark the position of the cyclotron frequencies, with $\Omega_{\mathrm{HeII}} < \Omega_p$. The dashed horizontal line corresponds to $Q = 1/2$.

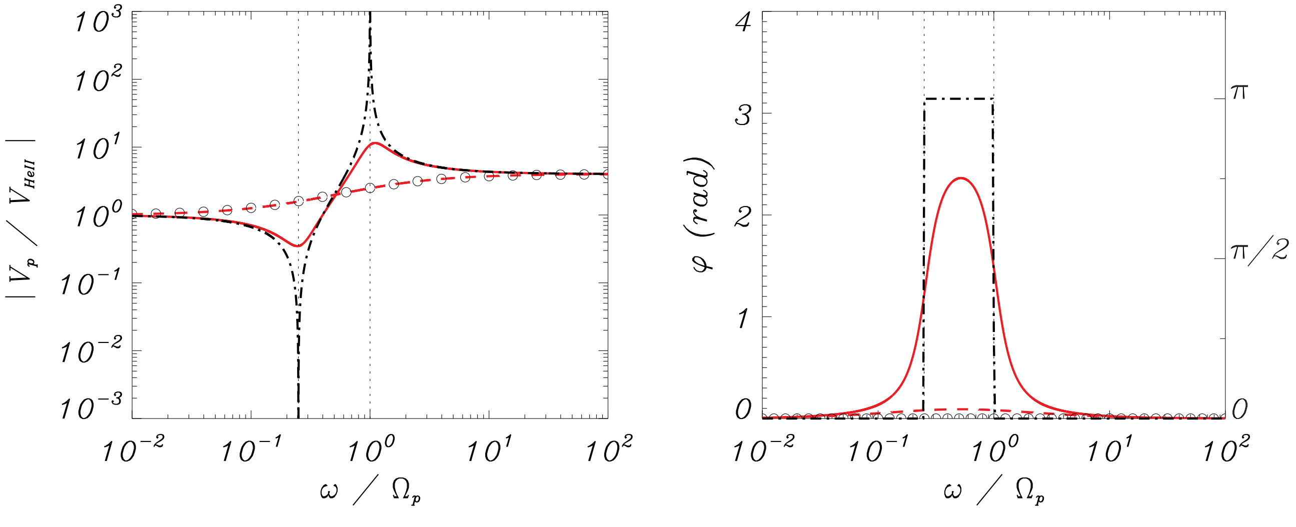

Figure 3.5: Ratio of amplitudes (left) and phase shift (right) of the velocities of protons and singly ionized helium computed from the results shown on the right panels of Figure 3.3 (chromospheric conditions).

ratios reach extreme values when collisions are neglected.

The paragraphs above have been devoted to the analysis of a plasma with upper chromospheric conditions but nothing has been said about the other two environments studied in the previous section. The behavior of waves in the solar corona and the solar wind at 1 AU can be anticipated from the collisionless solutions displayed in Figures 3.3 and 3.5, but keeping in mind that now the second ionized species is He III instead of He II. This change implies that the positions of the lower resonance and the lower bound of the first cutoff region are modified accordingly.

3.4 Analysis of the dispersion relation for three-ion plasmas

The addition of a third ion to the plasma increases the complexity of the problem to be analyzed, which is reflected in a much longer and more complicated formula for the dispersion relation due to the presence of a great number of additional terms associated to collisions. Hence, it will not be shown here. Nonetheless, the abridged version in which the elastic collisions between the different ions are neglected can be used to analyze some of the general properties. This simpler collisionless version is given by

$$\omega_{\pm}^2\left[Z_1 n_1\left(\omega_{\pm}\mp\Omega_2\right)\left(\omega_{\pm}\mp\Omega_3\right)+Z_2 n_2\left(\omega_{\pm}\mp\Omega_1\right)\left(\omega_{\pm}\mp\Omega_3\right)+Z_3 n_3\left(\omega_{\pm}\mp\Omega_1\right)\left(\omega_{\pm}\mp\Omega_2\right)\right] \pm\frac{B_x k_x^2}{e\mu_0}\left(\omega_{\pm}\mp\Omega_1\right)\left(\omega_{\pm}\mp\Omega_2\right)\left(\omega_{\pm}\mp\Omega_3\right)=0. \tag{3.28}$$

The dispersion relations for waves in a three-ion plasma are fourth-degree polynomials in ω. Thus, for the case of waves generated by an impulsive driver, an additional oscillation mode appears for each polarization with respect to the system with only two ions. By exploring analytically the limit of small wavenumbers, as in Section 3.3.1, it can be checked that the new mode is related to the cyclotron frequencies. Each polarization still has only two Alfvénic modes, with $\omega\approx\pm\omega_{\mathrm{A}}$, where the Alfvén speed is computed using the sum of the densities of the three ions. The frequencies of the remaining modes are $\omega_{\pm}=\pm\widetilde{\Omega}_1$ and $\omega_{\pm}=\pm\widetilde{\Omega}_2$, where $\widetilde{\Omega}_1$ and $\widetilde{\Omega}_2$ are the solutions to

$$Z_1 n_1\left(\omega-\Omega_2\right)\left(\omega-\Omega_3\right)+Z_2 n_2\left(\omega-\Omega_1\right)\left(\omega-\Omega_3\right)+Z_3 n_3\left(\omega-\Omega_1\right)\left(\omega-\Omega_2\right)=0, \tag{3.29}$$

and are given by

$$\begin{aligned}\widetilde{\Omega}_1=&\frac{Z_1 n_1\left(\Omega_2+\Omega_3\right)+Z_2 n_2\left(\Omega_1+\Omega_3\right)+Z_3 n_3\left(\Omega_1+\Omega_2\right)}{2 n_e}\\ &-\frac{1}{2 n_e}\left[\left(Z_1 n_1\left(\Omega_2+\Omega_3\right)+Z_2 n_2\left(\Omega_1+\Omega_3\right)+Z_3 n_3\left(\Omega_1+\Omega_2\right)\right)^2\right.\\ &\left.-4 n_e\left(Z_1 n_1 \Omega_2 \Omega_3+Z_2 n_2 \Omega_1 \Omega_3+Z_3 n_3 \Omega_1 \Omega_2\right)\right]^{1/2}\end{aligned} \tag{3.30}$$

and

$$\begin{aligned}\widetilde{\Omega}_2=&\frac{Z_1 n_1\left(\Omega_2+\Omega_3\right)+Z_2 n_2\left(\Omega_1+\Omega_3\right)+Z_3 n_3\left(\Omega_1+\Omega_2\right)}{2 n_e}\\ &+\frac{1}{2 n_e}\left[\left(Z_1 n_1\left(\Omega_2+\Omega_3\right)+Z_2 n_2\left(\Omega_1+\Omega_3\right)+Z_3 n_3\left(\Omega_1+\Omega_2\right)\right)^2\right.\\ &\left.-4 n_e\left(Z_1 n_1 \Omega_2 \Omega_3+Z_2 n_2 \Omega_1 \Omega_3+Z_3 n_3 \Omega_1 \Omega_2\right)\right]^{1/2}.\end{aligned} \tag{3.31}$$

In contrast, no additional solution appears in the case of a periodic driver, although a third resonance is present when $\omega_\pm = \pm\Omega_3$.

As already mentioned in the previous section, the abundances of protons and doubly ionized helium in the solar corona and the solar wind are much larger than the abundances of other ions. Hence, the addition of a third ion would hardly modify the results from the two-ion model when applied to those two environments. However, the presence of a third ion can have a significant effect in upper chromosphere. The model F of Fontenla et al. [1993] predicts that at a height of $\sim$ 2016 km over the top of the photosphere the number densities are $n_p \approx 7 \times 10^{16}$ m^{-3}, $n_{\text{He II}} \approx 6 \times 10^{15}$ m^{-3}, and $n_{\text{He III}} \approx 10^{15}$ m^{-3}. Therefore, at that height the contribution of the three ions should be considered, although protons are still the dominant species. The temperature at that height is $T \approx 2 \times 10^4$ K and the magnetic field is $B_x \approx 35$ G. This set of parameters leads to the following collision and cyclotron frequencies: $\nu_{p\text{HeII}} \approx 2000$ Hz, $\nu_{\text{HeII}p} \approx 5840$ Hz, $\nu_{p\text{HeIII}} \approx 1260$ Hz, $\nu_{\text{HeIII}p} \approx 22100$ Hz, $\nu_{\text{HeIIHeIII}} \approx 540$ Hz, $\nu_{\text{HeIIIHeII}} \approx 3250$ Hz, $\Omega_p = 335268$ rad s^{-1}, $\Omega_{\text{HeII}} = 83817.1$ rad s^{-1}, and $\Omega_{\text{HeIII}} = 167634$ rad s^{-1}. The Alfvén speed is $c_{\text{A}} \approx 244$ km s^{-1}.

The results of the study of waves generated by an impulsive driver are shown in Figure 3.6. Once more the solutions to the collisionless dispersion relation are not plotted because there are no appreciable differences in the real part of the frequency (left panel) with the case in which collisions are included and because the imaginary part is equal to zero if friction is neglected. Again, only the solutions with $\omega_R > 0$ are displayed.

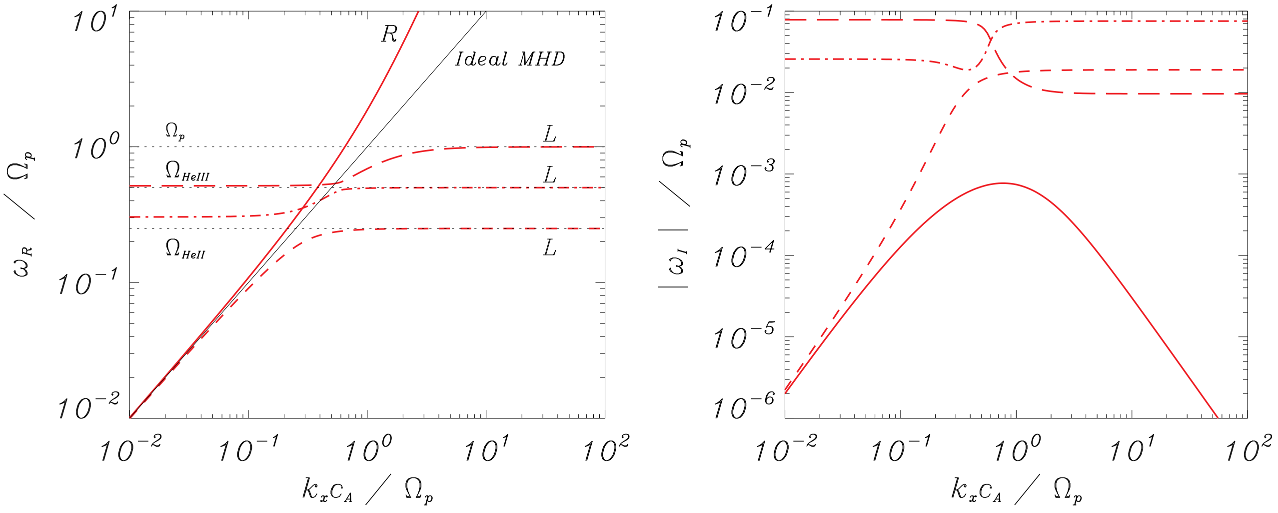

Figure 3.6: Solutions to the dispersion relations of a three-ion plasma with $n_p = 7 \times 10^{16}$ m^{-3}, $n_{\text{HeII}} = 6 \times 10^{15}$ m^{-3}, $n_{\text{HeIII}} = 10^{15}$ m^{-3}, $B_x = 35$ G, $\nu_{p\text{HeII}} \approx 2000$ Hz, $\nu_{\text{HeII}p} \approx 5840$ Hz, $\nu_{p\text{HeIII}} \approx 1260$ Hz, $\nu_{\text{HeIII}p} \approx 22100$ Hz, $\nu_{\text{HeIIHeIII}} \approx 540$ Hz, and $\nu_{\text{HeIIIHeII}} \approx 3250$ Hz. Left: normalized real part of the frequency as a function of the normalized wavenumber. Right: absolute value of the normalized damping as a function of $k_x c_{\text{A}}/\Omega_p$. Red dashed lines represent the L modes and the red solid line represents the R mode. The black thin line corresponds to the solution of ideal MHD.

In the limit of small wavenumbers, it can be seen that two of the solutions of the multi-fluid model coincide with the Alfvén frequency provided by the single-fluid description, while the

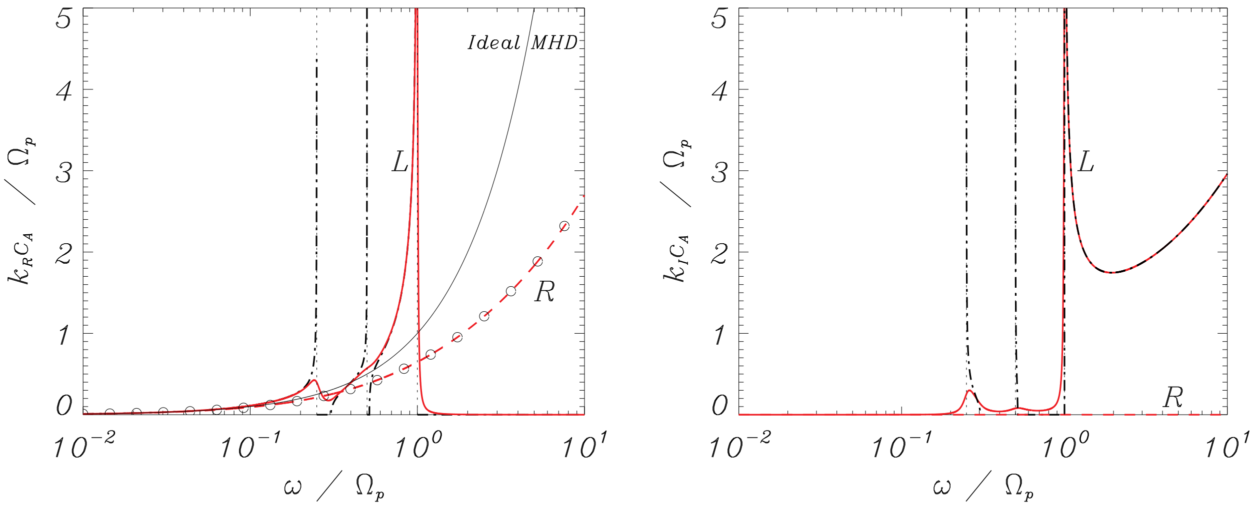

Figure 3.7: Solutions of the dispersion relations for waves generated by a periodic driver in a three-ion plasma with the same parameters as those used in Figure 3.6.

other two are given by the values $\widetilde{\Omega}_1$ and $\widetilde{\Omega}_2$. When $k_x c_{\rm A}/\Omega_p$ increases, the Alfvénic L mode (represented by the dashed line) turns into an ion cyclotron mode and its frequency tends to the lower cyclotron frequency. This is the same behavior as that found in the two-ion description). The remaining L modes tend to the limiting values $\Omega_{\rm He\ III}$ and Ω_p, and they conserve their order: the mode associated with $\widetilde{\Omega}_2$ (which is larger than $\widetilde{\Omega}_1$) tends to the upper cyclotron frequency. Finally, the Alfvénic R mode becomes the whistler wave and its frequency is always higher than the Alfvén frequency.

The right panel of Figure 3.6 shows that the R mode is again the less affected by collisions and its normalized damping is $|\omega_I|/\Omega_p < 10^{-5}$ for very small and very large wavenumbers, with a maximum of $|\omega_I|/\Omega_p \approx 10^{-3}$ around $k_x c_{\rm A}/\Omega_p = 1$. For small wavenumbers, the solutions with stronger damping are those related to $\widetilde{\Omega}_1$ and $\widetilde{\Omega}_2$: the damping of the former (represented by the dotted-dashed line) decreases with the wavenumber until it reaches a minimum around $k_x c_{\rm A}/\Omega_p = 0.5$, then increases again and becomes constant for very large wavenumbers, with $|\omega_I|/\Omega_p \approx 0.75$. The damping of the mode associated with $\widetilde{\Omega}_2$ decreases very fast in the region around $k_x c_{\rm A}/\Omega_p = 1$ and then stabilizes in $|\omega_I|/\Omega_p \approx 0.025$. Finally, the damping of the Alfvénic L mode increases with the wavenumber until it reaches the value $|\omega_I|/\Omega_p \approx 0.06$ when $k_x c_{\rm A}/\Omega_p \gg 1$.

The analysis of waves generated by a periodic driver is illustrated by Figure 3.7. As before, only the solutions with $k_R > 0$ are plotted. It can be noted that the collisionless L mode, represented by the black dotted-dashed line, exhibits the expected three resonances: the wavenumber tends to infinity at the three cyclotron frequencies. There are also three cutoff regions, instead of the two cut-offs that exist in the two-ion case. The wavenumber is equal to zero in the following intervals: $\omega \in \left(\Omega_{\rm HeII}, \widetilde{\Omega_1}\right)$, $\omega \in \left(\Omega_{\rm HeIII}, \widetilde{\Omega_2}\right)$ or $\omega > \Omega_p$, where $\widetilde{\Omega_1} \approx 0.3\Omega_p$ and $\widetilde{\Omega_2} \approx 0.52\Omega_p$. The solutions corresponding to the case with $\nu_{st} \neq 0$ show that the singularities are substituted by extrema of the normalized wavenumber, where the highest peak corresponds to the most abundant species, i.e., protons. Again, the momentum transfer removes the cutoff regions. Regarding the R mode, the same behavior explained for the case of two-ion plasmas is found here: there are no resonances, the normalized wavenumber increases with the frequency and the spatial damping is inefficient in the whole frequency range.

Therefore, the overall results obtained in the three-ion model appear as natural extensions to the results of the two-ion case. Hence, the generalization to plasmas with a larger number of ions seems straightforward.

3.5 Numerical simulations

After the analysis of the properties of the dispersion relations in two-ion and three-ion plasmas, it is interesting to compute the full time-dependent evolution of the perturbations by means of numerical simulations.

The results presented in this section are obtained by using the numerical code MolMHD (Bona et al. [2009]), which is based on the method of lines (Sarmin and Chudov [1963], Schiesser [1991]), to compute the temporal evolution of the system of equations detailed in Section 2.2. As explained by Hamdi et al. [2007], the method of lines transforms a system of partial differential equations (PDEs) into a system of ordinary differential equations (ODEs) by replacing the spatial derivatives with algebraic approximations. For instance, to solve a PDE of the form

$$\frac{\partial u(x,t)}{\partial t} + h(x,t)\frac{\partial f(x,t)}{\partial x} = 0, \tag{3.32}$$

the derivative with respect to x can be substituted by the following finite differences approximation:

$$\frac{\partial f(x,t)}{\partial x} \approx \frac{f_i - f_{i-1}}{\Delta x}, \tag{3.33}$$

where the subscript i represents the position of a point in the grid that covers the domain in x and Δx is the separation between two adjacent points of the grid. Thus, an approximation to Equation (3.32) is given by the following system of ODEs:

$$\frac{\partial u_i(x,t)}{\partial t} \approx -h_i(x,t)\frac{f_i - f_{i-1}}{\Delta x}, \quad 1 \leq i \leq N, \tag{3.34}$$

where N is the number of points of the grid.

The numerical integration of the previous system can be performed by substituting the temporal derivative with another finite differences approximation, which leads to

$$\frac{u_i^{n+1} - u_i^n}{\Delta t} \approx -h_i(x,t)\frac{f_i - f_{i-1}}{\Delta x}, \quad 1 \leq i \leq N, \tag{3.35}$$

where the superscript n denotes timesteps which are separated by a time given by Δt. Hence, the solution of the system at the timestep $n+1$ is given by

$$u_i^{n+1} \approx u_i^n - h_i\frac{\Delta t}{\Delta x}(f_i - f_{i-1}), \quad 1 \leq i \leq N. \tag{3.36}$$

The generalization of this procedure to a larger number of spatial dimensions is straightforward.

The MolMHD version used for this investigation computes spatial derivatives by means of a 4th order of accuracy central finite differences scheme (except for the points closer to the boundaries, where second order forward and backward schemes are used for the lower and upper boundaries, respectively). Thus, for instance, the derivative with respect to the coordinate x for the interior points is given by

$$\frac{\partial f_i}{\partial x} \approx \frac{f_{i-2} - 8f_{i-1} + 8f_{i+1} - f_{i+2}}{12\Delta x}, \quad 4 < i < N - 4. \tag{3.37}$$

The temporal variable is advanced through an explicit 3rd degree TVD Runge-Kutta method, where TVD refers to total variation diminishing (Harten [1983]). The CFL condition (Courant et al. [1928]) imposes a strong constraint to the maximum time step which can be used in the simulations. This is mainly due to the presence of the ion cyclotron frequencies, but also to the diffusion scales related to collisions. The use of this explicit scheme in 2D and 3D is not practical due to the small time-steps required but for the purposes of this Thesis, which focuses on 1D scenarios, it is acceptable.

With the aim of comparing the outcome of the numerical simulations with the results provided by the dispersion relations examined in the previous sections, 1D simulations with an initially uniform and static background, i.e., $\rho_s(x) = \rho_{s,0}$ and $\boldsymbol{V_{s,0}} = 0$, are performed. The background magnetic field is given by $\boldsymbol{B_0}(x) = (B_x, 0, 0)^T$.

It must be noted that the equations used in the numerical code are nonlinear. However, the goal of this chapter is the analysis of the linear regime of small-amplitude perturbations, although nonlinear effects are consistently computed in the simulations. The study of nonlinearities will be carried out in Chapter 5.

3.5.1 Impulsive driver

To simulate waves excited by an impulsive driver, an initial perturbation is superimposed to the background and then is left to evolve. In this study, a uniform grid of $N = 401$ points is used to cover the domain $x \in [-l, l]$, where l is a length scale and the initial perturbation is chosen to be the fundamental standing wave in the closed domain. As boundary conditions, the velocity perturbations are set equal to zero at $x = \pm l$. The initial condition for the velocities can be written as

$$\boldsymbol{V_s}(x, t = 0) = \begin{pmatrix} 0 \\ A_{s,y} \cos\left(k_x x\right) \\ A_{s,z} \cos\left(k_x x\right) \end{pmatrix}, \tag{3.38}$$

where the wavenumber is $k_x = \pi/(2l)$, while there are no initial perturbation of the remaining variables (magnetic field, densities and pressures). In addition, to simplify the analysis, the amplitude $A_{s,z}$ is set to zero, so that the initial perturbation has only a y-component in velocity. Due to the symmetry of the system, the results would be equivalent if the amplitudes are chosen as $A_{s,y} = 0$ and $A_{s,z} \neq 0$, instead. The linear regime can be analyzed by imposing that $A_{s,y} \ll c_{\mathrm{A}}$.

Two-ion plasmas

As in the section devoted to the examination of the dispersion relations, it is useful to start with the investigation of the most simple case, i.e., that of two-ion plasmas. The analysis of the dispersion relations has shown that the effect of collisions between the two fluids is much more relevant in the upper chromosphere than in the solar corona or the solar wind. Thus, here only the former environment will be considered.

Figure 3.8 displays the results of a simulation in which the initial perturbations are

$$V_{p,y}(x,t=0)=V_{\mathrm{He\,II},y}(x,t=0)=10^{-3}c_{\mathrm{A}}\cos\left(k_x x\right), \tag{3.39}$$

and $k_x=\pi/10^5$ m^{-1}. The top panel displays the y-component of the velocity of protons (solid red line) and singly ionized helium (black diamonds). The bottom panel shows the respective z-components. As the simulation stays in the linear regime, the values of the amplitudes of the perturbations are not important, and only the ratios between those magnitudes are relevant. Therefore, the results are normalized with respect to the initial amplitude of the y-component of the velocity of protons, $V_{y,0}\equiv V_{p,y}(t=0)$.

The y-components of the velocities of the two ions are strongly coupled, as it can be seen in the top panel: both species oscillate with the same frequency, amplitude and phase. In contrast, the z-components show some differences in the first steps of the simulations. During those first steps, there is a phase shift in the oscillation of He II with respect to that of protons, but as time increases the phase shift is reduced. In addition, the amplitude of the z-component is initially much smaller than that of the y-component. This is due to the fact that the investigated wave is a combination of various modes of oscillation. From any of the two panels it can be checked that both ions oscillate with a frequency $\omega\approx 6.41$ rad s^{-1}, which coincides with the low-frequency solutions obtained from Equation (3.13). The solutions from the multi-fluid dispersion relation that are associated with the cyclotron frequencies are not found in this simulation. This absence may be due to an insufficient temporal resolution or it may be caused by the specific choice of the initial conditions.

The waves that appear in the simulations may be a combination of several of the modes predicted by the dispersion relation. Since those modes have been computed by assuming that the perturbations are proportional to $\exp(-i\omega t)$, each component of the velocity perturbations can be written as

$$V_{s,\alpha}(x,t)=V_{s,\alpha 0}(x)\exp(-i\omega t)=V_{s,\alpha 0}\left[\cos(\omega t)+i\sin(\omega t)\right], \tag{3.40}$$

with $\alpha=\{x,y,z\}$. Thus, taking into account the definition of the polarized variables given by Equation (3.8), the L and R modes for velocity can be expressed as

$$\boldsymbol{V_{s,\pm}}(x,t)=\begin{pmatrix}0\\ V_{s,y}(x,t)\\ \pm iV_{s,z}(x,t)\end{pmatrix}=\begin{pmatrix}0\\ V_{s,y0}(x)\left[\cos\left(\omega_{\pm}t\right)+i\sin(\omega_{\pm}t)\right]\\ V_{s,y0}(x)\left[\pm i\cos(\omega_{\pm}t)\mp\sin\left(\omega_{\pm}t\right)\right]\end{pmatrix}, \tag{3.41}$$

since $V_{s,y0}(x)=V_{s,z0}(x)$ for the case of circular polarization. It must be noted that only the real part of the previous expression has a physical meaning. Hence,

$$\boldsymbol{V_{s,\pm}}(x,t)=\begin{pmatrix}0\\ V_{s,y0}(x)\cos\left(\omega_{\pm}t\right)\\ \mp V_{s,y0}(x)\sin\left(\omega_{\pm}t\right)\end{pmatrix}=\begin{pmatrix}0\\ A_{s,y}\cos(k_x x)\cos\left(\omega_{\pm}t\right)\\ \mp A_{s,y}\cos(k_x x)\sin\left(\omega_{\pm}t\right)\end{pmatrix}, \tag{3.42}$$

where the relation $V_{s,y0}(x)=A_{s,y}\cos(k_x x)$ has been taken from the initial condition given by Equation (3.38).

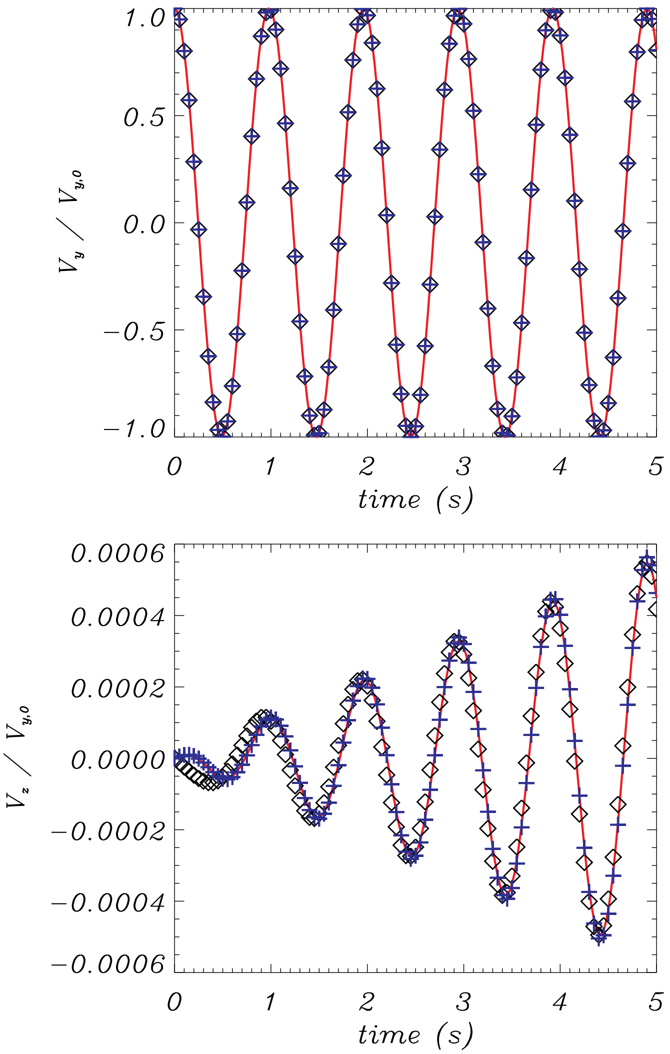

Figure 3.8: Simulation of an Alfvén wave in a two-ion plasma with chromospheric conditions: $n_p = 10^{17}$ m^{-3}, $n_{\mathrm{HeII}} = 0.1 n_p$, $B_x = 35$ G, and $\nu_{p\mathrm{HeII}} = 8500$ Hz. The initial perturbation is given by Equation (3.39) and the wavenumber is $k_x = \pi/10^5$ m^{-1}. The top panel shows the normalized y-component of the velocity of ions, $V_y/V_{y,0}$, at the position $x = 0$; the z-component, $V_z/V_{y,0}$, is shown in the bottom panel. The red lines represent the velocity of protons, the black diamonds represent the velocity of HeII and the blue crosses correspond to the analytic fits given by Equation (3.45).

From Equation (3.13) six modes are obtained: three of them are left-hand polarized and the other three are right-hand polarized. But, as already mentioned, in the simulation illustrated in Figure 3.8, two of them cannot be found. Hence, the oscillation at $x = 0$ may be expressed as the following combination of the remaining four modes:

$$\boldsymbol{V_s}(0,t) = \begin{pmatrix} 0 \\ A_{s,y}\left[\cos\left(\omega_{+,1}t\right) + \cos\left(\omega_{+,2}t\right) + \cos\left(\omega_{-,1}t\right) + \cos\left(\omega_{-,2}t\right)\right] \\ A_{\mathrm{s,y}}\left[-\sin\left(\omega_{+,1}t\right) - \sin\left(\omega_{+,2}t\right) + \sin\left(\omega_{-,1}t\right) + \sin\left(\omega_{-,2}t\right)\right] \end{pmatrix} \qquad (3.43)$$

where $\omega_{\pm,1}$ and $\omega_{\pm,2}$ are the roots of the dispersion relation. Those modes have also an imaginary part but it has been shown in Section 3.3.1 that the imaginary part is negligible. It must be noted that in the most general case each oscillation mode has a different amplitude. However, here, they have been chosen to have the same amplitude, which is consistent with the results presented in Section 3.3.1. Furthermore, for this particular case, the dispersion relation shows that $\omega_{-,1} = -\omega_{+,1}$ and $\omega_{-,2} = -\omega_{+,2}$. Hence, Equation (3.43) can be rewritten as

$$\boldsymbol{V_s}(0,t) = \begin{pmatrix} 0 \\ 2A_{s,y}\left[\cos\left(\omega_{+,1}t\right) + \cos\left(\omega_{+,2}t\right)\right] \\ -2A_{s,y}\left[\sin\left(\omega_{+,1}t\right) + \sin\left(\omega_{+,2}t\right)\right] \end{pmatrix}, \tag{3.44}$$

or, equivalently,

$$\boldsymbol{V_s}(0,t) = \begin{pmatrix} 0 \\ 4A_{s,y}\cos\left(\frac{\omega_{+,1}+\omega_{+,2}}{2}t\right)\cos\left(\frac{\omega_{+,1}-\omega_{+,2}}{2}t\right) \\ -4A_{s,y}\sin\left(\frac{\omega_{+,1}+\omega_{+,2}}{2}t\right)\cos\left(\frac{\omega_{+,1}-\omega_{+,2}}{2}t\right) \end{pmatrix}, \tag{3.45}$$

which represents the composition of a carrier wave with frequency $\theta_C = \left(\omega_{+,1} - \omega_{+,2}\right)/2$ and an envelope wave with frequency $\theta_E = \left(\omega_{+,1} + \omega_{+,2}\right)/2$ (it must be noted that $\omega_{+,1}$ and $\omega_{+,2}$ have opposite signs). Setting $A_{s,y} = 1/4$, the previous formula fits very well the velocity of ions, as shown by the blue crosses in Figure 3.8, with the exception of the very first instants.

The next step in the present investigation is to perform a simulation with the same parameters as in the previous one but with different initial conditions and to check how the temporal evolution of the perturbations is affected. Now, the singly ionized helium fluid is set to be initially at rest, i.e., $V_{\text{He II}}(x, t = 0) = 0$, while the initial perturbation for the proton fluid is again $V_{p,y}(x, t = 0) = 10^{-3}c_{\text{A}}\cos(k_x x)$. Figure 3.9 illustrates the results of this simulation and reveals some differences in the oscillation with respect to those plotted in Figure 3.8.

In the first place, it can be seen in the top panel that there is an extremely short relaxation time during which the y-components of velocities of the two ions tend to become equal. After this relaxation time, the two fluids oscillate in phase and with the same amplitude as if they were a single fluid. By performing several simulations with different physical parameters and initial conditions, an empirical expression can be deduced for the amplitude of the oscillation after the relation time, namely

$$\overline{V}(x) = \frac{\sum_s \rho_s V_s\left(x, t = 0\right)}{\sum_s \rho_s}. \tag{3.46}$$

However, the most important difference is revealed by the insets in the figure, which focus on the initial time steps of the simulation. A new oscillation mode, which has a high frequency and is damped, is found in those insets. By fitting it with an exponentially decaying sinusoidal function, it can be checked that its frequency is $\omega_R \approx 106672.7$ rad s^{-1} and that its damping rate is $\omega_I \approx 29756$ s^{-1}. Those values agree with the solution from the dispersion relation that could not be found in the preceding simulation. Moreover, the two species oscillate in anti-phase, which is the behavior predicted for that root of the dispersion relation. Hence, this additional mode, which is associated with the cyclotron frequencies, is only present in the initial stages of the simulations when the initial velocity amplitudes of the two ions are different.

After focusing on the limit of very small values of the wavenumber (i.e., large wavelengths), it is interesting to turn to the high wavenumber range, where all the normal modes predicted by

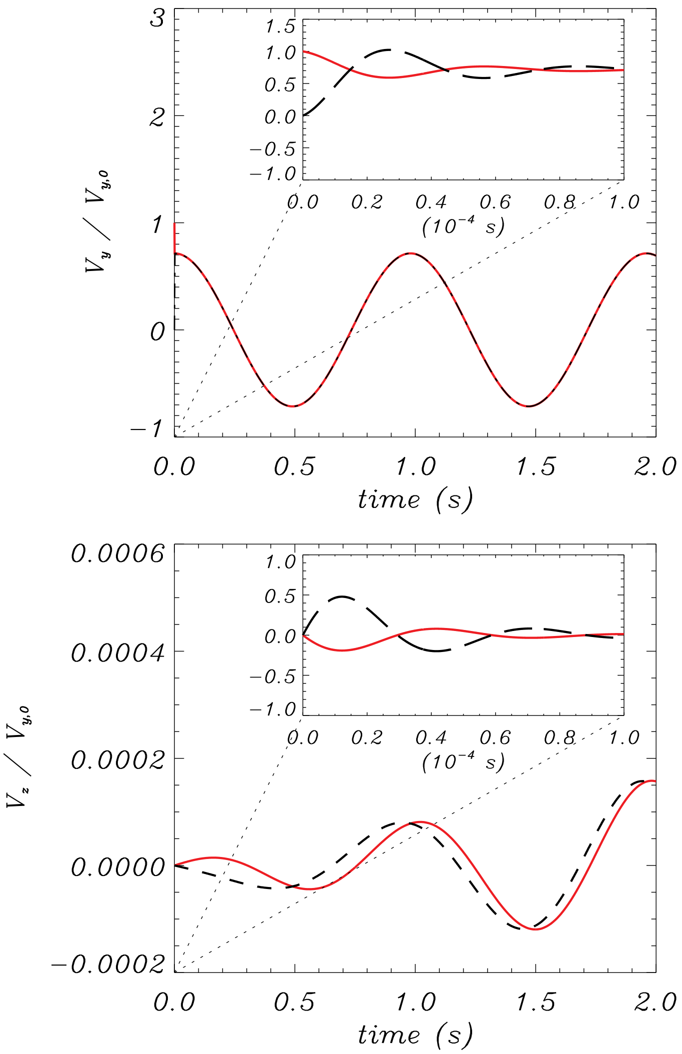

Figure 3.9: Simulation with the same physical parameters as Figure 3.8 (chromospheric conditions) but with a smaller timestep and a different initial perturbation so that the He II fluid is initially at rest. The red solid lines represent the velocity of protons and the black dashed lines represent the velocity of singly ionized helium. The top panel corresponds to the normalized y-component of the velocity and the bottom one to the normalized z-component.

the dispersion relation have high frequencies. This range can be studied, for instance, by setting the wavenumber as $k_x = \pi/5 \ \mathrm{m}^{-1}$ (which corresponds to a normalized value of $k_x c_{\mathrm{A}}/\Omega_p \approx 0.38$).

Figure 3.10 shows the results of a simulation for this high wavenumber range, in which the same initial conditions as for Figure 3.9 have been used. Two different situations are analyzed here. The left panels correspond to the case where the effect of collisions is ignored, while the right panels represent the case when the collisional interaction between the two ionized species has been taken into account.

The top panels of Figure 3.10 show the y-component of the velocity of each species, the red solid line corresponding to the proton fluid while the singly ionized fluid is represented by

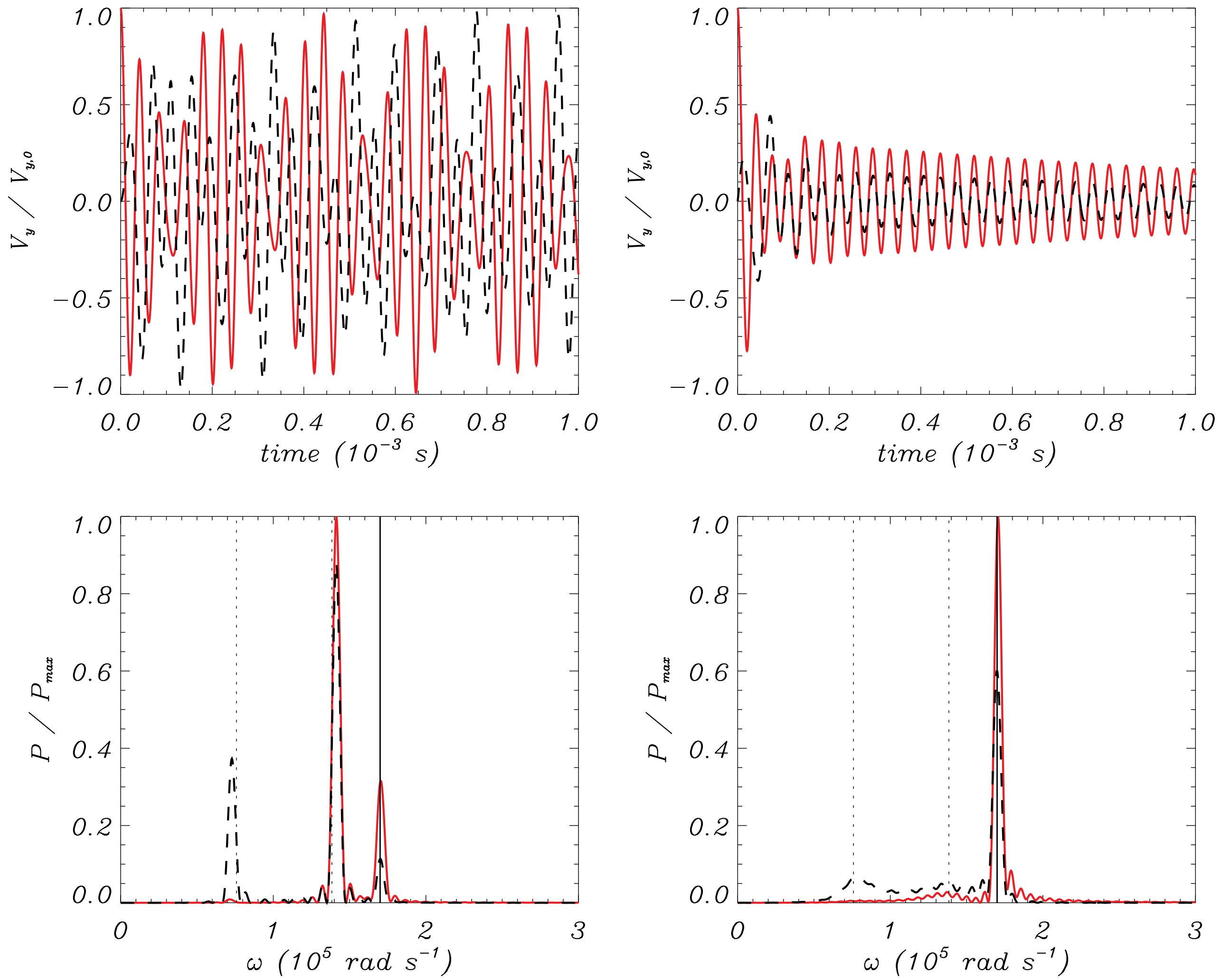

Figure 3.10: Normalized y-component of the velocities of ions (top panels) and spectra of the oscillations (bottom panels) from two different simulations of a two-ion plasma with upper chromospheric conditions. The left and right panels represent the cases without and with collisions, respectively. The wavenumber is $k_x = \pi/5$ m^{-1}. The vertical lines on the bottom panels show the solutions of the dispersion relation: the dotted lines correspond to the L modes and the solid lines correspond to the R modes.

the black dashed line. The z-components are not plotted here because they do not provide additional relevant information and it is enough to look at the y-components to explain the important physics of the problem.

In comparison with the case of small wavenumbers, the motions plotted in Figure 3.10 are much more complex. Thus, the oscillations cannot be so easily related to the modes predicted by the dispersion relation. However, it is possible to compute their power spectrum and check if the frequencies predicted by the dispersion relation are present. The corresponding power spectra are shown in the bottom panels, and they are normalized with respect to the maximum power of the oscillations of protons. In a power spectrum, the position of the peaks informs about the frequencies of the modes that compose the analyzed oscillation and their heights show their relative contribution. In addition, here some vertical lines have been added to mark the position of the roots of the dispersion relations. In the left-bottom panel, three main peaks can be found. They are in very good agreement with the solutions given by the dispersion relation. However, the heights of the peaks vary in a remarkable way from the power spectrum of one fluid to the other. This means that each mode has a clearly different contribution to the motions of each fluid. The motions of both fluids are dominated by the mode associated to the central peak, which corresponds to the upper L mode. However, the influence of the remaining modes has some evident dissimilarities. For instance, the contribution of the lower L mode (which tends to $\Omega_{\mathrm{He\ II}}$ at very large wavenumbers) is negligible in the motion of protons, while it cannot be overlooked for the case of singly ionized helium. On the contrary, the contribution of the R mode is greater for protons than for helium.

The right panels of Figure 3.10 bring into view the striking effect that collisions have on the high-frequency waves. During the first steps of the simulation, the three oscillation modes are present. However, the two L modes are strongly damped and they disappear in a very short time, while the R mode survives for a longer time. This circumstance is reflected in the power spectrum by the very small peaks associated to the L modes, whose heights are much lower than the peak corresponding to the R mode.

Three-ion plasmas

Here, an additional third ion, namely doubly ionized helium, is considered in the study of a region with upper chromospheric conditions. Thus, the parameters for the simulations are the following: $n_p = 7 \times 10^{16}$ m^{-3}, $n_{\mathrm{He\ II}} = 6 \times 10^{15}$ m^{-3}, $n_{\mathrm{He\ III}} = 10^{15}$ m^{-3}, $T = 2 \times 10^4$ K, and $B_x = 35$ G.

Figure 3.11 displays the result of two simulations where the initial perturbation for the proton fluid is given by

$$V_{p,y}(x, t = 0) = 10^{-3} c_{\mathrm{A}} \cos(k_x x), \tag{3.47}$$

while the two helium fluids are initially at rest. The chosen wavenumber for the initial perturbation is $k_x = \pi/5$ m^{-1}, which corresponds to a normalized value of $k_x c_{\mathrm{A}}/\Omega_p \approx 0.46$, i.e., it is in the large range of wavenumbers. As in the section devoted to two-ion plasmas, here a comparison between the cases with and without collisions is performed. The left panels of Figure 3.11 represent the former, while the right panels correspond to the latter. Again, the y-components of the velocity and the power spectra are plotted in the top and the bottom panels, respectively.

From the dispersion relations analyzed in Section 3.4 four different solutions can be obtained, three of them corresponding to left-hand polarized waves and only one to the right-hand polarization. In the left-bottom panel of Figure 3.11, it can be seen that the power spectra exhibits the expected four peaks. Again, there are important differences in the contribution of each mode to the oscillation of each ionized fluid. The modes with frequencies close to the cyclotron frequency of one of the ionized species mainly affect the motion of that species, while their impact on the other fluids is much smaller. This statement can be checked by looking, for instance, at the leftmost peak: its position is close to $\Omega_{\mathrm{He\ II}}$ and its height is around 0.7 for the He II fluid but is almost zero for the other ions. Thus, that oscillation mode seems to affect only the singly ionized helium while its influence on the other ions is negligible.

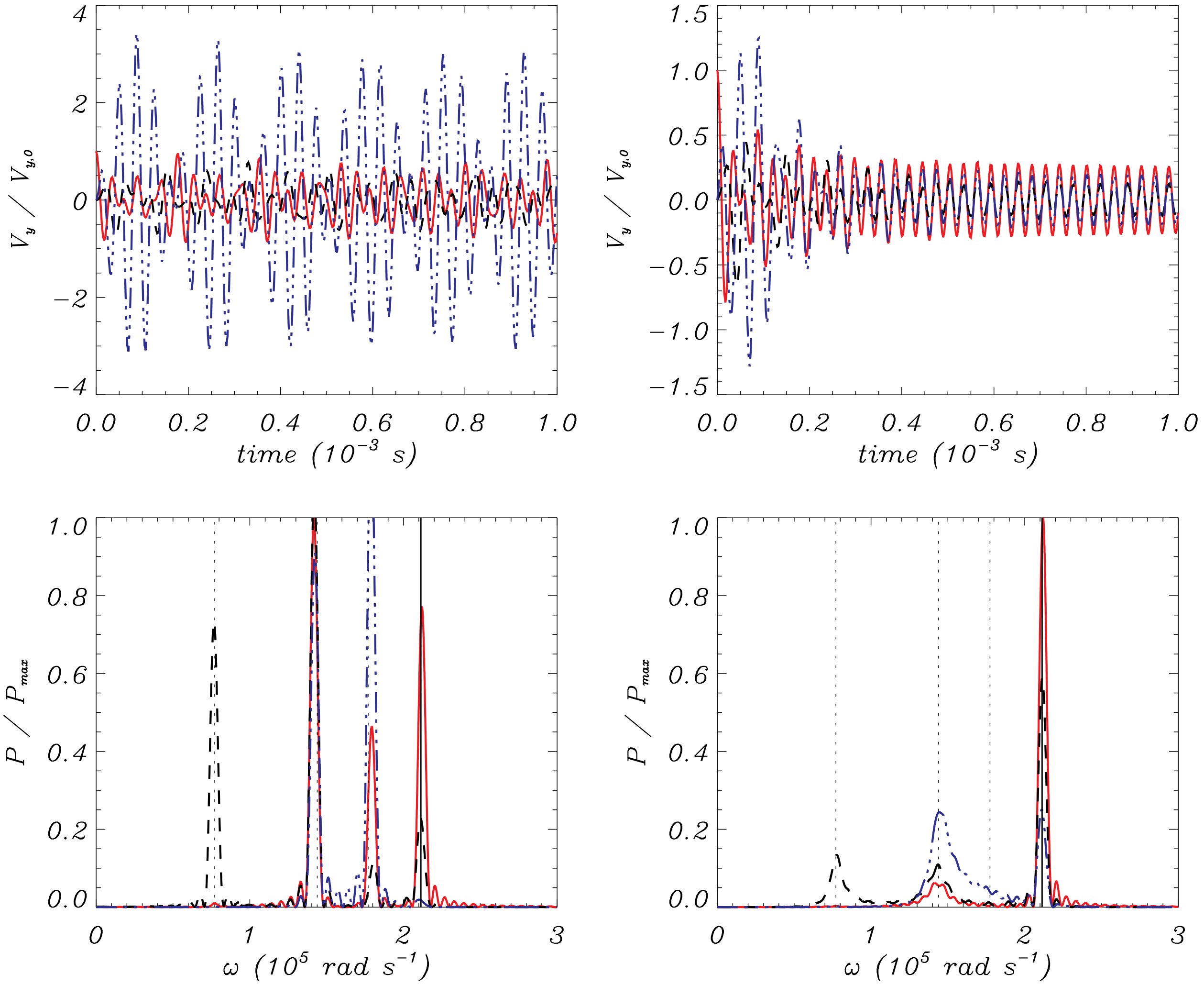

Figure 3.11: Results of a simulation of a three-ion plasma with upper chromospheric conditions. The top panels show the y-component of the velocity of ions and the bottom panels show the power spectra of the oscillations. On the left panels, the effect of collisions is ignored. On the right panels collisions are taken into account. The wavenumber is $k_x = \pi/5$ m^{-1}. The red solid, blue dot-dashed and black dashed lines correspond to p, He II and He III, respectively.

On the right panels of Figure 3.11, a similar behavior than that already explained for two-ion plasmas is found: collisions between the three ionized species cause the L modes to be more attenuated than the R mode.

After exploring the large wavenumber range, it is the turn to focus on the opposite limit. According to the dispersion relations, at small wavenumbers there are two Alfvénic modes with $\omega \approx \omega_{\rm A}$ and two modes related to the cyclotron frequencies. Hence, the results of the simulations for three-ion plasmas are qualitatively similar to those for two-ion plasmas shown in Figures 3.8 and 3.9. Apart from the new value of the Alfvén speed and the corresponding Alfvén frequency, the relevant difference can be found during the relaxation time. For the case of three-ion plasmas, two oscillation modes are present during that short time and their frequencies are given by Equations (3.30) and (3.31). After the relaxation time, the magnetic field produces a strong coupling on the three fluids so that they behave as a single fluid. Then, their motion is well described by the same formulas used for the two-ion case, i.e., Equation (3.43) (or its equivalent expressions) and Equation (3.46).

3.5.2 Periodic driver

The effect of a periodic driver can be simulated by applying to a given point of the domain a perturbation that is a periodic function of time. For convenience, in the simulations studied in this section, the driver will act on the point $x = 0$ and the spatial domain of the simulation will be $x \in [0, l]$.

In general, during the first steps of the simulations, some transient effects appear before an oscillation that can be related to a normal mode starts to form. Those transients are not of interest for this investigation and, therefore, will be ignored.

Two-ion plasmas

Figure 3.12 shows the results of a simulation with the parameters for the upper chromospheric region considering that the plasma is composed of only two species. The driver is given by

$$V_{p,y}(x=0,t) = V_{\mathrm{HeII},y}(x=0,t) = 10^{-3} c_{\mathrm{A}} \cos\left(\omega t\right), \tag{3.48}$$

with a frequency $\omega = 10^{-3}\Omega_p$. The length of the spatial domain is $l = 2.5 \times 10^4$ m and an uniform grid of $N = 401$ points has been used to cover that domain. Each frame of the figure corresponds to a different time of the simulation. It can be checked that the perturbation propagates at a phase speed of ~ 200 km s^{-1}, which is in good agreement with the Alfvén speed of this plasma. The two fluids (protons and singly ionized helium) oscillate with the same phase and amplitude, in anti-phase with respect to the magnetic field, which is the expected behavior for Alfvén waves.

To compare the simulation with the predictions of the dispersion relation, the oscillation can be fitted with a function $f(x) \sim \cos(k_x x)$. In that case, the following value of the wavenumber is obtained: $k_x \approx 0.001643$ m^{-1}. Equation (3.27) yields two solutions with $k_{R,+} \approx 0.001644$ m^{-1} and $k_{R,-} \approx 0.001642$ m^{-1}. Hence, the two approaches used in this investigation show a good agreement.

It must be noted that, as in the case of the impulsive driver, the resulting wave is a combination of the left-hand and the right-hand polarized modes. Thus, a composition of a carrier wave and an envelope wave should appear. Here, the wavenumber of the carrier wave would be $\kappa_C = (k_{R,+} + k_{R,-})/2$ and the wavenumber of the envelope wave would be $\kappa_E = (k_{R,+} - k_{R,-})/2$. The frequency chosen for the driver in this simulation leads to $\kappa_E \approx 1.49 \times 10^{-6}$ m^{-1}, which is equivalent to a wavelength $\lambda_E \approx 4.2 \times 10^6$ m. Such value is much larger than the length of the domain. That is the reason why the existence of the envelope wave cannot be discerned in this simulation.

Since for low frequencies, the single-fluid and the multi-fluid models provide the same results, the most interesting range of frequencies for this research is that where the single-fluid approach is not applicable, i.e., the range of high frequencies. As shown in Section 3.3.2, as the frequency of the driver approaches the cyclotron frequencies of the ions, the properties of

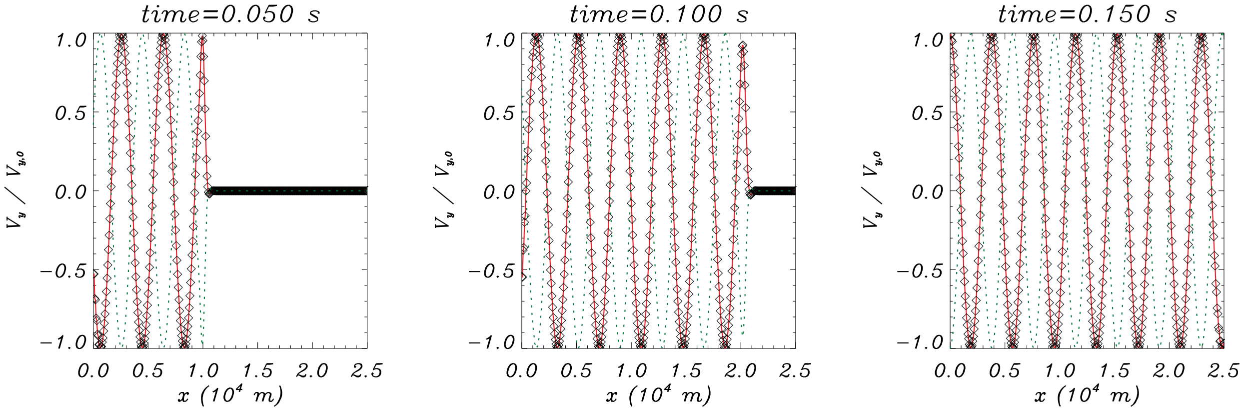

Figure 3.12: Wave generated by a periodic driver in a two-ion plasma with chromospheric conditions. The frequency of the driver is $\omega = 10^{-3}\Omega_p$. The y-component of the velocity of the ions is shown as a function of the coordinate x. The red line represents the velocity of protons and the black symbols the velocity of the He II fluid. The green dotted lines show the normalized magnetic field perturbation, $B_{1,y}c_{\mathrm{A}}/(V_{y,0}B_x)$.

the two different modes exhibit great dissimilarities. So, it seems convenient to analyze them separately. However, the driver employed in the previous simulation causes the excitation of both modes. Nevertheless, it is possible to find other kinds of drivers that lead to the excitation of one of the two modes exclusively. For instance, to study the left-hand mode (+) or only the right-hand mode (-), the following configuration for the velocity and magnetic field perturbations may be used:

$$\boldsymbol{V_{s,\pm}}(x=0,t) = \begin{pmatrix} 0 \\ V_0\cos(\omega t) \\ \mp V_0 \sin(\omega t) \end{pmatrix} \tag{3.49}$$

and

$$\boldsymbol{B_{1,\pm}}(x=0,t) = \begin{pmatrix} 0 \\ B_{1,0}\cos(\omega t) \\ \mp B_{1,0} \sin(\omega t) \end{pmatrix}, \tag{3.50}$$

where the amplitudes of the perturbations are linked by $B_{1,0} = -B_x V_0/c_{\mathrm{A}}$.

The left panels of Figure 3.13 show the results of a simulation of the L mode at frequency of resonance $\omega = \Omega_{\mathrm{He\ II}}$. It must be reminded that, in the collisionless case, perturbations cannot propagate at the resonance frequencies since the phase speed tends to zero. However, the effect of collisions has been included in the simulation and the graphic shows that there is propagation of the perturbation, although it is strongly damped. A total of $N = 2001$ points have been used to cover a domain with $l = 500$ m, even though only the interval $x \in [0, 50]$ is represented in the figure. The motivation for using a bigger domain than the one shown is to avoid the interference of unwanted numerical effects caused by the rightmost boundary.

As already mentioned, the perturbation presents a very strong attenuation in space: it does not propagate beyond a distance $x \approx 30$ m from the point where the driver has been applied. The dotted curves represent the exponential decay given by the dispersion relation and it can be seen that they fit well the damping of the oscillation. In addition, using those curves as a

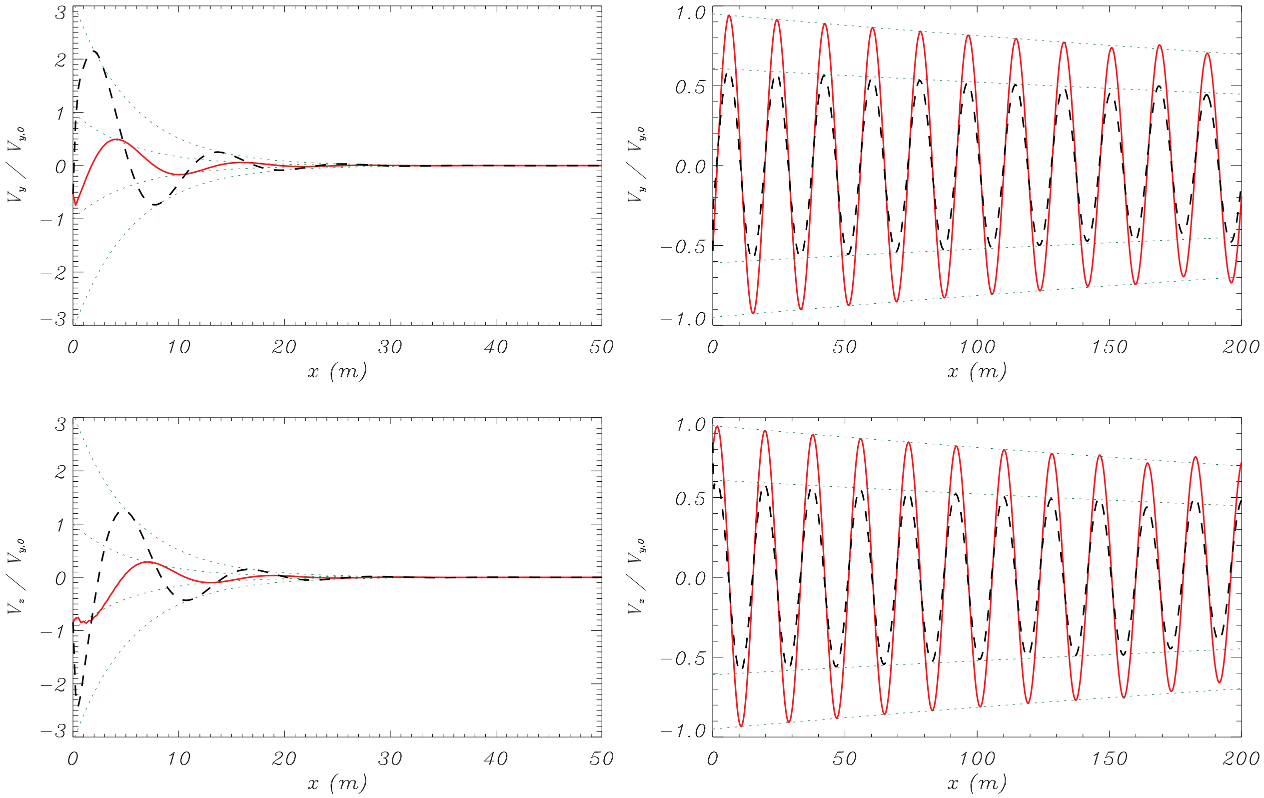

Figure 3.13: Left (right): velocities of ions at a time $t = 10^{-3}$ s in a simulation in which the L mode (R mode) is excited by a driver with frequency $\omega = \Omega_{\mathrm{HeII}}$. The y-components and z-component are shown in the top and the bottom panels, respectively. The red solid lines correspond to the protons and the black dashed lines correspond to the singly ionized helium. The dotted curves outline the spatial exponential decay computed through the dispersion relation, Equation (3.27). (Animations of the left and right panels of this figure are available.)

reference, the velocity amplitude ratio can be computed. The result is $|V_p/V_{\mathrm{He\ II}}| \approx 0.35$, which is in good agreement with the results displayed in Figure 3.5. The analysis of the dispersion relation also predicts that there is a phase shift between the velocities of the two fluids. Once again, that feature is observed in the simulation.

The right panels of Figure 3.13 show the results of a simulation with the same parameters of that in the left panels but for a driver that excites the right-hand mode. There are remarkable differences with respect to the previous simulation. In the first place, the phase speed of the R mode is higher. Then, the damping is much lower. Thus, the perturbation propagates much faster and to farther distances than in the previous case. Another fact that contrasts with the ion cyclotron mode is that here the protons oscillate with a larger amplitude than the singly ionized helium. It can be checked that the amplitude ratio is $|V_p/V_{\mathrm{He\ II}}| \approx 1.6$, which is consistent with the analysis from the dispersion relation. One final difference is that the two fluids oscillate in phase.

At the upper resonance, which corresponds to the proton cyclotron frequency, the behavior of the two modes is analogous to what has been explained in the preceding paragraphs for the lower resonance. The differences reside in that the damping lengths are shorter and that the amplitude ratio of the L mode is greater than unity, i.e., the amplitude of the oscillation of protons is larger than that of singly ionized helium.

Three-ion plasmas

As it has been shown in Section 3.4, the addition of more ionized species to the system does not cause the appearance of further oscillation modes when a periodic driver is considered. Thus, the motions of all the species in the plasma are still governed by the combination of only one left-hand mode and one right-hand mode. This fact contrasts with the case of the impulsive driver, where two extra modes (one for each polarization) appear for each new ion taken into account. However, there are still some dissimilarities with the two-ion case: an additional resonance frequency arise for each supplementary ionized species. This brief section focuses on the properties of the L waves at that resonance frequency.

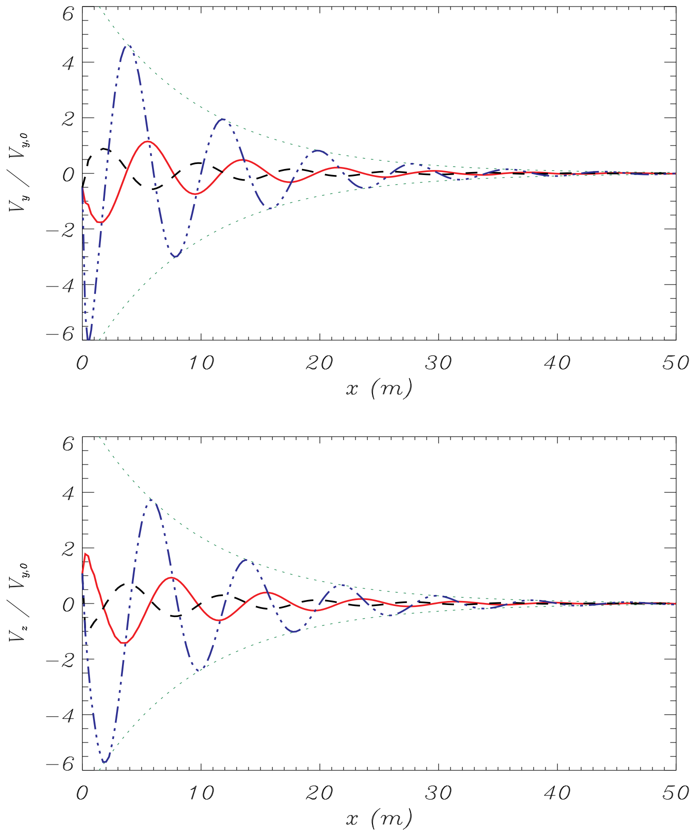

Figure 3.14: Velocities of ions at the time $t = 10^{-3}$ s of a simulation of the L-mode at the frequency of resonance $\omega = \Omega_{\mathrm{HeII}}$ in a three-ion plasma with chromospheric conditions. The red solid lines represent the y-component of the normalized velocity of the protons; the black dashed lines correspond to the velocity of singly ionized helium and the blue dotted-dashed lines correspond to the velocity of the doubly ionized helium. The dotted curves outline the spatial damping computed through Equation (3.12).

Figure 3.14 shows a simulation of a left-hand polarized wave in a three-ion plasma with chromospheric conditions, i.e., the presence of doubly ionized helium is considered. The frequency of the driver is $\omega = \Omega_{\text{He III}}$. A total of $N = 2001$ points have been used to cover the domain $x \in [0, 500]$ although, again, the figure only shows a fraction of that domain. On the one hand, as in the two-ion case, it can be seen that the perturbation is strongly damped and cannot propagate far from where it has been originated. On the other hand, here, the ion that oscillates with a larger amplitude is the doubly ionized helium, as it would be expected, since the driver is exciting waves with the cyclotron frequency of that species.

3.6 Discussion

In this chapter, the multi-fluid model detailed in Chapter 2 has been applied to the investigation of transverse waves in fully ionized plasmas, focusing on the effects due to Coulomb collisions between the different ionized species. The linear regime of small-amplitude perturbations has been considered, which has allowed to derive the dispersion relations for several particular cases and analyze their normal modes. Then, by means of numerical simulations, the full temporal evolution of those perturbations has been computed and it has been checked that the results of the simulations are consistent with the predictions of the dispersion relations.

Both the cases of waves generated by an impulsive driver and by a periodic driver have been studied, and a comparison with the predictions provided by the single-fluid model of ideal MHD has been performed. The first difference that has been found between the two models is that ideal MHD predicts the existence of only two oscillation modes independently of the kind of driver chosen, and it is not necessary to study the two cases separately, as they are equivalent. For the case of the periodic driver, the multi-fluid model gives also two solutions, regardless how many species compose the plasma. In contrast, when an impulsive driver is investigated, the number of normal modes increases with each additional ionized species considered. Furthermore, the waves described by ideal MHD are linearly polarized, while the waves from the multi-fluid description are circularly polarized.

It has been checked that if the various ionized species are exposed to perturbations with frequencies much lower than the cyclotron frequencies, they react as if they were a single fluid and the properties of the corresponding waves are well described by ideal MHD: they oscillate with the Alfvén frequency, in phase and with the same velocity amplitude, which is given by Equation (3.46). The reason for that behavior is that the magnetic field produces a strong coupling between those species. However, at higher frequencies, the interaction through the magnetic field is not enough to keep all the fluids as tightly coupled as before and the amplitude and the phase of the oscillations are different for each mode. At this regime, ideal MHD does not provide accurate results and the use of the multi-fluid approach is required. In addition, the effect of elastic collisions should not be neglected, since the frictional force associated to the velocity drifts may lead to an intense damping of the waves. This investigation has shown that the damping is stronger for the modes with the left-hand polarization than for the right-hand modes.

The multi-fluid model has been used to study the propagation of waves in three different solar plasmas: the lower solar corona, the solar wind at 1 AU, and the upper chromosphere. It has been found that for the solar corona the friction coefficient between the ions is small and the effect of collisions is relevant only for times longer than several periods of the Alfvén wave.

The friction coefficient in the solar wind has an even smaller value and hence, this environment can be treated as a collisionless fluid from the perspective of this work, since the damping times of the oscillations are in the order of 10^6 s or larger. Nevertheless, the multi-fluid model is generally still required to illustrate the properties of waves in those plasmas, in view of the fact that only perturbations with wavelengths larger than the critical value given by Equation (3.25) are described with a reasonable accuracy by ideal MHD. The critical wavelengths are $\sim 10^3$ km for the solar wind and ~ 750 m for the solar corona. In contrast, the collision frequencies obtained for a plasma with upper chromospheric conditions are not negligible in comparison with the cyclotron frequencies and, consequently, friction has a strong impact in the properties of the oscillation modes, specially at the high-frequency range.

Finally, the investigation of waves excited by a periodic driver has revealed another important reason to take into account the effect of elastic collisions. The momentum transfer associated to that interaction removes the resonances and the strict cutoffs that appear in the collisionless case. Friction produces diffusion of the energy of the perturbations. Thus, left-hand waves generated by a driver with a frequency that coincides with any of the cyclotron frequencies or is in the range of the cutoffs can propagate, instead of having a null phase speed or being evanescent. However, they are still strongly damped in space.

Appendix 3.A:

Coefficients of the matrices $\mathrm{A}_{\pm}$

$$A_{11,\pm} = (\omega \mp \Omega_p) \pm \frac{Z_p n_p \Omega_p}{n_e} + i(\nu_{p\mathrm{H}} + \nu_{p\mathrm{He}} + \nu_{p\mathrm{He\,II}} + \nu_{p\mathrm{He\,III}} + \nu_{pe}) + i\frac{Z_p^2 n_p^2 e^2}{\rho_p}\eta - i\frac{2Z_p n_p}{n_e}\nu_{pe} \tag{A.1}$$

$$A_{12,\pm} = \pm\frac{Z_{\mathrm{HeII}} n_{\mathrm{He\,II}} \Omega_p}{n_e} - i\nu_{p\mathrm{He\,II}} + i\frac{Z_p n_p Z_{\mathrm{He\,II}} n_{\mathrm{He\,II}} e^2}{\rho_p}\eta - i\frac{Z_{\mathrm{HeII}} n_{\mathrm{He\,II}}}{n_e}\nu_{pe} - i\frac{Z_p n_p}{n_e}\frac{\alpha_{\mathrm{He\,II}e}}{\rho_p} \tag{A.2}$$

$$A_{13,\pm} = \pm\frac{Z_{\mathrm{HeIII}} n_{\mathrm{He\,II}} \Omega_p}{n_e} - i\nu_{p\mathrm{He\,III}} + i\frac{Z_p n_p Z_{\mathrm{He\,III}} n_{\mathrm{He\,III}} e^2}{\rho_p}\eta - i\frac{Z_{\mathrm{HeIII}} n_{\mathrm{He\,III}}}{n_e}\nu_{pe} - i\frac{Z_p n_p}{n_e}\frac{\alpha_{\mathrm{He\,III}e}}{\rho_p} \tag{A.3}$$

$$A_{14,\pm} = -i\nu_{p\mathrm{H}} - i\frac{Z_p n_p}{n_e}\frac{\alpha_{e\mathrm{H}}}{\rho_p} \tag{A.4}$$

$$A_{15,\pm} = -i\nu_{p\mathrm{He}} - i\frac{Z_p n_p}{n_e}\frac{\alpha_{e\mathrm{He}}}{\rho_p} \tag{A.5}$$

$$A_{16,\pm} = \frac{k_x \Omega_p}{e n_e \mu_0} \pm i\frac{e k_x Z_p n_p}{\rho_p \mu_0}\eta \mp i\frac{k_x}{e n_e \mu_0}\nu_{pe} \tag{A.6}$$

$$A_{21,\pm} = \pm\frac{Z_p n_p \Omega_{\mathrm{He\,II}}}{n_e} - i\nu_{\mathrm{He\,II}p} + i\frac{Z_p n_p Z_{\mathrm{He\,II}} n_{\mathrm{He\,II}} e^2}{\rho_{\mathrm{He\,II}}}\eta - i\frac{Z_p n_p}{n_e}\nu_{\mathrm{He\,II}e} - i\frac{Z_{\mathrm{He\,II}} n_{\mathrm{He\,II}}}{n_e}\frac{\alpha_{pe}}{\rho_{\mathrm{He\,II}}} \tag{A.7}$$

$$\begin{aligned} A_{22,\pm} &= (\omega \mp \Omega_{\mathrm{He\,II}}) \pm \frac{Z_{\mathrm{He\,II}} n_{\mathrm{He\,II}}}{n_e} \\ &+ i(\nu_{\mathrm{He\,II}p} + \nu_{\mathrm{He\,IIH}} + \nu_{\mathrm{He\,IIHe}} + \nu_{\mathrm{He\,IIHe\,III}} + \nu_{\mathrm{He\,II}e}) \\ &+ i\frac{Z_{\mathrm{He\,II}}^2 n_{\mathrm{He\,II}}^2 e^2}{\rho_{\mathrm{He\,II}}}\eta - i\frac{2Z_{\mathrm{He\,II}} n_{\mathrm{He\,II}}}{n_e}\nu_{\mathrm{He\,II}e} \end{aligned} \tag{A.8}$$

$$\begin{aligned} A_{23,\pm} &= \pm\frac{Z_{\mathrm{He\,III}} n_{\mathrm{He\,III}} \Omega_{\mathrm{He\,II}}}{n_e} - i\nu_{\mathrm{He\,IIHe\,III}} + i\frac{Z_{\mathrm{He\,II}} n_{\mathrm{He\,II}} Z_{\mathrm{He\,III}} n_{\mathrm{He\,III}} e^2}{\rho_{\mathrm{He\,II}}}\eta \\ &- i\frac{Z_{\mathrm{He\,II}} n_{\mathrm{He\,II}}}{n_e}\frac{\alpha_{\mathrm{He\,III}e}}{\rho_{\mathrm{He\,II}}} - i\frac{Z_{\mathrm{He\,III}} n_{\mathrm{He\,III}}}{n_e}\nu_{\mathrm{He\,II}e} \end{aligned} \tag{A.9}$$

$$A_{24,\pm} = -i\nu_{\mathrm{He\,IIH}} - i\frac{Z_{\mathrm{He\,II}} n_{\mathrm{He\,II}}}{n_e}\frac{\alpha_{e\mathrm{H}}}{\rho_{\mathrm{He\,II}}} \tag{A.10}$$

$$A_{25,\pm} = -i\nu_{\mathrm{He\,IIHe}} - i\frac{Z_{\mathrm{He\,II}} n_{\mathrm{He\,II}}}{n_e}\frac{\alpha_{e\mathrm{He}}}{\rho_{\mathrm{He\,II}}} \tag{A.11}$$

$$A_{26,\pm} = \frac{k_x \Omega_{\mathrm{He\ II}}}{e n_e \mu_0} \pm i \frac{e k_x Z_{\mathrm{He\ II}} n_{\mathrm{He\ II}}}{\mu_0 \rho_{\mathrm{He\ II}}} \eta \mp i \frac{k_x}{e n_e \mu_0} \nu_{\mathrm{He\ II}e} \tag{A.12}$$

$$\begin{aligned} A_{31,\pm} &= \pm \frac{Z_p n_p \Omega_{\mathrm{He\ III}}}{n_e} - i\nu_{\mathrm{He\ III}p} + i \frac{Z_p n_p Z_{\mathrm{He\ III}} n_{\mathrm{He\ III}} e^2}{\rho_{\mathrm{He\ III}}} \eta - i \frac{Z_p n_p}{n_e} \nu_{\mathrm{He\ III}e} \\ &- i \frac{Z_{\mathrm{He\ III}} n_{\mathrm{He\ III}}}{n_e} \frac{\alpha_{pe}}{\rho_{\mathrm{He\ III}}} \end{aligned} \tag{A.13}$$

$$\begin{aligned} A_{32,\pm} &= \pm \frac{Z_{\mathrm{He\ II}} n_{\mathrm{He\ II}} \Omega_{\mathrm{He\ III}}}{n_e} - i\nu_{\mathrm{He\ IIIHe\ II}} + i \frac{Z_{\mathrm{He\ II}} n_{\mathrm{He\ II}} Z_{\mathrm{He\ III}} n_{\mathrm{He\ III}} e^2}{\rho_{\mathrm{He\ III}}} \eta \\ &- i \frac{Z_{\mathrm{He\ II}} n_{\mathrm{He\ II}}}{n_e} \nu_{\mathrm{He\ III}e} - i \frac{Z_{\mathrm{He\ III}} n_{\mathrm{He\ III}}}{n_e} \frac{\alpha_{\mathrm{He\ II}e}}{\rho_{\mathrm{He\ III}}} \end{aligned} \tag{A.14}$$

$$\begin{aligned} A_{33,\pm} &= (\omega \mp \Omega_{\mathrm{He\ III}}) \pm \frac{Z_{\mathrm{He\ III}} n_{\mathrm{He\ He\ III}} \Omega_{\mathrm{He\ III}}}{n_e} \\ &+ i(\nu_{\mathrm{He\ III}p} + \nu_{\mathrm{He\ IIIH}} + \nu_{\mathrm{He\ IIIHe}} + \nu_{\mathrm{He\ IIIHe\ II}} + \nu_{\mathrm{He\ III}e}) \\ &+ i \frac{Z_{\mathrm{He\ III}}^2 n_{\mathrm{He\ III}}^2 e^2}{\rho_{\mathrm{He\ III}}} \eta - i \frac{2 Z_{\mathrm{He\ III}} n_{\mathrm{He\ III}}}{n_e} \nu_{\mathrm{He\ III}e} \end{aligned} \tag{A.15}$$

$$A_{34,\pm} = -i\nu_{\mathrm{He\ IIIH}} - i \frac{Z_{\mathrm{He\ III}} n_{\mathrm{He\ III}}}{n_e} \frac{\alpha_{e\mathrm{H}}}{\rho_{\mathrm{He\ III}}} \tag{A.16}$$

$$A_{35,\pm} = -i\nu_{\mathrm{He\ IIIHe}} - i \frac{Z_{\mathrm{He\ III}} n_{\mathrm{He\ III}}}{n_e} \frac{\alpha_{e\mathrm{He}}}{\rho_{\mathrm{He\ III}}} \tag{A.17}$$

$$A_{36,\pm} = \frac{k_x \Omega_{\mathrm{He\ III}}}{e n_e \mu_0} \pm i \frac{e k_x Z_{\mathrm{He\ III}} n_{\mathrm{He\ III}}}{\mu_0 \rho_{\mathrm{He\ III}}} \eta \mp i \frac{k_x}{e n_e \mu_0} \nu_{\mathrm{He\ III}e} \tag{A.18}$$

$$A_{41,\pm} = -i\nu_{\mathrm{H}p} - i \frac{Z_p n_p}{n_e} \nu_{\mathrm{H}e} \tag{A.19}$$

$$A_{42,\pm} = -i\nu_{\mathrm{HHe\ II}} - i \frac{Z_{\mathrm{He\ II}} n_{\mathrm{He\ II}}}{n_e} \nu_{\mathrm{H}e} \tag{A.20}$$

$$A_{43,\pm} = -i\nu_{\mathrm{HHe\ III}} - i \frac{Z_{\mathrm{He\ III}} n_{\mathrm{He\ III}}}{n_e} \nu_{\mathrm{H}e} \tag{A.21}$$

$$A_{44,\pm} = \omega + i(\nu_{\mathrm{H}p} + \nu_{\mathrm{HHe}} + \nu_{\mathrm{HHe\ II}} + \nu_{\mathrm{HHe\ III}} + \nu_{\mathrm{H}e}) \tag{A.22}$$

$$A_{45,\pm} = -i\nu_{\mathrm{HHe}} \tag{A.23}$$

$$A_{46,\pm} = \mp i \frac{k_x}{e n_e \mu_0} \nu_{\mathrm{H}e} \tag{A.24}$$

$$A_{51,\pm} = -i\nu_{\mathrm{He}p} - i\frac{Z_p n_p}{n_e}\nu_{\mathrm{He}e} \tag{A.25}$$

$$A_{52,\pm} = -i\nu_{\mathrm{HeHe\ \textsc{ii}}} - i\frac{Z_{\mathrm{He\ \textsc{ii}}} n_{\mathrm{He\ \textsc{ii}}}}{n_e}\nu_{\mathrm{He}e} \tag{A.26}$$

$$A_{53,\pm} = -i\nu_{\mathrm{HeHe\ \textsc{iii}}} - i\frac{Z_{\mathrm{He\ \textsc{iii}}} n_{\mathrm{He\ \textsc{iii}}}}{n_e}\nu_{\mathrm{He}e} \tag{A.27}$$

$$A_{54,\pm} = -i\nu_{\mathrm{HeH}} \tag{A.28}$$

$$A_{55,\pm} = \omega + i(\nu_{\mathrm{He}p} + \nu_{\mathrm{HeH}} + \nu_{\mathrm{HeHe\ \textsc{ii}}} + \nu_{\mathrm{HeHe\ \textsc{iii}}} + \nu_{\mathrm{He}e}) \tag{A.29}$$

$$A_{56,\pm} = \mp i\frac{k_x}{en_e\mu_0}\nu_{\mathrm{He}} \tag{A.30}$$

$$A_{61,\pm} = \frac{k_x B_x Z_p n_p}{n_e} \pm iek_x Z_p n_p \eta \mp i\frac{k_x}{en_e}\alpha_{pe} \tag{A.31}$$

$$A_{62,\pm} = \frac{k_x B_x Z_{\mathrm{He\ \textsc{ii}}} n_{\mathrm{He\ \textsc{ii}}}}{n_e} \pm iek_x Z_{\mathrm{He\ \textsc{ii}}} n_{\mathrm{He\ \textsc{ii}}} \eta \mp i\frac{k_x}{en_e}\alpha_{\mathrm{He\ \textsc{ii}}e} \tag{A.32}$$

$$A_{63,\pm} = \frac{k_x B_x Z_{\mathrm{He\ \textsc{iii}}} n_{\mathrm{He\ \textsc{iii}}}}{n_e} \pm iek_x Z_{\mathrm{He\ \textsc{iii}}} n_{\mathrm{He\ \textsc{iii}}} \eta \mp i\frac{k_x}{en_e}\alpha_{\mathrm{He\ \textsc{iii}}e} \tag{A.33}$$

$$A_{64,\pm} = \mp i\frac{k_x}{en_e}\alpha_{e\mathrm{H}} \tag{A.34}$$

$$A_{65,\pm} = \mp i\frac{k_x}{en_e}\alpha_{e\mathrm{He}} \tag{A.35}$$

$$A_{66,\pm} = \omega \pm \frac{k_x^2 B_x}{en_e\mu_0} + i\frac{k_x^2}{\mu_0}\eta \tag{A.36}$$

Chapter 4

Small-amplitude perturbations in partially ionized plasmas*

4.1 Introduction

The consideration of the effects of partial ionization is of wide interest due to the fact that there are many astrophysical and laboratory plasmas where neutrals represent a non-negligible fraction of the total mass. Thus, the presence of those neutral species may produce an important deviation from the behavior predicted by MHD for a fully ionized plasma. For instance, Piddington [1956] and Watanabe [1961a] showed that the exchange of momentum between ions and neutrals by means of collisions causes the damping of Alfvén waves. Moreover, when the collision frequency is large compared to the oscillation frequency, the phase speed of Alfvén waves is reduced in comparison with the fully ionized case because the inertia of the neutrals has to be taken into account in addition to that of ions, as shown by, e.g., Kumar and Roberts [2003]. Nevertheless, partial ionization does not only affect the properties of waves in plasmas but there is a huge number of physical situations in which it may play an important role. In laboratory plasmas, the effects of the interaction between the ionized and the neutral species has been studied by, e.g., Woods [1962], Jephcott and Stocker [1962] or Mueller [1974] in experiments involving discharge tubes. Regarding astrophysical plasmas, the presence of neutrals has been taken into account, for instance, in the investigation of heating and gravitational collapse of interstellar gas clouds (Scalo [1977], Black and Scott [1982]), magnetic reconnection (Zweibel [1989]), driving of chromospheric spiculles (Haerendel [1992]), star formation (Mestel and Spitzer [1956], Fiedler and Mouschovias [1992, 1993], Pinto et al. [2008]), acceleration of the solar wind (Allen et al. [1998]), the support of solar prominences against gravity (Terradas et al. [2015]) or solar coronal rain (Oliver et al. [2016]).

As shown by the works of Braginskii [1965], De Pontieu et al. [2001], Khodachenko et al. [2004], Forteza et al. [2007] or Soler et al. [2009a], the single-fluid approximation for the study of partially ionized plasmas is appropriate when the frequency of waves is lower than the collision frequencies between ionized and neutral species. However, it becomes inaccurate when waves have frequencies of the order of or larger than the collision frequencies. In that range, each

---

[*] This chapter is based on: Martínez-Gómez, D., Soler, R. and Terradas, J.; 2016, *Multif-fluid approach to high-frequency waves in plasmas. II. Small-amplitude regime in partially ionized media*, The Astrophysical Journal, 837:80 (Martínez-Gómez et al. [2017])

species may have a different dynamics and the single-fluid approach fails to properly describe the behavior of the waves in the plasma. Hence, a more general model is required, which is the motivation of the investigation presented in this chapter. Thus, the multi-fluid detailed in Chapter 2 will be applied here to partially ionized plasmas, with a focus on several regions of the solar atmosphere.

The parameters of the plasmas chosen for this study can be found in Tables 4.1 and 4.2: region I corresponds to the upper chromosphere, at a height of 2016 km over the photosphere, where the number density of ions exceeds by an order of magnitude the number density of neutrals; region II represents a cool prominence, where neutrals and ions have similar densities; and region III corresponds to a plasma of the lower chromosphere at a height of 500 km above the photosphere, which is a very weakly ionized environment. The collision frequencies presented in Table 4.2 are computed from the friction coefficients given by Equations (2.60) and (2.62). However, it must be noted that only half of the total collision frequencies involved in the problem are shown; the remaining ones can be computed taking into account that $\alpha_{st} = \alpha_{ts}$, so that $\rho_s \nu_{st} = \rho_t \nu_{ts}$. The values of the magnetic field for the chromospheric regions are obtained from the semi-empirical model of Leake and Arber [2006], which represents the magnetic field strength in a chromospheric expanding tube as

$$|\boldsymbol{B_0}| = B_{ph} \left(\frac{\rho}{\rho_{ph}} \right)^{0.3}, \tag{4.1}$$

where ρ is the total density at the given height, and B_{ph} and ρ_{ph} are the magnetic field and the total density, respectively, at the photospheric level. The chosen reference values are $B_{ph} \approx 1500$ G and $\rho_{ph} \approx 2 \times 10^{-4}$ kg m^{-3}. The Alfvén speed, c_{A}, is given by

$$c_{\mathrm{A}} = \frac{|\boldsymbol{B_0}|}{\sqrt{\mu_0 \rho_i}}, \tag{4.2}$$

where ρ_i is the sum of the densities of the ionized species.

Table 4.1: Parameters of different partially ionized plasmas solar plasmas

Region	I	II	III
n_p (m^{-3})	7×10^{16}	1.4×10^{16}	1.9×10^{16}
n_{H} (m^{-3})	6×10^{15}	2×10^{16}	2.7×10^{21}
n_{He} (m^{-3})	10^{15}	2×10^{15}	2.7×10^{20}
$n_{\mathrm{He\ II}}$ (m^{-3})	6×10^{15}	–	6.5×10^{11}
$n_{\mathrm{He\ III}}$ (m^{-3})	10^{15}	–	7.2
T (K)	20000	10000	4700
B_0 (G)	22	10	480
c_{A} (km s^{-1})	153	184	7600
Ω_p (rad s^{-1})	210740	95800	4.6×10^6
$\Omega_{\mathrm{He\ II}}$ (rad s^{-1})	52685	23950	1.15×10^6
$\Omega_{\mathrm{He\ III}}$ (rad s^{-1})	105370	47900	2.3×10^6

Regions I and III correspond to the chromosphere at heights 2016 km and 500 km above the photosphere, respectively; temperatures and number densities are taken from the Model F of Fontenla et al. [1993]. Region II represents a prominence at an altitude of 10000 km and gas pressure of $P_g = 0.005$ Pa according to Heinzel et al. [2015].

Table 4.2: Collision frequencies in Hz

Region	I	II	III
$\nu_{p\mathrm{H}}$	120	270	2.5×10^{7}
$\nu_{p\mathrm{He}}$	2.5	3.5	320000
$\nu_{p\mathrm{He\ II}}$	2000	–	1.7
$\nu_{p\mathrm{He\ III}}$	1260	–	7×10^{-11}
ν_{pe}	660	330	1240
ν_{HHe}	3.5	5.2	480000
$\nu_{\mathrm{HHe\ II}}$	3.2	–	2×10^{-4}
$\nu_{\mathrm{HHe\ III}}$	0.2	–	8×10^{-16}
$\nu_{\mathrm{H}e}$	7.5	1	0.9
$\nu_{\mathrm{HeHe\ II}}$	29	–	1.5×10^{-3}
$\nu_{\mathrm{HeHe\ III}}$	0.03	–	10^{-16}
$\nu_{\mathrm{He}e}$	0.6	0.1	0.1
$\nu_{\mathrm{He\ IIHe\ III}}$	540	–	4×10^{-11}
$\nu_{\mathrm{He\ II}e}$	170	–	320
$\nu_{\mathrm{He\ III}e}$	640	–	1200

The reason for choosing the above mentioned environments is that the variety of degrees of ionization represented by those three plasmas allows to get a more general insight into the effects of partial ionization on the propagation of waves.

Several issues of great relevance can be addressed with the application of the multi-fluid theory to the chosen set of partially ionized plasmas. For instance, as shown in the previous chapter, the multi-fluid theory predicts the existence of various additional oscillation modes that are overlooked by the single-fluid models. Therefore, since three different kinds of collisions will be considered in this chapter, namely magnetic resistivity, which is caused by collisions with electrons, and ion-ion and ion-neutral momentum transfer collisions, a comparison of the effect of each diffusive mechanism on the periods and the damping rates of each oscillation mode can be performed. Thus, the relative influence on the properties of waves of those three interactions can be studied for different degrees of ionization and ranges of frequencies and wavenumbers. Then, it is also possible to analyze the particular behavior of each component of the plasma after a perturbation has been applied to the whole fluid and to check how this behavior varies for a wide range of frequencies. In addition, the multi-fluid theory reveals another property of Alfvén waves in partially ionized plasmas that is not predicted by the single-fluid approximations: according to Kulsrud and Pearce [1969] and Pudritz [1990], under certain circumstances, Alfvén waves may have cutoffs caused by the friction between ions and neutrals.

In the same way as in Chapter 3, here the investigation will be performed by means of two methods. In the first place, Section 4.2 shows the results obtained from the analysis of the dispersion relation for small-amplitude perturbations. Then, Section 4.3 presents the results of several numerical simulations, which are then shown to be consistent with those obtained from the dispersion relation, but also include some nonlinear effects that cannot be addressed by the previous method. For instance, the increase of the internal energy of the plasmas due to the frictional dissipation of the energy of the initial perturbation is explored.

4.2 Analysis of the dispersion relation

As in the previous chapter, the dispersion relation for small-amplitude incompressible perturbations can be obtained from Equation (3.12). However, in contrast with the fully ionized case, here the terms associated with the neutral species and with electron collisions are taken into account instead of being neglected. Since plasmas composed of five species (apart from electrons) are considered, a sixth-order polynomial in ω is obtained for each direction of polarization. Due to their complexity, each of those equations are solved numerically.

4.2.1 Waves excited by an impulsive driver

In the same way as in Section 3.3.1, to analyze the behavior of waves excited by an impulsive driver, the dispersion relations are solved as functions of a real wavenumber, k_x, assuming that the solution frequency may be complex, i.e., $\omega = \omega_R + i\omega_I$.

The results of solving the dispersion relation with parameters corresponding to the upper chromospheric region are shown in Figure 4.1, where only the solutions with $\omega_R > 0$ are represented (it must be reminded that the solutions with $\omega_R < 0$ can be obtained by reflecting with respect to the horizontal axis those shown here but exchanging the polarizations). To understand the influence of resistivity, two different situations have been analyzed: on the left panels the effect of collisions with electrons has been included, while on the right panels it has not been taken into account. It can be seen that resistivity has a negligible effect in the low wavenumber range but that it greatly enhances the damping of the R mode at high wavenumbers. On the other hand, the L modes are almost unaffected by this type of collisions. This huge contrast in the way resistivity affects each polarization can be understood as follows. Since the inertia of electrons has been neglected, they are frozen to the magnetic field. On the contrary, ions, whose direction of gyration coincides with the rotation of the left-hand polarized waves, are not as tight to the magnetic field at high frequencies due to Hall's effect. Thus, the velocity drifts between electrons and ions, $\boldsymbol{V_e} - \boldsymbol{V_i}$, are larger when the gyration of ions is opposite the rotation of waves, i.e., for the R modes. Consequently, the friction forces associated to collisions with electrons are larger for R modes than for L modes.

The right panels of Figure 4.1 can be also compared with the results for the fully ionized case shown in Figure 3.6. It can be seen that in both graphics the real part of the four solutions associated with the ionized species is almost identical, with the dissimilarities appearing in the imaginary part: the inclusion of collisions with neutrals produces a larger damping on the four modes. This enhanced damping is more obvious in the Alfvénic modes at small wavenumbers. Hence, it can be concluded that at small wavenumbers, the damping of waves is dominated by the collisions with neutrals, while the contribution of collisions between ionized species is more important at large wavenumbers. The reason for such a behavior is that waves are more efficiently damped when the collision frequency is closer to the oscillation frequency (see, e.g., Leake et al. [2005], Zaqarashvili et al. [2011a], Soler et al. [2013b]), and, as shown in Table 4.2, the interactions with neutrals have lower frequencies than the collisions between ions.

Another remarkable difference that arises in the partially ionized case with respect to the fully ionized one is the appearance of two additional modes associated with the two neutral species. These modes are represented in Figure 4.1 by the blue dotted and dashed-dotted lines and have received in previous works the names of vortex modes (Zaqarashvili et al. [2011b]) or forced neutral oscillations (Vranjes and Kono [2014]). According to Soler et al. [2013b], the

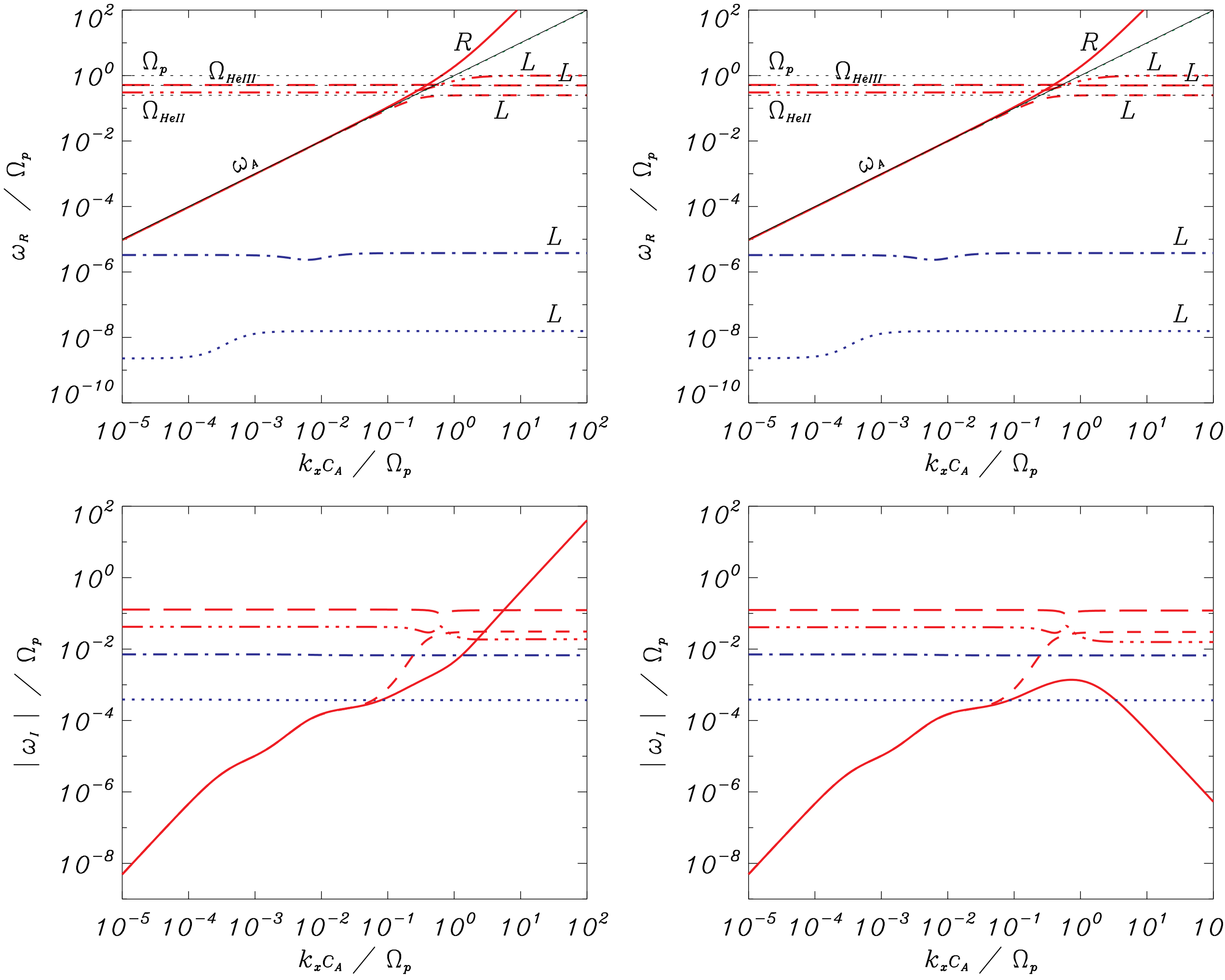

Figure 4.1: Solutions of Equation (3.12) for the case of an impulsive driver and upper chromospheric conditions, with resistivity (left panels) and without (right). Top: normalized frequency, ω_R/Ω_p, as a function of the normalized wavenumber, $k_x c_{\mathrm{A}}/\Omega_p$; bottom: absolute value of the normalized damping rate, $|\omega_I|/\Omega_p$, as a function of the normalized wavenumber. The blue lines are solutions associated to the presence of neutral species. The solid black lines represent the Alfvén frequency, ω_{A}. The horizontal dotted lines represent the cyclotron frequencies of the three ionized species, with $\Omega_p > \Omega_{\mathrm{HeIII}} > \Omega_{\mathrm{HeII}}$.

vortex modes describe how vorticity perturbations in the neutral fluid decay in time due to the interaction of neutrals with ions. In a collisionless plasma, these modes do not propagate, since they have a null frequency. But when collisions are considered, their frequency becomes different from zero, although with $|\omega_R \ll \omega_I|$; hence, such modes are heavily overdamped.

The results described in the previous paragraphs correspond to a plasma where the abundance of neutrals is lower than that of ions. Thus, the dynamics of the plasma is dominated by the behavior of ions, although there is a small influence from the neutral species. This influence is expected to be larger in the other two regions that are going to be studied next because of the larger amount of neutrals.

The case of a plasma with properties akin to those in solar prominences is illustrated in Figure 4.2, where the modes associated with the helium ions are not represented because Table 4.1 does not provide data about the abundances of those elements. Indeed, the temperature in prominence cores is low enough to assume that helium is fully neutral. In contrast with the previous figure, the effect of the presence of neutrals can be clearly distinguished at low wavenumbers in the top panel: due to the strong coupling between ions and neutrals at this range, the Alfvénic modes do not oscillate with the classical Alfvén frequency $\omega_{\mathrm{A}} = k_x c_{\mathrm{A}}$, but with a smaller modified Alfvén frequency given by

$$\widetilde{\omega}_{\mathrm{A}} = k_x \widetilde{c}_{\mathrm{A}} = \frac{\omega_{\mathrm{A}}}{\sqrt{1 + \rho_n/\rho_i}}, \tag{4.3}$$

where ρ_n is the sum of the densities of the neutral species. This equation is a generalization of Equation (27) from Soler et al. [2013b] or Equation (19) from Zaqarashvili et al. [2013], applicable when the collision frequencies between neutrals and ions are much larger than the Alfvén frequency. In that limit, the coupling between all species is so strong that they behave as a single fluid and the inertia of the neutrals must be taken into account in the description of Alfvén waves.

Then, it can be seen that as the wavenumber increases and the Alfvén frequency is no longer much lower than the ion-neutral collision frequencies, the oscillation frequencies of the Alfvénic modes tend to the ω_{A} before splitting into two different branches. The damping of these solutions is small for small wavenumber but becomes important for larger values, particularly in the case of the R mode, which is predominantly affected by collisions with electrons.

The vortex modes shown in Figure 4.2 have much lower oscillation frequencies than the Alfvénic modes. This is due to their excitation being indirectly caused by the magnetic field through the collisions of neutrals with ions. On the other hand, their damping is higher at

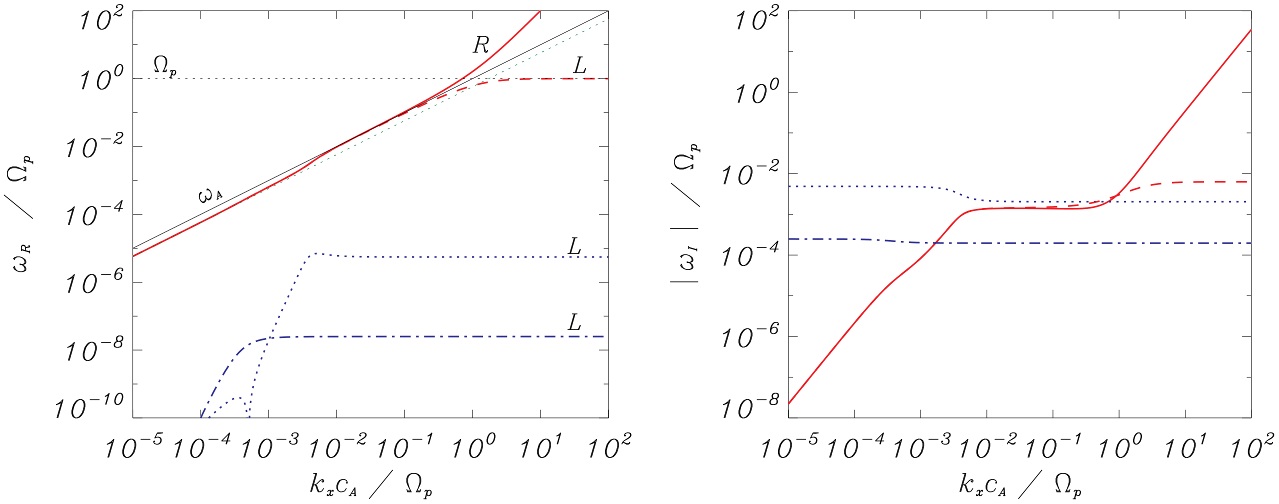

Figure 4.2: Solutions of Equation (3.12) for the case of an impulsive driver and prominence conditions. The colors and styles are the same as in Figure 4.1, with the addition of a green dotted line that represents the normalized modified Alfvén frequency, $\widetilde{\omega}_{\mathrm{A}}/\Omega_p$.

small wavenumbers. Thus, these modes are much more short-lived.

Using a two-fluid model to describe Alfvén waves in a partially ionized hydrogen plasma, Soler et al. [2013b] found approximate expressions for the damping of the evanescent or vortex mode. In the limit when the collision frequency is much smaller than the Alfvén frequency, they found that the damping rate is given by $\omega_{I,vort} \approx -\nu_{\mathrm{H}p}$, while in the opposite limit, it is given by $\omega_{I,vort} \approx -(1+\chi)\nu_{\mathrm{H}p}$, where $\chi = \rho_n/\rho_i$. The vortex solutions plotted in the right panel of Figure 4.2 display a behavior consistent with those analytic approximations. They tend to a constant value in each limit, with the damping being larger at low wavenumbers, where $\nu \gg k_x c_{\mathrm{A}}$. A precise expression for those limiting values is not provided, since it involves a combination of a great number of parameters and its calculation is not as straightforward as the one obtained by Soler et al. [2013b].

Inspecting the top panel of Figure 4.2 it can be seen that the L mode represented by a dotted line has a quite strange behavior in the low wavenumber limit: it displays a sharp minimum in frequency at about $k_x c_{\mathrm{A}}/\Omega_p \approx 5 \times 10^{-4}$ while none of the other modes show those abrupt variations. It has been found that this behavior is a consequence of the electron-neutral interaction. This statement is supported by Figure 4.3, where the analysis of the simpler case of a plasma composed of protons, electrons and neutral hydrogen is represented. The sharp minimum appears only on the right panel, which corresponds to the case in which the effect of electron-neutral collisions has been included. Nevertheless, it must be noted that the sharp minimum is just apparent and is caused by the way in which the solutions are represented in Figures 4.2 and 4.3. Its apparent nature is revealed in Figure 4.4, where the solutions with $\omega_R < 0$ are also plotted. Due to collisions with electrons, the L vortex has $\omega_R < 0$ at small wavenumbers, and they change to $\omega_R > 0$ when the wavenumber increases. The opposite happens to the R modes.

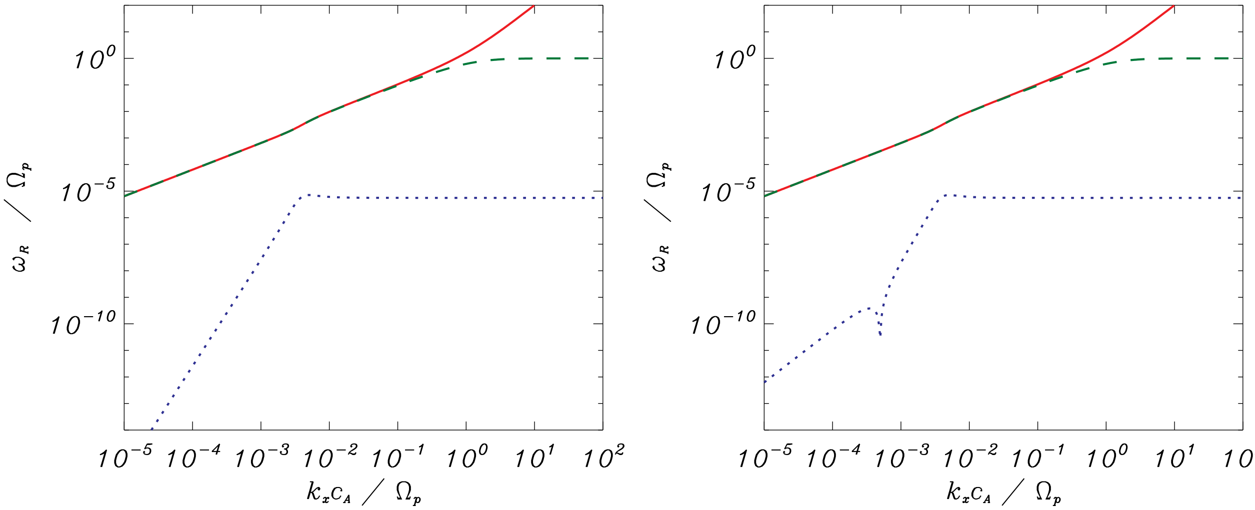

Figure 4.3: Normalized oscillation frequency as a function of the normalized wavenumber for a two-fluid plasma (protons-electrons + neutral hydrogen). The left panel shows the solutions for $\nu_{He} = 0$, while the right panel represent the case where collisions between neutral hydrogen and electrons has been taken into account.

Next, Figure 4.5 shows the results which correspond to a plasma in the low chromosphere

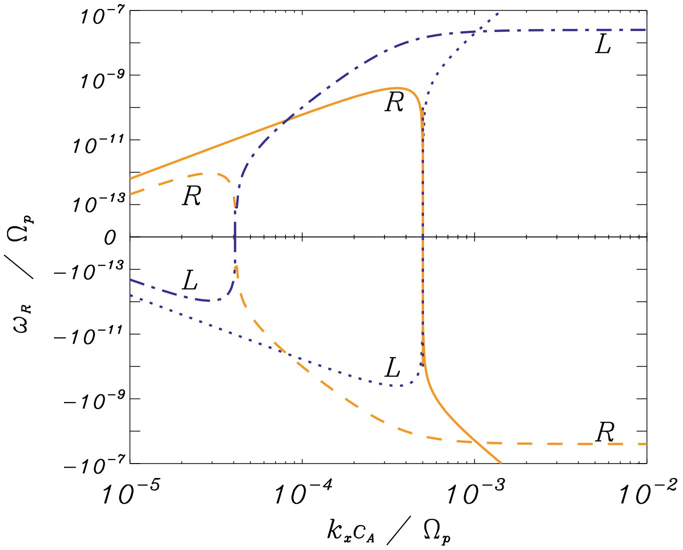

Figure 4.4: Magnification of the small-wavenumber and low-frequency region of the top panel of Figure 4.2 (including also the solutions with $\omega_R < 0$). The blue lines represent the L modes, while the orange lines represent the R modes.

at a height of 500 km above the photosphere. There, the abundance of neutral particles is several orders of magnitude larger than the abundances of ions. In addition, the large densities lead to high values of collision frequencies. Both circumstances cause a huge departure of the modified Alfvén frequency from ω_{A}, as can be checked in the top panel. An important difference from the results obtained in plasmas with a higher degree of ionization is that now it is not easy to distinguish between the vortex, Alfvénic, and ion-cyclotron modes. Their properties seem to be mixed up when the plasma is mainly composed of neutrals. For instance, at small wavenumbers, there is one solution that in the previous cases was identified as a vortex mode but that here has a higher oscillation frequency than the Alfvénic modes, and that for large wavenumbers tends to the proton cyclotron frequency, as if it were an ion-cyclotron wave. Also, the L mode that emerges from the Alfvénic branch does not tend to the cyclotron frequency of any ion but to the value $\Omega_p/(1+\chi)$, as if it were an effective cyclotron frequency (Mueller [1974]) for this plasma. These results point out the dramatic effect of neutrals on the behavior of the waves in conditions of very low ionization.

In Chapter 3, it has been shown that a very useful tool to analyze the properties of the perturbations is the quality factor, which, for waves generated by an impulsive driver, is defined as $Q_\omega \equiv 1/2|\omega_R/\omega_I|$. Hence, it will be employed in this chapter also. Figure 4.6 displays the quality of (a) the solutions for the case of the higher chromosphere with resistivity, (b) the case of the prominence, and (c) the lower chromosphere. It can be seen that, in the three studied regions, the vortex modes are overdamped, specially at small wavenumbers, and, hence, the energy associated to these modes is not transported far from where the perturbation originates but it is dissipated *in situ*. The remaining perturbations are underdamped. The R mode (red solid line) has the larger Q_ω of all modes at all values of $k_x c_{\mathrm{A}}/\Omega_p$, except for the case of the lower chromosphere: in panel (c) it can be seen that there is a region, between $k_x c_{\mathrm{A}}/\Omega_p \approx 10^{-3}$ and $k_x c_{\mathrm{A}}/\Omega_p \approx 2$, where one of the cyclotron modes has a larger value of Q_ω. None of the

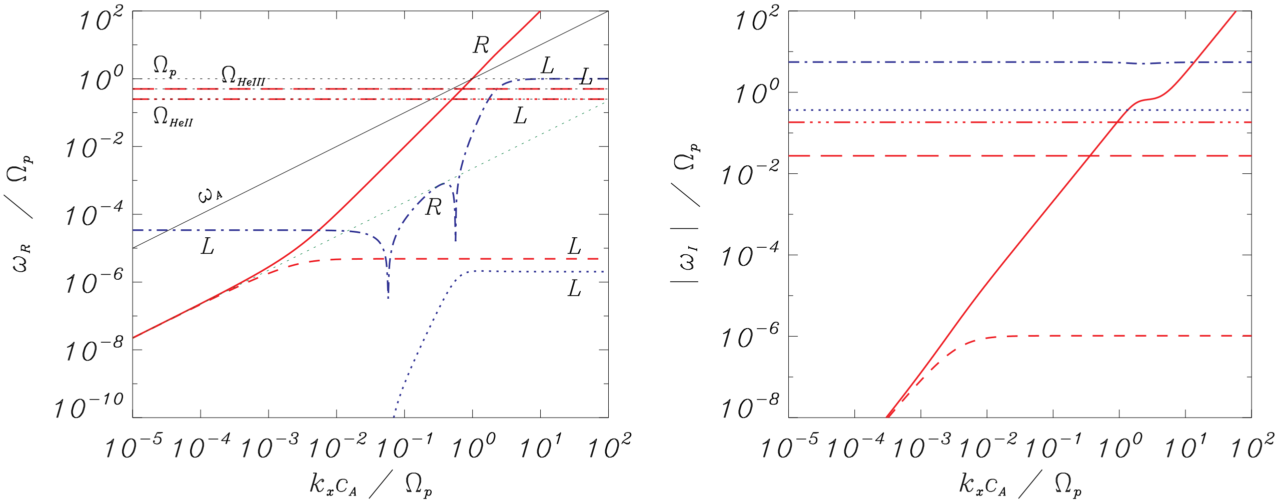

Figure 4.5: Solutions of Equation (3.12) for the case of an impulsive driver and parameters that correspond to a region in the low chromosphere. The colors and styles are the same as in Figure 4.1, with the addition of a green dotted line that represents the normalized modified Alfvén frequency.

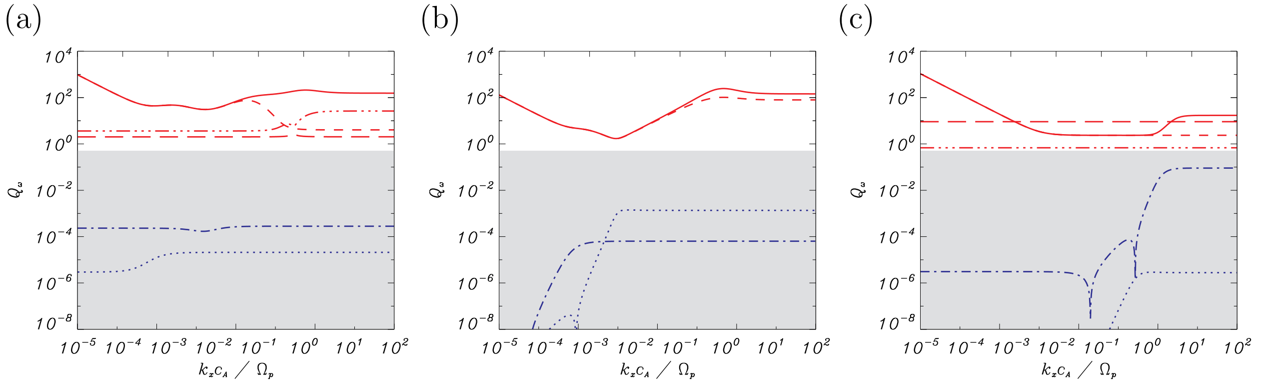

Figure 4.6: The panels (a), (b) and (c) represent the quality factors of the solutions shown in the left panels of Figure 4.1, in Figure 4.2 and in Figure 4.5, respectively. The grey areas correspond to values of $Q_\omega < 1/2$, where the waves are overdamped.

modes is evanescent.

Apart from all the properties of waves already investigated throughout this section, there is another characteristic worth analyzing, namely the existence of cutoff regions caused by the interaction between ions and neutrals. This issue is of considerable relevance, because it demonstrates how multi-fluid models may reveal effects that are overlooked by the single-fluid approximations. By means of two-fluid models, Kulsrud and Pearce [1969] and Pudritz [1990] found that partially ionized plasmas may present regions of wavenumbers where all modes are evanescent: oscillatory modes are suppressed in those cutoff intervals due to the strong friction caused by the collisions of ions with neutrals. However, this behavior is not found in all partially ionized plasmas but only in those which fulfill the condition $\chi > 8$, as shown by Soler et al. [2013b]. By inspecting Table 4.1, it can be seen that the region of the lower chromosphere studied in this section clearly fulfills that condition. Nonetheless, according to Figure 4.6, it has no cutoffs regions. Hence, it seems to contradict the findings of those previous works.

In a later work, Soler et al. [2015a] took into account the effects of Hall's term, resistivity, electron inertia, and viscosity in the study of wave damping in partially ionized plasmas in the solar chromosphere and showed that in a more realistic situation there are no strict cutoffs. They found that Alfvén waves may be underdamped or overdamped depending on the specific physical parameters of the plasma but that those modes can always be excited. Those authors also demonstrated that the removal of the cutoffs is due to the effect of Hall's current (see, e.g., Lighthill [1960], Pandey and Wardle [2008], Zaqarashvili et al. [2012]), and electron inertia. Since in the present investigation electron inertia has not been considered, the mechanism that explains the absence of the cutoffs in the studied region of the lower chromosphere is Hall's current: electrons dynamics is different than that of ions; they stay more coupled to the magnetic field than ions, allowing the propagation of Alfvén waves, while ion-neutrals collisions would be able to completely suppress the oscillations if electrons were tightly coupled to ions.

Nevertheless, the regions of the solar chromosphere analyzed by Soler et al. [2015a] do not coincide with those studied in this section and, hence, a direct comparison between the results of the two investigations cannot be made. Those authors explored an altitude range from 600 to 2000 km, while here only two specific heights, which are out of that range, have been analyzed. Thus, to perform an appropriate comparison, the next step is to compute the quality factor of waves at an altitude that is inside the range chosen by Soler et al. [2015a]. Figure 4.7 displays the results for a height of 1175 km over the photosphere, with parameters taken again from the Model F of Fontenla et al. [1993]. At such height, the magnetic field is $B_0 \approx 110$ G and the temperature is $T \approx 6500$ K. This figure shows that there is an interval of wavenumbers, between $k_x c_{\mathrm{A}} \approx 10^{-2}$ and $k_x c_{\mathrm{A}}/\Omega_p \approx 0.1$, where all the represented modes are overdamped. This is in good agreement with the results shown in Figures 3(b) and (d) of Soler et al. [2015a]. Thus, although there are no strict cutoff regions in the middle chromosphere either, an interval of wavenumbers for which the solutions are overdamped remains even when Hall's current and electron-neutral collisions are taken into account.

4.2.2 Waves excited by a periodic driver

The investigation of fully ionized plasmas detailed in Section 3.4 showed that the addition of new ionized species to a multi-fluid plasma does not increase the number of oscillations modes in the case of waves generated by a periodic driver. The same occurs when the additional

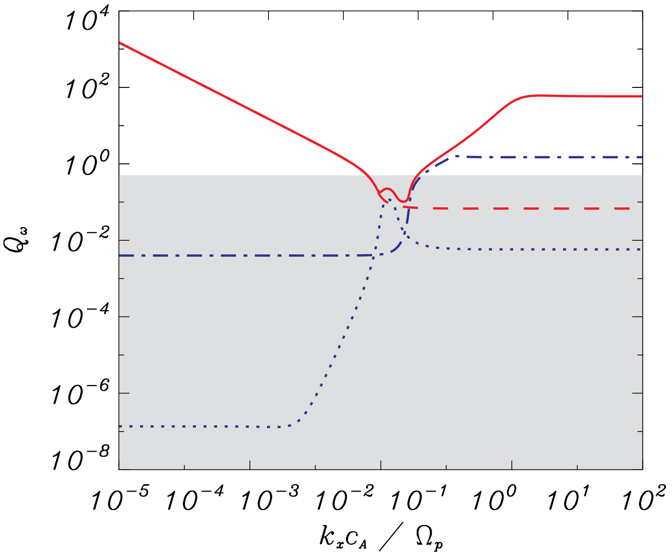

Figure 4.7: Quality factor of waves excited by an impulsive driver in a plasma with conditions of the chromosphere at a height of 1175 km over the photosphere (for the sake of clarity, the cyclotron modes associated to the helium ions are not plotted here).

species are neutral, as it will be checked in this section. Hence, if the dispersion relations are solved as functions of a real frequency ω, only two solutions of the form $k_x = k_R + ik_I$ will be obtained for each polarization.

In the following lines, the same regions of the solar atmosphere as in the case of the impulsive driver will be studied. In the first place, Figure 4.8 shows the results for a plasma with parameters corresponding to a region in the chromosphere at an altitude of 2016 km over the photosphere. Several different cases have been represented in this figure, with the goal of obtaining a better understanding of the relevance of the different collisional interactions included in the model. For instance, the left panels display a comparison between the case in which all types of collisions are considered and the one in which interaction with neutrals is neglected. It can be seen that the effect of neutrals is particularly important in the low-frequency range, where it produces a remarkably stronger damping than when only collisions between ionized species are taken into account. At higher frequencies, there are no appreciable differences between the two situations, which means that the collisions with neutrals are not as relevant as the collisions between ions.

On the right panels of Figure 4.8, the case that includes all the collisions between the species is compared with the situation in which resistivity is ignored. The results demonstrate that the inclusion of resistivity produces a larger damping of the R mode at high frequencies, while the damping of the L mode is not modified. However, concerning the real part of the wavenumber, it is the ion-cyclotron mode that is more affected: at high frequencies, it has a larger wavenumber when collisions with electrons are involved and hence, it propagates at a smaller speed. The real part of the wavenumber of the R mode shows no variations. In addition, by inspecting any of the four panels, it can be checked that all solutions are finite at the cyclotron frequencies, which means that the resonances are removed due to the friction between species. The cutoff regions are removed as well.

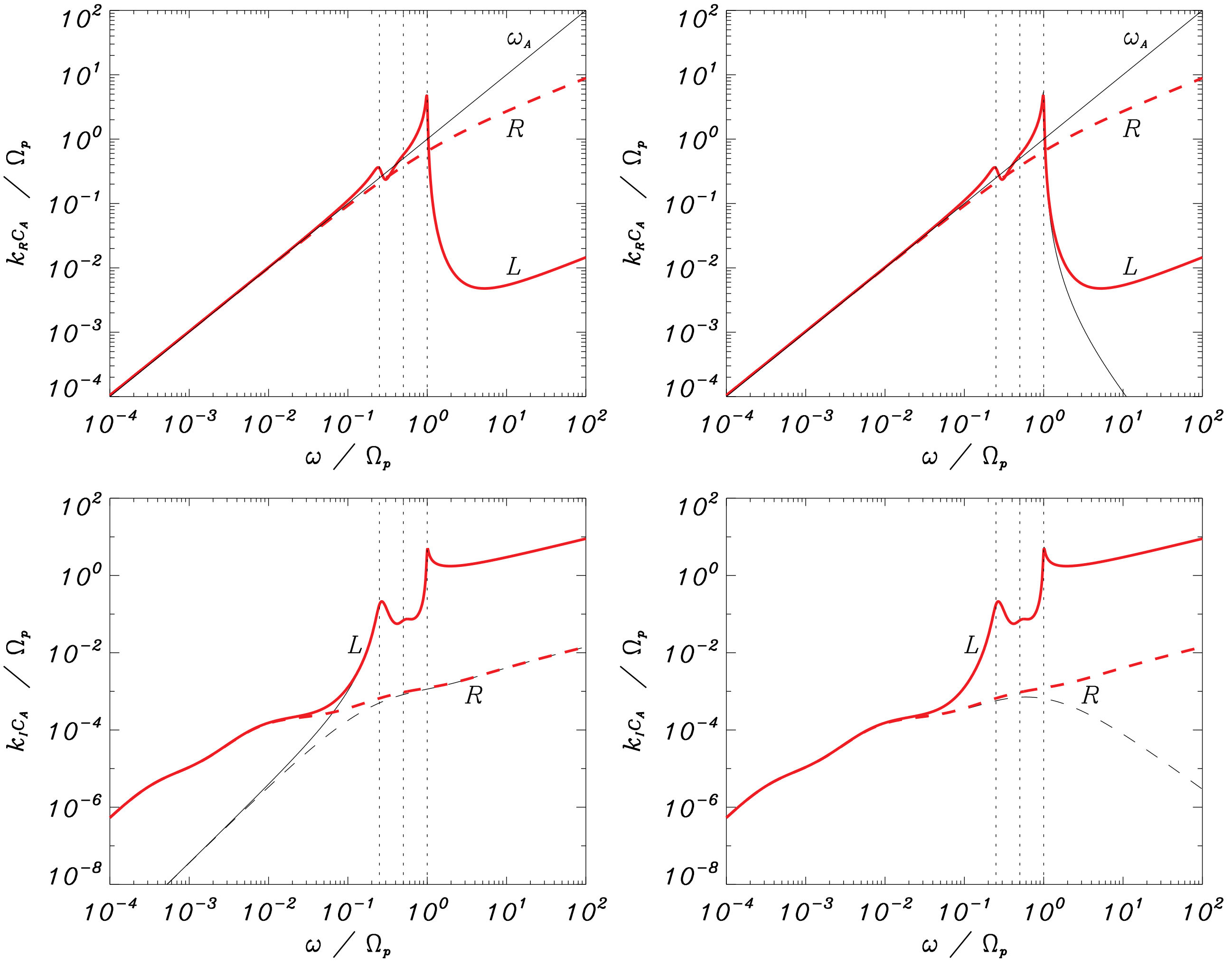

Figure 4.8: Solutions of Equation (3.12) for the case of a periodic driver and parameters corresponding to a region in the high chromosphere (region I from Table 4.1). The wavenumber and the spatial damping are shown as functions of the frequency in the top and the bottom panels, respectively. The thin black lines on the left panels represent the solutions when the collisions with neutrals have been ignored. On the right panels, the thin black lines represent the case without resistivity. The diagonal black line corresponds to the Alfvén frequency, ω_{A}. The red lines correspond to the case where all the effects have been taken into account. The dotted vertical lines mark the position of the frequencies of resonances, with $\Omega_p > \Omega_{\mathrm{He\ III}} > \Omega_{\mathrm{He\ II}}$.

Next, the results corresponding to the remaining two regions, where neutrals are the most abundant species, are shown in Figure 4.9. The left panels correspond to a plasma with conditions akin to that of a prominence, and the right panels display the results for a region in the low chromosphere. On the left area of the top panels, a range in which the frequency of the driver is smaller than the collision frequencies, all the fluids are strongly coupled and the wavenumber of the oscillations is larger than in the fully ionized case (represented by the black solid line). Thus, the perturbations propagate at a slower speed, given by $\widetilde{c}_{\mathrm{A}}$. Moreover, since all the species behave in that range almost as a single fluid, the spatial damping of the perturbations is smaller than at higher frequencies, where the coupling is not as strong and the frictional force increases due to the velocity drifts between the species.

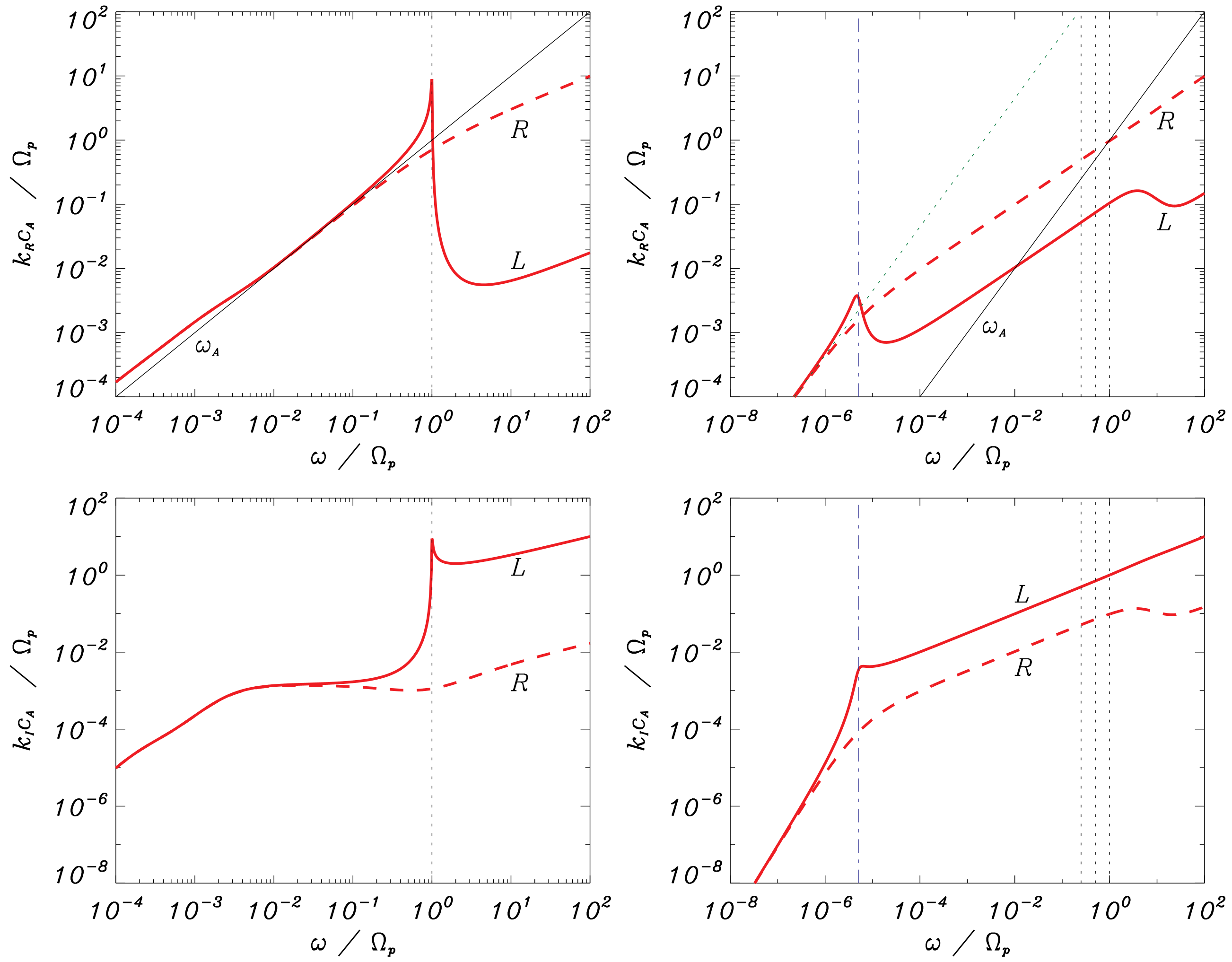

Figure 4.9: Normal modes of perturbations excited by a periodic driver. The left panels correspond to prominence conditions, while the right panel correspond to conditions of a region in the low chromosphere. The green dotted line on the top right panel represents the wavenumber related to the modified Alfvén speed. The vertical blue lines on the right panels represent the position of the Hall frequency, ω_{H}.

As the frequency of the driver increases, the separation between the L and the R modes becomes evident. For the case of the prominence, the separation occurs when the frequency of the driver approaches the lower ion-cyclotron frequency, a behavior similar to that shown in Figure 4.8 or in the fully ionized plasmas studied in Chapter 3. However, the right panels of Figure 4.9 show that when the abundance of neutrals is much higher than the abundance of ions and there is a very strong coupling between them, the split appears at values much lower than the cyclotron frequencies. This fact can be related to the investigations of Pandey and Wardle [2008] and Pandey and Dwivedi [2015]. By means of a single-fluid description of three-component plasmas (electrons, ions and neutrals), those authors found that the effect of Hall's current becomes important and, hence, there is a clear distinction in the properties of the L and R waves when the frequency ω is of the order of or larger than the so-called Hall frequency, which is defined as

$$\omega_{\mathrm{H}} \equiv \frac{\rho_i}{\rho_i + \rho_n} \Omega_i. \tag{4.4}$$

It must be noted that this definition coincides with what in Section 4.2.1 has been called the effective cyclotron frequency. The Hall frequency plays in weakly ionized plasmas the same role as the cyclotron frequency in fully ionized plasmas. Moreover, it is straightforward to check that $\omega_{\mathrm{H}} = \Omega_i$ in the latter case. In contrast, when a weakly ionized plasma is considered, e.g., in the lower solar chromosphere, $\omega_{\mathrm{H}} \ll \Omega_i$, which means that Hall diffusion has a great influence on the dynamics of the plasma even at very low frequencies. Thus, the results shown in the right panels of Figure 4.9 are consistent with the findings of Pandey and Wardle [2008] and Pandey and Dwivedi [2015]. It can be checked that the position of the peak that appears in both the top and the bottom panels, and that resembles the resonances found in fully ionized plasmas, corresponds to the Hall frequency, $\omega_{\mathrm{H}} \approx 5 \times 10^{-6} \Omega_p$.

Following the same procedure as in previous section, now the quality factor of the perturbations, which for a periodic driver is defined as $Q_k \equiv 1/2|k_R/k_I|$, will be computed. Figures 4.10(a)-(c) represent the quality factor of the normal modes shown in the left panels of Figure 4.8, and the left and right panels of Figure 4.9, respectively. In Figure 4.10(a), it can be seen that the low-frequency modes have a smaller Q_k when collisions with neutrals are taken into account than when only collisions between ions are considered. However, in both cases, Q_k is of the order of or larger than ~ 100, which means that the perturbations are underdamped and it would take several periods to find a remarkable decrease in their amplitudes. At higher frequencies, the L and R modes display very contrasting behaviors. The quality factor of the former tends to the critical value $Q_k = 1/2$ when the frequency of the driver approaches the lower ion-cyclotron frequency and, after a short interval in which it slightly increases again, finally crosses that boundary at the higher ion-cyclotron frequency, meaning that it becomes overdamped. On the other hand, the R mode is always underdamped, with values of $Q_k \gtrsim 100$.

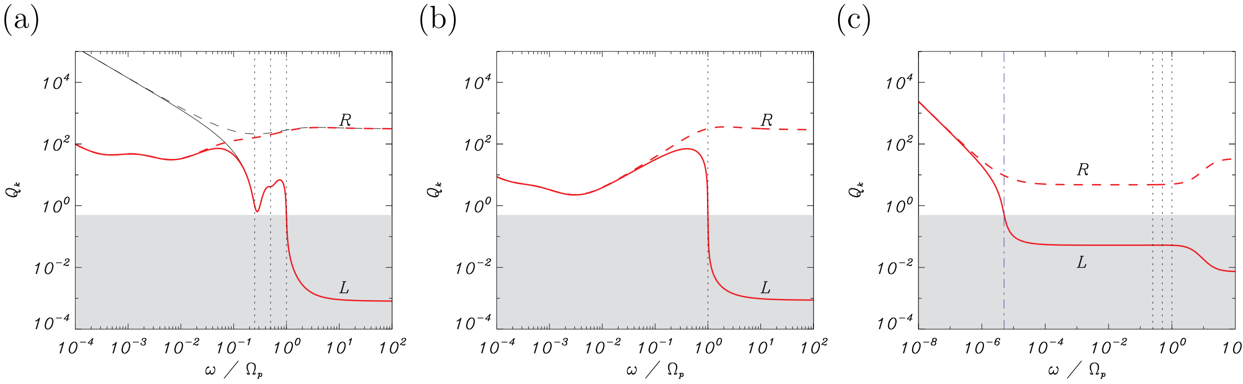

Figure 4.10: Quality factor, Q_k, of waves excited by a periodic driver. The left panel corresponds to the results shown on the left panels of Figure 4.8. The middle and the right panels correspond to the results shown on the left and right panels of Figure 4.9, respectively.

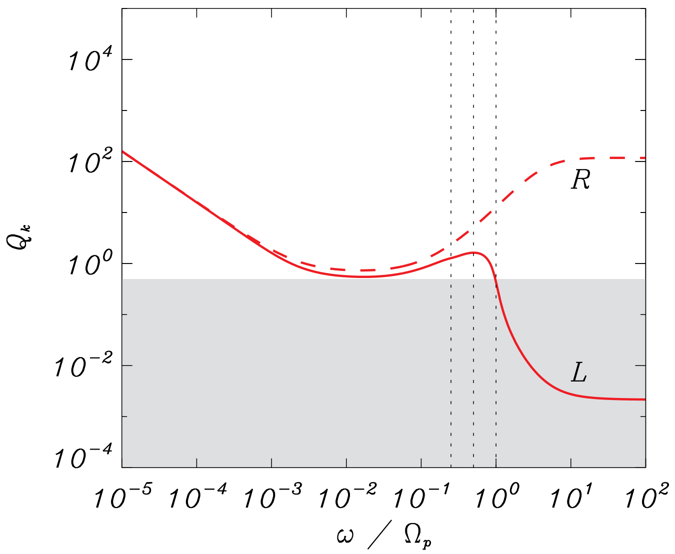

Figure 4.11: Quality factor of waves excited by a periodic driver in a plasma with conditions of the chromosphere at a height of 1175 km over the photosphere.

Similar behavior is found in Figure 4.10(b), although the Alfvénic modes have a lower Q_k due to a larger presence of neutrals in this plasma that produces greater friction and dissipation of the energy carried by the perturbation. Figure 4.10(c), which represents the weakly ionized environment of the low chromosphere, shows that the point where the L mode becomes overdamped coincides with the Hall frequency given by Equation (4.4), and that there are approximately two orders of magnitude of difference between the quality factors of the two polarizations, even at low frequencies.

Once more, it is interesting to compare the results presented in the paragraphs above with those detailed in Soler et al. [2015a] regarding the subject of the possible existence of cutoffs or intervals of frequencies where the perturbations are overdamped. In the ranges of heights and frequencies studied by those authors, the perturbations are found to be underdamped instead of overdamped. As in the previous section, the comparison with that work is performed by means of the analysis of a region of the low chromosphere at 1175 km over the photosphere. The results are plotted in Figure 4.11. It can be checked that there is an interval of frequencies, $\omega/\Omega_p \gtrsim 1$, where the L mode is overdamped. However, such interval has not been explored in the investigation of Soler et al. [2015a], so that it is not relevant for the present comparison. At lower frequencies, both modes are underdamped, which seems to be in good agreement with what is shown in Figures 4(b) and (d) of Soler et al. [2015a]. However, there are some slight differences between the two studies: in the cited paper, no noteworthy dissimilarities can be seen in the quality factor of the two polarizations; on the other hand, Figure 4.11 shows that the quality factor of the R mode is slightly larger than that of the L mode. This small discrepancy may be caused by some of the effects that Soler et al. [2015a] included in their model, like viscosity of each species or the electron inertia, which have been neglected in the present analysis.

4.3 Numerical simulations

In this section, the full temporal evolution of small-amplitude perturbations on homogeneous partially ionized plasmas is computed by means of the numerical code MolMHD. All the simulations presented here will be one-dimensional and the focus will be put in the linear regime, although some nonlinear effects will be briefly explored. A more comprehensive study of the nonlinear regime is left for the next chapter.

4.3.1 Impulsive driver

Numerical simulations of waves excited by an impulsive are performed by superimposing an initial perturbation to the background and letting it evolve according to the equations described in Chapter 2. In Section 3.5.1, the initial perturbation corresponded to the fundamental standing mode of the numerical domain. This procedure could be applied to the present investigation. However, another kind of perturbation has been chosen here: a Gaussian profile, which can be expressed as

$$f(x,t=0)=f_0 \exp\left(-\left(\frac{x-x_0}{\sqrt{2}\sigma_x}\right)^2\right), \tag{4.5}$$

where f_0 is the amplitude of the perturbation, x_0 the position of the peak, and σ_x the root-mean-square width, which is related to the FWHM by the formula $FWHM = 2\sqrt{2\ln 2}\sigma_x$. The perturbation is then superimposed on a static medium with a background magnetic field given by $\boldsymbol{B_0}(x) = (B_0, 0, 0)^T$.

Here, not all the regions of the solar atmosphere investigated in the previous section will be studied but only those where neutrals have a larger impact in the dynamics of the plasma. Hence, simulations will be performed with the parameters of regions II and III of Table 4.1.

In the first place, the case of the solar prominence will be explored. The initial perturbation is applied to the y-component of the velocity of every species, with the peak at the position $x = 0$. Thus,

$$V_{s,y}(x,t=0)=V_{y,0} \exp\left(-\left(\frac{x}{\sqrt{2}\sigma_x}\right)^2\right), \tag{4.6}$$

where the amplitude is chosen as $V_{y,0} = 10^{-3} c_{\mathrm{A}}$ to ensure that the simulation stays in the linear regime. The value of σ_x is chosen in a way that $FWHM = 1.5 \times 10^4$ m and the domain of the simulation is $x \in [-l, l]$, with $l = 2 \times 10^5$ m. The results of this simulation are shown in Figure 4.12. On the one hand, it can be seen that protons and hydrogen are strongly coupled and that they behave almost as a single fluid. On the other hand, the coupling with other species is weaker in the case of helium. Thus, the latter fluid reacts with some delay with respect to the protons and hydrogen to the fluctuations in the plasma. the perturbation of the proton-hydrogen fluid is propagating approximately at the modified Alfvén speed, $\widetilde{c}_{\mathrm{A}}$, while the helium is trailing behind at a slightly slower speed. As time advances, the initial perturbation splits into two smaller Gaussian-like functions that propagate in opposite directions. In a case without collisions, the amplitudes of each bulge would be one-half of the original, and they would remain constant during the whole simulation. But here, their amplitudes decrease with time; moreover, the shapes of the perturbations are not symmetric with respect to the position of their peaks, and their FWHMs increase with time. Such a departure from the collisionless behavior is caused by the loss of kinetic energy and the dispersion of the normal modes due to friction.

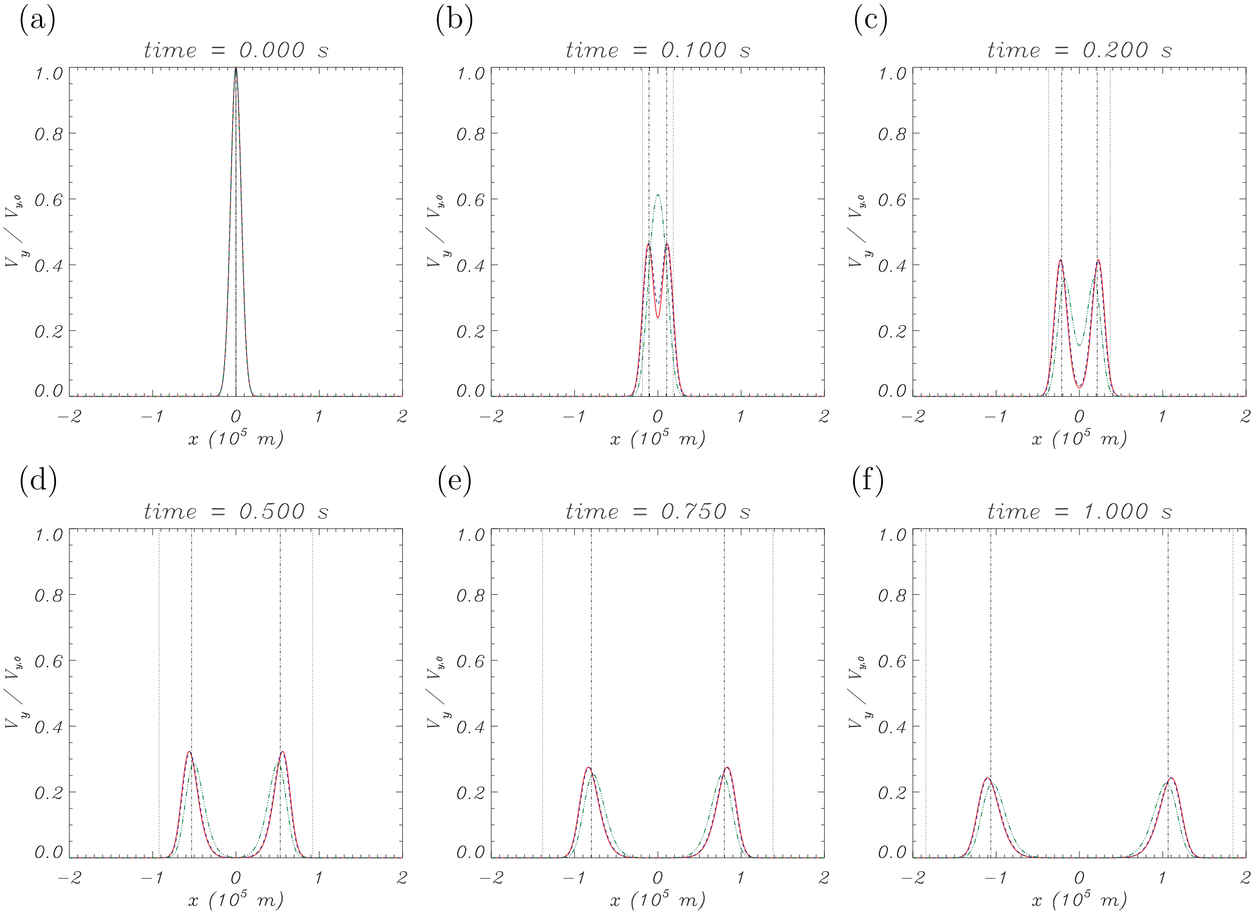

Figure 4.12: Simulation of waves generated by an impulsive driver with a Gaussian profile for prominence conditions. The red solid line corresponds to the protons, the blue dashed line shows the motion of neutral hydrogen and the green dotted-dashed line corresponds to the neutral helium. The dotted vertical line represents the position of points moving at Alfvén speed, while the vertical dotted-dashed line represents a motion at the modified Alfvén speed, $\widetilde{c}_{\mathrm{A}}$. (An animation of this figure is available.)

Next, Figure 4.13 displays the results of a simulation with lower chromospheric conditions. The characteristic length for this simulation is $l = 2.5 \times 10^5$ m. It must be noted that in this environment helium ions are also present. However, their abundances are negligible in comparison with those of protons, neutral hydrogen, and neutral helium. Moreover, they are strongly coupled to protons due to the action of the magnetic field. For those reasons, the motions of singly and doubly ionized are not represented in this plot. The simulation illustrates the high level of coupling that exists between the neutrals and ions in this region of the chromosphere: it can be checked that their perturbations propagate together at the modified Alfvén speed ($\widetilde{c}_{\mathrm{A}} \approx 17$ km s^{-1}), which is much smaller than the classical Alfvén speed ($c_{\mathrm{A}} \approx 7600$ km s^{-1}), due to the density of neutrals being much higher than that of ions. Comparing Figure 4.13 with Figure 4.12, it can be seen that the decrease of the amplitude of the perturbations and the deformations of the Gaussian profiles are smaller in the former. The reason is that in the case of the lower chromosphere the velocity drifts and the friction forces associated with them are smaller than in the prominence.

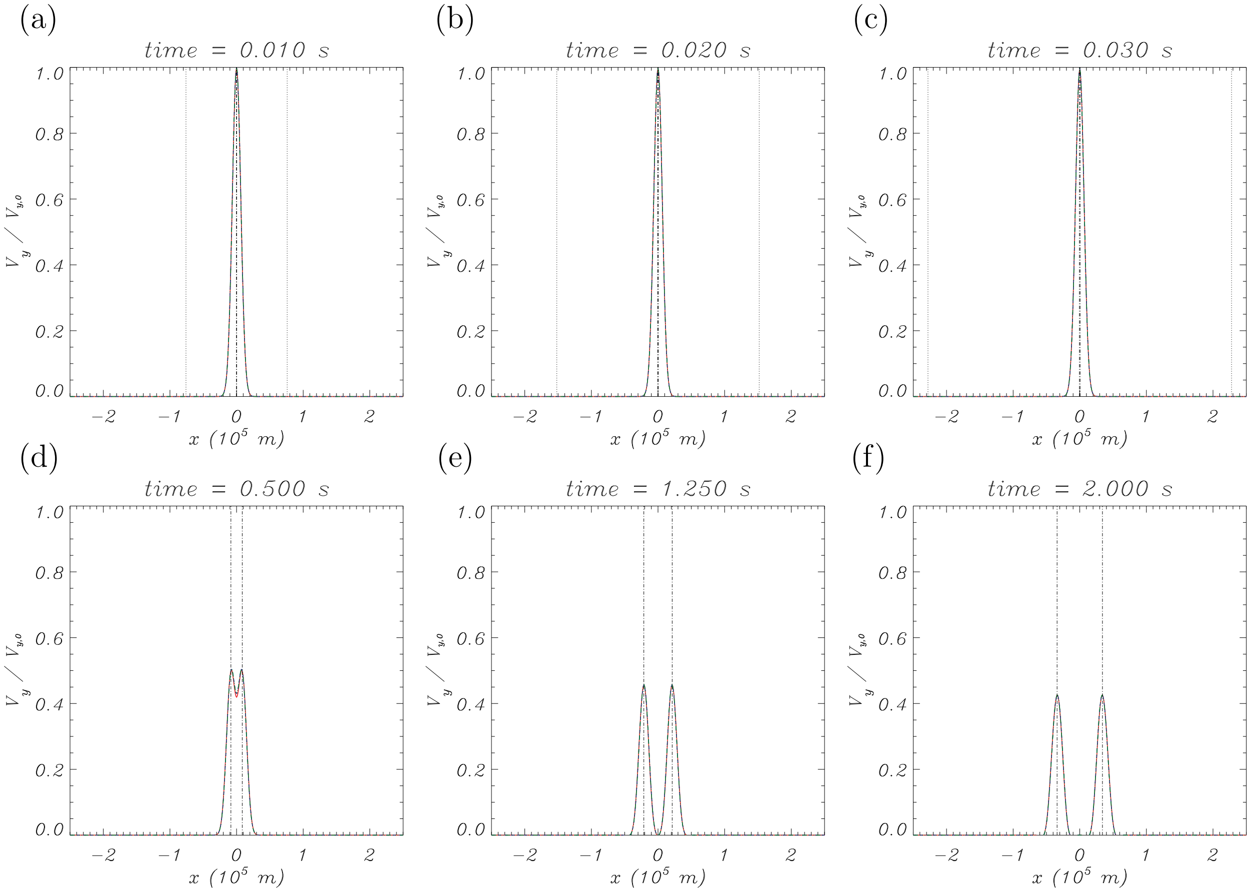

Figure 4.13: Simulation of waves generated by an impulsive driver with a Gaussian profile for conditions of the lower chromosphere. (An animation of this figure is available.)

It is also interesting to study the evolution of the different components of the wave energy density during the simulations. The kinetic, magnetic and internal components of the spatially-averaged energy density are defined as

$$e_K = \frac{1}{2l}\int_{-l}^{l} \frac{1}{2}\sum_s \rho_s(x) V_s(x)^2 \, dx, \tag{4.7}$$

$$e_B = \frac{1}{2l}\int_{-l}^{l} \frac{1}{2}\frac{B_1(x)^2}{\mu_0} \, dx, \tag{4.8}$$

$$e_P = \frac{1}{2l}\int_{-l}^{l} \sum_s \frac{P_{1,s}(x)}{\gamma - 1} \, dx, \tag{4.9}$$

respectively. For the magnetic and the internal energy, only the perturbed values are taken into account. The background values are not included because they are constant and only the fluctuations are of interest here. The behavior of the total energy density and its three

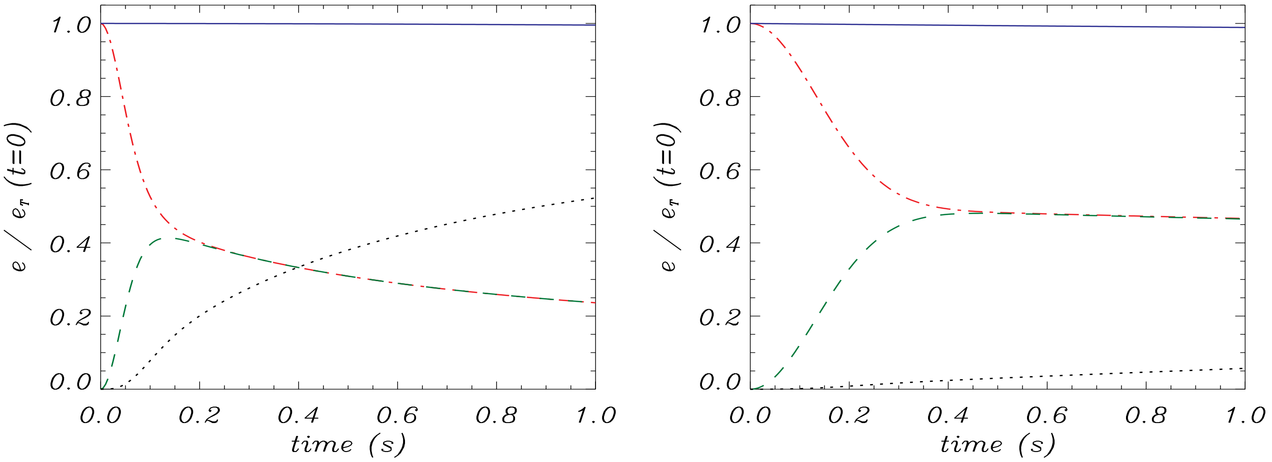

Figure 4.14: Temporal evolution of the total energy density, e_T (blue solid lines), kinetic energy density (red dotted-dashed lines), magnetic energy density (green dashed lines) and internal energy density (black dotted lines). The left and right panels correspond to the simulations shown in Figures (4.12) and (4.13), respectively.

components during the simulations shown in Figures 4.12 and 4.13 is represented in the left and right panels of Figure 4.14. It can be seen that in the initial time all the energy is kinetic, as it would be expected since it corresponds to the initial perturbation. As time evolves, a fraction of the kinetic energy is transformed into magnetic and internal energies. After certain time step, the kinetic and magnetic components have the same magnitude, i.e., there is equipartition of magnetic and kinetic energy. In addition, the relative increase of internal energy is larger for the case of the prominence (left panel) than for the low chromosphere (right). This is another demonstration of the greater friction forces that are present in the prominence in comparison with the lower chromosphere. In the prominence, the species are not as strongly coupled as in the lower chromosphere and thus, there are larger differences in their velocities, which lead to a larger dissipation of energy.

It must be reminded that, according to Equation (2.57), the energy transfer due to elastic collisions is directly proportional to the collision frequencies but it has a quadratic dependence of the velocity drifts. Thus, this heat transfer is a nonlinear effect and since the perturbations studied here are in the linear regime, the increase of internal energy due to the perturbed pressures is negligible compared with the internal energy associated with the total background pressure.

4.3.2 Periodic driver

To simulate waves generated by a periodic driver, the same procedure as in Section 3.5.2 will be used here: a periodic function of time will be imposed at a certain point of the numerical domain. As it has already been shown, depending on the chosen driver, it may be possible to excite both the L and R modes or only one of them. Here, the focus will be put on the L modes only. There are two reasons to do so. First, the study of the fully ionized case performed in the previous chapter and the analysis of the dispersion relations for partially ionized plasmas in the present chapter have shown that the properties of the two modes are almost identical at frequencies much lower than the Hall frequency. Hence, it is not necessary to study both of them and display twice the same results. The second reason is that the L modes are the ones that present resonances (when collisions are not taken into account) in the range of frequencies explored in this investigation.

Figure 4.15 shows the results of several simulations of waves excited by a periodic driver using the physical conditions that correspond to region I of Table 4.1, i.e., the high chromosphere. The driver, applied to the point $x = 0$, is given by

$$\boldsymbol{V_{s,+}}(x=0,t) = \begin{pmatrix} 0 \\ V_0 \cos(\omega t) \\ -V_0 \sin(\omega t) \end{pmatrix} \tag{4.10}$$

and

$$\boldsymbol{B_{1,+}}(x=0,t) = \begin{pmatrix} 0 \\ B_{1,0} \cos(\omega t) \\ -B_{1,0} \sin(\omega t) \end{pmatrix}, \tag{4.11}$$

which produces the excitation of the L mode. The amplitude of the magnetic perturbation is given by $B_{1,0} = -|\boldsymbol{B_0}|V_0/c_{\mathrm{A}}$, which corresponds to the relation that exists between those two variables when Alfvén waves are considered. To ensure that the simulations stay in the linear regime and that non-linear effects can be neglected, the amplitude of the driver is chosen as $V_0 = 10^{-3}c_{\mathrm{A}}$.

Figure 4.15 shows that at a driving frequency of $\omega = 10^{-4}\Omega_p$, there is a strong coupling between all the species and the perturbations travels at the speed $\widetilde{c}_{\mathrm{A}}$. In addition, the damping of the wave is in good agreement with that predicted by the dispersion relation, which is represented by the black dotted lines. When the frequency of the driver is increased, it can be found that the species begin to uncouple from each other. This behavior can be noticed in Figure 4.15(b), where the first species to decouple from the others is neutral helium. The reason is that the driving frequency, $\omega = 10^{-3}\Omega_p \approx 210$ rad s^{-1}, is larger than the collision frequencies of helium, which are, for instance, $\nu_{p\mathrm{He}} \approx 2.5$ Hz, $\nu_{\mathrm{He}p} \approx 43$ Hz, or $\nu_{\mathrm{HHe}} \approx 3.5$ Hz, but is of the order of or smaller than the collision frequencies of the other species, e.g., $\nu_{p\mathrm{H}} \approx 120$ Hz or $\nu_{\mathrm{H}p} \approx 1400$ Hz. Thus, during one period of the oscillation, neutral helium particles do not collide frequently enough with the other species for the neutral helium fluid to completely follow the magnetic field oscillations.

If the driving frequency is increased up to $\omega = 10^{-2}\Omega_p$, the hydrogen fluid starts to exhibit a similar behavior as the one explained for helium, as can be checked in Figure 4.15(c). Now, the interaction of neutral helium with the other species is even weaker than before and the amplitude of its oscillation is greatly reduced. Finally, Figure 4.15(d) shows that at frequencies of the order of $\omega = 0.1\Omega_p \approx 21000$ rad s^{-1}, even the ionized species begin to uncouple from each other, due to the fact that ω is in this case larger than $\nu_{p\mathrm{He\ II}}$, $\nu_{\mathrm{He\ II}p}$, $\nu_{p\mathrm{He\ III}}$, or $\nu_{\mathrm{He\ III}p}$. At these frequencies, there is almost no interaction with the neutral species, and at even higher frequencies, the perturbation behaves as if the medium were fully ionized, ignoring the presence of neutrals. Hence, there is almost no propagation of the perturbation in the neutral fluids at the high-frequency range.

To conclude this section, the case of a plasma with parameters corresponding to the lower

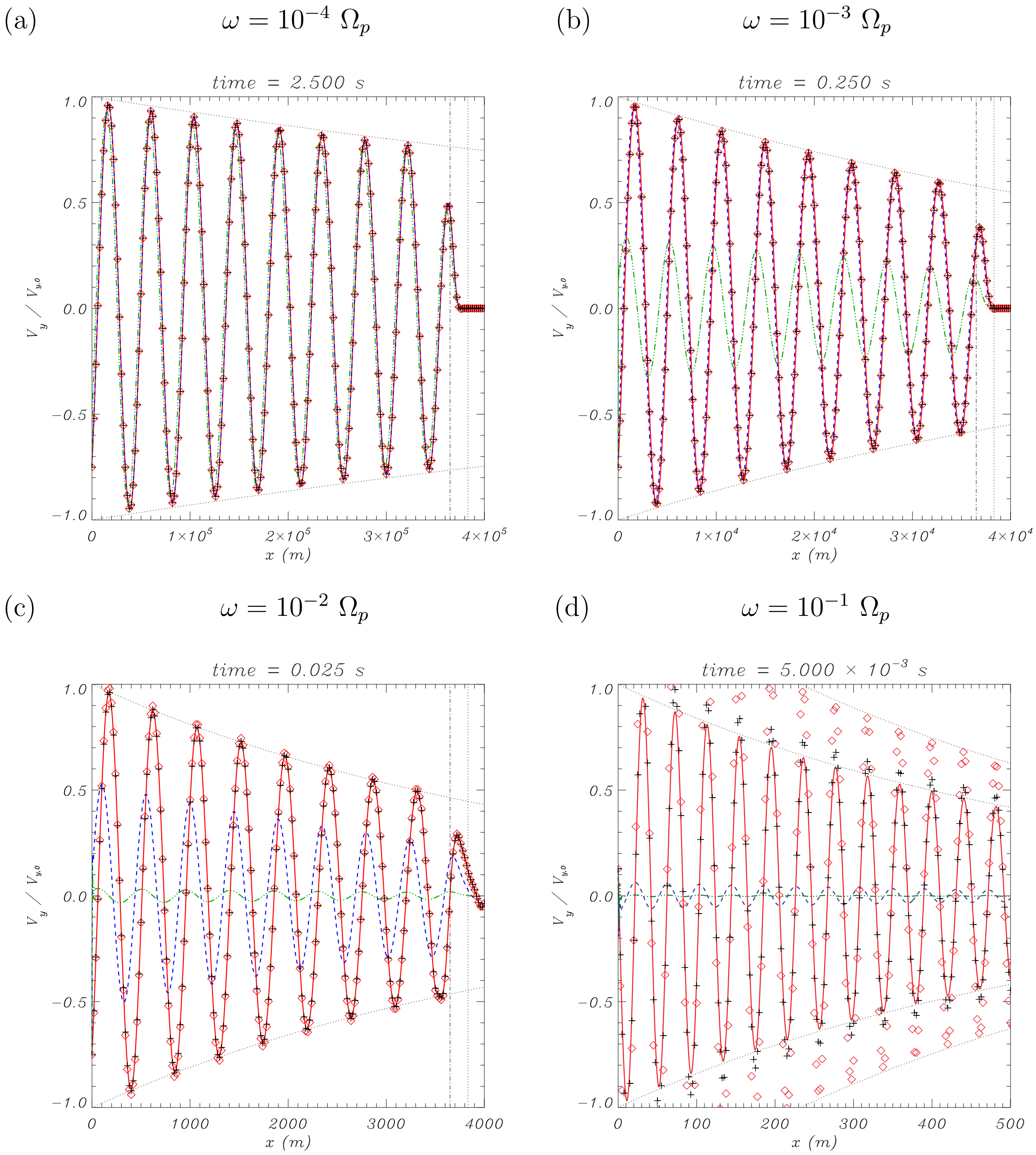

Figure 4.15: Simulations of waves generated by a periodic driver with different frequencies in a region of the solar chromosphere at a height of 2016 km over the photosphere. The red solid, blue dashed and green dotted-dashed lines represent the y-component of the velocity of protons, neutral hydrogen and neutral helium, respectively. The red diamonds and the black crosses represent the singly and the doubly ionized helium, respectively. The vertical dotted and dotted-dashed lines represent the position of points moving at the Alfvén and the modified Alfvén speeds, respectively. The remaining black dotted lines show the damping computed from the dispersion relation. (Animations of each panel of this figure are available: (a), (b), (c) and (d)).

chromosphere will be analyzed. Figure 4.16 represents a simulation with a driver given by

$$\boldsymbol{V_s}(x=0,t) = \begin{pmatrix} 0 \\ V_0 \cos(\omega t) \\ -V_0 \sin(\omega t) \end{pmatrix}, \tag{4.12}$$

and a frequency of $\omega = 10^{-3}\Omega_p$. Although this value is much lower than the cyclotron frequencies, it is also much larger than the Hall frequency, $\omega_{\mathrm{H}} \approx 5 \times 10^{-6}\Omega_p$. Hence, according to the results displayed in Figure 4.10, it is expected that the perturbation is strongly overdamped. We have used 2001 points to cover the domain $x \in [0,2]$ km, but only the section $x \in [0,0.5]$ km is shown in the plot. Although the relevant physical behavior occurs in the displayed section, the larger domain is used to avoid possible unwanted numerical effects caused by the rightmost boundary.

It can be seen that there is a weak coupling between the motion of ions and neutrals. Neutrals stay almost at rest, except close to $x = 0$, while the driver causes motion in the ions that is spatially overdamped. While the amplitude oscillates with time according to the driver imposed, an oscillatory behavior in space cannot be found, with the exception of the small oscillation present in the left area. However, it has been checked that the extension and amplitude of this oscillation depends on the spatial resolution resolution used in the simulation. Thus, it is not a real physical behavior but it is a numerical artifact. Finally, as in the previous cases, it can be seen that the damping of the perturbation agrees with the prediction from the dispersion relation analyzed in Section 4.2.2.

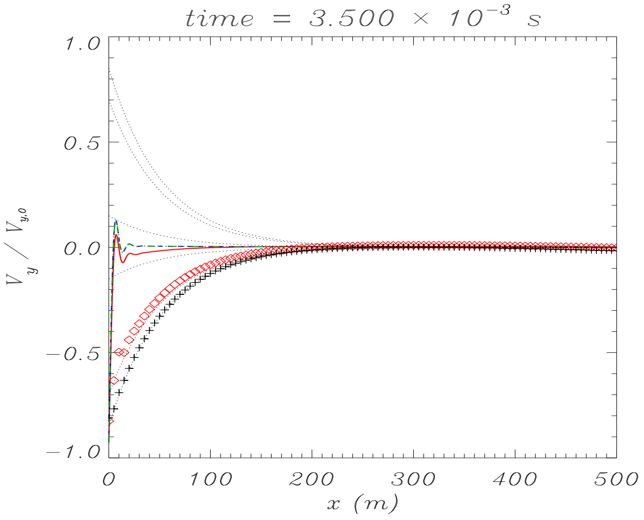

Figure 4.16: Simulation of waves generated by a periodic driver with frequency $\omega = 10^{-3}\ \Omega_p$ in a region of the solar chromosphere at a height of 500 km over the photosphere. The meaning of the colors and styles of the lines is the same as in Figure 4.15. (An animation of this figure is available.)

4.4 Discussion

In this chapter, the multi-fluid model presented in Chapter 2 has been applied to the investigation of partially ionized plasmas of the solar atmosphere. Three specific regions have been studied: the high chromosphere at a height of 2016 km over the photosphere (where $\chi < 1$), a typical cool prominence (with $\chi \approx 1$), and the lower chromosphere at 500 km over the photosphere (a weakly ionized plasma with $\chi \gg 1$). The investigation and comparison of environments with such different degrees of ionization lead to a better understanding of the influence of neutral species on the propagation of small-amplitude perturbations. In addition, the effect of Ohm's diffusion (or magnetic resistivity) has been taken into account thanks to a more complete version of the generalized Ohm's law. This improvement has allowed to check that resistivity has a negligible influence on the properties of low-frequency waves, but that it becomes an important effect when the frequency is increased, leading to a remarkable rise of the damping of the R modes.

It has been found that the inclusion of neutral components in the plasma modifies the oscillation period of the low-frequency waves and produces a damping on the perturbations, as previously demonstrated by the works of Piddington [1956], Haerendel [1992], Forteza et al. [2007], Soler et al. [2009a, 2012a] or Zaqarashvili et al. [2011a,b]. Then, in good agreement with Soler et al. [2015a], it has been shown that in weakly ionized plasmas there are no strict cutoffs for Alfvén waves generated by an impulsive driver, but that there may be intervals of wavenumbers where the perturbations are overdamped.

The exploration of a wide range of frequencies and kinds of collisions between the species has allowed to check that the damping of Alfvén waves is dominated by collisions with neutrals, while the damping of the higher-frequency L and R modes is dominated by collisions with ions and electrons. Such behavior is explained by the fact that the damping is more efficient when the collision frequency is of the order of the oscillation frequency (Zaqarashvili et al. [2011a], Soler et al. [2013b]) and that collisions with neutrals have lower frequencies than those between charged species.

As in the case of fully ionized plasmas, it has been shown that the properties of the L modes clearly diverge from those of the R modes at high enough frequencies due to the effect of Hall's current. For instance, the quality factors of the R modes are larger than those of the L modes. In fully ionized plasmas, this separation occurs at oscillation frequencies of the order of the lower cyclotron frequency. However, in the case of weakly ionized plasmas with ion-neutral collision frequencies comparable or larger than the cyclotron frequencies, the effective gyrofrequency of ions is greatly reduced (Pandey and Wardle [2008]) and Hall's current greatly affects the dynamics of the plasma even at frequencies of the order of the Hall frequency, ω_{H}, which is much smaller than Ω_i. Here, it has been found that for the the studied region of the lower chromosphere, Hall's current plays a very important role in the propagation of waves even for frequencies as low as 20 rad s^{-1}, approximately. Moreover, it has been shown that in partially ionized plasmas, due to the friction caused by ion-neutral collisions, there are no resonances or cutoffs associated to the cyclotron frequencies, in contrast with the case of collisionless fully ionized plasmas (see, e.g., Rahbarnia et al. [2010]). Hence, waves can propagate at any frequency, although they are heavily damped at frequencies higher than ω_{H}.

The simulations of waves excited by an impulsive driver have shown that, with the physical conditions considered for a solar prominence and for a region in the lower chromosphere, there is a strong coupling between all the species that compose the plasma. Therefore, the perturbations generated by an initial Gaussian profile propagate approximately at the modified Alfvén speed, $\widetilde{c}_{\rm A}$, which in the case of the lower chromosphere is two orders of magnitude smaller than the classic Alfvén speed. This behavior agrees with the results obtained from the analysis of the dispersion relation. The simulations also reflect that the friction force caused by collisions dissipates a fraction of the kinetic energy of the initial perturbation and transforms it into internal energy, which implies an increment of the temperature of the plasma. However, this heating is a nonlinear effect and, due to the small amplitude of the perturbations investigated in this chapter, the temperature rise obtained is negligible compared to the background value. The study of the heating caused by large-amplitude perturbations will be performed in the next chapter.

Finally, the simulations of waves generated by a periodic driver have shown that as the frequency of the driver in increased, the different species begin to decouple. Neutral species only remain strongly coupled to the ions at low frequencies. In the high-frequency limit, the plasma behaves almost as if it were composed of the ionized species only, with minimal influence from the neutral components. In addition, it has been checked the prediction from the dispersion relation that, in the weakly ionized environment of the lower solar chromosphere, the L mode is strongly overdamped if $\omega > \omega_{\rm H}$: the kinetic energy of the perturbation is completely dissipated in a few hundreds of meters.

Chapter 5

Nonlinear perturbations

5.1 Introduction

The previous chapters have focused on the study of small-amplitude Alfvénic waves in the solar atmosphere. However, as already commented in the introduction of this Thesis, large-amplitude perturbations, whose velocity amplitudes are not negligible in comparison with the Alfvén speed, have also been detected. In the present chapter, the study of the effects of the collisional interactions between the different species in multi-component plasmas is extended by incorporating the nonlinear effects that arise when large-amplitude perturbations are considered.

The study of nonlinear waves is more complex than that of their linear counterpart and it is typically performed by means of numerical simulations [see, e,g., Murawski and Roberts, 1993, Oliver et al., 1998]. Some more recent numerical results can be found in Matsumoto and Shibata [2010], who studied Alfvén waves driven by photospheric motions, Suzuki [2011], who investigated solar and stellar winds driven by Alfvén waves, or Karpen et al. [2017], whose results suggest that coronal-hole jets are a possible origin for nonlinear Alfvén waves in the interplanetary medium.

Nevertheless, analytical results can also be obtained if certain approximations are taken. A common analytical procedure is to assume a perturbative expansion, where the variables that describe the properties of the plasma are expressed as a sum of a background value plus a series of terms that represent the linear and higher-order perturbations. The series is truncated at some given order and systems of equations are derived for the chosen perturbations, while higher-order effects are neglected. This procedure was followed, e.g., by Hollweg [1971], who studied second-order effects of Alfvén waves, or by Rankin et al. [1994], Tikhonchuk et al. [1995] and Verwichte et al. [1999], who examined the properties of up to third-order perturbations. Those works have shown that nonlinear Alfvén waves induce a ponderomotive force that causes variations in the density and pressure of the plasma, in contrast with the incompressibility of linear Alfvén waves. In addition, third-order effects also produce a steepening of the wave and the generation of higher harmonics.

Other examples of works in the field of nonlinear MHD waves are listed next. For instance, Roberts et al. [1983] investigated their influence on the generation of short period radio pulsations from the solar corona, Ofman and Davila [1995] studied the nonlinear evolution of resonant absorption of Alfvén waves, and Boynton and Torkelsson [1996] examined the effect of gravitational stratification. Moreover, nonlinear magnetoacoustic waves were analyzed by, e.g., Murawski et al. [2001] and Vranjes and Pandey [2013]. Terradas and Ofman [2004] studied the density enhancements by MHD waves in coronal loops, Terradas et al. [2008a] analyzed nonlinear kink oscillations in magnetic flux tubes and the properties of Alfvén-cyclotron waves in multi-ion plasmas were investigated by Marsch and Verscharen [2011].

In most of the works mentioned in the previous paragraphs the plasma is considered to be fully ionized and treated as a single-fluid. The assumption of fully ionization is valid for the solar corona and the solar wind, where the presence of neutral particles is negligible. However, it is not applicable to other regions of the solar atmosphere, such as the chromosphere, or to structures like prominences, in which neutrals are the dominant component of the plasma and have a dramatic effect on the properties of MHD waves (see, e.g., Piddington [1956], Watanabe [1961b], Haerendel [1992], Soler et al. [2013a]). In addition, as shown in Chapters 3 and 4, the use of single-fluid models is only appropriate when the phenomena of interest is associated with low frequencies, i.e., much lower than the ion cyclotron frequencies in fully ionized plasmas or the ion-neutral collisions frequencies in partially ionized plasmas. Conversely, at higher frequencies, multi-fluid approaches are required due to the fact that the components of the plasma are not strongly coupled and they react to perturbations in different timescales.

In the present chapter, the multi-fluid model described in Chapter 2 is applied to the investigation of nonlinear waves in partially ionized plasmas, paying special attention to the heating due to ion-neutral collisions. The issue of heating is of great interest for the solar atmosphere (see, e.g., Goodman [2011], Parnell and De Moortel [2012], Song and Vasyliūnas [2011], Khomenko and Collados [2012], Tu and Song [2013], Gilbert [2015], Heinzel [2015], Arber et al. [2016], Soler et al. [2016]). It has been shown that Alfvénic waves can transport a huge amount of energy from the photosphere to higher layers of the solar atmosphere (Tomczyk et al. [2007], McIntosh et al. [2011], Srivastava et al. [2017]). However, it remains unclear whether all the energy carried by the waves is deposited in the plasma. A dissipative mechanism is required to transform that energy into heat and, in the case of partially ionized plasma, the ion-neutral collisional interaction is one of the possible mechanisms. The topic of heating by means of ion-neutral collisions was briefly examined in Chapter 4 when small-amplitude perturbations were studied. However, since heating is a nonlinear effect with a quadratic dependence on the velocity drifts, as shown by Equation (2.57), it is expected to have a more relevant role when large-amplitude waves are considered.

This chapter is organized as follows. In Section 5.2, the effect of partial ionization on nonlinear standing waves is investigated: numerical simulations are performed for the case of a plasma with prominence conditions, and analytical results are derived for the case of a two-fluid plasma. In Section 5.3, large-amplitude impulsive perturbations are considered and the heating due to ion-neutral collisions is examined. Finally, Section 5.4 summarizes the results.

5.2 Nonlinear standing waves

In this section, nonlinear standing waves in a uniform and static partially ionized plasma are analyzed. The temporal evolution is governed by the equations detailed in Section 2.2. Due to the complexity of the equations, 1.5D numerical simulations with the MolMHD code are performed.

Figure 5.1 shows the results of a simulation in a plasma with conditions that correspond to a quiescent prominence core at an altitude of 10,000 km over the photosphere and with gas pressure of $P_g = 0.005$ Pa, according to Heinzel et al. [2015]. The physical parameters used in this simulation are given in Tables 4.1 and 4.2. A uniform background magnetic field, $\boldsymbol{B_0}$, along the x-direction is considered. A typical value of the magnetic field strength in quiescent prominences is $B_0 = 10$ G. The fundamental standing mode of the transverse Alfvén waves is excited by applying the initial perturbation

$$V_{s,y}(x, t = 0) = V_{y,0} \cos(k_x x) \tag{5.1}$$

to every species s of the plasma, where $V_{s,y}$ is the y-component of the velocity and k_x is the longitudinal wavenumber. No initial perturbation is applied to the other variables. The domain of the simulation is $x \in [-l, l]$, with $l = 2.5 \times 10^5$ m. For the fundamental mode, the wavenumber is $k_x = \pi/(2l)$ and the boundary conditions impose that the three components of the velocity are equal to zero at $x = \pm l$. The amplitude of the perturbation is given by $V_{y,0} = 2.5 \times 10^{-2} c_{\mathrm{A}}$, where $c_{\mathrm{A}} = |\boldsymbol{B_0}|/\sqrt{\mu_0 \rho_p}$ is the Alfvén speed, with μ_0 the vacuum magnetic permeability. Note that the present definition of Alfvén speed only takes into account the density of ions. For the parameters given above, the Alfvén speed is $c_{\mathrm{A}} \approx 184$ km s^{-1}. The wavenumber of the perturbation is given by $k_x = \pi/(5 \times 10^5)$ m^{-1}.

The top row of Figure 5.1 shows several time steps of the evolution of the perturbation, which is perpendicular to the background magnetic field. Initially, the three species of the plasma have the same velocity but, since the coupling between them is not perfect, some small velocity drifts appear when the Alfvén wave starts its oscillation. As time advances, the collisional friction causes the damping of the wave, as is better illustrated by the top left panel of Figure 5.2. This is the same behavior as the one already explained in Chapter 4 for small-amplitude waves. Nevertheless, due to the much larger amplitude of the perturbation used in the present investigation, the nonlinearities are not negligible and, in contrast, perturbations along the direction of the background magnetic field are also excited. Thus, the second row of Figure 5.1 displays the x-component of the velocity, normalized with respect to the amplitude of the driver, $V_{y,0}$, at various time steps. Apart from the smaller amplitude of V_x in comparison with V_y, the main difference is that its wavenumber is twice the wavenumber of the initial perturbation and there is a spatial phase shift: while V_y is proportional to $\cos(k_x x)$, V_x is proportional to $\sin(2k_x x)$. Furthermore, the right top panel of Figure 5.2 shows that the oscillation in V_x does not attenuate as fast as the oscillation in V_y.

The third and bottom rows of Figure 5.1 show the relative variation of density, defined as the ratio between the perturbation in density and its background value, i.e., $\Delta\rho/\rho_0$, with $\Delta\rho \equiv \rho(x,t) - \rho_0$, and the ratio between the perturbation of temperature and the initial temperature, $\Delta T/T_0$, with $\Delta T \equiv T(x,t) - T_0$, respectively. These two variables are proportional to $\cos(2k_x x)$. The relative variation of density shows that matter accumulates at the center of the domain and is displaced from the ends during the first steps of the simulation but later this process is inverted and a oscillation appears. The amplitude of this variation of density is around 2% of the initial background value. Finally, the bottom panels show that the mean temperature of the plasma rises as time advances. The main reason for this increment is the dissipation of the kinetic energy of the initial perturbation which is transformed into heat by means of ion-neutral collisions.

More details of the simulation can be analyzed by inspecting Figure 5.2, where the temporal evolution of the same variables displayed in Figure 5.1 at selected representative points of the

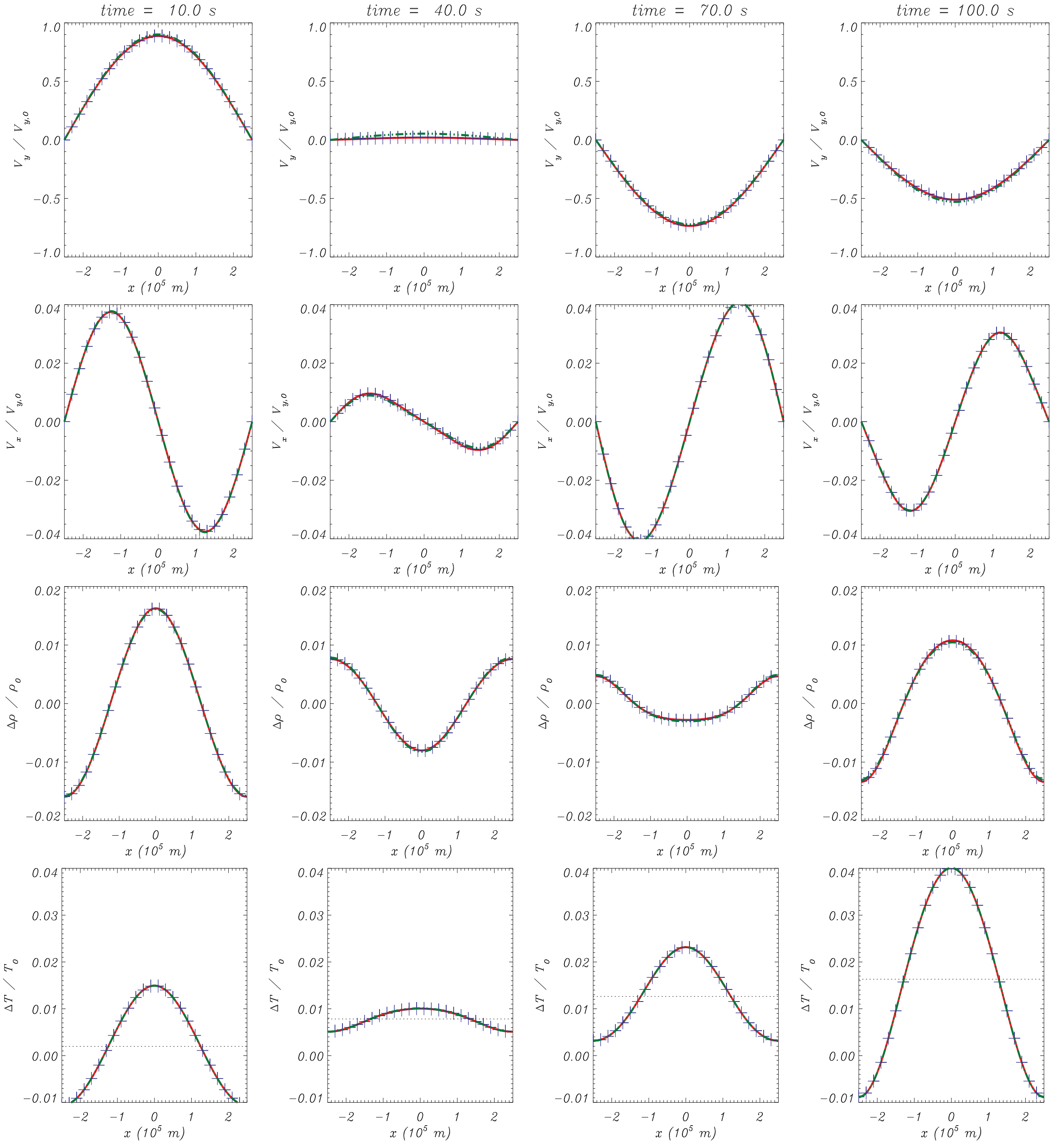

Figure 5.1: Results of a simulation of the fundamental standing mode of the Alfvén waves of initial amplitude $V_{y,0} = 2.5 \times 10^{-2} c_{\mathrm{A}}$ with $k_x = \pi/(5 \times 10^5)$ m^{-1} in a medium with $n_p = 1.4 \times 10^{16}$ m^{-3}, $n_{\mathrm{H}} = 2 \times 10^{16}$ m^{-3} and $n_{\mathrm{He}} = 2 \times 10^{15}$ m^{-3}. The magnetic field is $B_0 = B_x = 10$ G and the initial temperature is $T_0 = 10^4$ K. From top to bottom: normalized y- and x-components of the velocity, relative variation of density and relative variation of temperature. The red solid lines, blue crosses and dotted-dashed green lines represent protons, neutral hydrogen and neutral helium, respectively. The horizontal dotted line in the bottom panels represents the spatially-averaged value of $\Delta T/T_0$. (An animation of this figure is available.)

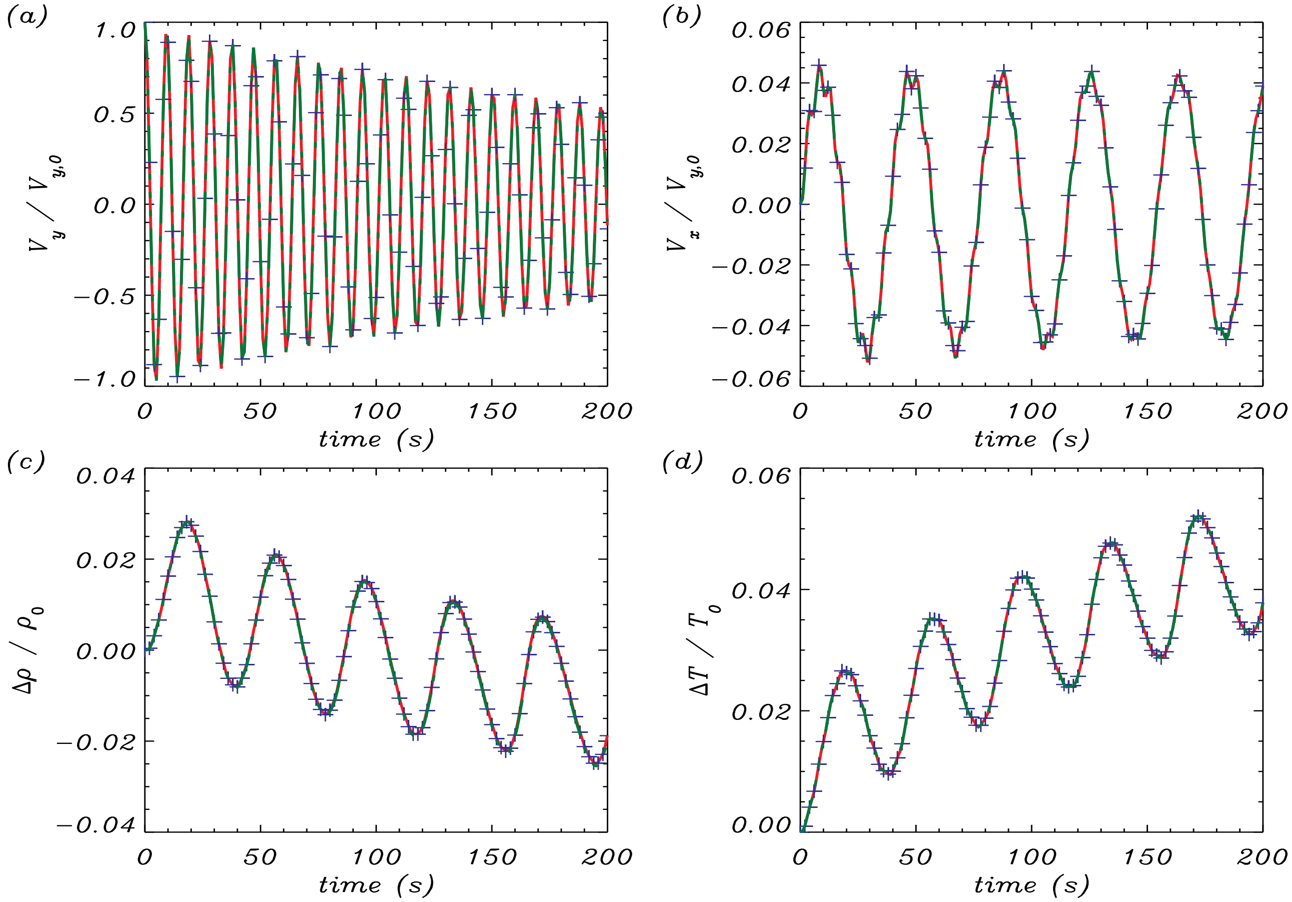

Figure 5.2: Temporal evolution of V_y at $x = 0$ (top left), V_x at $x = -l/2$ (top right), the relative variation of density at $x = 0$ (bottom left) and $\Delta T / T_0$ at $x = 0$ (bottom right) from the simulation shown in Figure 5.1.

domain is plotted. The representative point for V_x is different from the position chosen for the rest of variables because $x = 0$ is a node for this component of the velocity. Hence, a better location to analyze V_x is $x = -l/2$.

By fitting the oscillation displayed in Figure 5.2(a) with an exponentially decaying sinusoidal of frequency ω, we find that $\omega \approx 0.67$ rad s^{-1} (which corresponds to a period of 9.4 s). This frequency agrees well with the result obtained by solving the dispersion relation derived in Chapter 3 for linear perturbations, namely Equation (3.12). If the collision frequencies between the different fluids is compared with the oscillation frequency divided by 2π (rigorously speaking, the collision and the oscillation frequencies cannot be compared directly because they are expressed in different units), it is found that $\omega/(2\pi) < \nu_{st}$. This fact explains why the three species oscillate with almost the same velocity but there is still some damping due to friction.

The top right panel of Figure 5.2 shows a wave in the x-component of the velocity that seems to be composed of at least two different oscillation modes. The motion in this direction is dominated by a mode that oscillates with a frequency much lower than the frequency of the oscillation of the V_y component and is weakly damped. The analysis of the oscillation reveals that the frequencies of those two modes are $\omega_1 \approx 0.16$ rad s^{-1} and $\omega_2 \approx 1.34$ rad s^{-1}. We show later that these frequencies are related to the weighted mean sound speed of the whole fluid and the Alfvén speed (modified by the inclusion of the density of neutrals), respectively.

Panel (c) of Figure 5.2 shows the temporal evolution of $\Delta\rho/\rho_0$ at $x = 0$. It can be seen that at the central point of the simulation domain the density rises during the initial seconds, it reaches a maximum and then the fluctuation can be described as the composition of an oscillation and a linear decrease with time. It can be checked that the frequency of the oscillation coincides with that of the dominant mode of the wave in V_x and that there is a slight temporal phase shift between $\Delta\rho/\rho_0$ and V_x. Finally, panel (d) shows a growing trend of the temperature at $x = 0$, combined with an oscillation similar to that found in the density. This increase of temperature is a consequence of the friction due to ion-neutral collisions. A fraction of the energy of the Alfvén wave is transformed into heat and, thus, the internal energy of the plasma grows.

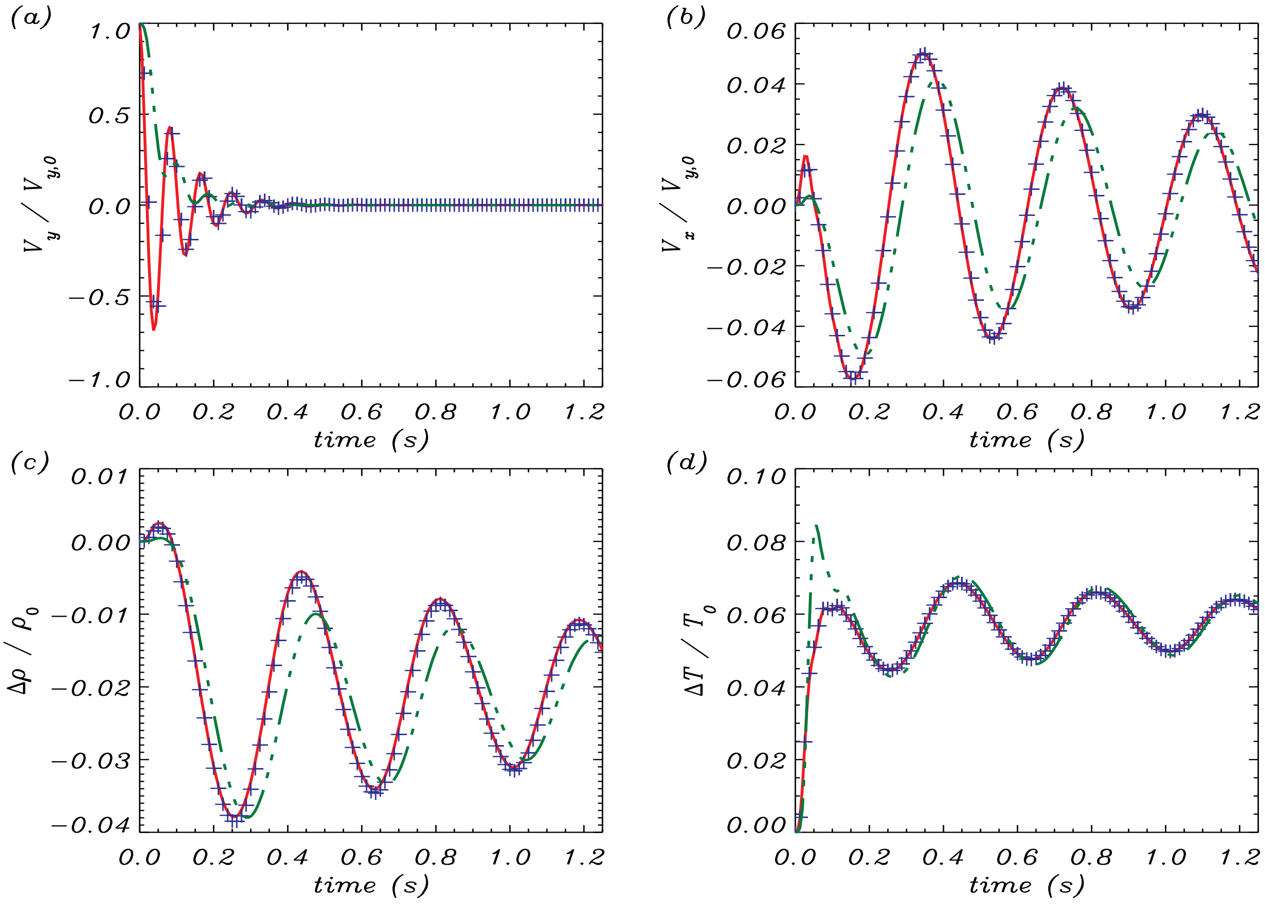

Figure 5.3: Same as Figure 5.2 but for $k_x = \pi/(5 \times 10^3)$ m.

The previous results have been obtained for a case with a strong coupling between the three fluids of the plasma. It is interesting to repeat the simulations but when the interaction between fluids is weaker. This can be achieved by considering a wave with $\omega/(2\pi) > \nu_{p\mathrm{He}}$. To that goal, we perform a simulation with a larger wavenumber, $k_x = \pi/(5 \times 10^3)$ m^{-1}. The dispersion relation predicts a frequency $\omega \approx 75.14$ rad s^{-1} for the Alfvén wave, which is higher than $2\pi\nu_{p\mathrm{He}}$ and $2\pi\nu_{\mathrm{HHe}}$, but lower than $2\pi\nu_{p\mathrm{H}}$. The results of this simulation are displayed in Figure 5.3. Remarkable differences with respect to the previous case can be found. Now, the ratio between the damping rate and the oscillation frequency is much larger than in Figure 5.2 and the Alfvén wave dissipates after few periods. Moreover, neutral helium is found to be decoupled from the other species. In contrast with the previous case, panel (b) shows that the wave in the x-component of velocity is more attenuated with time and, in addition, only one oscillation mode can be clearly noticed instead of the two modes present in the first simulation. Some hints of the second mode may be found during the first instants of the motion but it disappears fast. Again, it is evident that neutral helium is not as strongly coupled to protons and neutral hydrogen as before. The decoupling of neutral helium from the rest of species is a purely multi-fluid effect.

Figure 5.3(c) shows that the density only increases at the center of the domain during a very short time. Then, the relative variation of density becomes negative and oscillates about $\Delta\rho/\rho_0 \approx -0.02$. Hence, the net result of this nonlinear effect is that matter is displaced from the central part of the domain and directed towards the ends. This behavior may be related to the increase of the fluid pressure which is associated with the initial fast grow of temperature shown in panel (d). The quick rise of temperature and pressure is caused by the fast dissipation of the Alfvén wave due the collisional friction. This issue is addressed with more detail later. It is also remarkable that during the first steps of the simulation, neutral helium reaches a larger temperature than the other two fluids and then tends to a thermal equilibrium with them. This is all caused by collisions, which tend to equalize the temperatures of all species in a timescale of the order of the collision frequency.

To gain a better understanding of the nonlinear effects presented up to this point, it would be useful to derive some analytical expressions from the multi-fluid equations. However, a three-fluid system is quite complex for this goal and it would be difficult to extract some clear conclusions. A simpler scenario that can be investigated analytically is the case of partially ionized plasmas composed of only two distinct fluids. Such analysis is described in the following section.

5.2.1 Nonlinear waves in a partially ionized two-fluid plasma

Here, a partially ionized two-fluid plasma is considered as a simpler, toy model that can help us to understand the numerical results given in the previous section. One of the fluids is composed of ions and electrons, and the other one is composed of neutrals. For the sake of simplicity, Hall's term and Ohm's diffusion are neglected from the induction equation. Therefore, the equations that describe the dynamics of this plasma are a simplified version of those used in the previous simulations, namely

$$\frac{\partial \rho_i}{\partial t} + \nabla \cdot \left(\rho_i \boldsymbol{V_i}\right) = 0, \tag{5.2}$$

$$\frac{\partial \rho_n}{\partial t} + \nabla \cdot \left(\rho_n \boldsymbol{V_n}\right) = 0, \tag{5.3}$$

$$\frac{\partial \left(\rho_i \boldsymbol{V_i}\right)}{\partial t} + \nabla \cdot \left(\rho_i \boldsymbol{V_i} \boldsymbol{V_i}\right) = -\nabla P_{ie} + \frac{\nabla \times \boldsymbol{B}}{\mu_0} \times \boldsymbol{B} + \alpha_{in}\left(\boldsymbol{V_n} - \boldsymbol{V_i}\right), \tag{5.4}$$

$$\frac{\partial \left(\rho_n \boldsymbol{V_n}\right)}{\partial t} + \nabla \cdot \left(\rho_n \boldsymbol{V_n} \boldsymbol{V_n}\right) = -\nabla P_n + \alpha_{in}\left(\boldsymbol{V_i} - \boldsymbol{V_n}\right) \tag{5.5}$$

and

$$\frac{\partial \boldsymbol{B}}{\partial t} = \nabla \times \left(\boldsymbol{V_i} \times \boldsymbol{B}\right), \tag{5.6}$$

where P_n is the pressure of neutrals, P_{ie} is the sum of the pressures of ions and electrons and α_{in} is the ion-neutral friction coefficient.

To study the properties of non-linear perturbations, a perturbative expansion is performed. Thus, each variable, $\boldsymbol{f}$, in the previous system of equations is rewritten as follows:

$$\boldsymbol{f} = \boldsymbol{f}^{(0)} + \epsilon \boldsymbol{f}^{(1)} + \epsilon^2 \boldsymbol{f}^{(2)} + \ldots, \tag{5.7}$$

where ϵ is a dimensionless parameter proportional to the velocity amplitude of Alfvén waves, the superscript "(0)" refers to the background values and the superscripts "(1)" and "(2)" correspond to the first-order and second-order perturbations, respectively. Since a static uniform background is considered, $\boldsymbol{V_i}^{(0)} = \boldsymbol{V_n}^{(0)} = 0$ and the remaining background values are constant.

Then, the terms in Equations (5.2)-(5.6) can be gathered according to their powers of ϵ, and separated systems of equations can be obtained for each order of the perturbative expansion.

If the initial perturbations are chosen to be transverse to the direction of the background magnetic field (assumed here to be in the x-direction) and let to propagate along that same direction, the first-order (or linear) system leads to the equation for Alfvén waves,

$$\left[\frac{\partial^3}{\partial t^3} + (1+\chi)\,\nu_{ni}\frac{\partial^2}{\partial t^2} - c_{\mathrm{A}}^2\frac{\partial}{\partial t}\frac{\partial^2}{\partial x^2} - c_{\mathrm{A}}^2\nu_{ni}\frac{\partial^2}{\partial x^2}\right]\boldsymbol{V}_{\boldsymbol{i},\perp}^{(1)} = 0, \tag{5.8}$$

where $\chi = \rho_n/\rho_i$ is the ionization ratio, $\nu_{ni} = \alpha_{in}/\rho_n$ is the neutral-ion collision frequency, and $\boldsymbol{V}_{\boldsymbol{i},\perp}^{(1)} \equiv V_{i,y}^{(1)}\hat{\boldsymbol{\jmath}} + V_{i,z}^{(1)}\hat{\boldsymbol{k}}$ is the perturbation of the velocity of ions in the perpendicular direction. After solving this equation, the first-order perturbation of magnetic field can be found through the equation

$$\frac{\partial \boldsymbol{B}_{\perp}^{(1)}}{\partial t} = B_0 \frac{\partial \boldsymbol{V}_{\boldsymbol{i},\perp}^{(1)}}{\partial x}, \tag{5.9}$$

where $B_0 \equiv B_x^{(0)}$ is the background magnetic field and $\boldsymbol{B}_{\perp}^{(1)} \equiv B_y^{(1)}\hat{\boldsymbol{\jmath}} + B_z^{(1)}\hat{\boldsymbol{k}}$.

The solutions of Equation (5.8) in the form of normal or Fourier modes have been analyzed in the past by, e.g., Piddington [1956], Kulsrud and Pearce [1969], Pudritz [1990], Martin et al. [1997] or Kamaya and Nishi [1998], and more recently by Kumar and Roberts [2003], Zaqarashvili et al. [2011a], Mouschovias et al. [2011] or Soler et al. [2013b]. At first order, there is no coupling between the perpendicular and longitudinal components of the perturbations, which means that there is no coupling between Alfvén and sound waves. In contrast, a coupling appears at the second-order, as shown by the following equations, which are related to the velocities in the longitudinal direction:

$$\frac{\partial \rho_n^{(2)}}{\partial t} + \rho_n^{(0)}\frac{\partial V_{n,x}^{(2)}}{\partial x} = 0, \tag{5.10}$$

$$\frac{\partial \rho_i^{(2)}}{\partial t} + \rho_i^{(0)}\frac{\partial V_{i,x}^{(2)}}{\partial x} = 0, \tag{5.11}$$

$$\rho_n^{(0)}\frac{\partial V_{n,x}^{(2)}}{\partial t} = -\frac{\partial P_n^{(2)}}{\partial x} + \alpha_{in}\left(V_{i,x}^{(2)} - V_{n,x}^{(2)}\right), \tag{5.12}$$

$$\rho_i^{(0)}\frac{\partial V_{i,x}^{(2)}}{\partial t}=-\frac{\partial P_{ie}^{(2)}}{\partial x}-\frac{\partial}{\partial x}\left(\frac{B_\perp^2}{2\mu_0}\right)+\alpha_{in}\left(V_{n,x}^{(2)}-V_{i,x}^{(2)}\right), \tag{5.13}$$

where $B_\perp^2\equiv\left(B_y^{(1)}\right)^2+\left(B_z^{(1)}\right)^2$. Thus, the second-order perturbation of the velocity of ions is related to the first-order perturbation of the magnetic field and, in turn, produces a fluctuation in the rest of the variables, namely $V_{n,x}^{(2)}$, $\rho_i^{(2)}$, and $\rho_n^{(2)}$. It must be noted that the second-order equations corresponding to the perpendicular components have the same form as those of first-order and hence, they describe the same behavior as Equations (5.8) and (5.9).

The sound speeds of the ionized and of the the neutral fluids are defined as $c_{ie}=\sqrt{\gamma P_{ie}^{(0)}/\rho_i^{(0)}}$ and $c_{S,n}=\sqrt{\gamma P_n^{(0)}/\rho_n^{(0)}}$, respectively. In the fully ionized single-fluid case, the second-order perturbations of pressure and density are related by the expression $P_{ie}^{(2)}=c_{ie}^2\rho_i^{(2)}$ (see, e.g, Hollweg [1971], Rankin et al. [1994]). When multi-fluid plasmas are considered, that relation is not accurate because of the heat transfer terms in the evolution equation of pressure (see Equation (2.54)). Nevertheless, for the purposes of this analytical study, it can be taken as a good approximation. Thus, assuming that $P_n^{(2)}\approx c_{S,n}^2\rho_n^{(2)}$ and combining Equations (5.10)-(5.13), it is possible to obtain the following equation that describes the second-order perturbations of the density of ions (a similar equation can be cast for neutrals and for the x-component of the velocities of ions and neutrals):

$$\left[\frac{\partial^4}{\partial t^4}+(\nu_{in}+\nu_{ni})\frac{\partial^3}{\partial t^3}-\left(c_{S,n}^2+c_{ie}^2\right)\frac{\partial^2}{\partial t^2}\frac{\partial^2}{\partial x^2}-\left(\nu_{in}c_{S,n}^2+\nu_{ni}c_{ie}^2\right)\frac{\partial}{\partial t}\frac{\partial^2}{\partial x^2}+c_{ie}^2c_{S,n}^2\frac{\partial^4}{\partial x^4}\right]\rho_i^{(2)}=$$
$$\left(\frac{\partial^2}{\partial t^2}\frac{\partial^2}{\partial x^2}-c_{S,n}^2\frac{\partial^4}{\partial x^4}+\nu_{ni}\frac{\partial}{\partial t}\frac{\partial^2}{\partial x^2}\right)\left(\frac{B_\perp^2}{2\mu_0}\right). \tag{5.14}$$

An interesting limiting case of the previous equation can be found if ν_{ni} is assumed to tend to infinity, which corresponds to a strong coupling between the two fluids. The following expression is obtained:

$$\left[(1+\chi)\frac{\partial^3}{\partial t^3}-\left(\chi c_{S,n}^2+c_{ie}^2\right)\frac{\partial}{\partial t}\frac{\partial^2}{\partial x^2}\right]\rho_i^{(2)}=\frac{\partial}{\partial t}\frac{\partial^2}{\partial x^2}\left(\frac{B_\perp^2}{2\mu_0}\right), \tag{5.15}$$

where the relation $\nu_{in}/\nu_{ni}=\chi$ has been used. The integration with respect to time leads to

$$\left[\frac{\partial^2}{\partial t^2}-\left(\frac{c_{ie}^2+\chi c_{S,n}^2}{1+\chi}\right)\frac{\partial^2}{\partial x^2}\right]\rho_i^{(2)}=\frac{\partial^2}{\partial x^2}\left(\frac{B_\perp^2}{2\mu_0(1+\chi)}\right), \tag{5.16}$$

where an integration constant has been taken equal to zero. This is the 1-dimensional inhomogeneous wave equation, with the right-hand representing a driving term. Using the initial conditions $\rho_i^{(2)}(x,t=0)=0$ and $\frac{\partial}{\partial t}\rho_i^{(2)}(x,t=0)=0$, respectively, the solution to this equation can be computed as

$$\rho_i^{(2)}(x,t)=\frac{1}{2\widetilde{c}_S}\int_0^t\int_{x-\widetilde{c}_S(t-\tau)}^{x+\widetilde{c}_S(t-\tau)}\frac{\partial^2}{\partial x^2}\left[\frac{B_\perp^2(\xi,\tau)}{2\mu_0(1+\chi)}\right]d\xi d\tau. \tag{5.17}$$

The only speed that explicitly appears in Equation (5.17) is the effective sound speed, $\widetilde{c}_S$, defined as

$$\widetilde{c}_S = \left(\frac{c_{ie}^2 + \chi c_{S,n}^2}{1+\chi} \right)^{1/2} . \tag{5.18}$$

However, since the driving wave is assumed to be Alfvénic, the evolution of $B_\perp^2$ depends on the Alfvén speed. Hence, the evolution of $\rho_i^{(2)}(x,t)$ depends on both sound and Alfvén speeds.

From Equation (5.14) it is also possible to recover the differential equation that describes the second-order perturbations of density in a fully ionized plasma. If the collision frequencies are taken equal to zero (meaning that neutrals are decoupled and do not interact with ions), it is possible to rewrite Equation (5.14) as

$$\left(\frac{\partial^2}{\partial x^2} - c_{S,n}^2 \frac{\partial^2}{\partial x^2} \right) \left(\frac{\partial^2}{\partial x^2} - c_{ie}^2 \frac{\partial^2}{\partial x^2} \right) \rho_i^{(2)} = \left(\frac{\partial^2}{\partial x^2} - c_{S,n}^2 \frac{\partial^2}{\partial x^2} \right) \frac{\partial^2}{\partial x^2} \left(\frac{B_\perp^2}{2\mu_0} \right) , \tag{5.19}$$

which leads to

$$\left(\frac{\partial^2}{\partial t^2} - c_{ie}^2 \frac{\partial^2}{\partial x^2} \right) \rho_i^{(2)} = \frac{\partial^2}{\partial x^2} \left(\frac{B_\perp^2}{2\mu_0} \right) , \tag{5.20}$$

an equation that has already been derived by Hollweg [1971], Tikhonchuk et al. [1995] or Terradas and Ofman [2004]. It can be seen that Equations (5.16) and (5.20) represent the same type of behavior, with differences appearing in the velocity of propagation of waves and the amplitude of the driving term. These are two effects caused by the ion-neutral interaction.

If the initial perturbation applied to the equilibrium state is given by

$$V_y^{(1)}(x,t) = V_{y,0} \cos(k_x x), \tag{5.21}$$

and the strongly coupled limit is applied to Equations (5.8) and (5.9), the first-order perturbation of the magnetic field is

$$B_\perp(x,t) = \frac{-B_0}{\widetilde{c}_{\mathrm{A}}} V_{y,0} \sin(\widetilde{c}_{\mathrm{A}} k_x t) \sin(k_x x), \tag{5.22}$$

with $\widetilde{c}_{\mathrm{A}}$ the Alfvén speed modified by the inclusion of the inertia of neutrals, i.e., $\widetilde{c}_{\mathrm{A}} = B_0 / \sqrt{\mu_0 \rho_{i,0} (1+\chi)}$. Then, the solution to Equation (5.16) is

$$\rho_i^{(2)}(x,t) = \frac{B_0^2 V_{y,0}^2 \left[\widetilde{c}_{\mathrm{A}}^2 - \vec{c}_S^2 + \vec{c}_S^2 \cos(2\widetilde{c}_{\mathrm{A}} k_x t) - \widetilde{c}_{\mathrm{A}}^2 \cos(2\bar{c}_S k_x t) \right] \cos(2k_x x)}{8 \widetilde{c}_{\mathrm{A}}^2 \widetilde{c}_S^2 (\widetilde{c}_{\mathrm{A}}^2 - \vec{c}_S^2) \mu_0 (1+\chi)} . \tag{5.23}$$

The resulting perturbation is the combination of two standing modes with frequencies $2\widetilde{c}_{\mathrm{A}} k_x$ and $2\widetilde{c}_S k_x$, respectively, and whose wavenumber is twice the wavenumber of the original perturbation. The solution for the fully ionized case is recovered by substituting $\widetilde{c}_S$ with c_{ie}, $\widetilde{c}_{\mathrm{A}}$ with c_{A} and taking $\chi = 0$.

If the sound speed is much lower than the Alfvén speed, as it occurs in the simulations performed in this work, Equation (5.23) can be approximated as

$$\rho_i^{(2)}(x,t) \approx \frac{B_0^2 V_{y,0}^2}{8\mu_0 \widetilde{c}_{\mathrm{A}}^2 (1+\chi)} \left[\frac{1 - \cos(2\widetilde{c}_S k_x t)}{\widetilde{c}_S^2} \right] \cos(2k_x x), \tag{5.24}$$

which shows that the perturbation is dominated by the oscillation mode associated with the weighted sound speed.

Then, the relative variation of density, which in Figures 5.1-5.3 is represented as $\Delta\rho/\rho_0$, can be computed as the ratio between the second-order perturbation and the background density. Hence,

$$\frac{\Delta\rho_i}{\rho_{i,0}} \equiv \frac{\rho_i^{(2)}(x,t)}{\rho_{i,0}} \approx \frac{V_{y,0}^2}{8\widetilde{c}_S^2}\left[1-\cos(2\widetilde{c}_S k_x t)\right]\cos(2k_x x), \tag{5.25}$$

An interesting conclusion can be extracted from the previous equation: since the relative variation of density is proportional to $V_{y,0}^2/\widetilde{c}_S^2$ for partially ionized plasmas while it is proportional to $V_{y,0}^2/c_{ie}^2$ for fully ionized fluids and $c_{ie} > \widetilde{c}_S$, the relative variation of density is larger when the effect of partial ionization is taken into account. This is an important result caused by partial ionization.

A comparison between the fully ionized case and the partially ionized case with strong coupling is shown in Figure 5.4. Numerical simulations with the same total mass, with $n_p = n_{\mathrm{H}}$ (i.e., $\chi = 1$) for the partially ionized plasma, and the same amplitude of the initial perturbation in velocity have been performed. The collision frequency for the partially ionized case is much larger than the oscillation frequency. It can be seen that the amplitude of the relative variation of density is larger when the plasma is partially ionized. Furthermore, the fully ionized plasma oscillates with a slightly higher frequency than the partially ionized one, as it would be expected since $c_{ie} > \widetilde{c}_S$. The numerical results are in almost perfect agreement with the approximate analytical expressions. The small differences that appear in the partially ionized case are caused by the collisional friction between ions and neutrals. This friction causes the damping of the amplitude of the oscillation and a slight modification of its frequency. For simplicity, damping has not been taken into account in the analytic approximations given above.

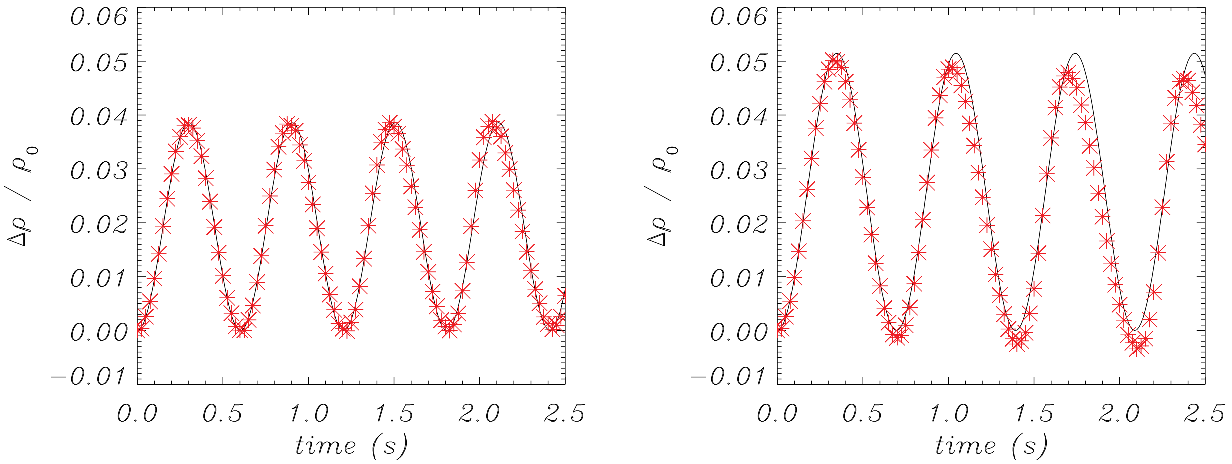

Figure 5.4: Relative variation of density caused by the ponderomotive force due to an Alfvén wave with $k_x = \pi/10^4$ m^{-1} in a fully ionized plasma (left) and a partially ionized plasma with a strong coupling between the two fluids (right). The solid lines represent the analytical solution given by Equation (5.25) and the red symbols represent the results of the numerical simulations.

If the wavenumber of the perturbation increases, the frequency of the Alfvén wave increases as well and departs from the limit where $\omega/(2\pi) \ll \nu_{ni}$, which means that the coupling between the two fluids is not as strong as for smaller wavenumbers. Hence, it would be expected that Equation (5.25) becomes inaccurate at larger wavenumbers. Moreover, it has been shown in Chapters 3 and 4 that Hall's term should be taken into account in the large wavenumber range. However, such term has been neglected here in the derivation of the equations for the second-order perturbations.

The three-fluid simulations represented in Figures 5.2 and 5.3 show that, under the chosen physical parameters, the friction due to ion-neutral collisions is more efficient in attenuating the Alfvénic waves than the acoustic modes. For instance, it can be checked that in Figure 5.3 the first-order Alfvén wave has almost disappeared after $t = 0.5$ s, but the second-order perturbation in the x-component of the velocity lasts for a longer time. In a two-fluid plasma, the oscillation frequency and damping rate of the remaining second-order wave may be obtained from Equation (5.14) in the following way. Since the driving wave, i.e., the first-order Alfvén wave, vanishes due to collisions, after a given time the term on the right-hand side of Equation (5.14) becomes equal to zero. Then, the remaining oscillations are governed by the homogeneous version of the differential equation, with the initial conditions given by the wave previously induced by the driver. After the primary Alfvén wave is completely damped, the second-order perturbation of the density of ions can be expressed as

$$\rho_i^{(2)} \sim \exp\left[i(-\omega t + \kappa x)\right], \tag{5.26}$$

where, in this case, the wavenumber is twice the wavenumber of the original driving wave, i.e., $\kappa = 2k_x$. This procedure leads to the following dispersion relation,

$$\omega^4 + i\left(\nu_{ni} + \nu_{in}\right)\omega^3 - \kappa^2\left(c_{S,n}^2 + c_{ie}^2\right)\omega^2 - i\kappa^2\left(\nu_{in}c_{S,n}^2 + \nu_{ni}c_{ie}^2\right)\omega + c_{ie}^2 c_{S,n}^2 \kappa^4 = 0, \tag{5.27}$$

which depends on the sound speeds but not on the Alfvén speed. This is the same dispersion relation that would be obtained for linear acoustic waves in a two-species fluid in which only the collisional interaction between ions and neutrals is taken into account and the influence of magnetic fields is neglected (see, e.g., Vranjes and Poedts [2010]). It coincides with Equation (9) from Vranjes and Poedts [2010] if the factors proportional to the electron-neutral collision frequency of that formula are neglected, and it can also be recovered from Equation (47) of Soler et al. [2013a], where magnetoacoustic waves in partially ionized plasmas have been studied, if the Alfvén speed is set equal to zero.

It must be noted that for a certain range of collision frequencies, the driving wave may last more than the acoustic wave and, strictly, the dispersion relation, Equation (5.27) should not be applicable because the driver is still working. This is a consequence of the damping due to ion-neutral collisions being most efficient when the oscillation frequency is similar to the collision frequency (Zaqarashvili et al. [2011a], Soler et al. [2013b]). Since $\widetilde{c}_S \ll \widetilde{c}_{\mathrm{A}}$, the acoustic modes are more damped than the Alfvénic ones at low collision frequencies and the opposite would occur at high frequencies. Nevertheless, as shown by Equations (5.23) and (5.24), if the Alfvén speed is much larger than the sound speed, the second-order oscillation is dominated by the acoustic mode. Hence, the results from Equation (5.27) are still good approximations at any range of collision frequencies. This statement can be checked by inspecting Figure 5.5, which illustrates a study of the dependence of the oscillation frequency, ω_R, and the damping rate, ω_I, of the second-order acoustic wave on the ion-neutral collision frequency (only the modes with $\omega_R \geq 0$ are displayed). According to the dispersion relation, at low values of ν_{in}/ω_S (where

$\omega_S = \kappa\widetilde{c}_S$ is a normalization parameter), the Alfvén wave induces four acoustic modes with $\omega_R = \pm\kappa c_{S,n}$ and $\omega_R = \pm\kappa c_{ie}$, respectively. At higher collision frequencies, two of those modes tend to $\omega_R = \pm\kappa\widetilde{c}_S$, while the other two become evanescent, i.e., they have $\omega_R = 0$ and do not oscillate. In addition, the damping of the oscillatory modes is larger at the intermediate range of collision frequencies. The results from the simulation show a general good agreement with the predictions from Equation (5.27). In addition, the behavior represented by this figure is analog to that shown in Figures 4(c)-(d) of Soler et al. [2013a] for the modes denoted as *slow*, *acoustic* and *modified slow*.

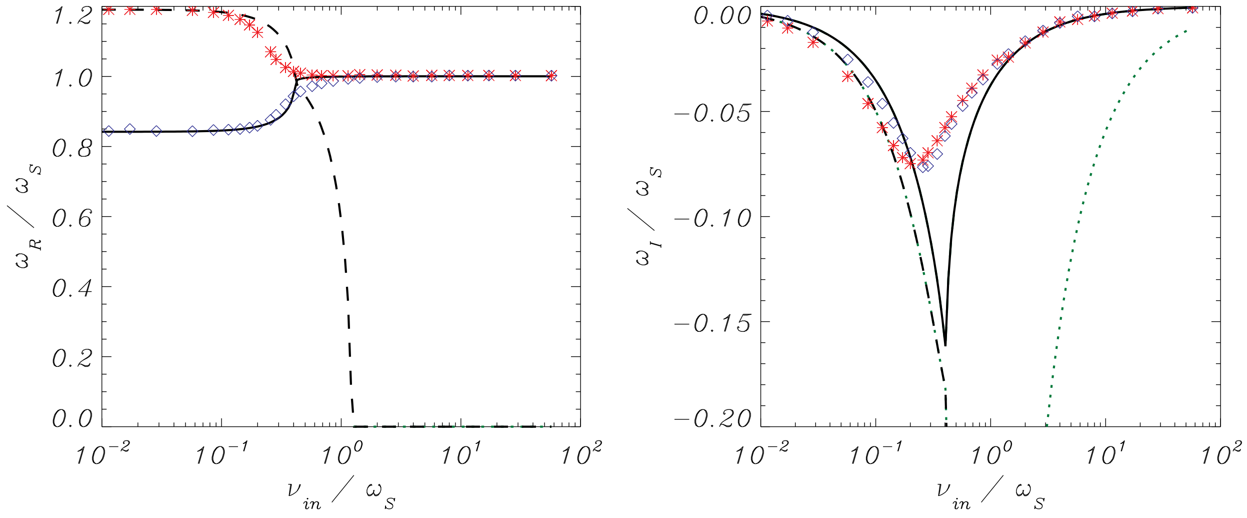

Figure 5.5: Oscillation frequency (left) and damping rate (right) of the second-order acoustic mode generated by the Alfvén wave in a two-fluid plasma as functions of the collision frequency. The normalization constant is $\omega_S = \kappa\widetilde{c}_S$. The lines correspond to the solutions from Equation (5.27) while the symbols represented the results from the simulations. At low ν_{in}/ω_S, the blue diamonds and the solid lines represent the mode associated with neutrals, and the red stars and dashed lines represents the mode associated with ions. At large collision frequencies, the green dotted lines correspond to an evanescent mode.

5.2.2 Ponderomotive force

After the simplified two-fluid model has helped us to understand some of the results of the numerical simulations, we return back to the three-fluid model with the complete induction equation and consider again conditions akin to those of solar prominences.

A series of simulations has been performed to investigate the dependence of the ponderomotive force on the wavenumber. The same number densities, magnetic fields and temperatures as those employed to obtain the results displayed in Figure 5.1 have been used here. The results of this study are represented in Figure 5.6, where the normalized oscillation frequency of waves, $\omega_R/\omega_{\mathrm{A}}$, is plotted as a function of the wavenumber k_x.

The black lines on the left panel of Figure 5.6 correspond to the predictions of the dispersion relation given by Equation (3.12) for the Alfvénic modes when applied to the case of partially ionized plasmas, as shown in Chapter 4. It must be noted that the dispersion relation has been obtained for small-amplitude perturbations but it can be also applied to the first-order perturbations of the nonlinear case. The solutions of the dispersion relation shown in this figure are the same as those represented in the top panel of Figure 4.2: the solid line corresponds to the R-mode and the dashed line represents the L-mode. For the sake of simplicity, we refer readers to Chapter 4 for detailed explanations of the differences between these two solutions. The symbols represent the results of the numerical simulations. It can be seen that the simulations are in perfect agreement with the predictions of the dispersion relation for the first-order perturbations. Hence, the discussion already given in Chapter 4 can be directly applied to these results and it is not necessary to repeat it here. Consequently, the focus is put on the second-order perturbations.

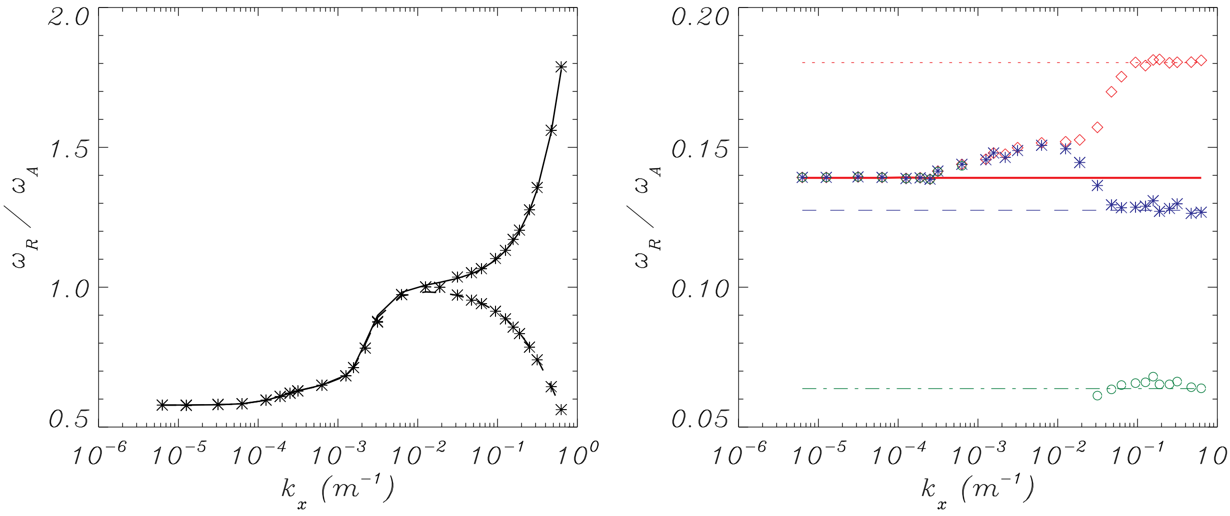

Figure 5.6: Dependence of the normalized frequency, $\omega_R/\omega_{\rm A}$, of the Alfvénic first-order perturbations (left) and the second-order acoustic modes (right) on the wavenumber. Black lines represent the solutions of the dispersion relation for linear Alfvénic waves, with the solid and dashed lines corresponding to the R and L modes, respectively. The solid red line on the right panel represents the frequency of the second-order acoustic mode given by Equation (5.25), i.e., $\omega^{(2)} = 2\widetilde{c}_S k_x$. The green dotted-dashed line, the blue dashed line and the dotted red line represent the frequencies $2c_{S,\rm He}k_x$, $2c_{S,\rm H}k_x$ and $2c_{ie}k_x$, respectively. The symbols are the results from the numerical simulations: red diamonds for protons, blue stars for neutral hydrogen, and green circles for neutral helium.

According to the simulations, the frequency of the second-order acoustic modes, which is denoted by $\omega_{sim}^{(2)}$, has three clearly different regimes depending on the wavenumber of the first-order perturbation. At small wavenumbers, the frequency given by the simulations is in very good agreement with that predicted by Equation (5.25), i.e., $\omega_{sim}^{(2)} \approx 2\widetilde{c}_S k_x$, with $\widetilde{c}_S$ now given by

$$\widetilde{c}_S^2 = \frac{\sum_t \rho_t c_{S,t}^2}{\sum_t \rho_t}, \tag{5.28}$$

where $c_{S,t} = \sqrt{\gamma P_{t,0}/\rho_{t,0}}$ is the sound speed of species t. However, as k_x is increased, $\omega_{sim}^{(2)}$ departs from that value. To understand this behavior, it is necessary to remind the collision

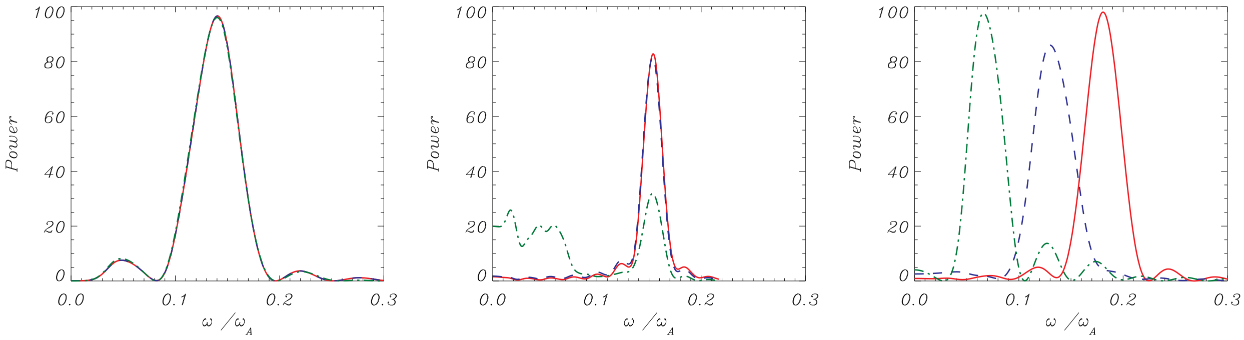

Figure 5.7: Power spectrum of the oscillations in V_x for three different wavenumbers of the initial perturbation: $k_x = \pi/(5 \times 10^5)$ m^{-1} (left), $k_x = \pi/500$ m^{-1} (middle) and $k_x = \pi/10$ m^{-1} (right). The red solid lines, blue dashed lines and green dotted-dashed correspond to protons, neutral hydrogen and neutral helium, respectively.

frequencies between the three fluids (protons, neutral hydrogen and neutral helium) that compose the partially ionized plasma: $\nu_{p\mathrm{H}} = 270$ Hz, $\nu_{p\mathrm{He}} = 3.5$ Hz, and $\nu_{\mathrm{HHe}} = 5.2$ Hz. Hence, the three regimes of $\omega_{sim}^{(2)}$ can be understood in terms of the coupling degree between the fluids as follows. At small wavenumbers, the oscillation frequency of the first-order perturbation, $\omega_{sim}^{(1)}$, is lower than the collision frequencies. Thus, there is a considerably strong coupling between the three components of the plasma, they behave almost as a single fluid whose effective sound speed is given by $\widetilde{c}_S$. The resulting acoustic mode has a normalized frequency given by $\omega_{sim}^{(2)}/\omega_{\mathrm{A}} = 2\widetilde{c}_S k_x/\omega_{\mathrm{A}} \approx 0.14$. At intermediate wavenumbers, $\omega_{sim}^{(1)}$ is larger than $\nu_{p\mathrm{He}}$ and ν_{HHe}, but smaller than $\nu_{p\mathrm{H}}$, which means that neutral helium is weakly coupled to the other two fluids but protons and neutral hydrogen still have a strong interaction. Consequently, the effective sound speed is given by the weighted mean of those of protons and hydrogen, without the contribution of neutral helium, and is slightly larger than $\widetilde{c}_S$. With this new sound speed, the normalized oscillation frequency is $\omega_{sim}^{(2)}/\omega_{\mathrm{A}} \approx 0.15$. Finally, at large wavenumbers, $\omega_{sim}^{(1)} \gg \nu_{p\mathrm{H}}$ and the coupling between protons and hydrogen is weak. The sound speed of the proton fluid is c_{ie} and $\omega_{sim}^{(2)}/\omega_{\mathrm{A}} \approx 0.18$, which corresponds approximately to the result expected for a fully ionized plasma. The neutral hydrogen and neutral helium fluids oscillate with the normalized frequencies $2k_x c_{S,\mathrm{H}}/\omega_{\mathrm{A}} \approx 0.13$ and $2k_x c_{S,\mathrm{He}} \approx 0.065$, respectively.

On the right panel of Figure 5.6, the interval $k_x \in [10^{-3}, 2 \times 10^{-2}]$ m^{-1} does not show data corresponding to the helium fluid. The reason is that, in such region of wavenumbers, the oscillation of helium is composed of several modes and not only one. This can be checked in Figure 5.7, where the power spectrum of the x-component of the velocities of the three fluids has been represented for three different wavenumbers of the original perturbation. The left and right panels, corresponding to the small and large limits of wavenumbers, demonstrate that the oscillation of each fluid is dominated by only one normal mode. At intermediate wavenumbers, protons and neutral hydrogen are still strongly coupled and their oscillations are governed by the same mode. However, the coupling with helium is weaker and additional modes appear, reflected in a noisier spectrum of rather difficult interpretation.

Apart from the acoustic oscillation mode, Equation (5.23) states that the second-order perturbation of density is also composed of an Alfvénic mode. As already mentioned, when

$\widetilde{c}_S \ll \widetilde{c}_{\mathrm{A}}$, with

$$\widetilde{c}_A = \frac{c_{\mathrm{A}}}{\sqrt{1+\sum_t \chi_t}}, \tag{5.29}$$

where $\chi_t = \rho_t / \rho_p$, the amplitude of the Alfvénic mode is much smaller than that of the acoustic one. Nonetheless, it still can be detected in some of the simulations, although it has not been represented in Figure 5.6 for the sake of clarity, and it is possible to check that it has a similar behavior than the first-order Alfvénic modes: at small wavenumbers its frequency is associated with the modified Alfvén speed; at larger wavenumbers it is related to the classical Alfvén speed, c_{A}, as in a fully ionized plasma.

Furthermore, the simulations represented in Figure 5.1-5.3 reveal another contrast between the partially ionized and the fully ionized cases. In the latter, the ponderomotive force produces an accumulation of matter around the nodes of the Alfvén wave magnetic field perturbation. In a pressureless fluid, the accumulation continues without limit. However, when the effect of the gas pressure is taken into account, the density at that node reaches a certain maximum and starts to oscillate between that maximum and its background value (see, e.g., Rankin et al. [1994], Tikhonchuk et al. [1995]). On the other hand, Figures 5.2 and 5.3 show that in partially ionized plasmas, the density tends to accumulate at the node only for a brief period of time. After, the relative variation of density, $\Delta\rho/\rho_0$, decreases and oscillates around negative values, which means that the plasma becomes lighter at that point in comparison with the equilibrium state. This behavior can be understood in terms of the effect of gas pressure and collisions as follows.

According to Equation (5.13), the second-order longitudinal motion of ions mainly depends on the balance between the forces given by the gradients of the thermodynamic and magnetic pressures. The study of fully ionized plasmas (see, e.g., Rankin et al. [1994], Tikhonchuk et al. [1995]) shows that the gradient of magnetic pressure moves the plasma towards the nodes of the first-order magnetic field perturbation. The gradient of the second-order perturbation of pressure acts in the opposite way, i.e., it displaces the matter from those locations. These statements can be checked by computing the corresponding gradients using the expressions of $B_\perp$ and $\rho_i^{(2)}(x,t)$ given by Equations (5.22) and (5.23), respectively, and assuming the relation $P_{ie}^{(2)} \approx c_{ie}^2 \rho_i^{(2)}$. Which effect dominates during the first steps of the temporal evolution depends on the time scales associated to them. Under the physical conditions used in this investigation, the Alfvén frequency is higher than the frequency of sound waves, meaning that magnetic pressure has a smaller time scale than the thermodynamic pressure. Therefore, in the first place, the matter accumulates at the nodes. Later, the effect of the thermodynamic pressure becomes noticeable and the resulting motion is a consequence of the combination of the two forces. In partially ionized plasmas, friction due to ion-neutral collisions dissipates the energy of Alfvén waves and turns it into internal energy of the plasma, i.e., it increases the thermodynamic pressure. As time advances the term of the motion equation associated with the driving Alfvénic wave becomes less relevant in comparison with the gradient of the thermodynamic pressure. Consequently, the longitudinal motion is dominated by the force that moves the matter away from the nodes of the magnetic field perturbation.

It must be noted that in this section the amplitude of the perturbations has been chosen in a way that only first- and second-order effects are relevant for the dynamics of the investigated plasmas. However, if the amplitudes are increased, higher-order terms may be also of great importance. As detailed by Tikhonchuk et al. [1995], the higher-order terms may produce, for

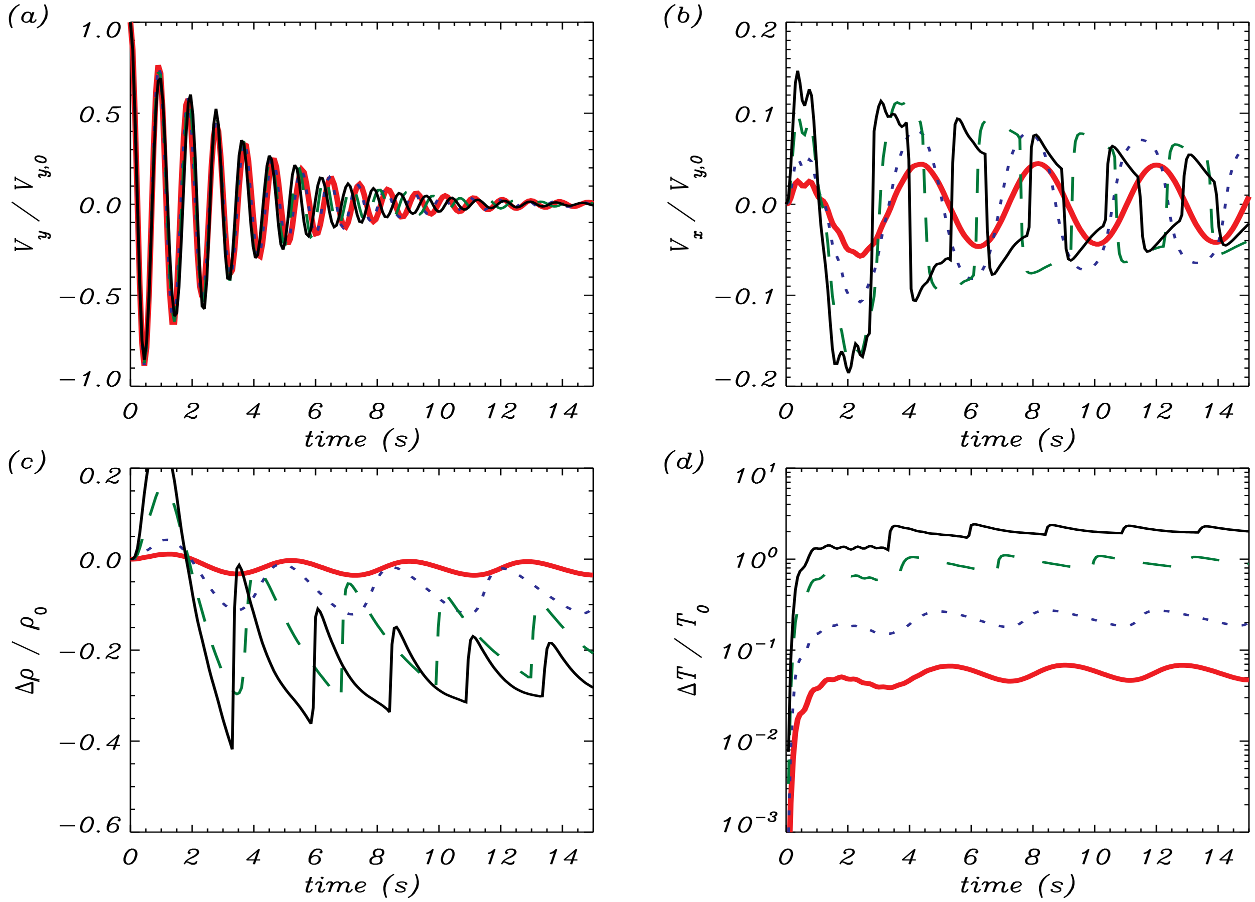

Figure 5.8: Comparison of the oscillations in the proton fluid generated by standing Alfvén waves with different initial amplitudes: $V_{y,0} = 0.025c_{\mathrm{A}}$ (red solid lines), $V_{y,0} = 0.05c_{\mathrm{A}}$ (blue dots), $V_{y,0} = 0.1c_{\mathrm{A}}$ (green dashes), and $V_{y,0} = 0.15c_{\mathrm{A}}$ (black thin lines). The wavenumber of the initial perturbations is $k_x = \pi/(5 \times 10^4)$ m^{-1} in all cases.

instance, the steepening of the fluctuations, which may lead to the formation of shocks, and the appearance of higher harmonics of the Alfvén waves. Some of those higher-order effects can be found in Figure 5.8, where the results of simulations with different amplitudes of the initial perturbation are compared. The steepening of the waves when the amplitudes are increased is clearly shown in panels (b) and (c), corresponding to the normalized x-component of the velocity at the point $x = -l/2$ and the variation of density at $x = 0$, respectively. The top left panel represents the first-order Alfvén wave at $x = 0$ and it can be seen that, after the initial steps, its frequency raises in the cases with the larger amplitudes. This is due to the decrease of density shown in panel (c). The change in frequency can also be noticed in the other three panels: a larger number of periods can be found for $V_{y,0} = 0.15c_{\mathrm{A}}$ than for $V_{y,0} = 0.025c_{\mathrm{A}}$. Finally, panel (d) represents the variation of temperature at $x = 0$. After a very fast growth, the temperature tends to oscillate around a value that increases with the square of the driver amplitude, consistent with the dependence shown by the heating term given by Equation (2.57).

The results displayed in Figure 5.8(d) correspond to a specific point of the numerical domain. Although they are representative of the general behavior of heating of the plasma, differences appear (for example, in amplitude and in the phase of the oscillations) when other points are considered. Thus, it is interesting to compute the average value over the spatial domain. The temporal evolution of the spatially-averaged temperature, given by $1/(2l)\int_{-l}^{l}T(x)\,dx$, is represented in Figure 5.9. Comparing this figure with Figure 5.8, it can be seen that the temperature reaches an equilibrium value after most of the energy of the Alfvén wave has been dissipated, while the contribution of the second-order acoustic waves to heating is negligible. This is due to ion-neutral collisions being inefficient in damping the acoustic modes under the parameters chosen for these simulations. When the amplitude of the initial perturbation is $V_{y,0} = 0.025c_{\mathrm{A}}$, the temperature rises up to $\sim 10,360$ K (i.e., the variation is $\Delta T \approx 360$ K). For the amplitudes $V_{y,0} = 0.05c_{\mathrm{A}}$, $V_{y,0} = 0.1c_{\mathrm{A}}$ and $V_{y,0} = 0.15c_{\mathrm{A}}$, the final temperatures are $11,470$ K ($\Delta T \approx 1470$ K), $16,170$ K ($\Delta T \approx 6170$ K), and 24470 K ($\Delta T \approx 14,470$ K), respectively. Hence, the dependence of the increment of temperature on the amplitude of the perturbation is approximately quadratic.

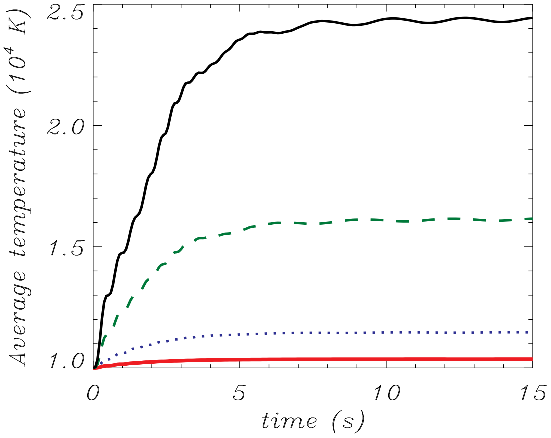

Figure 5.9: Spatially-averaged temperature variation in a plasma with prominence conditions due to the dissipation of standing Alfvén waves with $k_x = \pi/(5\times10^4)$ m^{-1} and amplitudes $V_{y,0} = 0.025c_{\mathrm{A}}$ (red solide line), $V_{y,0} = 0.05c_{\mathrm{A}}$ (blue dotted line), $V_{y,0} = 0.1c_{\mathrm{A}}$ (green dashed line), and $V_{y,0} = 0.15c_{\mathrm{A}}$ (black line).

The formation of shocks through the ponderomotive coupling of Alfvén waves to sound modes was investigated by Arber et al. [2016]. Their 1.5D numerical study suggests that in the chromosphere the heating due to shocks is larger than that caused directly by ion-neutral collisions. Here, we have shown that shocks associated with the second-order sound waves may develop in a quiescent prominence. Hence, shock heating may have an important contribution to the total heating of partially ionized prominences. Nevertheless, the equations of our model do not include the necessary terms to properly address the viscous heating due to shocks.

5.3 Numerical simulations of impulsive perturbations

In this section, the evolution of a velocity pulse as it propagates through a uniform partially ionized plasma is analyzed. A similar study was performed by Verwichte et al. [1999] for the case of fully ionized plasma. Hence, it is interesting to examine how the results of that work are modified by the inclusion of partial ionization effects. Moreover, according to Rankin et al. [1994], the effects of nonlinearity are stronger for standing waves than for propagating waves. Thus, third- or higher-order terms are only expected to have a strong impact on the evolution of the pulse for larger amplitudes than those used in the previous section and the main nonlinearities that appear in this section are due to the second-order terms. As before, we consider 1.5D numerical simulations.

Now, the perturbation applied to the plasma at $t = 0$ has a Gaussian profile, i.e., it is given by

$$f^{(1)}(x, t = 0) \sim \exp\left[-\left(\frac{x - x_0}{\sqrt{2}\sigma_x}\right)^2\right], \qquad (5.30)$$

where σ_x is the root-mean-square width and is related to the full width at half maximum (FWHM) of the Gaussian by the formula $\text{FWHM} = 2\sqrt{2\ln 2}\sigma_x$, and x_0 is the central position of the peak.

Figure 5.10 shows the Alfvén wave that is generated when the perturbation given by Equation (5.30) is applied to the y-component of the velocity of all species of a plasma with prominence conditions (the same used in the previous section). The amplitude of the perturbation is $V_{y,0} = 5 \times 10^{-2} c_{\rm A}$ and its width is $\text{FWHM} = 2 \times 10^5$ m. As expected, the initial pulse splits into two smaller Alfvénic pulses, with half the height of the initial pulse, and propagate towards opposite directions. There is a strong coupling between the three species (protons, neutral hydrogen and neutral helium) and the transverse velocity pulses of each fluid propagate together at the modified Alfvén speed, $\widetilde{c}_{\rm A}$. Notwithstanding, the height of the peaks decreases with time because the coupling is not perfect and there is friction that dissipates a fraction of the wave energy and turns it into internal energy of the plasma. Friction is caused by the small velocity drifts between species, which are not noticeable at the scale of Figure 5.10.

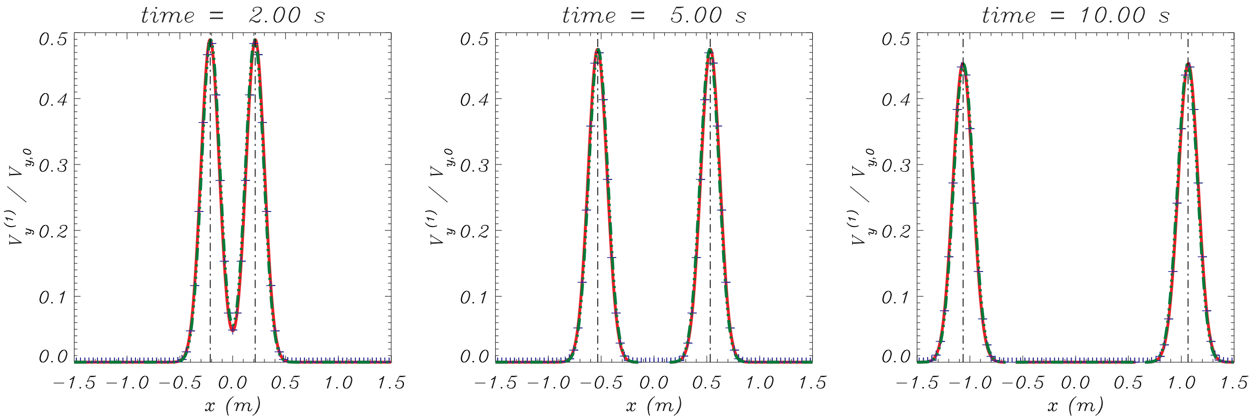

Figure 5.10: Component y of the velocity of protons (red solid line), neutral hydrogen (blue crosses), and neutral helium (green dotted-dashed line) from a simulation of a plasma with prominence conditions. The initial Gaussian pulse has a $FWHM = 2 \times 10^5$ m. As a reference, the vertical lines represent the position of a perturbation that would propagate with velocity $\widetilde{c}_{\rm A}$

.

The nonlinear effects generated by the Alfvénic pulse are represented in Figure 5.11. The panels in the top row display the perturbation on the x-component of the velocity. The amplitude of V_x is much smaller than that of V_y, of the order of 1.5% of $V_{y,0}$, as it would be expected. As in the case of standing waves, two clearly different waves appear in the longitudinal component of velocity. The faster one has a propagation speed that coincides with $\widetilde{c}_{\mathrm{A}}$, while the slower one propagates at the speed $\widetilde{c}_S$. The waves leave a small wake that is positive at $x > 0$ and negative at $x < 0$. This means that, after the wavefront has passed, the particles are slowly moved away from the center. Again, this is a nonlinear effect.

The relative variation of density is shown in the second row of Figure 5.11. Although their shapes are different, the perturbations found here have the same propagation speeds as those for V_x. Moreover, a similar behavior to that previously described for standing waves can be observed: matter accumulates at the center of the domain during the first steps of the simulation but later is displaced from that point.

The third and fourth rows of Figure 5.11 represent the second-order perturbations of pressure and temperature, respectively, with $\Delta P = P(x,t) - P_0$. These two rows show how a fraction of the energy of the perturbation is deposited into the plasma. An increase of temperature and pressure is found after the passing of the wave front, i.e., some of the energy of the wave has been transformed into internal energy of the plasma. The increase of pressure seems to be uniform along the plasma. In contrast, it can be checked that the growth of temperature is inversely proportional to the variation of density.

The results shown in Figure 5.10 and the first and second columns of Figure 5.11 can be compared with those in Figure 1 from Verwichte et al. [1999]. A similar behavior is found in fully and partially ionized plasmas during the first steps of the evolution of the density and velocity. The differences would appear in pressure and in temperature. Verwichte et al. [1999] did not plot the evolution of the pressure because, for the case of fully ionized plasmas, it has the same shape as that of density. In contrast, in partially ionized plasmas, the propagating waves leave a pressure wake due to the frictional dissipation of energy because of ion-neutral collisions, a phenomenon that is obviously absent from the fully ionized case of Verwichte et al. [1999].

Not all the kinetic energy of the initial perturbation is used in heating the plasma, but a fraction of it is inverted in generating the second-order propagating waves. Hence, it is interesting to investigate how the efficiency of the energy deposition depends on the properties of the initial perturbation. A series of simulations has been performed with different widths of the Gaussian velocity pulse but keeping the same initial kinetic energy, i.e., the amplitude of the pulse has been modified accordingly. The results of this study are displayed in Figure 5.12, where the data have been obtained in the following way: the domain of the simulation is $x \in [-4, 4] \times 10^6$ m but the analyzed energies have been computed for a smaller region, given by $x \in [l_1, l_1]$, where $l_1 = 10^6$ m; the reason to do so is that the background internal energy is computed after the two wavefronts, i.e., the Alfvénic pulse and the nonlinearly generated sonic pulse, have abandoned the smaller region and the larger domain is needed to avoid the eventual reflection that appears when the Alfvénic pulse reaches the boundaries. The initial kinetic energy is computed as

$$e_k(t=0) = \frac{1}{2l_1} \int_{-l_1}^{l_1} \sum_s \rho_s(x, t=0) \left[V_y^{(1)}(x, t=0)\right]^2 dx, \tag{5.31}$$

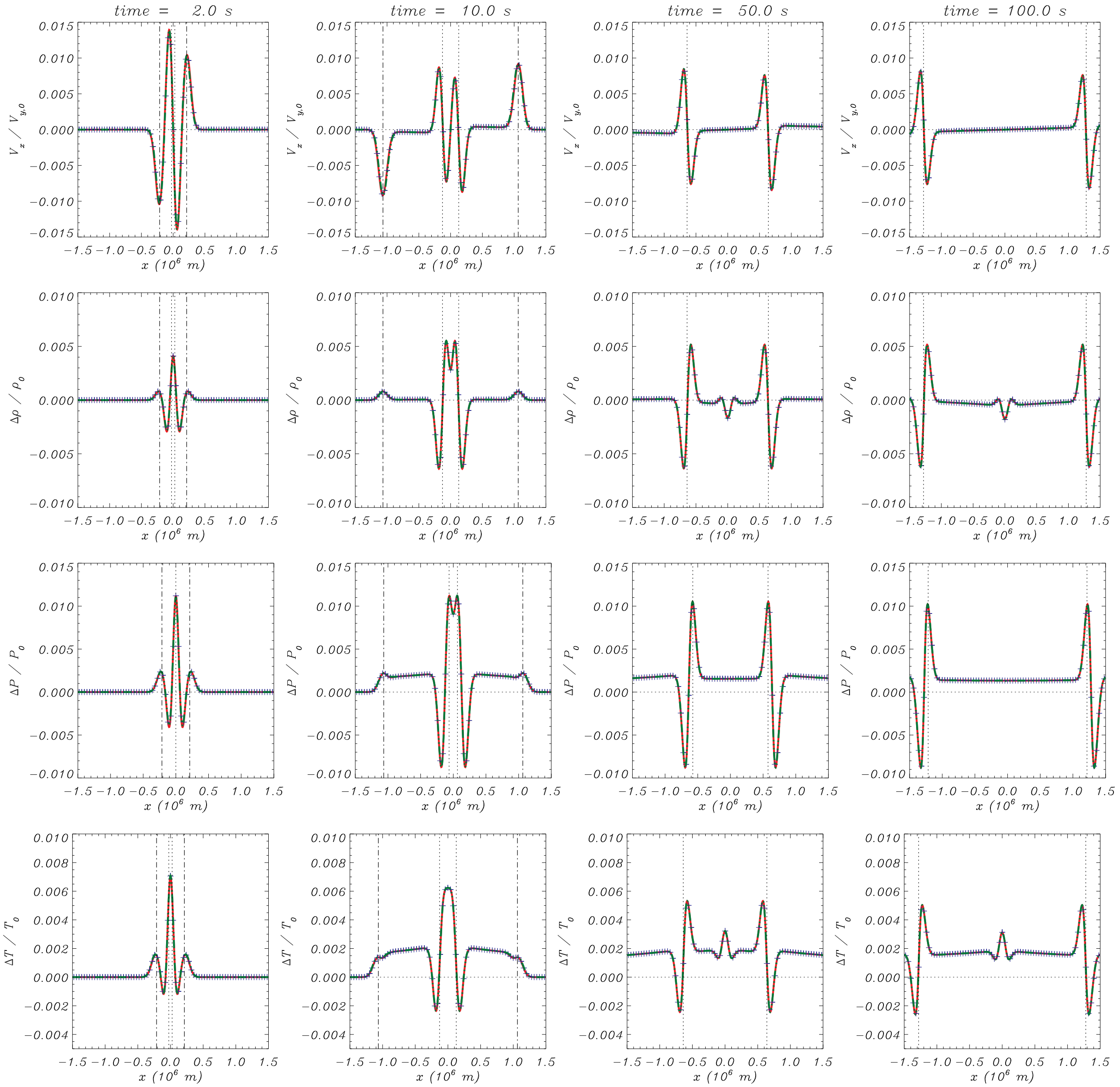

Figure 5.11: Second-order perturbations generated by the propagating Alfvénic pulses shown in Figure 5.10 at several times of the simulation. From top to bottom: x-component of the velocity, density, pressure, and temperature. The vertical dotted-dashed and dotted lines represent the position of points moving at $\widetilde{c}_{\mathrm{A}}$ and $\widetilde{c}_S$ from the origin. (An animation of this figure is available.)

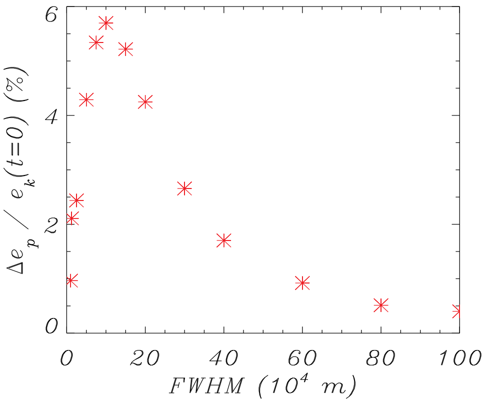

Figure 5.12: Percentage of the initial kinetic energy that is transformed into background internal energy as a function of the width of the initial pulse.

and the variation of the internal energy of the medium is given by

$$\Delta e_P(t) = \frac{1}{2l_1}\int_{-l_1}^{l_1}\sum_s \frac{P_s^{(2)}(x,t) - P_{s,0}(x)}{\gamma - 1}\, dx. \tag{5.32}$$

Figure 5.12 shows that the deposition of energy into the plasma has a remarkable dependence on the width of the pulse. A peak of $\Delta e_p/e_k(t=0) \approx 6\%$ is found at FWHM $= 10^5$ m, which corresponds to a perturbation with an amplitude of $V_{y,0} = 0.1 c_{\rm A}/\sqrt{2}$. At larger widths, the fraction of deposited energy decreases exponentially. This behavior can be understood by taking into account that the width of a Gaussian pulse is associated with a certain scale of wavelengths or wavenumbers. The previous statement can be checked by calculating the Fourier transform of the initial perturbation, which is defined as

$$\mathcal{F}\left[V_y^{(1)}\right] \equiv \frac{1}{2\pi}\int_{-\infty}^{\infty} V_y^{(1)}(x, t=0)\exp\left(-ik_x x\right)\, dx. \tag{5.33}$$

The Fourier transform of a Gaussian function in x is another Gaussian function in k_x. Moreover, the relation between the widths of the two Gaussians is inversely proportional, i.e., if the width of the initial perturbation is increased, the width of its Fourier transform becomes smaller. Hence, perturbations with larger widths are associated to smaller scales of wavenumbers and it has been shown in the previous studies that at smaller wavenumbers the coupling between the species of the plasma is stronger and the dissipation of energy is smaller. Figures 5.13 and 5.14 evidence this behavior. The top panels of Figure 5.13 show the evolution of the initial perturbation for the case of FWHM $= 2 \times 10^5$ m. For the sake of clarity, only the y-component of the velocity of protons is represented. The bottom panels display the corresponding Fourier transform. Although it is not very clear by simple inspection of the plot, it can be checked that the width of Fourier transform diminishes as time advances. The width in the initial step is FWHM $\approx 0.267 \times 10^{-4}$ m^{-1} and after 30 s it has been reduced to FWHM $\approx 0.204 \times 10^{-4}$ m^{-1}. Thus, the larger wavenumbers have been removed.

The reduction of the width is more obvious in Figure 5.14, which corresponds to an initial velocity pulse with FWHM $= 5 \times 10^4$ m. The Fourier transform on the left bottom panel has

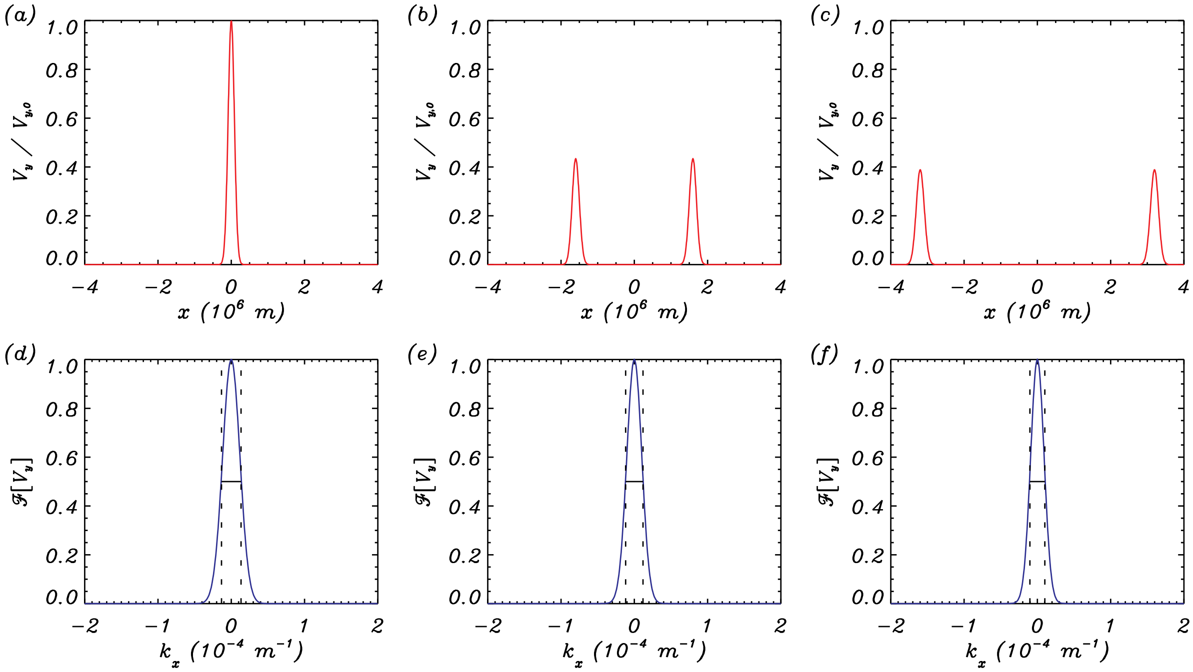

Figure 5.13: The upper panels show the normalized component y of the velocity of protons at (a) $t = 0$, (b) $t = 15$ s, and (c) $t = 30$ s of a simulation with an initial pulse with $FWHM = 2 \times 10^5$ m. The bottom panels show the corresponding normalized Fourier transform of the wave at the same times.

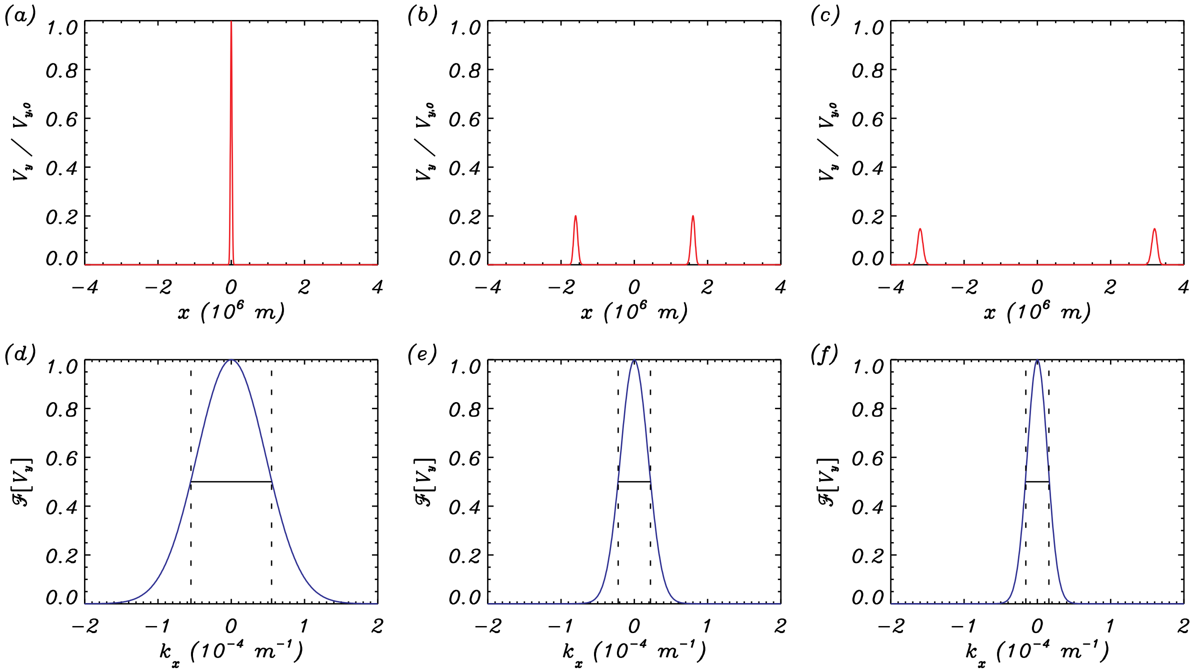

Figure 5.14: Same as Figure 5.13 but for a velocity pulse with $FWHM = 5 \times 10^4$ m.

a width given by FWHM $\approx 1.1 \times 10^{-4}$ m^{-1}, while the one displayed at the right panel has FWHM $\approx 0.31 \times 10^{-4}$ m^{-1}, i.e., it has been reduced to less than a third of the original width. In this case, large wavenumbers have been efficiently dissipated due to the effect of collisions and a non-negligible fraction of energy has been transfered to the background plasma.

Additional series of simulations have been performed to check if the trend examined in the previous paragraphs is also found under different conditions. In the first set of new simulations we apply the initial perturbation only to the ions, leaving neutrals initially at rest. In another series of simulations we perturb the y-component of the magnetic field instead of the velocity. The results are represented in the left and right panels of Figure 5.15, respectively. For the latter case, the magnetic energy density of the initial perturbation has been computed as

$$e_B(t=0) = \frac{1}{2l_1} \int_{-l_1}^{l_1} \frac{\left[B_y^{(1)}(x,t=0)\right]^2}{2\mu_0} dx. \tag{5.34}$$

The comparison of Figure 5.12 and the left panel of Figure 5.15 shows the same type of dependence of the energy deposition on the width of the perturbation. However, the peak value is $\sim 2\%$ when neutrals are initially at rest instead of $\sim 6\%$ when the perturbation is applied to all species. The reason may be that a considerable fraction of the energy has to be used in setting the neutrals in motion by means of collisions with ions: it must be reminded that under the chosen prominence conditions, neutrals account for 2/3 of the total mass of the plasma.

When the perturbation is applied to the y-component of the magnetic field, the dependence of the energy transfer is similar to the one found in the previous cases. The peak appears at FWHM $\approx 10^5$ m and it has the same value as in Figure 5.12, $\sim 6\%$. So, regarding the eventual energy deposition into the plasma due to wave dissipation, it is irrelevant whether the energy of the initial perturbation is kinetic or magnetic, as long as the total energy is the same.

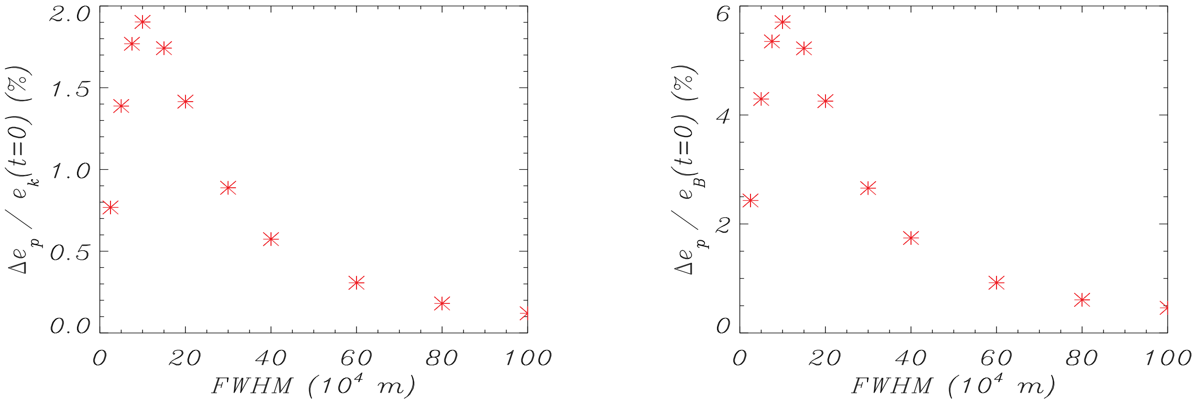

Figure 5.15: Percentage of the energy of the initial perturbation transformed into internal energy of the plasma. Left: the perturbation is applied to the y-component of the velocity of ions, leaving the neutrals at rest. Right: the perturbation is applied to the y-component of the magnetic field.

The results described in the paragraphs above seem to be in good agreement with the findings of Chapters 3 and 4, i.e., larger wavenumbers are more damped than smaller ones.

However, for very small values of the perturbation width, Figures 5.12 and 5.15 show a peculiar trend that diverges from what it might be expected: the efficiency of energy deposition decreases as the width of the initial perturbation is reduced (and the associated wavenumbers are larger). The reason may be related to the the fact that quite large amplitudes of the perturbations are needed when the widths are reduced in order to keep the initial energy the same in all simulations. As already mentioned, the energy of the initial perturbation is used in two ways, namely generation of waves and heating of the plasma. Hence, the internal energy has two components: one associated to the propagating wavefronts and another one related to energy gains and losses of the background plasma. A study of how those two components vary is illustrated by Figure 5.16, where the temporal evolution of the kinetic, magnetic, internal and total energy is displayed for four simulations.

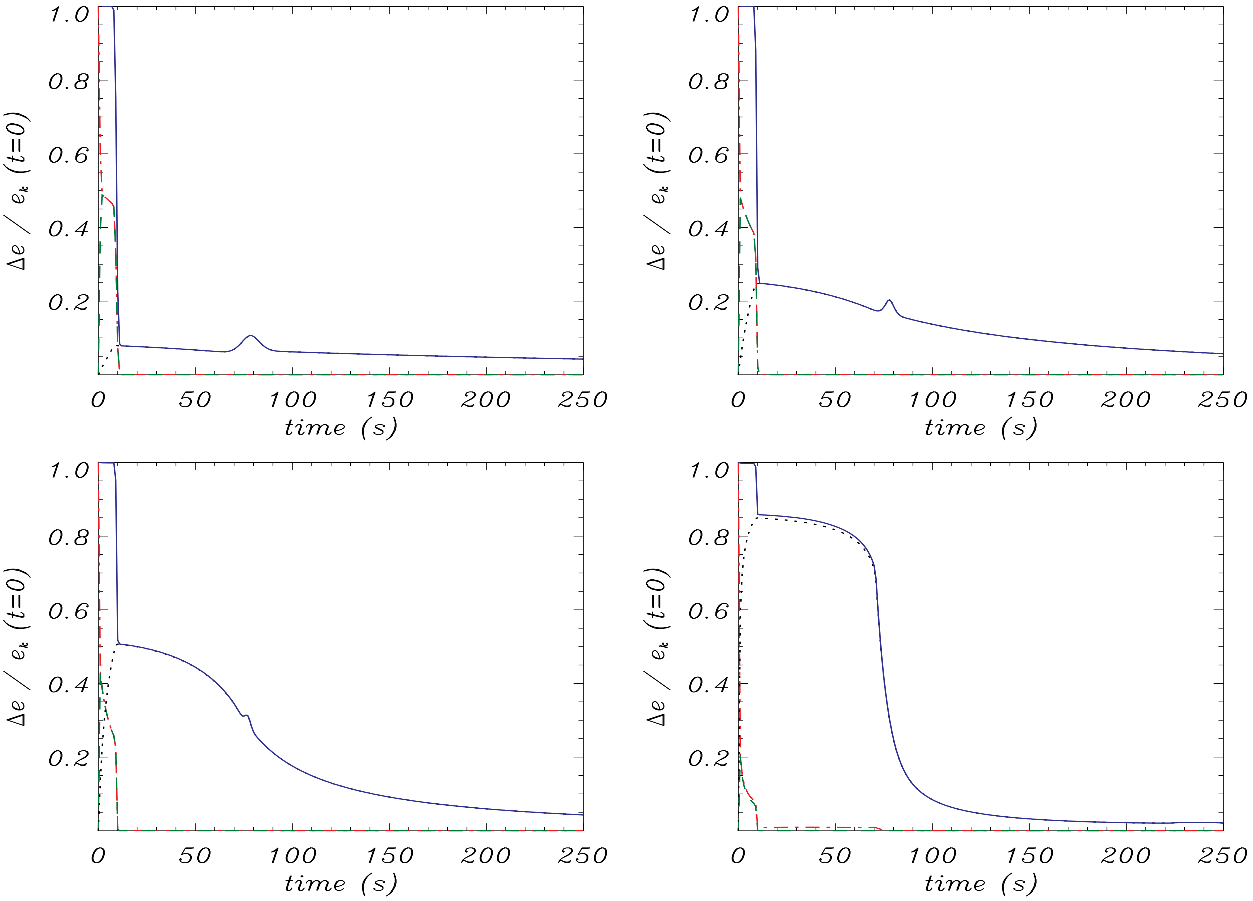

Figure 5.16: Temporal evolution of the different components of the energy density for several simulations where the initial perturbation has been applied to y-component of velocity. Red dashed lines represent the kinetic energy, green dashed lines represent the magnetic energy while the black dotted lines correspond to the internal energy. Finally, the blue solid lines represent the total energy, i.e., the sum of all three components. Top left: $V_{y,0} = 0.05c_{\mathrm{A}}$; top right: $V_{y,0} = 0.1/\sqrt{2}c_{\mathrm{A}}$; bottom left: $V_{y,0} = 0.1c_{\mathrm{A}}$; bottom right: $V_{y,0} = 0.2c_{\mathrm{A}}$.

The energies represented in Figure 5.16 are computed for the domain $x \in [-l_1, l_1]$. That is the reason why the total energy is not constant but diminishes with time: the waves are leaving the region of interest, carrying with them an important fraction of the initial total energy. This can be clearly noticed at $t \approx 10$ s, when most of the kinetic and magnetic energy goes to zero because Alfvén waves start crossing the boundaries. Later, the nonlinearly-generated sound waves also abandon the domain and the remaining energy is, then, truly associated with what is deposited in the plasma.

It must be noted that the peak that can be seen at $t \approx 80$ s is a consequence of the sound waves leaving the domain of interest. It does not mean that there is a sudden increase of energy in the simulation: when the whole domain of the simulation is considered, the total energy remains constant. The peak appears because the leading section of the sound wave has a negative contribution to the perturbation of the internal energy (as can be seen in the third row of Figure 5.11) and, as it leaves the smaller domain, generates the effect of an apparent rise of energy.

Focusing on the first seconds of the simulations, it can be seen that the amount of the initial energy that is transformed into internal energy increases with the amplitude of the perturbation (or, equivalently, when the width diminishes): the height of the dashed line (which represents the internal energy) at $t \approx 10$ s is larger in the bottom right panel, which corresponds to an amplitude of $V_{y,0} = 0.2c_{\mathrm{A}}$ and $\mathrm{FWHM} = 1.25 \times 10^4$ m. Thus, a larger amplitude of the initial perturbation corresponds to a larger increment of the internal energy. However, the distribution of this increment between the energy associated to the propagating wavefronts and that actually deposited into the plasma is not always the same: for instance, although the increase of internal energy is larger for $V_{y,0} = 0.2c_{\mathrm{A}}$ than for $V_{y,0} = 0.1c_{\mathrm{A}}$ (bottom left panel), at the end of the simulation the latter case retains more internal energy. This means that the contribution from waves represents a larger fraction of the internal energy when the amplitude of the perturbation increases, i.e., when the nonlinear effects are more relevant. The reason is that more energy is required to generate second-order waves when the amplitude of the first-order perturbation increases, which leaves a smaller fraction of the initial energy that can be used in heating the plasma.

5.4 Discussion

Nonlinear waves in partially ionized plasmas have been studied in this chapter by means of a multi-fluid model in which the effects of elastic collisions between all species of the plasma are taken into account. The general properties of nonlinear low-frequency Alfvén waves analyzed here are consistent with the results obtained by, e.g., Hollweg [1971], Rankin et al. [1994], Tikhonchuk et al. [1995] or Verwichte et al. [1999] for fully ionized plasmas, although differences appear due to the collisional interaction between ions and neutrals. For example, a second-order effect of nonlinear standing Alfvén waves is the appearance of a ponderomotive force that induces fluctuations in density, pressure and the longitudinal component of the velocity. For the case of standing waves in fully ionized plasmas, those variations are a combination of two modes with frequencies given by $2k_z c_{\mathrm{A}}$ and $2k_z c_{\mathrm{ie}}$, and their wavenumber is twice the value for the original perturbation. However, in partially ionized plasmas, the frequencies are proportional to the modified Alfvén speed, $\widetilde{c}_{\mathrm{A}}$ and the weighted mean sound speed, $\widetilde{c}_S$, respectively, when the small-wavenumber range is considered. Since in the plasmas that have been examined here $\widetilde{c}_{\mathrm{A}}$ is much lower than $\widetilde{c}_S$, the second-order oscillations induced by the ponderomotive force are dominated by the mode associated with the sound speed. Due to this ponderomotive force, the matter of the plasma tends to accumulate at the nodes of the magnetic field wave, although such accumulation is limited by the effect of pressure.

If the wavenumber of the perturbations is increased, the coupling between the different species is reduced and the collisional friction becomes relevant. It is then that multi-fluid effects become of interest. The plasma is heated and the effect of pressure against the accumulation of matter is enhanced. Due to the dissipation of the Alfvén wave and the increase of pressure by ion-neutral collisions, the result of the second-order perturbations is the displacement of matter from the nodes of the magnetic field towards the anti-nodes. At even higher frequencies, the species of the plasma become almost uncoupled from each other and the oscillation frequencies of the second-order waves tend to the values predicted for fully ionized plasmas, although they are strongly damped because of collisions. These results were obtained through the study of an initial perturbation that was weakly nonlinear. Cases with larger amplitudes have also been briefly analyzed and it was found that the profile of the nonlinear waves steepens as time advances and the frequency of the oscillations are slightly modified due to the more important variations of density, which is consistent with the findings of Tikhonchuk et al. [1995] or Verwichte et al. [1999].

The propagation of nonlinear pulses through a plasma with conditions akin to those of a solar quiescent prominence has also been examined. The simulations have shown that after the initial perturbation has been applied to the plasma, the pulse splits in two smaller pulses that propagate in opposite directions at a speed given by $\widetilde{c}_{\mathrm{A}}$. The amplitude of those pulses decreases with time due to the collisions between ions and neutrals, which dissipates a fraction of the energy of the initial perturbation. The amount of dissipated energy increases when the width of the perturbation decreases. A Fourier analysis has revealed that this behavior is due to the larger wavenumbers associated with a smaller width of the Gaussian pulse. According to the results from Chapter 4, waves with larger wavenumbers have shorter damping times due to ion-neutral collisions, while perturbations with smaller wavenumbers are more long-lived. Hence, the widths of the pulses increase and their amplitudes diminish with time as the larger wavenumbers are dissipated by the collisional friction.

As a second-order effect, the pulse generates two pairs of longitudinal waves that propagate in opposite directions. The phase speeds of those waves are given by $\widetilde{c}_{\mathrm{A}}$ and $\widetilde{c}_{S}$, respectively, as one of them is associated to the primary Alfvén wave and the other one with a nonlinearly generated sound wave. In addition, a fraction of the initial energy is deposited in the plasma in form of heat. Consequently, the temperature of the plasma rises. The numerical simulations show that the heating generally increases when the width of the pulse is decreased, which, as already mentioned, is associated with the efficient dissipation of small scales. However, at small enough widths, the computed heating decreases again. This may be explained by the highly nonlinear amplitude of the perturbations. When the amplitude of the initial perturbation is increased, the generation of the second-order waves requires a larger fraction of the initial energy; hence, there is a smaller fraction of energy available to be transformed into heat from the first-order wave. For conditions of solar quiescent prominences, the investigation presented here has found that a maximum of a 6% of the energy of the initial perturbation is finally used in heating the plasma. However, this value may vary if longer times, larger domains or different physical conditions are chosen for the simulations.

It must be noted that, in contrast with the previous chapters of this Thesis, here only the cases of standing and propagating waves generated by an impulsive driver have been considered.

Thus, it would be interesting to study in a future work how partial ionization affects nonlinear waves excited by a periodic driver. The continuous input of energy should have a stronger impact on the heating of the plasma in comparison with the limited energy provided by impulsive perturbations. Moreover, the effects of inhomogeneities, such as the gravitationally stratified plasma of the solar chromosphere, and realistic geometries for solar prominences should be investigated in the future. Furthermore, here we have limited ourselves to the simplest case of 1.5D simulations. More realistic studies in 2D and 3D, which would allow us to explore in depth the properties of magnetoacoustic waves, are left for future works.

Part III

Kelvin-Helmholtz instability in partially ionized plasmas

Chapter 6

KHI in partially ionized solar prominences*

6.1 Introduction

In the previous chapters, an extensive study of the propagation of perturbations in plasmas under the condition that the background medium is static has been presented. However, there are numerous physical situations, like, e.g., coronal mass ejections, astrophysical jets or supernova explosions, and environments like, for instance, molecular clouds, acretion disks or planetary magnetospheres, in which such condition is not applicable and needs to be removed. The consideration of non-static backgrounds leads to a rich variety of interesting phenomena like the Doppler shift of wave frequencies, the Rayleigh-Taylor instability, which may appear when a heavier fluid is superposed over a lighter one or when two fluids of different densities are accelerated toward each other (see Rayleigh [1882], Taylor [1950]), the two-stream instability caused by velocity drifts between the charged species that composed a plasma (see, e.g., Haeff [1949], Bohm and Gross [1949]), or the Kelvin-Helmholtz instability (KHI), which is the topic that will be analyzed in the present chapter, among many others.

It is known that the KHI is triggered by relative motions of the different layers of a stratified heterogeneous fluid or when there is a shear flow velocity at the interface that separates two fluids (see Helmholtz [1868], Thomson [1910]). In the presence of such a shear flow, if a small-amplitude perturbation is applied to the interface, a fraction of the energy of the flow is transferred to the perturbation and causes it to grow exponentially. However, this exponential growth is not maintained for all times but only during the interval in which the amplitudes of the perturbations are small compared to their respective background values, i.e., during the so-called linear regime. At longer times, the interface is greatly distorted and the initially small ripples are turned into vortexes before there is a turbulent mixing of the two fluids. This sequence of stages of the KHI is well illustrated by Figure 6.1, which represents a numerical simulation performed by Krasny [1988].

The investigation of the KHI is of great interest because it has been observed in a huge variety of environments. For instance, it has been seen in Earth's clouds and in Jupiter's atmo-

---

*This chapter is partially based on: Martínez-Gómez, D., Soler, R. and Terradas, J.; 2015, *Onset of the Kelvin-Helmholtz instability in partially ionized magnetic flux tubes*, Astronomy and Astrophysics, 578, A104 (Martínez-Gómez et al. [2015])

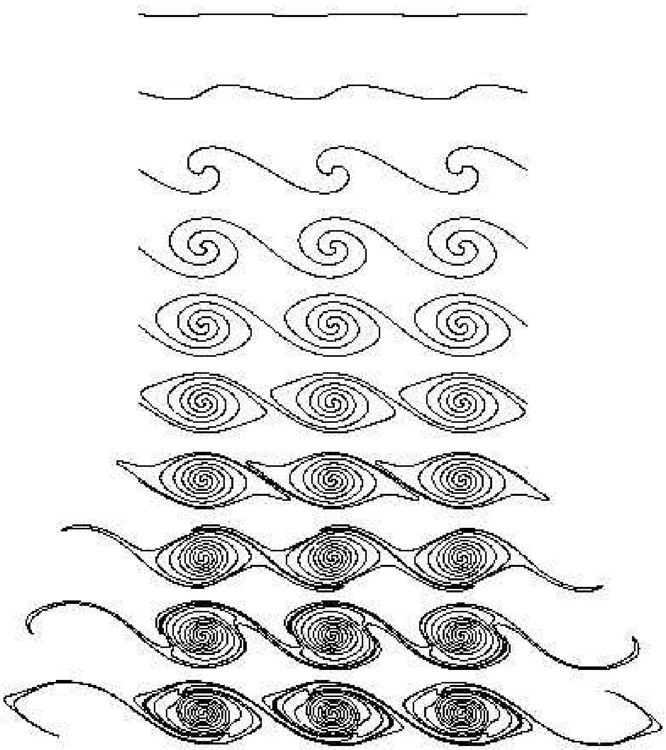

Figure 6.1: Development and evolution of a Kelvin-Helmholtz instability. Adapted from Krasny [1988].

sphere, as shown by Figure 6.2, or in the solar corona, from which an example is given in Figure 6.3. Furthermore, its presence has been suggested and studied in many other astrophysical contexts, such as Earth's aurora (Hallinan and Davis [1970]), the magnetopause (Hasegawa [1975]), planetary magnetospheres (Ogilvie and Fitzenreiter [1989]), protoplanetary disks (Gómez and Ostriker [2005]), cometary tails (Ershkovich et al. [1986]), jets and outflows (Keppens et al. [1999]), nebulae (Berné et al. [2010]) or molecular clouds (Shadmehri and Downes [2007]).

The main motivation of the investigation that will be performed later in this chapter is that observations of the solar atmosphere have shown the presence of turbulent flows in quiescent prominences (see, e.g., Berger et al. [2010], Ryutova et al. [2010]) and these phenomena have been interpreted in terms of the Rayleigh-Taylor instability and the KHI. Classical MHD studies (see, e.g., Chandrasekhar [1961], Drazin and Reid [1981]) have shown that, as a result of the effect of a longitudinal magnetic field, fully ionized incompressible plasmas are stable to small-amplitude perturbations if the velocity of the shear flow is lower than the root-mean-square Alfvén speed of the two fluids. Accordingly, the magnetohydrodynamic KHI can only be triggered by super-Alfvénic shear flows. Some of the turbulent flows detected in quiescent prominences exhibit a behavior that resembles the non-linear stage of the KHI. However, the measured velocities in those structures, which are lower than 30 km s^{-1} (Zirker et al. [1998], Berger et al. [2010]), are below the threshold for triggering this instability, which is of the order of 100 km s^{-1} (see, e.g., Terradas et al. [2008b]). Therefore, it might appear as if these turbulences cannot interpreted as consequences of KH instabilities. However, the condition previously mentioned only applies to fully ionized plasmas, and quiescent prominences are not

Figure 6.2: Left panel: clouds subject to the KHI (Credit: Brooks Martner, NOAA/ETL). Right panel: KHI in Jupiter's atmosphere seen during a Voyager 2 flyby (Credit: NASA.)

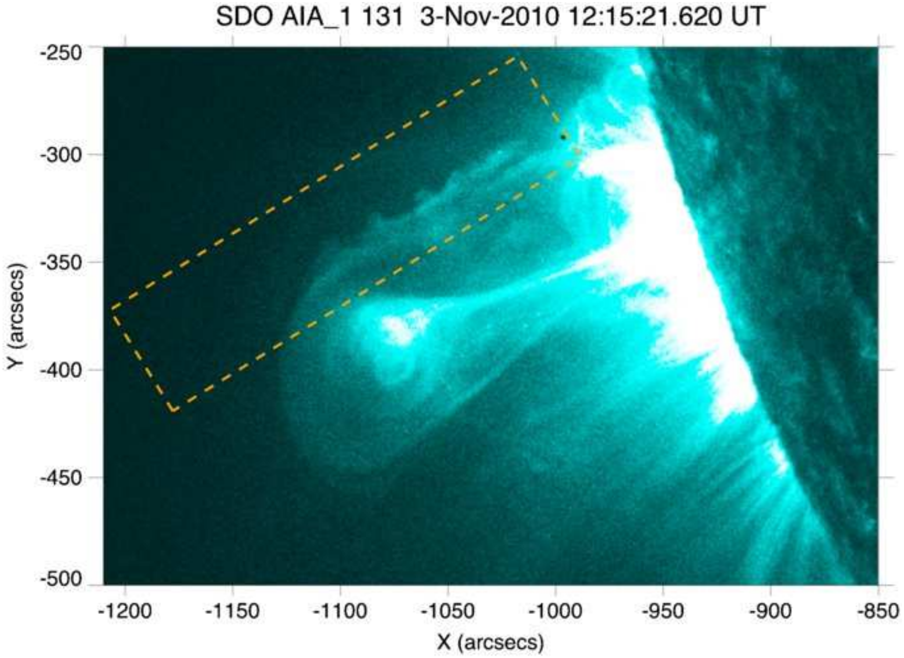

Figure 6.3: *SDO*/AIA image of KHI in a coronal mass ejection. From Foullon et al. [2011]

fully ionized, but are partially ionized, that is, they contain a neutral component that should not be overlooked. Those neutral particles do not feel the magnetic field and therefore ignore its stabilizing effect. The existence of this neutral component and its interaction with the charged particles may modify the criterion for the appearance of the KHI, possibly allowing the onset of the instability even for sub-Alfvénic velocities.

The KHI in partially ionized incompressible plasmas has already been studied, for example, by Watson et al. [2004] and Soler et al. [2012b], and it has been found that neutrals are unstable even for sub-Alfvénic flows and lead to the instability of the whole plasma. Therefore, in the absence of certain stabilizing factors such as surface tension, partially ionized incompressible plasmas are always unstable in the presence of a velocity shear. These results have been obtained for the case of a Cartesian interface but the magnetic field in the solar atmosphere is better represented by means of flux tubes. Hence, a step forward in the research of this topic is to analyze the possible onset of the KHI in partially ionized magnetic flux tubes. Such investigation is performed here by means of the multi-fluid theory presented in Chapter 2 and a model that considers a prominence thread to be a cool and dense cylindrical structure embedded in an hotter and lighter unbounded environment. The findings of this research are shown in Section 6.3, after some of the already mentioned basic results about the KHI are recovered and discussed in Section 6.2.

6.2 KHI in a Cartesian interface between two fully ionized plasmas

The linear regime of the Kelvin-Helmholtz instability in two media separated by a Cartesian interface has been extensively analyzed in, e.g., Chandrasekhar [1961]. In this section, the main results of that work are derived again, but following a different procedure similar to that shown in Soler et al. [2012b]. Such results are presented here with the goal of using them as a reference to compare with the analysis performed in the next section.

6.2.1 Hydrodynamic KHI

In the first place, the basic case of fluids that are not affected by magnetic fields is studied. To focus exclusively on how a longitudinal shear flow triggers the instability and produces an exponential growth of the amplitude of the perturbations before reaching the non-linear regime, effects like gravity, surface tension, compressibility or partial ionization of the fluids are neglected. The physical system to be analyzed is composed of two unbounded homogeneous fluids with densities ρ_a and ρ_b, respectively, which are separated by a sharp interface located at $x = 0$. Hence, the dependence of the density on the direction normal to the interface is given by

$$\rho(x) = \begin{cases} \rho_a & \text{if } x \leq 0, \\ \rho_b & \text{if } x > 0. \end{cases} \tag{6.1}$$

The two fluids are assumed to flow along the z-direction, with a discontinuous jump in the velocity $\boldsymbol{V_0}(x)$ at the interface. Hence, $\boldsymbol{V_0}(x) = (0, 0, U(x))^T$, with

$$U(x) = \begin{cases} U_a & \text{if } x \leq 0, \\ U_b & \text{if } x > 0. \end{cases} \tag{6.2}$$

At each of the two media separated by the interface, the incompressible small-amplitude perturbations obey the following equations:

$$\rho(x) \left(\frac{\partial \boldsymbol{V_1}}{\partial t} + \boldsymbol{V_0} \cdot \nabla \boldsymbol{V_1} \right) = -\nabla P_1 \tag{6.3}$$

and

$$\nabla \cdot \boldsymbol{V_1} = 0, \tag{6.4}$$

which can be combined to obtain the following expression for the pressure:

$$\nabla^2 P_1 = 0. \tag{6.5}$$

To perform a normal model analysis in time and Fourier analysis in space, the perturbations are expressed in the form $f(\boldsymbol{r}, t) = \hat{f}(x)\exp(i[k_y y + k_z z - \omega t])$. Therefore, Equation (6.5) leads to

$$\frac{\partial^2 \hat{P}_1}{\partial x^2} - \left(k_y^2 + k_z^2\right)\hat{P}_1 = 0, \tag{6.6}$$

whose solution is given by

$$\hat{P}_1(x) = A_1 \exp\left(k_\perp x\right) + A_2 \exp\left(-k_\perp x\right), \tag{6.7}$$

where the wavenumber $k_\perp$ is defined as $k_\perp \equiv \sqrt{k_y^2 + k_z^2}$. The pressure is required to vanish when $x \to \pm\infty$. Thus,

$$\hat{P}_1(x) = \begin{cases} A_1 \exp\left(k_\perp x\right) & \text{if } x \leq 0, \\ A_2 \exp\left(-k_\perp x\right) & \text{if } x > 0. \end{cases} \tag{6.8}$$

The boundary conditions require that the pressure is the same at both sides of the interface. Therefore, $A_1 = A_2 \equiv A$. Furthermore, the x-component of the Lagrangian displacement should also be continuous at $x = 0$. The relation between the velocities and the Lagrangian displacement, denoted by $\boldsymbol{\xi}$, is given by

$$\boldsymbol{V} = \frac{D\boldsymbol{\xi}}{Dt} \equiv \frac{\partial \boldsymbol{\xi}}{\partial t} + \boldsymbol{V} \cdot \nabla \boldsymbol{\xi}. \tag{6.9}$$

which, after linearization, leads to

$$V_{1x} = \frac{\partial \xi_x}{\partial t} + U(x)\frac{\partial \xi_x}{\partial z}, \tag{6.10}$$

Hence, the x-component of Equation (6.3) can be written as

$$\rho(x)\left(\frac{\partial}{\partial t} + U(x)\frac{\partial}{\partial z}\right)^2 \xi_x = -\frac{\partial P_1}{\partial x}. \tag{6.11}$$

The combination of Equations (6.11) and (6.8) produces the following relations:

$$\begin{cases} \rho_a \left(\omega - U_a k_z\right)^2 \xi_x = A k_\perp \exp\left(k_\perp x\right) & \text{if } x \leq 0, \\ \rho_b \left(\omega - U_b k_z\right)^2 \xi_x = -A k_\perp \exp\left(-k_\perp x\right) & \text{if } x > 0. \end{cases} \tag{6.12}$$

The boundary condition for the Lagrangian displacements at $x = 0$ implies that

$$\frac{A k_\perp}{\rho_a \left(\omega - U_a k_z\right)^2} = \frac{-A k_\perp}{\rho_b \left(\omega - U_b k_z\right)^2}. \tag{6.13}$$

Hence, the dispersion relation that describes the properties of the perturbations at the interface is given by

$$\rho_a \left(\omega - U_a k_z\right)^2 + \rho_b \left(\omega - U_b k_z\right)^2 = 0, \tag{6.14}$$

whose solution is

$$\omega = k_z \frac{\rho_a U_a + \rho_b U_b}{\rho_a + \rho_b} \pm i k_z \Delta U \frac{\sqrt{\rho_a \rho_b}}{\rho_a + \rho_b}, \tag{6.15}$$

where $\Delta U \equiv |U_a - U_b|$ is the shear flow velocity. The positive imaginary part of one of the two possible solutions means that the amplitude of the perturbations grows with time. This growing solution exists for any value of ΔU different from zero. Therefore, the studied fluid is always unstable in the presence of a longitudinal shear flow. However, it must be noted that the previous statement is only true for the conditions chosen for the present analysis. It is not accurate when more realistic conditions are studied, as shown in the work of Chandrasekhar [1961] for the cases when neither the effects of gravity nor of surface tension are neglected, when compressibility is taken into account, as shown by Soler et al. [2012b], or when the fluids are affected by magnetic fields, as it will be discussed below. Another remarkable conclusion that can be extracted from Equation (6.15) is that the growth rates are proportional to the wavenumber, k_z, which means that the shorter the wavelength, the most unstable the perturbation.

6.2.2 Magnetohydrodynamic KHI

Here, the effect of a magnetic field oriented in the same direction as the shear flow is studied. Under these conditions, the perturbations in each media are described by the following linearized equations:

$$\rho(x) \left(\frac{\partial}{\partial t} + U(x) \frac{\partial}{\partial z} \right) \boldsymbol{V_1} = -\nabla P_1 + \frac{1}{\mu_0} \left(\nabla \times \boldsymbol{B_1} \right) \times \boldsymbol{B_0}, \tag{6.16}$$

$$\left(\frac{\partial}{\partial t} + U(x) \frac{\partial}{\partial z} \right) \boldsymbol{B_1} = \nabla \times \left(\boldsymbol{V_1} \times \boldsymbol{B_0} \right), \tag{6.17}$$

and

$$\nabla \cdot \boldsymbol{V_1} = 0. \tag{6.18}$$

The equilibrium magnetic field may be different in each media, but the equilibrium total pressure must be continuous across the interface, which imposes some restrictions on the values of the equilibrium pressure and magnetic field strength. Here, the magnetic field is chosen to have the same value at both sides of the interface. Thus, it is given by $\boldsymbol{B_0} = (0, 0, B_0)^T$.

The combination of Equations (6.16) and (6.18) gives

$$\nabla^2 P_T = 0, \tag{6.19}$$

where the variable P_T is the sum of the thermal and magnetic pressure perturbations, i.e., $P_T \equiv P_1 + (B_0 B_{1z})/\mu_0$. Hence, the solutions to this equation have the same form as those shown in Equation (6.7).

Then, Equations (6.16) and (6.18) can be expressed as functions of the Lagrangian displacements,

$$\rho(x) \left(\frac{\partial}{\partial t} + U(x) \frac{\partial}{\partial z} \right)^2 \boldsymbol{\xi} = -\nabla P_T + \frac{1}{\mu_0} \boldsymbol{B_0} \cdot \nabla \boldsymbol{B_1}, \tag{6.20}$$

and

$$\left(\frac{\partial}{\partial t} + U(x) \frac{\partial}{\partial z} \right) \boldsymbol{B_1} = \nabla \times \left[\left(\frac{\partial}{\partial t} + U(x) \frac{\partial}{\partial z} \right) \boldsymbol{\xi} \times \boldsymbol{B_0} \right], \tag{6.21}$$

respectively. Following the same procedure as in the hydrodynamic case, it is possible to obtain a new dispersion relation, namely

$$\rho_a\left[(\omega - U_a k_z)^2 - \omega_{\mathrm{A},a}^2\right] + \rho_b\left[(\omega - U_b k_z)^2 - \omega_{\mathrm{A},b}^2\right] = 0, \tag{6.22}$$

where ω_A is the Alfvén frequency, which is different for each media. The solution to this equation is given by

$$\omega = k_z \frac{\rho_a U_a + \rho_b U_b}{\rho_a + \rho_b} \pm k_z \left[\frac{B_a^2 + B_b^2}{\mu_0(\rho_a + \rho_b)} - \Delta U^2 \frac{\rho_a \rho_b}{(\rho_a + \rho_b)^2}\right]^{1/2}. \tag{6.23}$$

Hence, the solutions have an imaginary part only when the term in brackets is lower than zero. Contrary to the hydrodynamic case, there is a velocity threshold below which the perturbations are stable and the magnetohydrodynamic KHI only appears if

$$\Delta U > \sqrt{\frac{B_a^2 + B_b^2}{\mu_0} \frac{\rho_a + \rho_b}{\rho_a \rho_b}}, \tag{6.24}$$

or, equivalently,

$$\Delta U > \sqrt{\frac{(\rho_a c_{\mathrm{A},a}^2 + \rho_b c_{\mathrm{A},b}^2)(\rho_a + \rho_b)}{\rho_a \rho_b}}. \tag{6.25}$$

The velocity threshold, which is super-Alfvénic as can be checked from the equation above, is caused by the effect of the longitudinal magnetic field.

6.3 KHI in partially ionized magnetic flux tubes

The two results presented in the previous section are applicable to fluids that are not affected by magnetic fields and to fully ionized plasmas, respectively, but they are not accurate when applied to the investigation of threads in solar prominences. There are two reasons for this inaccuracy. In the first place, as already mentioned, quiescent prominences are not fully ionized but are partially ionized. Hence, it is necessary to take into account the interaction between the ionized and the neutral components of the plasma to properly investigate the possible onset of the KHI in those environments. The second reason is geometrical: prominence threads are better represented by magnetic flux tubes embedded in a hotter and lighter medium.

In this section, a model that takes into account those two properties of prominence threads is developed. Then, the multi-fluid theory from Chapter 2 is applied to that model with the goal of investigating the influence of partial ionization on the onset of KHI in magnetic flux tubes and comparing the new results with those shown in Section 6.2 and with data from observations of solar prominences.

6.3.1 Model, equations and derivation of the dispersion relation

Here, the equilibrium state is a partially ionized cylindrical magnetic flux tube of radius a embedded in an unbounded medium. The system is described by means of cylindrical coordinates, namely r, φ, and z, for the radial, azimuthal, and longitudinal coordinates, respectively.

A sketch of the model can be found in Figure 6.4. The subscripts “0” and “*ex*” denote quantities related to the internal and the external plasma, respectively. The densities of ions and neutrals are ρ_i and ρ_n and only depend on the radial direction as

$$\rho_i(r) = \begin{cases} \rho_{i,0} & \text{if } r \leq a, \\ \rho_{i,ex} & \text{if } r > a, \end{cases} \tag{6.26}$$

$$\rho_{\mathrm{n}}(r) = \begin{cases} \rho_{n,0} & \text{if } r \leq a, \\ \rho_{n,ex} & \text{if } r > a. \end{cases} \tag{6.27}$$

Hence, there is an abrupt jump in density between the internal and external plasmas. The magnetic field is constant and pointing along the flux tube axis, with the same value in both media, $\boldsymbol{B_0}(r,\varphi,z) = (0,0,B_0)^T$. In addition, there is a longitudinal mass flow with constant velocity denoted by U. The flow velocity is discontinuous at the boundary of the flux tube.

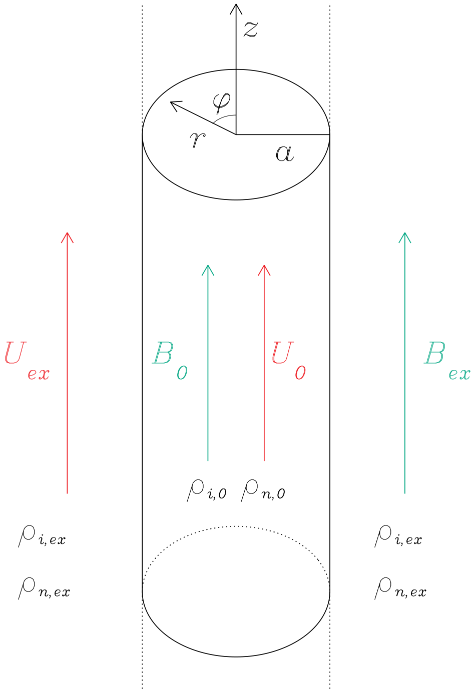

Figure 6.4: Sketch of the model

To study this system, a two-fluid theory, i.e., a simplified version of the system of equations presented in Chapter 2, is used. It assumes that the plasma is composed of an ionized fluid made of ions and electrons and a second fluid made of neutral particles only. Those two fluids may interact by means of momentum-transfer collisions between ions and neutrals. In addition, only small-amplitude perturbations are studied, so the linearized version of the equations is employed. The set of two-fluid equations that describe the behavior of linear incompressible perturbations superimposed on the equilibrium state is

$$\rho_i \left(\frac{\partial}{\partial t} + U \frac{\partial}{\partial z} \right) \boldsymbol{V_i} = -\nabla P_{ie} + \frac{1}{\mu_0} \left(\nabla \times \boldsymbol{B_1} \right) \times \boldsymbol{B_0} - \rho_n \nu_{ni} \left(\boldsymbol{V_i} - \boldsymbol{V_n} \right), \tag{6.28}$$

$$\rho_n \left(\frac{\partial}{\partial t} + U \frac{\partial}{\partial z} \right) \boldsymbol{V_n} = -\nabla P_n - \rho_n \nu_{ni} \left(\boldsymbol{V_n} - \boldsymbol{V_i} \right), \tag{6.29}$$

$$\left(\frac{\partial}{\partial t}+U\frac{\partial}{\partial z}\right)\boldsymbol{B_1}=\nabla\times\left(\boldsymbol{V_i}\times\boldsymbol{B_0}\right), \tag{6.30}$$

$$\nabla\cdot\boldsymbol{V_i}=\nabla\cdot\boldsymbol{V_n}=0, \tag{6.31}$$

where $\boldsymbol{V_i}$ and $\boldsymbol{V_n}$ are the velocity perturbations of ions and neutrals, and P_{ie} and P_n are the pressure perturbations of the ion-electrons and neutrals fluids.

Once again, it is helpful to use the Lagrangian displacements instead of the velocities as primary variables. In the present investigation, the relation between the perturbations of velocity and the Lagrangian displacements is given by

$$\boldsymbol{V_i}=\frac{\partial\boldsymbol{\xi_i}}{\partial t}+U\frac{\boldsymbol{\xi_i}}{\partial z};\ \boldsymbol{V_n}=\frac{\partial\boldsymbol{\xi_n}}{\partial t}+U\frac{\boldsymbol{\xi_n}}{\partial z}. \tag{6.32}$$

Thus, Equations (6.28)-(6.31) are transformed into

$$\rho_i\left(\frac{\partial}{\partial t}+U\frac{\partial}{\partial z}\right)^2\boldsymbol{\xi_i}=-\nabla P_{ie}+\frac{1}{\mu_0}\left(\nabla\times\boldsymbol{B_1}\right)\times\boldsymbol{B_0}-\rho_n\nu_{ni}\left(\frac{\partial}{\partial t}+U\frac{\partial}{\partial z}\right)\left(\boldsymbol{\xi_i}-\boldsymbol{\xi_n}\right), \tag{6.33}$$

$$\rho_n\left(\frac{\partial}{\partial t}+U\frac{\partial}{\partial z}\right)^2\boldsymbol{\xi_n}=-\nabla P_n-\rho_n\nu_{ni}\left(\frac{\partial}{\partial t}+U\frac{\partial}{\partial z}\right)\left(\boldsymbol{\xi_n}-\boldsymbol{\xi_i}\right), \tag{6.34}$$

$$\left(\frac{\partial}{\partial t}+U\frac{\partial}{\partial z}\right)\boldsymbol{B_1}=\nabla\times\left[\left(\frac{\partial}{\partial t}+U\frac{\partial}{\partial z}\right)\boldsymbol{\xi_i}\times\boldsymbol{B_0}\right], \tag{6.35}$$

and

$$\nabla\cdot\left(\frac{\partial}{\partial t}+U\frac{\partial}{\partial z}\right)\boldsymbol{\xi_i}=\nabla\cdot\left(\frac{\partial}{\partial t}+U\frac{\partial}{\partial z}\right)\boldsymbol{\xi_n}=0, \tag{6.36}$$

respectively.

The next step in the procedure to obtain the dispersion relation is to perform a normal mode analysis. Since the equilibrium is uniform in the azimuthal and longitudinal directions, the perturbations are expressed as proportional to $\exp(im\varphi+ik_z z)$, where m and k_z are the azimuthal and longitudinal wavenumbers, respectively. The dependence of the perturbations on the radial direction is retained and the temporal dependence is set as $\exp(-i\omega t)$, where ω is the angular frequency.

From the radial component of Equations (6.33), after combining it with the induction equation, and (6.34), it is possible to obtain the following expressions:

$$\frac{\partial P_T}{\partial r}=\rho_i\left(\Theta^2-\omega_A^2+i\chi\nu_{ni}\Theta\right)\xi_{r,i}-i\rho_n\nu_{ni}\Theta\xi_{r,n} \tag{6.37}$$

and

$$\frac{\partial P_n}{\partial r}=-i\rho_n\nu_{ni}\Theta\xi_{r,i}+\rho_n\Theta(\Theta+i\nu_{ni})\xi_{r,n}, \tag{6.38}$$

respectively, where $\Theta=\omega-Uk_z$ is the Doppler-shifted frequency, $\omega_{\mathrm{A}}=k_z c_{\mathrm{A}}$ is the Alfvén frequency, and the variable P_T is the sum of the thermal and magnetic pressures of the ionized fluid, and is defined as

$$P_T=P_{ie}+\frac{\boldsymbol{B_0}\cdot\boldsymbol{B_1}}{\mu}=P_{ie}+\frac{B_0B_{1z}}{\mu_0}. \tag{6.39}$$

Then, the azimuthal and longitudinal components of Equations (6.33), (6.34) and (6.35) can be combined with the incompressibility condition, Equation (6.36), to obtain the other two equations that are needed to solve the system, namely,

$$\rho_i \left(\widetilde{\Theta}^2 - \omega_{\mathrm{A}}^2\right) \frac{1}{r} \frac{\partial (r \xi_{r,i})}{\partial r} = \left(\frac{m^2}{r^2} + k_z^2\right) \left(P_T + i \frac{\nu_{ni}}{\Theta + i\nu_{ni}} P_n\right), \tag{6.40}$$

and

$$\begin{aligned} \rho_n \rho_i \left(\widetilde{\Theta}^2 - \omega_{\mathrm{A}}^2\right) \frac{1}{r} \frac{\partial (r \xi_{r,n})}{\partial r} &= i \frac{\nu_{ni}}{\Theta + i\nu_{ni}} \rho_n \left(\frac{m^2}{r^2} + k_z^2\right) P_T \\ &- \left(\frac{m^2}{r^2} + k_z^2\right) \left[\frac{\rho_n \nu_{ni}^2}{(\Theta + i\nu_{ni})^2} - \frac{\rho_i \left(\widetilde{\Theta}^2 - \omega_{\mathrm{A}}^2\right)}{\Theta(\Theta + i\nu_{ni})}\right] P_n, \end{aligned} \tag{6.41}$$

where the parameter $\widetilde{\Theta}$, which will be referred to as the modified frequency, is defined through the following relation:

$$\widetilde{\Theta}^2 = \Theta^2 \left(1 + \frac{i\chi\nu_{ni}}{\Theta + i\nu_{ni}}\right) \tag{6.42}$$

Now, the combination of Equations (6.37), (6.38), (6.40), and (6.41) leads to two uncoupled equations for the pressures, namely

$$\frac{\partial^2 P_T}{\partial r^2} + \frac{1}{r} \frac{\partial P_T}{\partial r} - \left(k_z^2 + \frac{m^2}{r^2}\right) P_T = 0, \tag{6.43}$$

and

$$\frac{\partial^2 P_n}{\partial r^2} + \frac{1}{r} \frac{\partial P_n}{\partial r} - \left(k_z^2 + \frac{m^2}{r^2}\right) P_n = 0, \tag{6.44}$$

whose solutions are combinations of modified Bessel functions of the first and second kind, $I_m(k_z r)$ and $K_m(k_z r)$, respectively. It is required that the solutions are regular at $r = 0$ and vanishing at $r \to \infty$. Hence,

$$P_T(r) = \begin{cases} A_1 I_m(k_z r) & \text{if } r \leq a, \\ A_2 K_m(k_z r) & \text{if } r > a, \end{cases} \tag{6.45}$$

$$P_n(r) = \begin{cases} A_3 I_m(k_z r) & \text{if } r \leq a, \\ A_4 K_m(k_z r) & \text{if } r > a, \end{cases} \tag{6.46}$$

where $A_1 - A_4$ are arbitrary constants. In turn, the radial components of the Lagrangian displacements of the two fluids are related to P_T and p_{n} by

$$\xi_{r,i} = \frac{1}{\rho_i \left(\widetilde{\Theta}^2 - \omega_{\mathrm{A}}^2\right)} \left(\frac{\partial P_T}{\partial r} + i \frac{\nu_{ni}}{\Theta + i\nu_{ni}} \frac{\partial P_n}{\partial r}\right) \tag{6.47}$$

and

$$\begin{aligned} \xi_{r,n} = &\left(\frac{1}{\rho_n \Theta \left(\Theta + i\nu_{ni}\right)} - \frac{\nu_{ni}^2}{\left(\Theta + i\nu_{ni}\right)^2} \frac{1}{\rho_i \left(\widetilde{\Theta}^2 - \omega_{\mathrm{A}}^2\right)}\right) \frac{\partial P_n}{\partial r} \\ &+ i \frac{\nu_{ni}}{\Theta + i\nu_{ni}} \frac{1}{\rho_i \left(\widetilde{\Theta}^2 - \omega_{\mathrm{A}}^2\right)} \frac{\partial P_T}{\partial r}. \end{aligned} \tag{6.48}$$

The dispersion relation that describes the behavior of the waves in this system is found by imposing the conditions that P_T, P_n, $\xi_{r,i}$ and $\xi_{r,n}$ are continuous at $r = a$, that is, at the boundary of the tube. After applying the boundary conditions, a system of algebraic equations for the constants $A_1 - A_4$ is obtained. The non-trivial solution to the system provides the dispersion relation, which is given by

$$\begin{aligned}\left[\frac{I'_m(k_z a)}{I_m(k_z a)}\rho_{n,ex}\Theta_{ex}\left(\Theta_{ex}+i\nu_{ni,ex}\right)-\frac{K'_m(k_z a)}{K_m(k_z a)}\rho_{n,0}\Theta_0\left(\Theta_0+i\nu_{ni,0}\right)\right]&\\ \times\left[\frac{I'_m(k_z a)}{I_m(k_z a)}\rho_{i,ex}\left(\widetilde{\Theta}^2_{ex}-\omega^2_{\mathrm{A,ex}}\right)-\frac{K'_m(k_z a)}{K_m(k_z a)}\rho_{i,0}\left(\widetilde{\Theta}^2_0-\omega^2_{\mathrm{A},0}\right)\right]&\\ +\frac{I'_m(k_z a)}{I_m(k_z a)}\frac{K'_m(k_z a)}{K_m(k_z a)}\frac{\rho_{n,0}\rho_{n,ex}\Theta_0\Theta ex}{\left(\Theta_0+i\nu_{ni,0}\right)\left(\Theta_{ex}+i\nu_{ni,ex}\right)}&\\ \times\left[\nu_{ni,0}\left(\Theta_{ex}+i\nu_{ni,ex}\right)-\nu_{ni,ex}\left(\Theta_0+i\nu_{ni,0}\right)\right]^2=0,&\qquad(6.49)\end{aligned}$$

where the prime denotes the derivative of the modified Bessel function with respect to its argument.

For a given longitudinal wavenumber, Equation (6.49) yields an infinite number of oscillation modes, each one associated to a particular azimuthal wavenumber, m. Some of these modes are known with specific names due to their importance in the investigations of waves in flux tubes (see, e.g., Edwin and Roberts [1983]). For instance, the mode with $m = 0$, which produces expansions and contractions of the plasma tube but without displacing its axis, is called the *sausage* mode, and the mode with $m = 1$, which is the only one that causes displacements of the axis of the cylinder, is known as *kink* mode.

In the limit when $k_z a \ll 1$, which is known as the thin tube (TT) aproximation, the dispersion relation becomes much simpler and some of the previous known results about the KHI can be recovered. For any azimuthal wavenumber $m \neq 0$, if an asymptotic expansion of the modified Bessel functions for small arguments and only the first term in the expansion is kept, the TT dispersion relation is given by

$$\begin{aligned}\left[\rho_{i,0}\left(\Theta_0\left(\Theta_0+i\chi_0\nu_{ni,0}\right)-\omega^2_{\mathrm{A},0}\right)+\rho_{i,ex}\left(\Theta_{ex}\left(\Theta_{ex}+i\chi_{ex}\nu_{ni,ex}\right)-\omega^2_{\mathrm{A},ex}\right)\right]&\\ \times\left[\rho_{n,0}\Theta_0\left(\Theta_0+i\nu_{ni,0}\right)+\rho_{n,ex}\Theta_{ex}\left(\Theta_{ex}+i\nu_{ni,ex}\right)\right]&\\ +\left[\rho_{n,0}\Theta_0\nu_{ni,0}+\rho_{n,ex}\Theta_{ex}\nu_{ni,ex}\right]^2=0.&\qquad(6.50)\end{aligned}$$

The expression above coincides with that already derived by Soler et al. [2012b] in their study of the KHI in a Cartesian interface. Hence, the geometrical effect associated with the cylindrical magnetic tube disappears when the TT approximation is considered. Furthermore, if the terms associated with the ion-neutral collisions are neglected, which means that ions are decoupled from neutrals, the dispersion relation becomes

$$\left[\rho_{i,0}(\Theta^2_0-\omega^2_{\mathrm{A},0})+\rho_{i,ex}(\Theta^2_{ex}-\omega^2_{\mathrm{A},ex})\right]\left[\rho_{n,0}\Theta^2_0+\rho_{n,ex}\Theta^2_{ex}\right]=0, \qquad (6.51)$$

from which it is easy to recover the solutions corresponding to the classical hydrodynamic and magnetohydrodynamic KHI already shown in Section 6.2.

To obtain the solutions for the coupled case, the full dispersion relation is generally solved using numerical methods. However, it is possible to find an approximate analytical solution when the ion-neutral coupling is strong and sub-Alfvénic flows are considered. It is known that for sub-Alfvénic flows, the only unstable solution in the uncoupled case is that associated with neutrals, since the magnetic field is able to stabilize ions. Thus, the way of obtaining the approximate solution is trying to find a correction to the neutrals-related solution due to ion-neutral collisions. To do so, the frequency is written as $\omega = \omega_0 + i\gamma$, where ω_0 is the neutrals' unstable solution given by Equation (6.15) and γ is a small correction. The previous expression for the frequency is inserted into the TT dispersion relation and only the terms up to first order in γ and second order in U_0 are kept, while the external flow velocity is taken to be zero, $U_{ex} = 0$. After some algebraic manipulations, a solution for γ can be found and the the approximate solution for the frequency is given by

$$\omega \approx \frac{k_z U_0 \rho_{n,0}}{\rho_{n,0} + \rho_{n,ex}} + i\frac{2k_z^2 U_0^2 \rho_{n,0}\rho_{n,ex}}{(\rho_{n,0} + \rho_{n,ex})(\nu_{ni,0}\rho_{n,0} + \nu_{ni,ex}\rho_{n,ex})}. \tag{6.52}$$

The previous formula shows that the approximated growth rate has a quadratic dependence on the flow velocity and is inversely proportional to the collision frequencies. Hence, the growth rate is lower in the strongly coupled case than in the uncoupled case, which means that ion-neutral collisions have a stabilizing effect on the neutral fluid. The question then arises: are ion-neutral collisions able to completely stabilize neutrals for sub-Alfvénic flows, as in the fully ionized case, or is the neutral component of the plasma always unstable?

6.3.2 Exploring the parameter space

In this section, a study of the dependence of the solutions of the dispersion relation with respect to various physical parameters will be performed. In addition, those results will be compared with the analytical approximation shown in the previous section and the range of validity of the latter will be checked. To keep this analysis as general as possible, dimensionless parameters will be used here, while actual physical parameters will be employed later in Section 6.3.3, in which an application to solar prominence threads will be given.

Here, for simplicity, the collision frequency is chosen to have the same value in both internal and external plasmas, i.e., $\nu_{ni,0} = \nu_{ni,ex} \equiv \nu_{ni}$. In addition, the focus is put on the kink mode; hence, $m = 1$.

The exploration of the parameter space is started with the study of the dependence of the solutions of the dispersion relation with respect to the shear flow velocity. Thus, ΔU is taken as a free variable. Then, the dispersion relation is solved using the following parameters: $\rho_{i,0}/\rho_{i,ex} = 2$, $\rho_{n,0}/\rho_{n,ex} = 2$, $\rho_{n,0}/\rho_{i,0} = 1$, $c_{\mathrm{A},0} = 1$ and $k_z a = 0.1$. The top and the bottom panels of Figure 6.5 display the normalized real and imaginary parts of the frequency, respectively, as functions of the normalized shear flow velocity, $\Delta U/c_{\mathrm{A},0}$ for three different degrees of coupling. The normalization parameter ω_k is known as the kink frequency, which corresponds to the frequency of the kink wave in the TT limit for a fully ionized plasma (see, e.g., Ryutov and Ryutova [1976], Spruit [1981]), and is given by

$$\omega_k = k_z\sqrt{\frac{\rho_{i,0}c_{A,0}^2 + \rho_{i,ex}c_{A,ex}^2}{\rho_{i,0} + \rho_{i,ex}}}. \tag{6.53}$$

Panels a), b) and c) correspond to the cases of weak coupling ($\nu_{ni}/\omega_k = 0.1$), intermediate coupling ($\nu_{ni}/\omega_k = 1$), and strong coupling ($\nu_{ni}/\omega_k = 10$), respectively. The red symbols

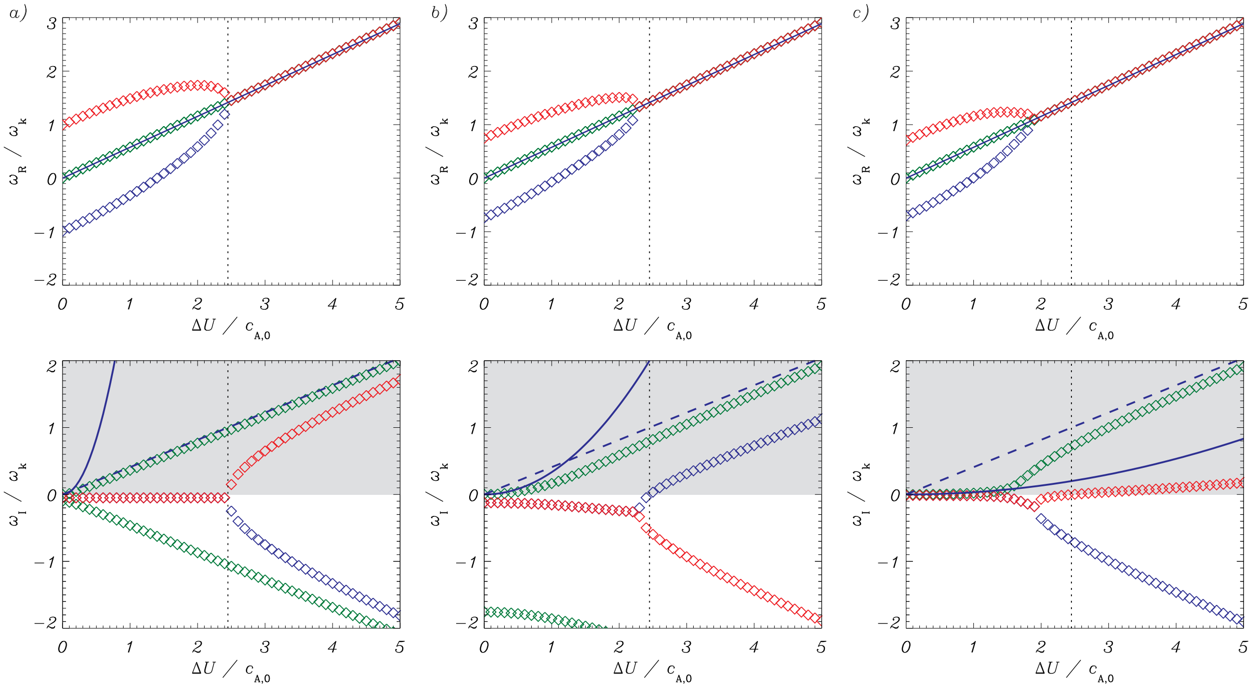

Figure 6.5: Upper panels: $\omega_{\rm R}/\omega_{\rm k}$ as a function of the normalized shear flow velocity, $\Delta U/c_{\rm A,0}$, for $k_z a = 0.1$, $m = 1$, and three different collision frequencies (***a)*** $\nu_{\rm ni}/\omega_{\rm k} = 0.1$, ***b)*** $\nu_{\rm ni}/\omega_{\rm k} = 1$ and ***c)*** $\nu_{\rm ni}/\omega_{\rm k} = 10$). Lower panels: $\omega_I/\omega_{\rm k}$ as a function of $\Delta U/c_{\rm A,0}$ for the same set of parameters as above. The symbols represent the solutions of the full dispersion relation, i.e., Equation (6.49); the blue solid lines correspond to the analytical approximation given by Equation (6.52), and the blue dashed lines show the unstable branch of the neutral fluid when there is no coupling (Equation (6.15)).

represent the solutions obtained numerically from the complete dispersion relation, Equation (6.49). This results are compared with the analytical solutions in the strongly coupled limit, which are represented by the blue solid lines, and in the uncoupled case, displayed as blue dashed lines. In addition, the classical shear flow velocity threshold for the KHI in a fully ionized plasma, given by Equation 6.25, is represented by the vertical dotted lines.

By inspecting the top panels of Figure 6.5, it can be seen that the real part of the frequency has a very similar behavior in the three studied cases. Initially, when the shear flow velocity is zero, there are two solutions with nonzero ω_R. These solutions are associated with the ionized fluid and correspond to the usual kink magnetohydrodynamic waves found in fully ionized tubes (Edwin and Roberts [1983]): the solution with $\omega_R > 0$ is the forward-propagating kink wave, while the one with $\omega_R < 0$ is the backward-propagating wave. A third solution with $\omega_R > 0$ emerges when the shear flow velocity increases from zero. It is associated with the neutral component of the plasma in the sense that it only appears in the presence of neutrals. However, it must be noted that such simple associations between solutions and fluids cannot be made when the coupling is high and ions and neutrals behave as a single fluid. As the flow velocity continues to increase, the three solutions converge for a critical flow velocity that depends on the collision frequency. The stronger the ion-neutral coupling, the lower the critical flow. From that point on, the real part of the frequency is proportional to ΔU and is well described by the real part of Equation (6.15) or, equivalently, Equation (6.52).

As it can be seen in the lower panel of Figure 6.5, the degree of coupling has a much more remarkable effect on the damping and growth rates of the perturbations than on their oscillation frequencies. The shaded zone in those panels highlights the region with $\omega_I > 0$, which corresponds to the area where the solutions are unstable and exponentially grow with time. Any of the three panels reveals that for low shear flow velocities there is only one unstable solution, corresponding to that originally associated with the neutral component of the plasma. A second unstable branch (originally associated with ions) appears for higher flow velocities above the classical super-Alfvénic threshold. By comparing the three panels, it is possible to conclude that ion-neutral collisions reduce to a great extent the growth rate of the instability that appears for sub-Alfvénic flows but are not able to completely suppress it (Watson et al. [2004], Soler et al. [2012b]). In addition, the analytical approximation shows that, in its range of applicability, the growth rate is directly proportional to the square of the shear flow velocity and inversely proportional to the ion-neutral collision frequency. As expected, the approximation agrees well with the numerical results for small shear flow velocities. For weak coupling, the approximation is reasonably good for flow velocities up to 40% of the internal Alfvén speed. When the collision frequency is increased, the range of agreement between the numerical results and the approximation is greatly extended even to super-Alfvénic speeds.

Now, to investigate in more detail the effect of ion-neutral collisions on the instability for slow flows, the shear flow velocity is fixed to the value $\Delta U/c_{\mathrm{A},0} = 1$ and the solutions of Equation (6.49) are computed as functions of the collision frequency, ν_{ni}. The chosen flow velocity is below the classical threshold for the KHI in fully ionized plasmas (Chandrasekhar [1961]), so that in principle only the neutral component is unstable in this configuration. The results of this study are displayed in Figure 6.6, where the solutions originally associated with

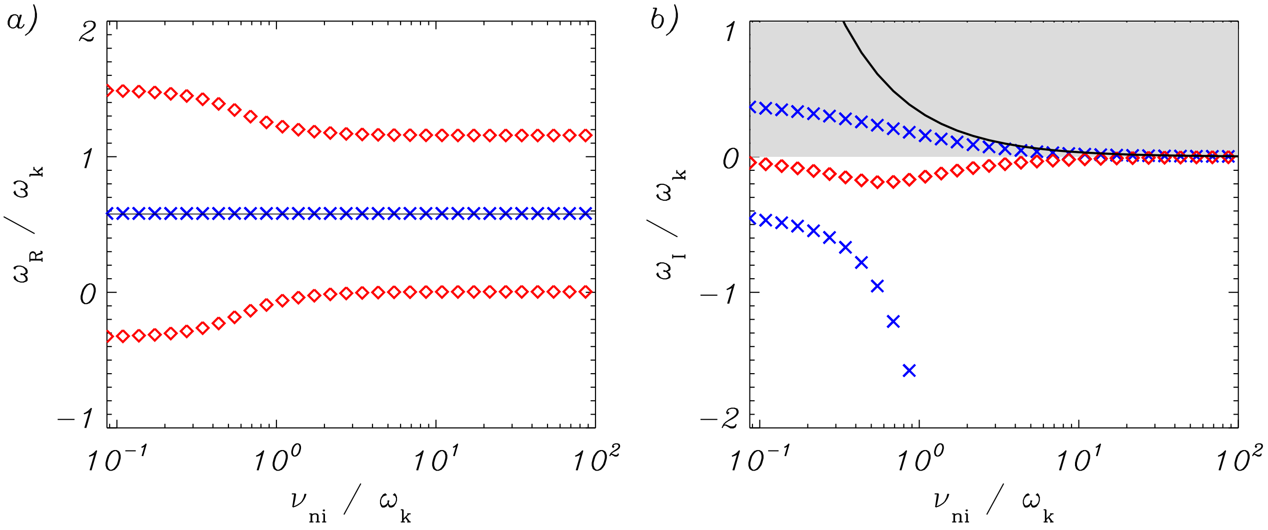

Figure 6.6: a) $\omega_{\mathrm{R}}/\omega_{\mathrm{k}}$ and b) $\omega_{\mathrm{I}}/\omega_{\mathrm{k}}$ for the kink mode (m=1) as a function of $\nu_{\mathrm{ni}}/\omega_{\mathrm{k}}$, with $\Delta U/c_{\mathrm{A},0} = 1$ and $k_z a = 0.1$. The red diamonds are the solutions originally associated with the ions when there is no coupling, while the blue crosses are the solutions for neutrals. The solid line is the analytical approximation given by Equation (6.52). In b) the shaded area denotes the region of instability.

ions are shown as red diamonds and those originally associated with neutrals are plotted with blue crosses. The right panel shows that there is always one unstable solution for any value of ν_{ni}, although its growth rate decreases when the collision frequency increases. The growth rate is reduced because neutrals feel indirectly, through the collisions with ions, the stabilizing effect of the magnetic field. In addition, as discussed before, the analytical approximation for the growth rate, agrees well with the numerical results for high values of the collision frequencies, as is consistent with the assumptions behind the approximation. Regarding the real part of the solutions, it can be checked that the absolute value of the frequency of the modes associated with ions decreases until it reaches a plateau for $\nu_{ni}/\omega_k > 1$ (Soler et al. [2013c]), while the frequency of the solutions associated with the neutral stays constant all over the range. The reason of the decrease in frequency of the former is that, due to the strong collisional coupling, the two species oscillate together as a single fluid. Hence, the inertia of neutrals is added to that of ions and the Alfvén frequency depends on the total density of the plasma (Kumar and Roberts [2003], Soler et al. [2013b]).

For the sake of completeness, the next step is to study the dependence of the solutions to Equation (6.49) on the azimuthal wavenumber. As shown by Equation (6.50), the results in the TT limit are independent of the value of m for $m \neq 0$; this fact implies that in the range of applicability of that approximation there will not be substantial variations in the behavior of the different modes. Hence, to observe some dissimilarities, it is necessary to choose parameters beyond the TT case. Figure 6.7 shows the results corresponding to a case with the same densities and magnetic field as in the previous analyses but with a higher value of the dimensionless longitudinal wavenumber, namely, $k_z a = 2$. Five different modes are represented, which correspond to the following azimuthal wavenumbers: $m = 0$, $m = 1$, $m = 2$, $m = 10$ and $m = 100$. The left panel shows that the oscillation frequency decreases when m increases. In

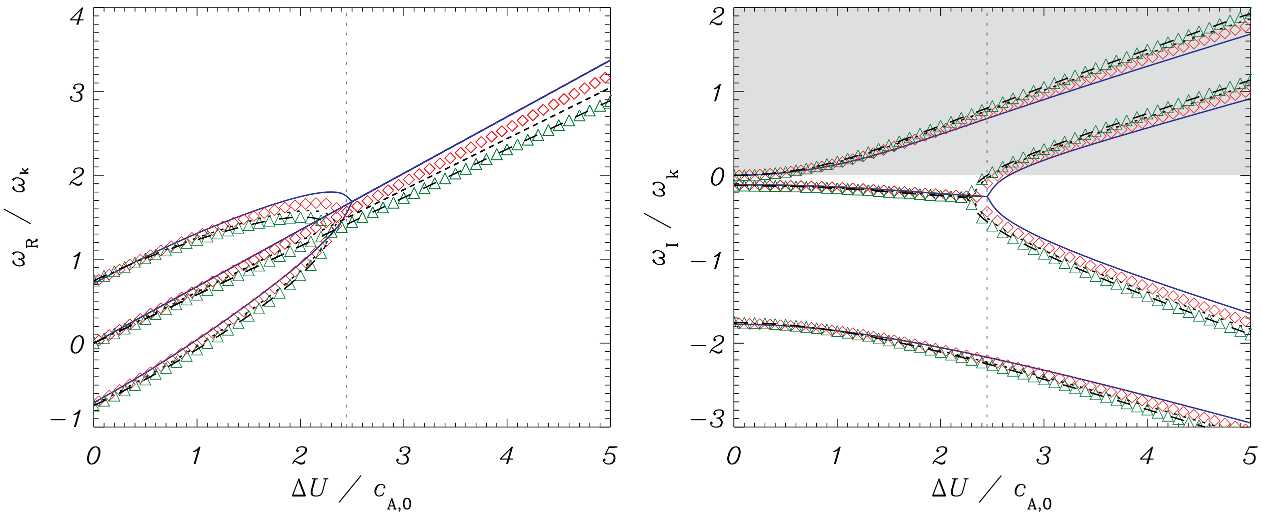

Figure 6.7: Solutions of Equation (6.49) as functions of the normalized shear flow for a normalized wavenumber of $k_z a = 2$. The gray area on the right panel shows the region where the solutions are unstable. The modes with $m = 0$, $m = 1$, $m = 2$, $m = 10$ and $m = 100$ are represented by the blue solid lines, red diamonds, black dotted lines, black dashed lines and green triangles, respectively.

contrast, the right panel reveals that the modes with larger growth rates are those with higher m. However, the dependence of the solutions on the azimuthal wavenumber is weak, specially when modes with large m are compared with each other.

6.3.3 KHI in solar prominence threads

Here, the model of partially ionized magnetic flux tubes subject to a longitudinal flow is applied to the investigation of solar prominence plasmas. The full dispersion relation, Equation (6.49), is solved with values representative of a quiescent prominence. Therefore, the internal medium represents a prominence thread with densities of protons and neutral hydrogen such that $\rho_{p,0} + \rho_{\mathrm{H},0} = 10^{-9}$ kg m^{-3}, a temperature of $T_0 = 7000$ K and radius of $a = 100$ km; the external plasma is composed of inter-thread plasma with $\rho_{p,ex} + \rho_{\mathrm{H},ex} = 2 \times 10^{-10}$ km m^{-3}, and $T_{ex} = 35000$ K, which corresponds to the regime of prominence-corona transition region (PCTR). Densities and temperatures are chosen so that the equilibrium condition of the total pressure (thermal plus magnetic) is fulfilled, that is, the total pressure is the same in both media. The magnetic fields are $B_0 = B_{ex} = 10$ G. The study is focused on the kink mode ($m = 1$).

The collision frequencies can be obtained from the friction coefficient given by Equation (2.62), recalling the relation $\nu_{ns} = \alpha_{sn}/\rho_n$. Thus, assuming that both species have the same temperature, the hydrogen-proton collision frequency is given by

$$\nu_{p\mathrm{H}} = \frac{\rho_p}{2m_p}\frac{4}{3}\sqrt{\frac{16k_{\mathrm{B}}T}{\pi m_p}}\sigma_{p\mathrm{H}}, \tag{6.54}$$

where, according to Table 2.1, the cross-section of this interaction is $\sigma_{p\mathrm{H}} = 10^{-18}$ m^{-2}.

Figure 6.8 displays the most unstable solution of Equation (6.49) as a function of the shear flow velocity for three different values of the ionization fraction: the red dashed lines represent the fully ionized case ($\chi = 0$), the blue crosses represent a partially ionized situation ($\chi = 4$), and the black diamonds depict a weakly ionized case ($\chi = 100$). The left panel shows the results for a wavelength $\lambda = 100$ km, which corresponds to a longitudinal wavenumber $k_z = 2\pi/\lambda = 2\pi \times 10^{-5}$ m^{-1}. In the right panel the wavelength used is $\lambda = 1000$ km, so $k_z = 2\pi \times 10^{-6}$ m^{-1}. The shaded zone of Figure 6.8 denotes a range of typical velocities (from 10 km s^{-1} to 30 km s^{-1}) that have been measured in quiescent prominences (Zirker et al. [1998], Berger et al. [2010]). The limits of this zone could slightly vary depending on the observations that are chosen as reference, but this variation is not significant for the present analysis.

It can be seen that for the fully ionized cases the instabilities only appear for shear velocities far from the detected values. In contrast, the cases with a neutral component show instabilities for the entire range of velocities. Hence, partial ionization may explain the occurrence of KHI in solar prominence plasmas even when the observed flows are below the classical threshold.

The growth rates displayed on the right panel of Figure 6.8 are lower than those in the left panel. More precisely, they are about one order of magnitude smaller when the shear flow velocities are high. Since the wavenumber in the right panel is one order of magnitude smaller than in the left panel, this behavior agrees with Equation (6.15). On the other hand, when the velocities are low, the growth rates on the right are two orders of magnitude smaller, which is consistent with the analytical approximation given by Equation (6.52).

In addition, the solid lines of Figure 6.8 represent the growth rates according to the analytical approximation. It can be checked that they are within the same order of magnitude than the

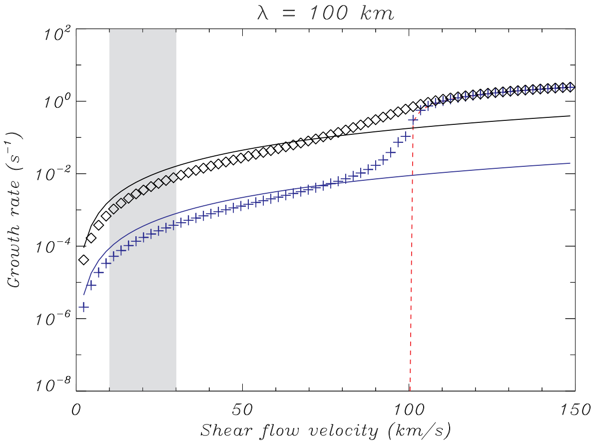

Figure 6.8: Application to solar prominence threads. Growth rates as functions of the shear flow velocity for the following set of parameters: $\rho_{\mathrm{i},0} + \rho_{\mathrm{n},0} = 10^{-9}$ kg m^{-3}, $\rho_{\mathrm{i,ex}} + \rho_{\mathrm{n,ex}} = 2 \times 10^{-10}$ kg m^{-3}, $B_0 = B_{\mathrm{ex}} = 10^{-3}$ T, $a = 100$ km, $T_0 = 7000$ K and $T_{\mathrm{ex}} = 35000$ K; in the left panel the wavenumber is $k_z = 2\pi/\lambda = 2\pi \times 10^{-5}$ m^{-1} and in the right panel it is $k_z = 2\pi \times 10^{-6}$ m^{-1}. The red dashed lines correspond to a fully ionized plasma ($\chi = 0$), the blue crosses to a partially ionized case ($\chi = 4$), and the black diamonds to a weakly ionized case ($\chi = 100$). The solid lines represent the solutions given by the analytical approximation in Equation (6.52). The shaded zone denotes the region of flow velocity values that have been frequently measured in solar prominences.

full numerical results. Thus, Equation (6.52) may be used to calculate estimates of growth rates of KHI in a real prominence thread without the need of solving the much more complex full dispersion relation.

Up to this point, the present analysis has demonstrated that KHI may be triggered in quiescent prominences in the presence of sub-Alfvénic flows as a result of the effect of partial ionization. However, it is not yet possible to state that this magnetohydrodynamic instability may explain the observed turbulent flows. Before doing so, it is necessary to check whether the growth rates given by the theory are consistent with an instability that can be actually observed. Estimated lifetimes of prominence threads are about 20 minutes (Lin et al. [2005]). The comparison between the theory and the observations is best performed by using as reference the growth times of the instability, defined as $\tau_I \equiv 1/\omega_I$, instead of the growth rates. Table 6.1 shows the growth times that correspond to the solutions presented in Figure 6.8 for shear flow velocities of 30 km s^{-1} (which is the highest value obtained from the already mentioned observations).

Table 6.1: KHI growth times (τ_I) in a prominence thread

	$\lambda = 100$ km	$\lambda = 1000$ km
$\chi = 4$	1000 s	10^5 s (~ 28 h)
$\chi = 100$	100 s	10^4 s (~ 2.8 h)

The growth times obtained for a perturbation with a wavelength $\lambda = 1000$ km are longer than the typical lifetime of a thread. Therefore, an instability originated by that perturbation cannot be the cause of the observed turbulent flows. Conversely, the growth times for the shortest wavelength are of the same order of magnitude or lower than the detected lifetimes. This means that during the life of a prominence thread there is enough time for the development of a KHI caused by a perturbations with that wavelength.

As the last item of this investigation, it is interesting to show that the analytical approximation given by Equation (6.52) may be a useful tool in the field of prominence seismology (Ballester [2014]). Introducing a new parameter $\bar{\nu}$, called mean collision frequency of the plasma, which is defined through the following relation

$$\frac{1}{\bar{\nu}} = \frac{2\rho_{\mathrm{n},0}\rho_{\mathrm{n,ex}}}{\left(\rho_{\mathrm{n},0} + \rho_{\mathrm{n,ex}}\right)\left(\rho_{\mathrm{n},0}\nu_{\mathrm{ni},0} + \rho_{\mathrm{n,ex}}\nu_{\mathrm{ni,ex}}\right)}, \tag{6.55}$$

the imaginary part of Equation (6.52) can be now written as

$$\gamma_{\mathrm{KHI}} = \frac{k_z^2 U_0^2}{\bar{\nu}} = \frac{1}{\bar{\nu}}\frac{4\pi^2}{\lambda^2}U_0^2 \Rightarrow \bar{\nu} = \frac{4\pi^2}{\lambda^2}\frac{U_0^2}{\gamma_{\mathrm{KHI}}}. \tag{6.56}$$

Values of the three parameters that appear in the right-hand side of the previous equation, namely the flow velocity, the perturbation wavelength, and the KHI growth rate, can be estimated from observations. Consequently, through this formula, it may be possible to estimate the coupling degree between the two components of the plasma.

6.4 Discussion

This final chapter has been devoted to the study of how the presence of neutral species in a plasma affects the propagation of waves and the possible occurrence of KHI in a cylindrical magnetic flux tube. The multi-fluid model detailed in Chapter 2 has been applied here to two-fluid plasmas in which all the ionized species and electrons are treated as a single component while there is an additional component that corresponds to the neutral species. A dispersion relation for small-amplitude incompressible waves has been derived, which is given by Equation 6.49, and the dependence of its solutions on several physical parameters, namely the shear flow velocity, the neutral-ion collision frequency, and the longitudinal and azimuthal wavenumbers, has been studied.

It has been found that perturbations at an interface separating two partially ionized plasmas are unstable for any velocity shear, contrary to what occurs in fully ionized plasmas, in which the effect of the magnetic field only allows the onset of the KHI for super-Alfvénic shear flows. It has been shown that the collisional coupling that exists between the two species of the partially ionized plasma reduces the growth rates of the instability associated to the neutral component, although it is not able to avoid its onset. These results are consistent with previous works like the ones developed in simpler configurations by Watson et al. [2004] and Soler et al. [2012b], for example. The dispersion relation derived here reduces to Equation (37) of Soler et al. [2012b] or Equation (26) of Watson et al. [2004] in the TT limit. Moreover, in the absence of an equilibrium flow and when the densities of neutrals go to zero, it is possible to recover from Equation (6.49) the incompressible limit of Equation (8a) of Edwin and Roberts [1983], which describes the properties of waves in a fully ionized cylindrical flux tube.

The study of the dependence of the normal modes on the azimuthal wavenumber has shown that the modes with a higher m are more unstable and have lower oscillation frequencies. However, this variation is only appreciable beyond the TT limit and has a small significance.

Then, the application of the two-fluid theory to threads of quiescent prominences has shown that, for a certain combination of parameters, the turbulent flows detected in those structures may be interpreted as consequences of KHI in partially ionized plasmas. For instance, the KHI growth times corresponding to a perturbation with $\lambda = 100$ km applied to a magnetic flux tube with densities and magnetic fields akin to those of a prominence thread are of the order of or lower than the typical lifetimes of those coronal features, which means that it is possible for this instability to develop before the thread disappears.

Furthermore, an analytical approximation of the KHI growth rates for slow shear flows and strong ion-neutral collisional coupling has been derived. This formula, given by Equation (6.52), is easier to handle than the full dispersion relation and thus easier to interpret: growth rates of the KHI have a quadratic dependence on the longitudinal wavenumber and the shear flow velocity, and are inversely proportional to the neutral-ion collision frequency. This analytical approximation may be useful in the field of prominence seismology: from this formula, it is possible to define a mean collision frequency $\bar{\nu}$, given by Equation (6.55), that may be computed from observational data to obtain an estimation of the coupling degree of ions and neutrals in solar prominences.

Concluding remarks and future work

In this Thesis, a multi-fluid model has been used to investigate how elastic collisions between the different components of a plasma affect the properties of low- and high-frequency waves and the development of the Kelvin-Helmholtz instability in fully and partially ionized environments. The model has been presented in such a general way that allows its application to a huge variety of astrophysical and laboratory plasmas. Nevertheless, this work has been dedicated to the research of plasmas of the solar atmosphere, with a focus on the chromospheric region and on prominences, although environments like the solar corona and the solar wind have also been studied.

It has been shown that the multi-fluid approach accounts for some effects and phenomena that cannot be addressed by single-fluid descriptions like ideal MHD. For instance, according to the results explained in Chapter 3 for fully ionized plasmas, the multi-fluid theory predicts the existence of more oscillatory modes than ideal MHD when the plasma is subject to low-wavenumber impulsive perturbations. Such additional modes are associated with the ion cyclotron frequencies. Moreover, when the effect of Coulomb collisions between ions is considered, those waves are highly damped in comparison with Alfvén waves. Actually, for Alfvén waves in the solar atmosphere, the damping times due to Coulomb collisions are so large that the effect of such interaction can be neglected. On the other hand, when the wavenumber of the impulsive driver is increased, the Alfvénic branch splits in two different modes: the high-frequency ion cyclotron and whistler modes, which are left-hand and right-hand circularly polarized waves, respectively. Those high-frequency modes are greatly affected by the friction between the different ionized species. In the solar atmosphere, they are much more short-lived than Alfvén waves, specially the ion-cyclotron waves. Furthermore, when a periodic driver is considered to act on a collisionless fluid, the L-modes have cut-off regions, in which the waves become evanescent, and resonances, where the phase speed is equal to zero and the perturbation does not propagate. Such cut-offs and resonances are removed when collisions are taken into account. Due to the diffusive effect of collisions, the perturbations can propagate at those regions and singular frequencies, although they are still strongly damped in space.

In Chapter 4, the effects of partial ionization and resistivity have been analyzed for plasmas with conditions akin to those at several heights of the chromosphere and of a quiescent prominence. The damping of the low-frequency waves has been found to be dominated by elastic collisions between ions and neutrals, while the damping of high-frequency oscillations is primarily due to Coulomb collisions between ions and to resistivity, with the R modes being the most affected by the latter mechanism. This behavior is explained by the fact that the damping is more efficient when the collisional frequencies are closer to the oscillation frequency, as proven by Leake et al. [2005], Zaqarashvili et al. [2011a] or Soler et al. [2013b], and that the interactions with neutrals have typically lower frequencies than the collisions with ions and electrons. In addition, it has been confirmed once more that, due to the presence of neutrals, the oscillation frequency and the propagation speed of Alfvén waves is reduced. It has also been demonstrated that Hall's current plays a very important role in weakly ionized environments like the lower chromosphere: in fully ionized plasmas, the divergence in the properties of the L and R modes starts at frequencies of the order of the cyclotron frequencies, but in weakly ionized plasmas such departure can occur at frequencies several orders of magnitude smaller. Hall's current also removes the cut-off region for Alvén waves in weakly ionized plasmas which was predicted by some two-fluid theories that used a simpler version of the induction equation. In addition, the performed numerical simulations have shown that the friction due to collisions transforms a fraction of the energy of a given initial perturbation into internal energy of the plasma, which implies an increment of its temperature. Hence, the plasma is heated by this kind of collisions.

The conclusions commented above have been derived from the study of small-amplitude perturbations. Nonetheless, in this Thesis, perturbations of large amplitude has also been examined. In Chapter 5, several second-order effects of non-linear waves have been analyzed. In fully ionized plasmas, the ponderomotive force caused by standing non-linear Alfvén waves produces an accumulation of matter at the nodes of the magnetic field wave. That accumulation is limited by the effect of pressure: a saturation value of density is reached and then an oscillatory motion appears. The results presented in Chapter 5 show that the effect of pressure is enhanced by partial ionization. The dissipation of Alfvén waves due to collisions between ions and neutrals generates a faster growth of the pressure, and as a consequence the matter tends to be displaced from the nodes of the magnetic field instead of accumulating at those points. In addition, the frequencies of the resulting oscillations in density and pressure are proportional to the modified Alfvén speed, $\widetilde{c}_{\mathrm{A}}$, and the weighted mean sound speed, $\widetilde{c}_{S}$. Another investigation described in the same chapter has examined how a velocity perturbation of large amplitude, of the order of $0.1c_{\mathrm{A}}$, affects the energetics of a plasma with properties akin to those of a solar prominence. The energy of the initial perturbation is transformed by means of collisions into internal energy, which has two components: the first one is associated with the nonlinearly generated second-order sound waves, while the other is related to the rise of the temperature of the plasma. In the numerical simulations performed here, up to a 6% of the initial energy has been deposited in the plasma after the propagation of the perturbation, which leads to an increment in temperature.

Finally, in Chapter 6 the effect of ion-neutral collisions on the onset of the Kelvin-Helmholtz instability in magnetic flux tubes has been analyzed. It has been shown that the neutral component of the plasma is unstable for any value of the velocity shear. Collisions reduce the growth rate of the instability, specially for sub-Alfvénic shear flows, but they cannot completely avoid its onset. Hence, in the absence of other stabilizing effects like gravity or surface tension, partially ionized plasmas are unstable for any value of the shear flow velocity. A cylindrical two-fluid model has been applied to the investigation of KHI in prominence threads and it has been found that, for certain wavelengths of the perturbations, the growth times of the instability may be of the order or lower than the typical lifetimes of the threads.

The results briefly commented in the previous paragraphs have been obtained for plasmas composed of up to three different ionized species but they can be easily generalized to plasmas with a larger number of charged species. Other ways of improvement are the following. In the first place, the majority of the research presented in this Thesis has focused on static homogeneous plasma. Hence, a reasonable improvement would be the consideration of non-homogeneous plasma. For example, it would be of interest the application of the multi-fluid model to the study of how the different kinds of waves propagate throughout the stratified solar atmosphere. In such a case, phenomena like wave amplification, shock generation, refraction and reflection of the waves or parametric decay may appear. It is also interesting to study the effect of the ponderomotive force caused by non-linear Alfvén waves in coronal loops taking into account their curved geometry. Another possible refinement is related to the equations that describe the dynamics of each fluid: higher-order moment transport approximation can be used to allow the examination of the influence of stress and heat flows. Moreover, even without the mentioned modifications, there are several issues worth inspecting. For instance, the theoretical model presented in this Thesis may be also applied to the investigation of magnetosonic waves in multi-component plasmas or the non-linear phase of the Kelvin-Helmholtz instability.

Bibliography

L. Abbo, L. Ofman, S. K. Antiochos, V. H. Hansteen, L. Harra, Y.-K. Ko, G. Lapenta, B. Li, P. Riley, L. Strachan, R. von Steiger, and Y.-M. Wang. Slow Solar Wind: Observations and Modeling. *SSRv*, pages 1–54, June 2016. doi:10.1007/s11214-016-0264-1.

M. R. Aellig, A. J. Lazarus, and J. T. Steinberg. The solar wind helium abundance: Variation with wind speed and the solar cycle. *GeoRL*, 28:2767–2770, 2001. doi:10.1029/2000GL012771.

I. A. Ahmad. Coronal He/+/ 304 A radiation. *SoPh*, 53:409–415, August 1977. doi:10.1007/BF00160284.

H. Alfvén. Existence of Electromagnetic-Hydrodynamic Waves. *Nature*, 150:405–406, October 1942. doi:10.1038/150405d0.

L. A. Allen, S. R. Habbal, and Y. Q. Hu. Thermal coupling of protons and neutral hydrogen in the fast solar wind. *JGR*, 103:6551, April 1998. doi:10.1029/97JA03435.

E. Anders and N. Grevesse. Abundances of the elements - Meteoritic and solar. *GeCoA*, 53:197–214, January 1989. doi:10.1016/0016-7037(89)90286-X.

E. Antonucci, A. H. Gabriel, and B. E. Patchett. Oscillations in EUV emission lines during a loop brightening. *SoPh*, 93:85–94, June 1984. doi:10.1007/BF00156654.

T. D. Arber, C. S. Brady, and S. Shelyag. Alfvén Wave Heating of the Solar Chromosphere: 1.5D Models. *ApJ*, 817:94, February 2016. doi:10.3847/0004-637X/817/2/94.

J. Arons and C. E. Max. Hydromagnetic Waves in Molecular Clouds. *Astrophysical Journal Letters*, 196:L77, March 1975. doi:10.1086/181748.

I. Arregui and J. L. Ballester. Damping Mechanisms for Oscillations in Solar Prominences. *SSRv*, 158:169–204, July 2011. doi:10.1007/s11214-010-9648-9.

I. Arregui, J. Terradas, R. Oliver, and J. L. Ballester. Damping of Fast Magnetohydrodynamic Oscillations in Quiescent Filament Threads. *Astrophysical Journal Letters*, 682:L141, August 2008. doi:10.1086/591081.

I. Arregui, R. Oliver, and J. L. Ballester. Prominence Oscillations. *Living Reviews in Solar Physics*, 9:2, April 2012. doi:10.12942/lrsp-2012-2.

M. J. Aschwanden. Theory of radio pulsations in coronal loops. *SoPh*, 111:113–136, March 1987. doi:10.1007/BF00145445.

M. J. Aschwanden, L. Fletcher, C. J. Schrijver, and D. Alexander. Coronal Loop Oscillations Observed with the Transition Region and Coronal Explorer. *ApJ*, 520:880–894, August 1999. doi:10.1086/307502.

W. I. Axford and J. F. McKenzie. The origin of high speed solar wind streams. In E. Marsch and R. Schwenn, editors, *Solar Wind Seven Colloquium*, pages 1–5, 1992.

J. L. Ballester. Prominence Seismology. In B. Schmieder, J.-M. Malherbe, and S. T. Wu, editors, *IAU Symposium*, volume 300 of *IAU Symposium*, pages 30–39, January 2014. doi:10.1017/S1743921313010703.

D. S. Balsara. Wave Propagation in Molecular Clouds. *ApJ*, 465:775, July 1996. doi:10.1086/177462.

H. Balthasar, M. Knoelker, E. Wiehr, and G. Stellmacher. Evidence for quasi-periodic Doppler motions in solar prominences. *A&A*, 163:343–346, July 1986.

H. Balthasar, E. Wiehr, H. Schleicher, and H. Wohl. Doppler oscillations in solar prominences simultaneously observed with two telescopes. Discovery of a 30 S oscillation. *A&A*, 277:635, October 1993.

D. Banerjee and S. Krishna Prasad. MHD Waves in Coronal Holes. *Washington DC American Geophysical Union Geophysical Monograph Series*, 216:419–430, February 2016. doi:10.1002/9781119055006.ch24.

A. R. Barakat and R. W. Schunk. Transport equations for multicomponent anisotropic space plasmas - A review. *Plasma Physics*, 24:389–418, April 1982. doi:10.1088/0032-1028/24/4/004.

V. S. Bashkirtsev and G. P. Mashnich. Oscillatory processes in prominences. *SoPh*, 91:93–101, March 1984. doi:10.1007/BF00213616.

V. S. Bashkirtsev, N. I. Kobanov, and G. P. Mashnich. The observations of 80-min oscillations in the quiescent prominences. *SoPh*, 82:443–445, January 1983. doi:10.1007/BF00145584.

J. W. Belcher and L. Davis, Jr. Large-amplitude Alfvén waves in the interplanetary medium, 2. *JGR*, 76:3534, 1971. doi:10.1029/JA076i016p03534.

J. W. Belcher, L. Davis, Jr., and E. J. Smith. Large-amplitude Alfvén waves in the interplanetary medium: Mariner 5. *JGR*, 74:2302, 1969. doi:10.1029/JA074i009p02302.

T. E. Berger, R. A. Shine, G. L. Slater, T. D. Tarbell, A. M. Title, T. J. Okamoto, K. Ichimoto, Y. Katsukawa, Y. Suematsu, S. Tsuneta, B. W. Lites, and T. Shimizu. Hinode SOT Observations of Solar Quiescent Prominence Dynamics. *Astrophysical Journal Letters*, 676:L89, March 2008. doi:10.1086/587171.

T. E. Berger, G. Slater, N. Hurlburt, R. Shine, T. Tarbell, A. Title, B. W. Lites, T. J. Okamoto, K. Ichimoto, Y. Katsukawa, T. Magara, Y. Suematsu, and T. Shimizu. Quiescent Prominence Dynamics Observed with the Hinode Solar Optical Telescope. I. Turbulent Upflow Plumes. *ApJ*, 716:1288–1307, June 2010. doi:10.1088/0004-637X/716/2/1288.

D. Berghmans and F. Clette. Active region EUV transient brightenings - First Results by EIT of SOHO JOP80. *SoPh*, 186:207–229, May 1999. doi:10.1023/A:1005189508371.

O. Berné, N. Marcelino, and J. Cernicharo. Waves on the surface of the Orion molecular cloud. *Nature*, 466: 947–949, August 2010. doi:10.1038/nature09289.

W. K. Berthold, A. K. Harris, and H. J. Hope. World-Wide Effects of Hydromagnetic Waves Due to Argus. *JGR*, 65:2233, August 1960. doi:10.1029/JZ065i008p02233.

L. Biermann. Zur Deutung der chromosphärischen Turbulenz und des Exzesses der UV-Strahlung der Sonne. *Naturwissenschaften*, 33:118–119, August 1946. doi:10.1007/BF00738265.

J. A. Bittencourt. *Fundamentals of Plasma Physics*. New York, Pergamon Press, 1986.

D. C. Black and E. H. Scott. A numerical study of the effects of ambipolar diffusion on the collapse of magnetic gas clouds. *ApJ*, 263:696–715, December 1982. doi:10.1086/160541.

D. Bohm and E. P. Gross. Theory of Plasma Oscillations. B. Excitation and Damping of Oscillations. *Physical Review*, 75:1864–1876, June 1949. doi:10.1103/PhysRev.75.1864.

C. Bona, C. Bona-Casas, and J. Terradas. Linear high-resolution schemes for hyperbolic conservation laws: TVB numerical evidence. *Journal of Computational Physics*, 228:2266–2281, April 2009. doi:10.1016/j.jcp.2008.12.010.

G. C. Boynton and U. Torkelsson. Dissipation of non-linear Alfven waves. *A&A*, 308:299–308, April 1996.

S. I. Braginskii. Transport Processes in a Plasma. *Reviews of Plasma Physics*, 1:205, 1965.

L. F. Burlaga. Micro-Scale Structures in the Interplanetary Medium. *SoPh*, 4:67–92, May 1968. doi:10.1007/BF00146999.

L. F. Burlaga. Hydromagnetic Waves and Discontinuities in the Solar Wind. *SSRv*, 12:600–657, December 1971. doi:10.1007/BF00173345.

James D. Callen. Coulomb collisions. In *Fundamentals of Plasma Physics*, chapter 2. Madison, Wisconsin, draft edition, June 2006.

M. Carbonell, R. Oliver, and J. L. Ballester. Time damping of linear non-adiabatic magnetohydrodynamic waves in an unbounded plasma with solar coronal properties. *A&A*, 415:739–750, February 2004. doi:10.1051/0004-6361:20034630.

M. Carbonell, P. Forteza, R. Oliver, and J. L. Ballester. The spatial damping of magnetohydrodynamic waves in a flowing partially ionised prominence plasma. *A&A*, 515:A80, June 2010. doi:10.1051/0004-6361/200913024.

J. Chae. The Formation of a Prominence in NOAA Active Region 8668. II. Trace Observations of Jets and Eruptions Associated with Canceling Magnetic Features. *ApJ*, 584:1084–1094, February 2003. doi:10.1086/345739.

J. Chae, C. Denker, T. J. Spirock, H. Wang, and P. R. Goode. High-Resolution Hα Observations of Proper Motion in NOAA 8668: Evidence for Filament Mass Injection by Chromospheric Reconnection. *SoPh*, 195: 333–346, August 2000. doi:10.1023/A:1005242832293.

J. Chae, K. Ahn, E.-K. Lim, G. S. Choe, and T. Sakurai. Persistent Horizontal Flows and Magnetic Support of Vertical Threads in a Quiescent Prominence. *Astrophysical Journal Letters*, 689:L73, December 2008. doi:10.1086/595785.

S. Chandrasekhar. *Hydrodynamic and hydromagnetic stability*. 1961.

R. D. Chapman, S. D. Jordan, W. M. Neupert, and R. J. Thomas. Evidence for the 300-SECOND Oscillation from OSO-7 Extreme-Ultraviolet Observations. *Astrophysical Journal Letters*, 174:L97, June 1972. doi:10.1086/180957.

F. F. Chen. *Introduction to Plasma Physics and Controlled Fusion*, volume 1. Plenum Press, 1984.

V. M. Chmyrev, S. V. Bilichenko, V. I. Pokhotelov, V. A. Marchenko, and V. I. Lazarev. Alfven vortices and related phenomena in the ionosphere and the magnetosphere. *PhyS*, 38:841–854, December 1988. doi:10.1088/0031-8949/38/6/016.

P. J. Coleman. Hydromagnetic waves in the interplanetary plasma. *Phys. Rev. Lett.*, 17:207–211, Jul 1966. doi:10.1103/PhysRevLett.17.207.

R. Courant, K. Friedrichs, and H. Lewy. Über die partiellen Differenzengleichungen der mathematischen Physik. *Mathematische Annalen*, 100:32–74, 1928. doi:10.1007/BF01448839.

N. F. Cramer. *The Physics of Alfvén Waves*. Wiley-VCH, December 2001.

W. Crookes. On radiant matter; a lecture delivered to the british association for the advancement of science. *Am. J. Sci. Series 3*, 18:241–262, 1879. doi:10.2475/ajs.s3-18.106.241.

C. de Jager. Structure and Dynamics of the Solar Atmosphere. *Handbuch der Physik*, 52:80, 1959.

B. De Pontieu, P. C. H. Martens, and H. S. Hudson. Chromospheric Damping of Alfvén Waves. *ApJ*, 558: 859–871, September 2001. doi:10.1086/322408.

B. De Pontieu, S. W. McIntosh, M. Carlsson, V. H. Hansteen, T. D. Tarbell, C. J. Schrijver, A. M. Title, R. A. Shine, S. Tsuneta, Y. Katsukawa, K. Ichimoto, Y. Suematsu, T. Shimizu, and S. Nagata. Chromospheric Alfvénic Waves Strong Enough to Power the Solar Wind. *Science*, 318:1574, December 2007. doi:10.1126/science.1151747.

B. De Pontieu, S. W. McIntosh, M. Carlsson, V. H. Hansteen, T. D. Tarbell, P. Boerner, J. Martinez-Sykora, C. J. Schrijver, and A. M. Title. The Origins of Hot Plasma in the Solar Corona. *Science*, 331:55, January 2011. doi:10.1126/science.1197738.

B. De Pontieu, M. Carlsson, L. H. M. Rouppe van der Voort, R. J. Rutten, V. H. Hansteen, and H. Watanabe. Ubiquitous Torsional Motions in Type II Spicules. *Astrophysical Journal Letters*, 752:L12, June 2012. doi:10.1088/2041-8205/752/1/L12.

C. E. DeForest and J. B. Gurman. Observation of Quasi-periodic Compressive Waves in Solar Polar Plumes. *Astrophysical Journal Letters*, 501:L217–L220, July 1998. doi:10.1086/311460.

H. G. Demars and R. W. Schunk. A multi-ion generalized transport model of the polar wind. *JGR*, 99: 2215–2226, February 1994. doi:10.1029/93JA02356.

A. S. Dickinson, M. S. Lee, and L. A. Viehland. The mobility of He$^+$ ions in helium gas. *Journal of Physics B Atomic Molecular Physics*, 32:4919–4930, October 1999. doi:10.1088/0953-4075/32/20/309.

B. T. Draine. Multicomponent, reacting MHD flows. *MNRAS*, 220:133–148, May 1986. doi:10.1093/mnras/220.1.133.

P. G. Drazin and W. H. Reid. *Hydrodynamic stability*, volume 82. 1981.

M. M. Echim, J. Lemaire, and Ø. Lie-Svendsen. A Review on Solar Wind Modeling: Kinetic and Fluid Aspects. *Surveys in Geophysics*, 32:1–70, January 2011. doi:10.1007/s10712-010-9106-y.

A. S. Eddington. c 1908 (Morehouse), the envelopes of. *MNRAS*, 70:442–458, March 1910. doi:10.1093/mnras/70.5.442.

P. M. Edwin and B. Roberts. Wave propagation in a magnetic cylinder. *Sol. Phys*, 88:179–191, October 1983. doi:10.1007/BF00196186.

O. Engvold. The fine structure of prominences. I - Observations - H-alpha filtergrams. *SoPh*, 49:283–295, August 1976. doi:10.1007/BF00162453.

O. Engvold. The small scale velocity field of a quiescent prominence. *SoPh*, 70:315–324, April 1981. doi:10.1007/BF00151336.

A. I. Ershkovich, D. Prialnik, and A. Eviatar. Instability of a comet ionopause - Consequences of collisions and compressibility. *JGR*, 91:8782–8788, August 1986. doi:10.1029/JA091iA08p08782.

S. Eto, H. Isobe, N. Narukage, A. Asai, T. Morimoto, B. Thompson, S. Yashiro, T. Wang, R. Kitai, H. Kurokawa, and K. Shibata. Relation between a Moreton Wave and an EIT Wave Observed on 1997 November 4. *PASJ*, 54:481–491, June 2002. doi:10.1093/pasj/54.3.481.

W. M. Farrell, R. J. Fitzenreiter, C. J. Owen, J. B. Byrnes, R. P. Lepping, K. W. Ogilvie, and F. Neubauer. Upstream ULF waves and energetic electrons associated with the lunar wake: Detection of precursor activity. *GeoRL*, 23:1271–1274, 1996. doi:10.1029/96GL01355.

R. A. Fiedler and T. C. Mouschovias. Ambipolar diffusion and star formation: Formation and contraction of axisymmetric cloud cores. I - Formulation of the problem and method of solution. *ApJ*, 391:199–219, May 1992. doi:10.1086/171336.

R. A. Fiedler and T. C. Mouschovias. Ambipolar Diffusion and Star Formation: Formation and Contraction of Axisymmetric Cloud Cores. II. Results. *ApJ*, 415:680, October 1993. doi:10.1086/173193.

A. Fludra, G. Del Zanna, D. Alexander, and B. J. I. Bromage. Electron density and temperature of the lower solar corona. *JGR*, 104:9709–9720, May 1999. doi:10.1029/1998JA900033.

J. M. Fontenla, E. H. Avrett, and R. Loeser. Energy balance in the solar transition region. III - Helium emission in hydrostatic, constant-abundance models with diffusion. *ApJ*, 406:319–345, March 1993. doi:10.1086/172443.

P. Forteza, R. Oliver, J. L. Ballester, and M. L. Khodachenko. Damping of oscillations by ion-neutral collisions in a prominence plasma. *A&A*, 461:731–739, January 2007. doi:10.1051/0004-6361:20065900.

P. Forteza, R. Oliver, and J. L. Ballester. Time damping of non-adiabatic MHD waves in an unbounded partially ionised prominence plasma. *A&A*, 492:223–231, December 2008. doi:10.1051/0004-6361:200810370.

C. Foullon, E. Verwichte, and V. M. Nakariakov. Detection of ultra-long-period oscillations in an EUV filament. *A&A*, 427:L5–L8, November 2004. doi:10.1051/0004-6361:200400083.

C. Foullon, E. Verwichte, and V. M. Nakariakov. Ultra-long-period Oscillations in EUV Filaments Near to Eruption: Two-wavelength Correlation and Seismology. *ApJ*, 700:1658–1665, August 2009. doi:10.1088/0004-637X/700/2/1658.

C. Foullon, E. Verwichte, V. M. Nakariakov, K. Nykyri, and C. J. Farrugia. Magnetic Kelvin-Helmholtz Instability at the Sun. *Astrophysical Journal Letters*, 729:L8, March 2011. doi:10.1088/2041-8205/729/1/L8.

S. B. Ganguli. The polar wind. *Reviews of Geophysics*, 34:311–348, August 1996. doi:10.1029/96RG00497.

S. B. Ganguli and P. J. Palmadesso. Generalized fluid model of plasma outflow processes in the topside ionosphere. *Advances in Space Research*, 8:69–78, 1988. doi:10.1016/0273-1177(88)90265-7.

H. Gilbert. Energy Balance. In J.-C. Vial and O. Engvold, editors, *Solar Prominences*, volume 415 of *Astrophysics and Space Science Library*, page 157, 2015. doi:10.1007/978-3-319-10416-4_7.

H. R. Gilbert, A. G. Daou, D. Young, D. Tripathi, and D. Alexander. The Filament-Moreton Wave Interaction of 2006 December 6. *ApJ*, 685:629-645, September 2008. doi:10.1086/590545.

J. P. H. Goedbloed and S. Poedts. *Principles of Magnetohydrodynamics*. UK: Cambridge University Press, August 2004.

G. C. Gómez and E. C. Ostriker. The Effect of the Coriolis Force on Kelvin-Helmholtz-driven Mixing in Protoplanetary Disks. *ApJ*, 630:1093–1106, September 2005. doi:10.1086/432086.

M. L. Goodman. Conditions for Photospherically Driven Alfvénic Oscillations to Heat the Solar Chromosphere by Pedersen Current Dissipation. *ApJ*, 735:45, July 2011. doi:10.1088/0004-637X/735/1/45.

K. I. Gringauz, V. V. Bezrokikh, V. D. Ozerov, and R. E. Rybchinskii. A Study of the Interplanetary Ionized Gas, High-Energy Electrons and Corpuscular Radiation from the Sun by Means of the Three-Electrode Trap for Charged Particles on the Second Soviet Cosmic Rocket. *Soviet Physics Doklady*, 5:361, September 1960.

D. A. Gurnett and C. K. Goertz. Multiple Alfven wave reflections excited by Io Origin of the Jovian decametric arcs. *JGR*, 86:717–722, February 1981. doi:10.1029/JA086iA02p00717.

A. V. Haeff. The electron-wave tube-a novel method of generation and amplification of microwave energy. *Proceedings of the IRE*, 37(1):4–10, Jan 1949. ISSN 0096-8390. doi:10.1109/JRPROC.1949.232968.

G. Haerendel. Weakly damped Alfven waves as drivers of solar chromospheric spicules. *Nature*, 360:241–243, November 1992. doi:10.1038/360241a0.

T. J. Hallinan and T. N. Davis. Small-scale auroral arc distortions. *Planet. Space Sci.*, 18:1735, December 1970. doi:10.1016/0032-0633(70)90007-3.

S. Hamdi, W. E. Schiesser, and G. W Griffiths. Method of lines. *Scholarpedia*, 2(7):2859, 2007. revision #124335.

A. Harten. High Resolution Schemes for Hyperbolic Conservation Laws. *JCoPh*, 49:357–393, March 1983. doi:10.1016/0021-9991(83)90136-5.

J. W. Harvey. *Magnetic Fields Associated with Solar Active-Region Prominences*. PhD thesis, UNIVERSITY OF COLORADO AT BOULDER., 1969.

A. Hasegawa. *Plasma instabilities and nonlinear effects*. 1975.

P. Heinzel. Radiative Transfer in Solar Prominences. In J.-C. Vial and O. Engvold, editors, *Solar Prominences*, volume 415 of *Astrophysics and Space Science Library*, page 103, 2015. doi:10.1007/978-3-319-10416-4_5.

P. Heinzel and U. Anzer. On the Fine Structure of Solar Filaments. *Astrophysical Journal Letters*, 643:L65–L68, May 2006. doi:10.1086/504980.

P. Heinzel, S. Gunár, and U. Anzer. Fast approximate radiative transfer method for visualizing the fine structure of prominences in the hydrogen Hα line. *A&A*, 579:A16, July 2015. doi:10.1051/0004-6361/201525716.

H. L. F von Helmholtz. On discontinuous movements of fluids. *Philosophical Magazine Series 4*, 36(244): 337–346, 1868. doi:10.1080/14786446808640073.

J. V. Hollweg. Density fluctuations driven by Alfvén waves. *JGR*, 76:5155, 1971. doi:10.1029/JA076i022p05155.

J. V. Hollweg. Waves and instabilities in the solar wind. *Reviews of Geophysics and Space Physics*, 13:263–289, February 1975. doi:10.1029/RG013i001p00263.

J. V. Hollweg and P. A. Isenberg. Generation of the fast solar wind: A review with emphasis on the resonant cyclotron interaction. *Journal of Geophysical Research (Space Physics)*, 107:1147, July 2002. doi:10.1029/2001JA000270.

J. V. Hollweg and S. A. Markovskii. Cyclotron resonances of ions with obliquely propagating waves in coronal holes and the fast solar wind. *Journal of Geophysical Research (Space Physics)*, 107:1080, June 2002. doi:10.1029/2001JA000205.

J. A. Ionson. Resonant absorption of Alfvenic surface waves and the heating of solar coronal loops. *ApJ*, 226: 650–673, December 1978. doi:10.1086/156648.

P. A. Isenberg and J. V. Hollweg. Finite amplitude Alfven waves in a multi-ion plasma - Propagation, acceleration, and heating. *JGR*, 87:5023–5029, July 1982. doi:10.1029/JA087iA07p05023.

P. A. Isenberg and J. V. Hollweg. On the preferential acceleration and heating of solar wind heavy ions. *JGR*, 88:3923–3935, May 1983. doi:10.1029/JA088iA05p03923.

P. A. Isenberg and B. J. Vasquez. A Kinetic Model of Solar Wind Generation by Oblique Ion-cyclotron Waves. *ApJ*, 731:88, April 2011. doi:10.1088/0004-637X/731/2/88.

D. F. Jephcott. Alfvén Waves in a Gas Discharge. *Nature*, 183:1652–1654, June 1959. doi:10.1038/1831652a0.

D. F. Jephcott and P. M. Stocker. Hydromagnetic waves in a cylindrical plasma: an experiment. *Journal of Fluid Mechanics*, 13:587–596, 1962. doi:10.1017/S0022112062000956.

D. B. Jess, M. Mathioudakis, R. Erdélyi, P. J. Crockett, F. P. Keenan, and D. J. Christian. Alfvén Waves in the Lower Solar Atmosphere. *Science*, 323:1582, March 2009. doi:10.1126/science.1168680.

D. B. Jess, R. J. Morton, G. Verth, V. Fedun, S. D. T. Grant, and I. Giagkiozis. Multiwavelength Studies of MHD Waves in the Solar Chromosphere. An Overview of Recent Results. *SSRv*, 190:103–161, July 2015. doi:10.1007/s11214-015-0141-3.

J. Jing, J. Lee, T. J. Spirock, Y. Xu, H. Wang, and G. S. Choe. Periodic Motion along a Solar Filament Initiated by a Subflare. *Astrophysical Journal Letters*, 584:L103–L106, February 2003. doi:10.1086/373886.

H. Kamaya and R. Nishi. Comments on Alfvén Waves and Plasma Drift in a Slightly Ionized Gas. *ApJ*, 500: 257–261, June 1998. doi:10.1086/305691.

J. T. Karpen, C. R. DeVore, S. K. Antiochos, and E. Pariat. Reconnection-Driven Coronal-Hole Jets with Gravity and Solar Wind. *ApJ*, 834:62, January 2017. doi:10.3847/1538-4357/834/1/62.

R. Keppens, G. Tóth, R. H. J. Westermann, and J. P. Goedbloed. Growth and saturation of the Kelvin-Helmholtz instability with parallel and antiparallel magnetic fields. *Journal of Plasma Physics*, 61:1–19, January 1999. doi:10.1017/S0022377898007223.

M. L. Khodachenko, T. D. Arber, H. O. Rucker, and A. Hanslmeier. Collisional and viscous damping of MHD waves in partially ionized plasmas of the solar atmosphere. *A&A*, 422:1073–1084, August 2004. doi:10.1051/0004-6361:20034207.

E. Khomenko and M. Collados. Heating of the Magnetized Solar Chromosphere by Partial Ionization Effects. *ApJ*, 747:87, March 2012. doi:10.1088/0004-637X/747/2/87.

E. Khomenko, M. Collados, A. Díaz, and N. Vitas. Fluid description of multi-component solar partially ionized plasma. *Physics of Plasmas*, 21(9):092901, September 2014. doi:10.1063/1.4894106.

B. Kliem, I. E. Dammasch, W. Curdt, and K. Wilhelm. Correlated Dynamics of Hot and Cool Plasmas in the Main Phase of a Solar Flare. *Astrophysical Journal Letters*, 568:L61–L65, March 2002. doi:10.1086/340136.

I. V. Konikov, O. A. Gorbachev, G. V. Khazanov, and A. A. Chernov. Hydrodynamical equations for thermal electrons taking into account their scattering on ion-cyclotron waves in the outer plasmasphere of the earth. *P&SS*, 37:1157–1168, October 1989. doi:10.1016/0032-0633(89)90011-1.

R. Krasny. Numerical simulation of vortex sheet evolution. *Fluid Dynamics Research*, 3(1-4):93, 1988. URL `http://iopscience.iop.org/1873-7005/3/1-4/A12`.

J. Krtička and J. Kubát. Isothermal two-component stellar wind of hot stars. *A&A*, 359:983–990, July 2000.

J. Krtička and J. Kubát. Multicomponent radiatively driven stellar winds. I. Nonisothermal three-component wind of hot B stars. *A&A*, 369:222–238, April 2001. doi:10.1051/0004-6361:20010121.

R. Kulsrud and W. P. Pearce. The Effect of Wave-Particle Interactions on the Propagation of Cosmic Rays. *ApJ*, 156:445, May 1969. doi:10.1086/149981.

N. Kumar and B. Roberts. ION-Neutral Collisions Effect on MHD Surface Waves. *Sol. Phys.*, 214:241–266, June 2003. doi:10.1023/A:1024299029918.

M. Kuperus and E. Tandberg-Hanssen. The Nature of Quiescent Solar Prominences. *SoPh*, 2:39–48, July 1967.

doi:10.1007/BF00155891.

N. Labrosse, X. Li, and B. Li. On the Lyman α and β lines in solar coronal streamers. *A&A*, 455:719–723, August 2006. doi:10.1051/0004-6361:20065059.

N. Labrosse, P. Heinzel, J.-C. Vial, T. Kucera, S. Parenti, S. Gunár, B. Schmieder, and G. Kilper. Physics of Solar Prominences: I-Spectral Diagnostics and Non-LTE Modelling. *SSRv*, 151:243–332, April 2010. doi:10.1007/s11214-010-9630-6.

J. M. Laming and U. Feldman. The Variability of the Solar Coronal Helium Abundance: Polar Coronal Holes Compared to the Quiet Sun. *ApJ*, 591:1257–1266, July 2003. doi:10.1086/375395.

D. A. Landman, S. J. Edberg, and C. D. Laney. Measurements of H-beta, He D3, and Ca/+/ 8542-A line emission in quiescent prominences. *ApJ*, 218:888–897, December 1977. doi:10.1086/155744.

I. Langmuir. Oscillations in Ionized Gases. *Proceedings of the National Academy of Science*, 14:627–637, August 1928. doi:10.1073/pnas.14.8.627.

J. E. Leake and T. D. Arber. The emergence of magnetic flux through a partially ionised solar atmosphere. *A&A*, 450:805–818, May 2006. doi:10.1051/0004-6361:20054099.

J. E. Leake, T. D. Arber, and M. L. Khodachenko. Collisional dissipation of Alfvén waves in a partially ionised solar chromosphere. *A&A*, 442:1091–1098, November 2005. doi:10.1051/0004-6361:20053427.

J. E. Leake, C. R. DeVore, J. P. Thayer, A. G. Burns, G. Crowley, H. R. Gilbert, J. D. Huba, J. Krall, M. G. Linton, V. S. Lukin, and W. Wang. Ionized Plasma and Neutral Gas Coupling in the Sun's Chromosphere and Earth's Ionosphere/Thermosphere. *SSRv*, 184:107–172, November 2014. doi:10.1007/s11214-014-0103-1.

B. Lehnert. Magneto-Hydrodynamic Waves in Liquid Sodium. *Physical Review*, 94:815–824, May 1954. doi:10.1103/PhysRev.94.815.

R. B. Leighton, R. W. Noyes, and G. W. Simon. Velocity Fields in the Solar Atmosphere. I. Preliminary Report. *ApJ*, 135:474, March 1962. doi:10.1086/147285.

N. R. Lewkow, V. Kharchenko, and P. Zhang. Energy Relaxation of Helium Atoms in Astrophysical Gases. *ApJ*, 756:57, September 2012. doi:10.1088/0004-637X/756/1/57.

B. Li and X. Li. Propagation of Non-Wentzel-Kramers-Brillouin Alfvén Waves in a Multicomponent Solar Wind with Differential Ion Flow. *ApJ*, 661:1222–1233, June 2007. doi:10.1086/514324.

B. Li and X. Li. Effects of Non-WKB Alfvén Waves on a Multicomponent Solar Wind with Differential Ion Flow. *ApJ*, 682:667-678, July 2008. doi:10.1086/588809.

D. H. Liebenberg and M. M. Hoffman. Temporal Observations of the λ" 5303 Emission Line Profile during the 74 Minute Totality from the Concorde SST at the 30 June 1973 Total Solar Eclipse: Preliminary Intensity Variations above an Active Region (presented by D. H. Liebenberg). In G. A. Newkirk, editor, *Coronal Disturbances*, volume 57 of *IAU Symposium*, page 485, 1974.

M. J. Lighthill. Studies on Magneto-Hydrodynamic Waves and other Anisotropic Wave Motions. *Philosophical Transactions of the Royal Society of London Series A*, 252:397–430, March 1960. doi:10.1098/rsta.1960.0010.

Y. Lin. *Magnetic Field Topology Inferred from Studies of Fine Threads in Solar Prominences*. PhD thesis, University of Oslo, 2004.

Y. Lin. Filament Thread-like Structures and Their Small-amplitude Oscillations. *SSRv*, 158:237–266, July 2011. doi:10.1007/s11214-010-9672-9.

Y. Lin, O. R. Engvold, and J. E. Wiik. Counterstreaming in a Large Polar Crown Filament. *SoPh*, 216:109–120, September 2003. doi:10.1023/A:1026150809598.

Y. Lin, O. Engvold, L. Rouppe van der Voort, J. E. Wiik, and T. E. Berger. Thin threads of solar filaments. *Solar Physics*, 226(2):239–254, 2005. ISSN 0038-0938. doi:10.1007/s11207-005-6876-3.

Y. Lin, O. Engvold, L. H. M. Rouppe van der Voort, and M. van Noort. Evidence of Traveling Waves in Filament Threads. *SoPh*, 246:65–72, November 2007. doi:10.1007/s11207-007-0402-8.

M. Luna and J. Karpen. Large-amplitude Longitudinal Oscillations in a Solar Filament. *Astrophysical Journal Letters*, 750:L1, May 2012. doi:10.1088/2041-8205/750/1/L1.

S. Lundquist. Experimental Demonstration of Magneto-hydrodynamic Waves. *Nature*, 164:145–146, July 1949. doi:10.1038/164145a0.

D. H. Mackay, J. T. Karpen, J. L. Ballester, B. Schmieder, and G. Aulanier. Physics of Solar Prominences: II-Magnetic Structure and Dynamics. *SSRv*, 151:333–399, April 2010. doi:10.1007/s11214-010-9628-0.

E. Marsch and D. Verscharen. On nonlinear Alfvén-cyclotron waves in multi-species plasma. *Journal of Plasma Physics*, 77:385–403, June 2011. doi:10.1017/S0022377810000541.

C. E. Martin, J. Heyvaerts, and E. R. Priest. Alfven wave support of a dwarf molecular cloud. I. an isothermal model. *A&A*, 326:1176–1186, October 1997.

D. Martínez-Gómez, R. Soler, and J. Terradas. Onset of the Kelvin-Helmholtz instability in partially ionized magnetic flux tubes. *A&A*, 578:A104, June 2015. doi:10.1051/0004-6361/201525785.

D. Martínez-Gómez, R. Soler, and J. Terradas. Multi-fluid Approach to High-frequency Waves in Plasmas: I. Small-amplitude Regime in Fully Ionized Medium. *ApJ*, 832:101, December 2016. doi:10.3847/0004-637X/832/2/101.

D. Martínez-Gómez, R. Soler, and J. Terradas. Multi-fluid Approach to High-frequency Waves in Plasmas. II. Small-amplitude Regime in Partially Ionized Media. *ApJ*, 837:80, March 2017. doi:10.3847/1538-4357/aa5eab.

T. Matsumoto and K. Shibata. Nonlinear Propagation of Alfvén Waves Driven by Observed Photospheric Motions: Application to the Coronal Heating and Spicule Formation. *ApJ*, 710:1857–1867, February 2010. doi:10.1088/0004-637X/710/2/1857.

S. W. McIntosh, B. de Pontieu, M. Carlsson, V. Hansteen, P. Boerner, and M. Goossens. Alfvénic waves with sufficient energy to power the quiet solar corona and fast solar wind. *Nature*, 475:477–480, July 2011. doi:10.1038/nature10235.

R. Mecheri. Properties of Ion-Cyclotron Waves in the Open Solar Corona. *SoPh*, 282:133–146, January 2013. doi:10.1007/s11207-012-0134-2.

R. Mecheri and E. Marsch. Drift instabilities in the solar corona within the multi-fluid description. *A&A*, 481: 853–860, April 2008. doi:10.1051/0004-6361:20079221.

E. T. Meier. *Modeling Plasmas with Strong Anisotropy, Neutral Fluid Effects, and Open Boundaries.* PhD thesis, University of Washington, 2011.

L. Mestel and L. Spitzer, Jr. Star formation in magnetic dust clouds. *MNRAS*, 116:503, 1956. doi:10.1093/mnras/116.5.503.

R. Molowny-Horas, E. Wiehr, H. Balthasar, R. Oliver, and J. L. Ballester. Prominence Doppler oscillations. In *JOSO Annu. Rep., 1998*, pages 126–127, 1999.

G. E. Moreton and H. E. Ramsey. Recent Observations of Dynamical Phenomena Associated with Solar Flares. *PASP*, 72:357, October 1960. doi:10.1086/127549.

R. J. Morton, G. Verth, D. B. Jess, D. Kuridze, M. S. Ruderman, M. Mathioudakis, and R. Erdélyi. Observations of ubiquitous compressive waves in the Sun's chromosphere. *Nature Communications*, 3:1315, December 2012. doi:10.1038/ncomms2324.

H. M. Mott-Smith. History of "plasmas". *Nature*, 233:219, 1971. doi:10.1038/233219a0.

T. C. Mouschovias, G. E. Ciolek, and S. A. Morton. Hydromagnetic waves in weakly-ionized media - I. Basic theory, and application to interstellar molecular clouds. *MNRAS*, 415:1751–1782, August 2011. doi:10.1111/j.1365-2966.2011.18817.x.

G. Mueller. Experimental study of torsional Alfven waves in a cylindrical partially ionized magnetoplasma. *Plasma Physics*, 16:813–822, September 1974. doi:10.1088/0032-1028/16/9/003.

K. Murawski and B. Roberts. Numerical simulations of fast MHD waves in a coronal plasma. IV - Impulsively generated nonlinear waves. *SoPh*, 145:65–75, May 1993. doi:10.1007/BF00627983.

K. Murawski, R. Oliver, and J. L. Ballester. Nonlinear fast magnetosonic waves in solar coronal holes. *A&A*, 375:264–274, August 2001. doi:10.1051/0004-6361:20010869.

N. Murphy, E. J. Smith, B. T. Tsurutani, A. Balogh, and D. J. Southwood. Further Studies of Waves Accompanying the Solar Wind Pick-up of Interstellar Hydrogen. *SSRv*, 72:447–452, April 1995. doi:10.1007/BF00768819.

R. W. Nightingale, M. J. Aschwanden, and N. E. Hurlburt. Time Variability of EUV Brightenings in Coronal Loops Observed with TRACE. *SoPh*, 190:249–265, December 1999. doi:10.1023/A:1005211618498.

L. Ofman. The origin of the slow solar wind in coronal streamers. *Advances in Space Research*, 33:681–688, 2004. doi:10.1016/S0273-1177(03)00235-7.

L. Ofman. Wave Modeling of the Solar Wind. *Living Reviews in Solar Physics*, 7:4, October 2010. doi:10.12942/lrsp-2010-4.

L. Ofman and J. M. Davila. Nonlinear resonant absorption of Alfvén waves in three dimensions, scaling laws, and coronal heating. *JGR*, 100:23427–23442, December 1995. doi:10.1029/95JA01907.

L. Ofman, M. Romoli, G. Poletto, G. Noci, and J. L. Kohl. Ultraviolet Coronagraph Spectrometer Observations of Density Fluctuations in the Solar Wind. *Astrophysical Journal Letters*, 491:L111–L114, December 1997. doi:10.1086/311067.

K. W. Ogilvie and R. J. Fitzenreiter. The Kelvin-Helmholtz instability at the magnetopause and inner boundary layer surface. *JGR*, 94:15113–15123, November 1989. doi:10.1029/JA094iA11p15113.

T. J. Okamoto, H. Nakai, A. Keiyama, N. Narukage, S. UeNo, R. Kitai, H. Kurokawa, and K. Shibata.

Filament Oscillations and Moreton Waves Associated with EIT Waves. *ApJ*, 608:1124–1132, June 2004. doi:10.1086/420838.

T. J. Okamoto, S. Tsuneta, T. E. Berger, K. Ichimoto, Y. Katsukawa, B. W. Lites, S. Nagata, K. Shibata, T. Shimizu, R. A. Shine, Y. Suematsu, T. D. Tarbell, and A. M. Title. Coronal Transverse Magnetohydrodynamic Waves in a Solar Prominence. *Science*, 318:1577, December 2007. doi:10.1126/science.1145447.

R. Oliver. Prominence Seismology Using Small Amplitude Oscillations. *SSRv*, 149:175–197, December 2009. doi:10.1007/s11214-009-9527-4.

R. Oliver, K. Murawski, and J. L. Ballester. Numerical simulations of impulsively generated MHD waves in a potential coronal arcade. *A&A*, 330:726–738, February 1998.

R. Oliver, R. Soler, J. Terradas, and T. V. Zaqarashvili. Dynamics of Coronal Rain and Descending Plasma Blobs in Solar Prominences. II. Partially Ionized Case. *ApJ*, 818:128, February 2016. doi:10.3847/0004-637X/818/2/128.

B. P. Pandey and C. B. Dwivedi. Surface wave propagation in non-ideal plasmas. *MNRAS*, 447:3604–3611, March 2015. doi:10.1093/mnras/stu2503.

B. P. Pandey and M. Wardle. Hall Magnetohydrodynamics of weakly-ionized plasma. *ArXiv Astrophysics e-prints*, July 2006.

B. P. Pandey and M. Wardle. Hall magnetohydrodynamics of partially ionized plasmas. *MNRAS*, 385:2269–2278, April 2008. doi:10.1111/j.1365-2966.2008.12998.x.

S. Parenti. Solar Prominences: Observations. *Living Reviews in Solar Physics*, 11:1, March 2014. doi:10.12942/lrsp-2014-1.

E. N. Parker. Dynamics of the Interplanetary Gas and Magnetic Fields. *ApJ*, 128:664, November 1958. doi:10.1086/146579.

C. E. Parnell and I. De Moortel. A contemporary view of coronal heating. *Philosophical Transactions of the Royal Society of London Series A*, 370:3217–3240, July 2012. doi:10.1098/rsta.2012.0113.

J. H. Piddington. Solar atmospheric heating by hydromagnetic waves. *MNRAS*, 116:314, 1956. doi:10.1093/mnras/116.3.314.

C. Pinto, D. Galli, and F. Bacciotti. Three-fluid plasmas in star formation. I. Magneto-hydrodynamic equations. *A&A*, 484:1–15, June 2008. doi:10.1051/0004-6361:20078818.

G. Pouget, K. Bocchialini, and J. Solomon. Oscillations in a solar filament: first observation of long periods in the HeI 584.33 Å line, modelling and diagnostic. *A&A*, 450:1189–1198, May 2006. doi:10.1051/0004-6361:20053886.

R. E. Pudritz. The stability of molecular clouds. *ApJ*, 350:195–208, February 1990. doi:10.1086/168373.

K. Rahbarnia, S. Ullrich, K. Sauer, O. Grulke, and T. Klinger. Alfvén wave dispersion behavior in single- and multicomponent plasmas. *Physics of Plasmas*, 17(3):032102, March 2010. doi:10.1063/1.3322852.

R. Rankin, P. Frycz, V. T. Tikhonchuk, and J. C. Samson. Nonlinear standing shear Alfvén waves in the Earth's magnetosphere. *JGR*, 99:21291–21302, November 1994. doi:10.1029/94JA01629.

Rayleigh. Investigation of the character of the equilibrium of an incompressible heavy fluid of variable density. *Proceedings of the London Mathematical Society*, s1-14(1):170–177, 1882. ISSN 1460-244X. doi:10.1112/plms/s1-14.1.170.

E. Robbrecht, E. Verwichte, D. Berghmans, J. F. Hochedez, S. Poedts, and V. M. Nakariakov. Slow magnetoacoustic waves in coronal loops: EIT and TRACE. *A&A*, 370:591–601, May 2001. doi:10.1051/0004-6361:20010226.

B. Roberts, P. M. Edwin, and A. O. Benz. Fast pulsations in the solar corona. *Nature*, 305:688–690, October 1983. doi:10.1038/305688a0.

B. Roberts, P. M. Edwin, and A. O. Benz. On coronal oscillations. *ApJ*, 279:857–865, April 1984. doi:10.1086/161956.

V. Rušin, M. Druckmüller, P. Aniol, M. Minarovjech, M. Saniga, Z. Mikić, J. A. Linker, R. Lionello, P. Riley, and V. S. Titov. Comparing eclipse observations of the 2008 August 1 solar corona with an MHD model prediction. *A&A*, 513:A45, April 2010. doi:10.1051/0004-6361/200912778.

D. A. Ryutov and M. P. Ryutova. Sound oscillations in a plasma with "magnetic filaments". *Soviet Journal of Experimental and Theoretical Physics*, 43:491, March 1976.

M. Ryutova, T. Berger, Z. Frank, T. Tarbell, and A. Title. Observation of Plasma Instabilities in Quiescent Prominences. *SoPh*, 267:75–94, November 2010. doi:10.1007/s11207-010-9638-9.

E. N. Sarmin and L. A. Chudov. On the stability of the numerical integration of systems of ordinary differential equations arising in the use of the straight line method. *U.S.S.R. Comput. Math. Math. Phys.*, 3:1537–1543,

1963. doi:10.1016/0041-5553(63)90256-8.

J. M. Scalo. Heating of dense interstellar clouds by magnetic ion slip - A constraint on cloud field strengths. *ApJ*, 213:705–711, May 1977. doi:10.1086/155200.

W.E. Schiesser. *The Numerical Method of Lines: Integration of Partial Differential Equations*. Academic Press, 1991. ISBN 9780126241303. URL `https://books.google.es/books?id=1vLFQgAACAAJ`.

B. Schmieder, R. Chandra, A. Berlicki, and P. Mein. Velocity vectors of a quiescent prominence observed by Hinode/SOT and the MSDP (Meudon). *A&A*, 514:A68, May 2010. doi:10.1051/0004-6361/200913477.

C. J. Schrijver, A. M. Title, T. E. Berger, L. Fletcher, N. E. Hurlburt, R. W. Nightingale, R. A. Shine, T. D. Tarbell, J. Wolfson, L. Golub, J. A. Bookbinder, E. E. Deluca, R. A. McMullen, H. P. Warren, C. C. Kankelborg, B. N. Handy, and B. de Pontieu. A new view of the solar outer atmosphere by the Transition Region and Coronal Explorer. *SoPh*, 187:261–302, July 1999. doi:10.1023/A:1005194519642.

R. W. Schunk. Mathematical structure of transport equations for multispecies flows. *Reviews of Geophysics and Space Physics*, 15:429–445, November 1977. doi:10.1029/RG015i004p00429.

N. A. J. Schutgens. Prominence oscillations and stability. Communicating the distant photospheric boundary. *A&A*, 323:969–985, July 1997a.

N. A. J. Schutgens. Vertical prominence oscillations and stability. A comparison of the influence of the distant photosphere in Inverse Polarity and Normal Polarity prominence models. *A&A*, 325:352–359, September 1997b.

M. Schwarzschild. On Noise Arising from the Solar Granulation. *ApJ*, 107:1, January 1948. doi:10.1086/144983.

M. Shadmehri and T. P. Downes. Kelvin Helmholtz instability in a weakly ionized layer. *Ap&SS*, 312:79–84, November 2007. doi:10.1007/s10509-007-9655-9.

E. C. Sittler, Jr. and M. Guhathakurta. Semiempirical Two-dimensional MagnetoHydrodynamic Model of the Solar Corona and Interplanetary Medium. *ApJ*, 523:812–826, October 1999. doi:10.1086/307742.

R. Soler, R. Oliver, and J. L. Ballester. Magnetohydrodynamic Waves in a Partially Ionized Filament Thread. *ApJ*, 699:1553–1562, July 2009a. doi:10.1088/0004-637X/699/2/1553.

R. Soler, R. Oliver, and J. L. Ballester. Resonantly Damped Kink Magnetohydrodynamic Waves in a Partially Ionized Filament Thread. *ApJ*, 707:662–670, December 2009b. doi:10.1088/0004-637X/707/1/662.

R. Soler, J. Andries, and M. Goossens. Resonant Alfvén waves in partially ionized plasmas of the solar atmosphere. *A&A*, 537:A84, January 2012a. doi:10.1051/0004-6361/201118235.

R. Soler, A. J. Díaz, J. L. Ballester, and M. Goossens. Kelvin-Helmholtz Instability in Partially Ionized Compressible Plasmas. *ApJ*, 749:163, April 2012b. doi:10.1088/0004-637X/749/2/163.

R. Soler, M. Carbonell, and J. L. Ballester. Magnetoacoustic Waves in a Partially Ionized Two-fluid Plasma. *ApJs*, 209:16, November 2013a. doi:10.1088/0067-0049/209/1/16.

R. Soler, M. Carbonell, J. L. Ballester, and J. Terradas. Alfvén Waves in a Partially Ionized Two-fluid Plasma. *ApJ*, 767:171, April 2013b. doi:10.1088/0004-637X/767/2/171.

R. Soler, A. J. Díaz, J. L. Ballester, and M. Goossens. Effect of partial ionization on wave propagation in solar magnetic flux tubes. *A&A*, 551:A86, March 2013c. doi:10.1051/0004-6361/201220576.

R. Soler, J. L. Ballester, and T. V. Zaqarashvili. Overdamped Alfvén waves due to ion-neutral collisions in the solar chromosphere. *A&A*, 573:A79, January 2015a. doi:10.1051/0004-6361/201423930.

R. Soler, M. Carbonell, and J. L. Ballester. On the Spatial Scales of Wave Heating in the Solar Chromosphere. *ApJ*, 810:146, September 2015b. doi:10.1088/0004-637X/810/2/146.

R. Soler, J. Terradas, R. Oliver, and J. L. Ballester. The role of Alfvén wave heating in solar prominences. *A&A*, 592:A28, July 2016. doi:10.1051/0004-6361/201628722.

P. Song and V. M. Vasyliūnas. Heating of the solar atmosphere by strong damping of Alfvén waves. *Journal of Geophysical Research (Space Physics)*, 116:A09104, September 2011. doi:10.1029/2011JA016679.

L. Spitzer. *Physics of Fully Ionized Gases*. Interscience, 1962.

H. C. Spruit. Motion of magnetic flux tubes in the solar convection zone and chromosphere. *A&A*, 98:155–160, May 1981.

A. K. Srivastava, J. Shetye, K. Murawski, J. G. Doyle, M. Stangalini, E. Scullion, T. Ray, D. P. Wójcik, and B. N. Dwivedi. High-frequency torsional Alfvén waves as an energy source for coronal heating. *Scientific Reports*, 7:43147, March 2017. doi:10.1038/srep43147.

T. H. Stix. *Waves in plasmas*. American Institute of Physics, 1992.

T. K. Suzuki. Self-consistent Simulations of Alfvén Wave Driven Winds from the Sun and Stars. *SSRv*, 158:339–363, July 2011. doi:10.1007/s11214-010-9709-0.

D. Sviatsky. L'Astronomie dans les Chroniques Russes. *L'Astronomie*, 37:418–420, 1923.

G. Taylor. The Instability of Liquid Surfaces when Accelerated in a Direction Perpendicular to their Planes. I. *Proceedings of the Royal Society of London Series A*, 201:192–196, March 1950. doi:10.1098/rspa.1950.0052.

J. Terradas and L. Ofman. Loop Density Enhancement by Nonlinear Magnetohydrodynamic Waves. *ApJ*, 610: 523–531, July 2004. doi:10.1086/421514.

J. Terradas, R. Molowny-Horas, E. Wiehr, H. Balthasar, R. Oliver, and J. L. Ballester. Two-dimensional distribution of oscillations in a quiescent solar prominence. *A&A*, 393:637–647, October 2002. doi:10.1051/0004-6361:20020967.

J. Terradas, M. Carbonell, R. Oliver, and J. L. Ballester. Time damping of linear non-adiabatic magnetoacoustic waves in a slab-like quiescent prominence. *A&A*, 434:741–749, May 2005. doi:10.1051/0004-6361:20041984.

J. Terradas, J. Andries, M. Goossens, I. Arregui, R. Oliver, and J. L. Ballester. Nonlinear Instability of Kink Oscillations due to Shear Motions. *Astrophysical Journal Letters*, 687:L115, November 2008a. doi:10.1086/593203.

J. Terradas, I. Arregui, R. Oliver, and J. L. Ballester. Transverse Oscillations of Flowing Prominence Threads Observed with Hinode. *Astrophysical Journal Letters*, 678:L153–L156, May 2008b. doi:10.1086/588728.

J. Terradas, R. Soler, R. Oliver, and J. L. Ballester. On the Support of Neutrals Against Gravity in Solar Prominences. *Astrophysical Journal Letters*, 802:L28, April 2015. doi:10.1088/2041-8205/802/2/L28.

J. J. Thomson. Xl. cathode rays. *Philosophical Magazine Series 5*, 44(269):293–316, 1897. doi:10.1080/14786449708621070.

W. Thomson. *Mathematical and Physical Papers*, volume 4 of *Cambridge Library Collection - Physical Sciences*. Cambridge University Press, 1910. doi:10.1017/CBO9780511996047.

V. T. Tikhonchuk, R. Rankin, P. Frycz, and J. C. Samson. Nonlinear dynamics of standing shear Alfvén waves. *Physics of Plasmas*, 2:501–515, February 1995. doi:10.1063/1.870975.

S. Tomczyk and S. W. McIntosh. Time-Distance Seismology of the Solar Corona with CoMP. *ApJ*, 697: 1384–1391, June 2009. doi:10.1088/0004-637X/697/2/1384.

S. Tomczyk, S. W. McIntosh, S. L. Keil, P. G. Judge, T. Schad, D. H. Seeley, and J. Edmondson. Alfvén Waves in the Solar Corona. *Science*, 317:1192, August 2007. doi:10.1126/science.1143304.

D. Tripathi, H. Isobe, and R. Jain. Large Amplitude Oscillations in Prominences. *SSRv*, 149:283–298, December 2009. doi:10.1007/s11214-009-9583-9.

T. Tsubaki. Observations of periodic oscillations or waves in the solar corona and prominences. In R. C. Altrock, editor, *Solar and Stellar Coronal Structure and Dynamics*, pages 140–149, 1988.

T. Tsubaki and A. Takeuchi. Periodic oscillations found in the velocity field of a quiescent prominence. *SoPh*, 104:313–320, April 1986. doi:10.1007/BF00159084.

C.-Y. Tu. A solar wind model with the power spectrum of Alfvenic fluctuations. *SoPh*, 109:149–186, September 1987. doi:10.1007/BF00167405.

C.-Y. Tu and E. Marsch. Two-Fluid Model for Heating of the Solar Corona and Acceleration of the Solar Wind by High-Frequency Alfven Waves. *SoPh*, 171:363–391, April 1997. doi:10.1023/A:1004968327196.

J. Tu and P. Song. A Study of Alfvén Wave Propagation and Heating the Chromosphere. *ApJ*, 777:53, November 2013. doi:10.1088/0004-637X/777/1/53.

Y. Uchida. Diagnosis of Coronal Magnetic Structure by Flare-Associated Hydromagnetic Disturbances. *PASJ*, 22:341, 1970.

T. W. J. Unti and M. Neugebauer. Alfvén Waves in the Solar Wind. *Physics of Fluids*, 11:563–568, March 1968. doi:10.1063/1.1691953.

G. H. J. van den Oord and M. Kuperus. The effect of retardation on the stability of current filaments. *SoPh*, 142:113–129, November 1992. doi:10.1007/BF00156636.

E. Verwichte, V. M. Nakariakov, and A. W. Longbottom. On the evolution of a nonlinear Alfvén pulse. *Journal of Plasma Physics*, 62:219–232, August 1999. doi:10.1017/S0022377899007771.

E. Verwichte, V. M. Nakariakov, and F. C. Cooper. Transverse waves in a post-flare supra-arcade. *A&A*, 430: L65–L68, January 2005. doi:10.1051/0004-6361:200400133.

J.-C. Vial and O. Engvold, editors. *Solar Prominences*, volume 415 of *Astrophysics and Space Science Library*. 2015. doi:10.1007/978-3-319-10416-4.

J. Vranjes and M. Kono. On the Alfvén wave cut-off in partly ionized collisional plasmas. *Physics of Plasmas*, 21(1):012110, January 2014. doi:10.1063/1.4862781.

J. Vranjes and P. S. Krstic. Collisions, magnetization, and transport coefficients in the lower solar atmosphere. *ApJ*, 554:A22, June 2013. doi:10.1051/0004-6361/201220738.

J. Vranjes and B. P. Pandey. Some unexplored features of the nonlinear compressive magnetoacoustic Alfvénic waves. *PhyS*, 88(3):035504, September 2013. doi:10.1088/0031-8949/88/03/035504.

J. Vranjes and S. Poedts. Features of ion acoustic waves in collisional plasmas. *Physics of Plasmas*, 17(2): 022104, February 2010. doi:10.1063/1.3309490.

T. Wang, S. K. Solanki, W. Curdt, D. E. Innes, and I. E. Dammasch. Doppler Shift Oscillations of Hot Solar Coronal Plasma Seen by SUMER: A Signature of Loop Oscillations? *Astrophysical Journal Letters*, 574: L101–L104, July 2002. doi:10.1086/342189.

A. Warmuth and G. Mann. A model of the Alfvén speed in the solar corona. *A&A*, 435:1123–1135, June 2005. doi:10.1051/0004-6361:20042169.

T. Watanabe. Waves in a rarefied ionized gas propagated transverse to an external magnetic field. *Canadian Journal of Physics*, 39:1044, 1961a. doi:10.1139/p61-114.

T. Watanabe. Alfvén waves in partially ionized gases. *Canadian Journal of Physics*, 39:1197, 1961b. doi:10.1139/p61-135.

C. Watson, E. G. Zweibel, F. Heitsch, and E. Churchwell. Kelvin-Helmholtz Instability in a Weakly Ionized Medium. *ApJ*, 608:274–281, June 2004. doi:10.1086/392500.

E. J. Weber. Multi-Ion Plasmas in Astrophysics. II: Motion of Isothermal Plasmas in a Gravitational Field. *Ap&SS*, 20:401–415, February 1973a. doi:10.1007/BF00642211.

E. J. Weber. Multi-Ion Plasmas in Astrophysics. I: General Requirements for the Existence of Critical Points. *Ap&SS*, 20:391–400, February 1973b. doi:10.1007/BF00642210.

D. G. Wentzel. Hydromagnetic surface waves on cylindrical fluxtubes. *A&A*, 76:20–23, June 1979.

Y. C. Whang and N. F. Ness. Observations and interpretation of the lunar mach cone. *JGR*, 75:6002, 1970. doi:10.1029/JA075i031p06002.

E. Wiehr, H. Balthasar, and G. Stellmacher. Oscillations of the H-alha emission in solar prominences. *SoPh*, 94:285–288, September 1984. doi:10.1007/BF00151318.

E. Wiehr, H. Balthasar, and G. Stellmacher. Doppler Velocity Oscillations in Quiescent Prominences. *Hvar Observatory Bulletin*, 13:131, 1989.

L. C. Woods. Hydromagnetic waves in a cylindrical plasma. *Journal of Fluid Mechanics*, 13:570–586, 1962. doi:10.1017/S0022112062000944.

Z. Yi and O. Engvold. Vertical velocities and oscillations in quiescent filaments. *SoPh*, 134:275–286, August 1991. doi:10.1007/BF00152648.

T. V. Zaqarashvili, M. L. Khodachenko, and H. O. Rucker. Magnetohydrodynamic waves in solar partially ionized plasmas: two-fluid approach. *A&A*, 529:A82, May 2011a. doi:10.1051/0004-6361/201016326.

T. V. Zaqarashvili, M. L. Khodachenko, and H. O. Rucker. Damping of Alfvén waves in solar partially ionized plasmas: effect of neutral helium in multi-fluid approach. *A&A*, 534:A93, October 2011b. doi:10.1051/0004-6361/201117380.

T. V. Zaqarashvili, M. Carbonell, J. L. Ballester, and M. L. Khodachenko. Cut-off wavenumber of Alfvén waves in partially ionized plasmas of the solar atmosphere. *A&A*, 544:A143, August 2012. doi:10.1051/0004-6361/201219763.

T. V. Zaqarashvili, M. L. Khodachenko, and R. Soler. Torsional Alfvén waves in partially ionized solar plasma: effects of neutral helium and stratification. *A&A*, 549:A113, January 2013. doi:10.1051/0004-6361/201220272.

J. B. Zirker, O. Engvold, and Z. Yi. Flows in quiescent prominences. *SoPh*, 150:81–86, March 1994. doi:10.1007/BF00712878.

J. B. Zirker, O. Engvold, and S. F. Martin. Counter-streaming gas flows in solar prominences as evidence for vertical magnetic fields. *Nature*, 396:440–441, December 1998. doi:10.1038/24798.

E. G. Zweibel. Magnetic reconnection in partially ionized gases. *ApJ*, 340:550–557, May 1989. doi:10.1086/167416.